THE HONG KONG
POLYTECHNIC UNIVERSITY
香港理工大學
Pao Yue-kong Library
包玉剛圖書館

Copyright Undertaking

This thesis is protected by copyright, with all rights reserved.

By reading and using the thesis, the reader understands and agrees to the following terms:

1. The reader will abide by the rules and legal ordinances governing copyright regarding the use of the thesis.
2. The reader will use the thesis for the purpose of research or private study only and not for distribution or further reproduction or any other purpose.
3. The reader agrees to indemnify and hold the University harmless from and against any loss, damage, cost, liability or expenses arising from copyright infringement or unauthorized usage.

IMPORTANT

If you have reasons to believe that any materials in this thesis are deemed not suitable to be distributed in this form, or a copyright owner having difficulty with the material being included in our database, please contact lbsys@polyu.edu.hk providing details. The Library will look into your claim and consider taking remedial action upon receipt of the written requests.

Pao Yue-kong Library, The Hong Kong Polytechnic University, Hung Hom, Kowloon, Hong Kong

http://www.lib.polyu.edu.hk

AMMONIUM TRANSPORT AND REDUCTION IN DEIONIZATION CELL INTEGRATED ANAEROBIC TREATMENT AND SOLID OXIDE FUEL CELLS AS A NET ENERGY PRODUCER

XU LINJI

PhD

The Hong Kong Polytechnic University

2018

The Hong Kong Polytechnic University

Department of Civil and Environmental Engineering

Ammonium Transport and Reduction in Deionization Cell Integrated Anaerobic Treatment and Solid Oxide Fuel Cells as A Net Energy Producer

XU Linji

A thesis submitted in partial fulfillment of the

requirements for the Degree of Doctor of Philosophy

October 2017

CERTIFICATE OF ORIGINALITY

I hereby declare that this thesis is my own work and that, to the best of my knowledge and belief, it reproduces no material previously published or written, nor material that has been accepted for the award of any other degree or diploma, except where due acknowledgement has been made in the text.

_____(Signed)

_____XU LINJI_____(Name of student)

ABSTRACT

Since human entered industrial era, our behaviors have accelerated energy scarcity and environmental pollution, which is threatening our unique living planet. To decelerate fuel consumption and prevent our earth from further deterioration, we are thinking of ways to save the traditional fossil fuels and search for sustainable energy. Biomass, as one type of new energy, has been investigated for some decades. Most of the biomass comes from organic wastes, especially from wastewater treatment plants. It is widely known that wastewater treatment plants represent a portion of the broader nexus between energy and water, which has raised the worldwide attention. Logically, energy capture from wastewater streams is considered to be a new and noteworthy approach for eliminating environmental pollution and offsetting the traditional fuel consumption. Such as anaerobic treatment (AT) combined thermal engines has been employed to convert the organic wastes to useful electricity. Yet, an enormous amount of recoverable energy like ammonia (NH_3) or hydrogen (H_2) has not been well considered up to date.

Toward this, this thesis reported a hybrid system of three techniques including anaerobic digestion (AD), electrodeionization (EDI), and solid oxide fuel cells (SOFCs), named AD/Landfill-EDI-SOFCs. This system was used to separate and remove different kinds of ammonium wastewater. When AD/Landfill-EDI-SOFCs was used to capture energy from anaerobic digestate and landfill leachate, the

experimental results displayed excellent performances of inorganic ion removal and energy conversion, which signified that this system would be a potential perspective of environment protection. Specifically, under the optimal conditions (3.0 V applied voltage and 7.5 mm internal electrode distance, IED), EDI section removed 70-95% NH_4^+ ion from 0.025-0.5 M synthetic NH_4^+-N wastewater. Regarding energy benefits of EDI, the energy balance Ratio (EBR) indicated that concentrated NH_4^+-N sewage (> 0.25 M) was its appropriate range according to collected fuels (NH_3 and H_2) and consumed electricity. In terms of electricity generation of SOFCs, synthetic gases (NH_3-H_2 and CH_4-CO_2) and the real biogas from the lab-scale reactor can be used as its fuels for electricity generation because it gained 900-1380 mW cm^{-2} peak power densities at 750 °C operating temperature. To assess the net energy benefit, the comparison of energy recovery between the existing process (landfill, ammonia stripping, and combined heat and power, Landfill-AS-CHP) and the proposed system (Landfill-EDI-SOFCs) was carried out via a municipal landfill site in Hong Kong as an example. The results demonstrated that EBR rose from 1.11 (Landfill-AS-CHP) to 1.75 (Landfill-EDI-SOFCs). The removal rate of inorganic ions reached 80% from the raw landfill leachate, and the removal rate of ammonium ion attached 99%. Hence, AD-EDI-SOFCs hybrid system was thought to be feasible for the upgrades of anaerobic processes for energy potential extraction from wastewater streams.

According to energy footprint of the AD-EDI-SOFCs system, whereas the process of NH_4^+ separation including the solution, ion exchange membrane, and electrochemical reactions consumed about 56% recovered energy by EDI. This would be owing to the weak conductivity of the ammonium electrolyte. To understand the reason for such a high level of energy consumption in this process on the earth, studies thus went to the mechanisms of ion separation and electrode behaviors. The effect of the supporting

electrolyte on NH_4^+ separation was initiated through experiments and theoretical calculations. The results signified that the concentrated Na_2SO_4 electrolyte (0.125-0.75 M) contributed an increase in current density from 1.6 mA cm^{-2} at 0.125 M to 40 mA cm^{-2} at 0.75 M. The concentration polarization between two sides of ion exchange membrane was described. The difference in the magnitude of concentration polarization: NH_4^+ concentration decreased to almost 0 M in the left-side boundary layer but increased to 0.65 M in the right-side boundary layer in 0.125-0.75 M. Also, the increase in Na_2SO_4 concentration contributed to increases in the limiting current density (LCD, from 14 mA cm^{-2} to 20 mA cm^{-2}), the total thickness of boundary layer (from 370 μm to 430 μm), and the potential (from 0.2 V to 2.0 V) at the corresponding concentration. As a result, the resistance of the bulk solution was dominant for the diluted Na_2SO_4 electrolyte (< 0.5 M) while the resistance of the boundary layer and water splitting became dominant for the concentrated Na_2SO_4 electrolyte (> 0.75 M).

Interestingly, NH_4^+ reduction ($NH_{4\,(aq)}^{+} + e^{-} \rightarrow 0.5H_{2(g)} + NH_{3(g)}$) was found at the EDI cathode during the ion separation. This reaction brought a positive impact on increasing the H_2 yield. Experiments demonstrated an increase in reduction performance of NH_4^+ when the Na_2SO_4 concentration increased at low Na_2SO_4 concentration, but this trend was reversed when the concentration was higher. So, in order to dig its fundamentals, the supporting electrolyte influencing on NH_4^+ reduction was studied via molecular dynamics (MD) simulation followed by experimental tests using 0-1.5 M Na_2SO_4 solution. The results indicated that the concentration of Na_2SO_4 supporting electrolyte significantly executed adverse effects on the reduction and migration of NH_4^+ ion in the electric double layer (EDL). In detail, NH_4^+ ion displayed a stronger competition capability than Na^+ ion at the diluted Na_2SO_4 solution (< 0.25 M). The competitive absorption of Na^+ formed a thick layer blocking NH_4^+

approaching and electron transfer in the EDL at the concentrated Na_2SO_4 electrolyte (>0.5 M). Concerning NH_4^+ recovery, Na_2SO_4 concentration thus should be not more than fed concentration (0.25 M). An unreported result that the migration rate of NH_4^+ (2.43×10^{-9} m^2 s^{-1}) was faster than that of Na^+ (1.54×10^{-9} m^2 s^{-1}) occurred at over-concentrated Na_2SO_4 was found, which was thought to be related to hydrogen bond. The mechanisms disclosed the co-ion competition molecularly and allowed the manipulation of EDI capacity optimization.

In short, the hybrid system (AD-EDI-SOFCs) proposed in thesis performed great potentials for energy recovery from wastewater, particularly suitable for the upgrades of processes used at landfill sites and concentrated NH_4^+-N wastewater treatment. The supporting electrolyte was indispensable from the results of this study. Nevertheless, the over-concentrated supporting electrolyte caused apparent concentration polarization and the fierce co-ion competition, which caused the intensive energy consumption and the decay of NH_4^+ reduction. Therefore, the concentration of Na_2SO_4 solution should be controlled within a specific range (0.25 M< c_{Na2SO4}< 0.5 M) as considering migration and reduction processes together.

PUBLICATIONS

1. **Linji Xu** *et al*. “Recent advances in molecular dynamics simulations of interfacial and transport phenomena in electric double layer” ACS Sustainable Chemistry & Engineering. (Prepared to submit)

2. **Linji Xu** *et al*. “Effects of sodium sulfate on ammonium transport and reduction in the cathode of electrodeionziation” Chemical Engineering Journal. (2018, under review)

3. Ling Leng, Peixian Yang, Shubham Singh, Huichuan Zhuang, **Linji Xu**, Wen-Hsing Chenb, Jan Dolfingc, Po-Heng Lee. “A critical review on the bioenergetics of microbial metabolism close to the thermodynamic limits for expanding in anaerobic digestion application” Bioresource technology DOI: 10.1016/j.biortech.2017.09.103

4. **Linji Xu**, Yiyi Zhang, Po-Heng Lee. “Concentration polarization in cation exchange membrane electrodeionization: Effect of cathodic supporting electrolyte concentration.” Journal of Membrane Science. (2017, under review)

5. **Linji, Xu**, *et al*. "Energy upcycle in anaerobic treatment: Ammonium, methane, and carbon dioxide reformation through a hybrid electrodeionization–solid oxide fuel cell system." Energy Conversion and Management 140 (2017): 157-166.

6. **Linji, Xu**, *et al*. "Trehalose enhancing microbial electrolysis cell for hydrogen generation in low temperature (0 °C)." Bioresource technology 166 (2014): 458-463.

CONFERENCE PRESENTATIONS & PAPERS

1. **Linji Xu**, Feifei Dong, Poheng Lee. "Energy Efficient Nitrogen Fertilizer Production from Waste(waters) via Integration of Anaerobic Digestion and Electrodeionization." The Electrochemical Energy Workshop, 2016, Hong Kong Univ., Oral.

2. **Linji Xu**, Poheng Lee. "Net energy increase in Solid Oxide Fuel Cell (SOFC) with biogas from Wastewater Treatment." The Second GIG-PolyU Joint Workshop on Environmental Science and Engineering, 2015, Guangzhou, Oral.

3. Poheng Lee, Meng Ni, **Linji Xu**, Feifei Dong. "Energy Generation from Carbonaceous and Nitrogenous Pollutants via Ammonium, Methane, and Carbon Dioxide Reformation." Materials for Energy, Efficiency and Sustainability: TechConnect Briefs 2017, pp. 261-264.

ACKNOWLEDGEMENTS

I sincerely express my gratefulness to the following persons who have contributed to this thesis throughout my Ph.D study.

Foremost, I would like to deliver my heartfelt appreciation to my chief supervisor, Dr. Lee Poheng. I am fortunate to be his student. Even though he was quite busy, he always made himself available to me when I had any ideas and questions about my research to discuss with him. His patience and persistence particularly encouraged me to overcome many challenges. Second, I would like to thank my co-supervisors, Prof. Ni Meng and Prof. Wang Tao, for their insightful comments on my project. Besides, I would like to fully show my heartfelt gratitude to Prof. Luo Tengfei for his tutorial about molecular dynamics simulation. Given that I did not have their suggestion and supports, I would not have managed to complete my Ph.D. project. Moreover, their rigorous attitudes, good tempers, and noble virtues brought profound and positive influences on me.

I will acknowledge the Hong Kong Polytechnic University for granting my study and offering excellent facilities to me. I will also thank the staff at the Hong Kong Polytechnic University, the University of Hong Kong and the University of Notre Dame for their professional and exceptional assistance to my experiments and theoretical calculations.

I would like to extend great thanks to my colleagues at Department of Civil and Environmental Engineering of the Hong Kong Polytechnic University and Department of Aerospace and Mechanical Engineering of the University of Notre Dame. Notably, Mr. Leng Ling, Ms. Yang Peixian, Mr. Zhuang Huichuan, Ms. Zhang Yiyi, Mr. Dong Feifei, Mr. He Wei, Mr. Wei Xingfei, Mr. Huang Dezhao, Mr. Pang Yunsong, Mr. Yang Junlong, and other colleagues. Their pertinent and appropriate feedbacks promoted the considerable progress of my study.

Last but not the least, I should to sincerely give my gratitude to my parents who unconditionally loved me at any time. Meanwhile, I will fully appreciate my husband (Dr. Huang Shunjun) who gave me material and spiritual support during the past four years. Also, I express thanks to my elder brother (Mr. XU Linquan) who always encouraged me. Besides, my thanks go to my intimate friend (Ms. Qiu Xiaoyan). She had participated in most of my bitter and sweet moments since we knew each other.

All in all, thank all my supervisors, families, friends, and colleagues for accompanying me to experience such a stressful but fruitful Ph.D. period.

TABLE OF CONTENTS

CERTIFICATE OF ORIGINALITY II

ABSTRACT III

PUBLICATIONS VII

CONFERENCE PRESENTATIONS & PAPERS IX

ACKNOWLEDGEMENTS X

TABLE OF CONTENTS XII

LIST OF FIGURES XVIII

LIST OF TABLES XXIII

LIST OF ABBREVIATIONS XXV

CHAPTER 1 INTRODUCTION 1

1.1 Background 1

1.1.1 Renewable energy resources from domestic waste and wastewater 2

1.1.2 Energy recovery technologies related to anaerobic treatment 11

1.1.3 Initiated strategy for electricity generation from wastewater 24

1.2 Objectives 25

1.3 Thesis structure 26

1.4 References 27

CHAPTER 2 LITERATURE REVIEW 36

2.1 Introduction 36

2.2 Electrodeionization principle 37

2.3 Concentration polarization in membrane separation processes 44

2.3.1 Concentration polarization phenomenon 44

2.3.2 Concentration polarization characterization 46

2.3.3 Concentration polarization consequences and improvements 54

2.4 Electric double layer at metal-solution interface 55

2.4.1 Electric double layer phenomenon 55

2.4.2 Classical electrical double layer theory 56

2.4.3 Molecular dynamic simulation of electric double layer 65

2.4.4 Electric double layer improvement 72

2.5 Perspectives 73

2.6 Summary 74

2.7 References 76

CHAPTER 3 ENERGY UPCYCLE IN ANAEROBIC TREATMENT: AMMONIUM, METHANE, AND CARBON DIOXIDE REFORMATION THROUGH A HYBRID ELECTRODEIONIZATION–SOLID OXIDE FUEL CELLS SYSTEM 84

3.1 Introduction 84

3.2 Materials and methods 89

3.2.1 Experiment setups and operations 89

3.2.2 Chemical analysis 98

3.2.3 Calculations 100

3.3 Results 102

3.3.1 Ammonium recovery 102

3.3.2 Ammonium reduction 111

3.3.3 Solid oxide fuel cell performances 114

3.3.4 Energy balance of EDI–SOFCs system 120

3.3.5 Inorganic ion removal 127

3.4 Summary 130

3.5 References 130

CHAPTER 4 CONCENTRATION POLARIZATION IN CATION EXCHANGE MEMBRANE ELECTRODEIONIZATION: EFFECT OF CATHODIC SUPPORTING ELECTROLYTE CONCENTRATION 137

4.1 Introduction 137

4.2 Model development 141

4.2.1 Modeling mass and current distribution 141

4.2.2 Electric resistance analysis 149

4.3 Experimental measurements 151

4.4.1 Electrodeionization setup 151

4.4.1 Current-voltage measurement 151

4.4.1 Electrochemical impedance spectroscopy measurements 151

4.4 Results and discussion 152

4.4.1 Model validation 152

4.4.2 Mass transport 154

4.4.3 Potential distribution 157

4.4.4 Electric resistance analysis 160

4.4.5 Diffusion boundary layer thickness 163

4.4.6 Electricdeionzation performances 168

4.5 Summary 176

4.6 References 177

CHAPTER 5 EFFECTS OF SODIUM SULFATE ON AMMONIUM TRANSPORT AND REDUCTION IN THE CATHODE OF ELECTRODEIONZIATION 181

5.1 Introduction 181

5.2 Experiments 185

5.2.1 Equipment setup 185

5.2.2 Cyclic voltammetry sweeping 185

5.3 Computational methods 187

5.3.1 Electrode/electrolyte interface set-up. 187

5.3.2 Equilibrium relaxation and data collection 191

5.3.3 Post process of data 192

5.4 Results 197

5.4.1 Current density of ammonium reduction 197

5.4.2 Ion transport in the solution 199

5.4.3 Ion transport in the electric double layer 202

5.4.4 Hydrogen bond formation in over-concentrated electrolyte 216

5.5 Summary 218

5.6 References 218

CHAPTER 6 CONCLUSIONS 222

6.1 Key findings and conclusions 222

6.2 Future work 225

Appendix I 227

Operation Parameters in Comsol 5.2 227

Appendix II 229

1. Simulation package set-up 229

2. Computer code explanations and modification 230

Model construction 230

LAMMPS data File 233

LAMMPS input file 236

LIST OF FIGURES

Figure 1-1 LMOP annual emission reductions (2000-2015) (The United States Environmental Protection Agency, 2015). 14

Figure 1-2 Mass flow in the form of COD in A-B process. 14

Figure 1-3 Electricity conversion efficiency of presently developed technologies (Lopez & Hestekin, 2015). 23

Figure 1-4 AD-EDI-SOFCs hybrid system converting biogas and digestate/leachate to electricity. 23

Figure 2-1 Schematic graphs of a single EDI and continuous EDI stack (Sadrzadeh & Mohammadi, 2008). 39

Figure 2-2 Relationship between ρ and L_P, L_{PD}, L_{DP}, and L_D (Tanaka, 2006). 43

Figure 2-3 Concentration polarization for cationic exchange membrane (Hoek & Tarabara, 2013). 45

Figure 2-4 Typical current-voltage curve for a cation exchange membrane (Scarazzato *et al.*, 2015). 50

Figure 2-5 Current-voltage curve (Membrane area 0.126 cm^2) (Tanaka *et al.*, 2012). 51

Figure 2-6 Calculated current-voltage curve (Spiegler, 1971) the blue line is the first item, and the red line is the second item in Eq. 2-19. 53

Figure 2-7 Schematic diagram of the EDL model of Gouy–Chapman–Stern and potential distribution of the double layer with constant dielectric constants (Ibrahim, 2011)..... 64

Figure 2-8 A graph of strength versus distance for the 12-6 Lennard-Jones potential (Hodgman, 1951) (a); Flowchart of molecular dynamics simulations (Yang *et al.*, 2015) (b). 71

Figure 3-1 Mechanism of SOFCs using CH_4 and H_2 (Mirzababaei & Chuang, 2014) (a); NH_3 as fuels (Nagaoka *et al.*, 2017) (b)..... 88

Figure 3-2 Lab-scale electrodeionization: A home-made single EDI reactor (a); a set-up for gas purification and collection (b); Electrochemical reaction detection (c)..... 91

Figure 3-3 Landfill leachate treatment: Landfill leachate collection from West New Territories (WENT) Landfill in Nim Wan, Tuen Mun, Hong Kong (a); Schematic graph of landfill leachate treatment (b); Home-made set-up for landfill leachate (c)..... 94

Figure 3-4 Lab-scale SOFCs (graphs provided by Dong's lab)..... 97

Figure 3-5 The standard curve of NH_4^+-N determination. 99

Figure 3-6 Deionization efficiency of EDI with 0.5-8.0 V applied voltage (a); Deionization efficiency at 7.5-80 mm IED (b); Deionization efficiency and rate as a function of operating time (c)..... 105

Figure 3-7 Drift velocity of NH_4^+ varying with the applied voltage (a); Drift velocity of NH_4^+ varying with the IED (b). 107

Figure 3-8 Total nitrogen mass balance in terms of ammonium, ammonia and other nitrogen species of synthetic wastewater (SW) and raw landfill leachate (RL) (a); CV curves of EDI at 0–1.23 V vs. Ag/AgCl under 0.5–10 mV s^{-1} for the anolyte (b)... 113

Figure 3-9 V-I and P-I polarization curves of the SOFCs fed with 100% H_2 at 550-750 °C (a); 0-60% NH_3 in H_2–NH_3 mixture at 750 °C (b)..... 116

Figure 3-10 V-I and P-I polarization curves of the SOFC fed with 20–80% CH_4 in CO_2–CH_4 mixture at 750 °C (a); Real biogas with a mixture of 68% CH_4 and 32% CO_2 (v/v) from a lab-scale AD reactor at 750 °C (b)..... 119

Figure 3-11 Comparisons of mass and energy flow between AS–CHP and EDI–SOFCs. 126

Figure 3-12 Mobility of ions as functions of ion radii and concentration (mg L^{-1}). 128

Figure 4-1 Schematic diagram of cation through ion exchange membrane..... 140

Figure 4-2 Schematic diagram of cation through ion exchange membrane..... 142

Figure 4-3 Geometric graph of 2D EDI model. 150

Figure 4-4 COMSOL 5.2 operation window..... 150

Figure 4-5 The removal efficiency of NH_4^+ for theoretical and experimental for 0.125-1.5 mol L^{-1} Na_2SO_4 electrolyte. 153

Figure 4-6 NH_4^+ and Na^+ concentration profile in the boundary layer (a) and in CEM (b) at 0.125-0.75 M Na_2SO_4. 156

Figure 4-7 Potential profile of EDI at 0.125 M to 0.75 M Na_2SO_4: (a) snapshot image of the electrolyte potential drop (0.5 M); (b) 1D cut-off surface of potential profile across the membrane. 159

Figure 4-8 Electrical resistance distribution at 0.125 M to 0.75 M Na_2SO_4 supporting electrolyte: (a) electrochemical impedance spectroscopies; (b) electrical resistance composition. 163

Figure 4-9 Current-potential curves at 0.125 M to 0.75 M Na_2SO_4..... 165

Figure 4-10 The real current density of the complete system at 0.125-0.75 M (a); Ion conductivity of the Na_2SO_4 solution (b). 169

Figure 4-11 The deionization efficiency (a); Deionization efficiency rate within 180 min for 0.125-0.75 M Na_2SO_4 solution (b). 171

Figure 4-12 The constitution of gas generated by EDI system at 125-0.75 M Na_2SO_4 solution (a); The average rate of gas production and effective area at 125-0.75 M Na_2SO_4 solution (b). 173

Figure 5-1 The schematic graph of ammonium reduction in the cathodic electric double layer. 184

Figure 5-2 Experiment setup without ion exchange membrane (a); The electrochemical working station for CV sweeping (b); Reference CV curve using 0.25 M ammonium sulfate (c). 186

Figure 5-3 Initial geometry in Material Studio (a); Trajectory of Pt-solution system (b). 188

Figure 5-4 System relaxation and equilibrium: Relaxed structure (a); Average temperature (299.85 K) for NVT (b); Average pressure (1.29 atm) for NPT (c). 196

Figure 5-5 Total current density as a function of Na_2SO_4 concentration (0-1.5 M) (a); Current-voltage curves at 0-0.8 V under 0-1.5 M Na_2SO_4 (b). 198

Figure 5-6 Molar conductivity and dynamic viscosity as a function of the Na_2SO_4 concentration (0.125 -1.5 M)..... 200

Figure 5-7 MSD values of N, Na and O-water in 0.5 ns (a); Diffusion rates of NH_4^+, Na^+, and H_2O molecules as a function of Na_2SO_4 concentration (b). 204

Figure 5-8 Single channel model of electrodeionization(a); NH_4^+ EDL film (b); concentration profiles of NH_4^+ and Na^+ as a function of Na_2SO_4 concentration (0 to 1.5 M) (c) and (d). 209

Figure 5-9 Charge density distributions (a) and (b); Potential NH_4^+ and Na^+ drops along the x-axis under 0 to 1.5 M Na_2SO_4 (c) and (d). 212

Figure 5-10 Partial NHw and OwHw radial distribution functions obtained at 0.5 M Na_2SO_4. 217

LIST OF TABLES

Table 1-1 Renewable energy and produce processes 3

Table 1-2 Energy potential of fats, proteins and carbohydrates, and energy conversion 5

Table 1-3 Leachate composition at dissimilar stages 15

Table 1-4 Comparison of NH_4^+-N treatment in wastewater among traditional, biological and innovational techniques 19

Table 2-1 Comparison of EDL theories..... 58

Table 2-2 Comparison of EDL simulations..... 66

Table 3-1 Characteristics of the Hong Kong West New Territories (WENT) Landfill* 93

Table 3-2 Current efficiencies of ion migration, water splitting, and ohmic loss 110

Table 3-3 Energy benefits from different concentrations of ammonium wastewater through the EDI–SOFCs system* 121

Table 3-4 Comparisons of ammonium removal/recovery processes integrated with anaerobic treatment per removal of 1 mole of NH_4^+ with 3.47 mole of biodegradable

COD (a biodegradable COD/N ratio of 7.9), typical of U.S. medium strength wastewater (Henze et al., 2008; Safoniuk, 2004)..... 123

Table 3-5 Comparison of net energy balances of the AS–CHP and EDI–SOFCs integrated systems in the Hong Kong West New Territories (WENT) Landfill (10^5 MW·h per year)..... 125

Table 3-6 Ions and metals removal/recovery performance from the raw landfill leachate through the semi-continuous EDI reactor 129

Table 4-1 The experimental and theoretical thicknesses of the boundary layer..... 166

Table 4-2 Comparison of energy balance at 0.125-1.5 M Na_2SO4 supporting electrolyte 175

Table 5-1 Atom composition of EDI system from 0-1.5 M Na_2SO_4..... 189

Table 5-2 Pair potential and cutoff distance between atoms 190

Table 5-3 Mobility and transport numbers of NH_4^+, Na^+, and SO_4^{2-} at 0–1.5 M Na_2SO_4 201

Table 5-4 The average slopes of NH_4^+, Na^+, and H_2O molecules at 0-1.5 M. 205

Table 5-5 Electric properties of NH_4^+ film and EDL capacitance..... 213

Table 5-6 EDL structures and thicknesses (NH_4^+ and Na^+) 215

LIST OF ABBREVIATIONS

Nomenclature	Description
AD	Anaerobic digestion
AT	Anaerobic treatment
Anammox	Anaerobic ammonium oxidation
AS	Ammonia stripping
BNR	Biological nitrogen removal
BOD_5	5-day Biochemical oxygen demand
CANDO	Coupled aerobic-anoxic nitrous decomposition operation
CHP	Combined heat and power
COD	Chemical oxygen demand
CV	Cyclic voltammetry
DFT	Density functional theory
EBR	Energy balance ratio
EDI	Electriodeionization
EDL	Electric double layer
EIS	Electrochemical impedance spectroscopy
HRT	Hydraulic retention time
IED	Internal electrode distance
LCD	Limiting current density

LMOP	Landfill methane outreach program
MD	Molecular dynamics
MBP	Modified Poisson Boltzmann
MSD	Mean square displacement
OCV	Open circuit voltage value
PGSE-NMR	Pulsed gradient spin echo nuclear magnetic resonance
PPP	Particle-particle particle-mesh
RDF	Radial distribution function
SOFCs	Solid oxide fuel cells
SS	Suspended solid
TKN	Total Kjeldahl nitrogen
TN	Total nitrogen
VFAs	Volatile fatty acids
VS	Volatile solid
WENT	West new territories

CHAPTER 1 INTRODUCTION

1.1 Background

Energy consumption has been soaring at an annual rate of 2.15% on average from a global viewpoint (Fuerte *et al.*, 2009). Among energy consumption infrastructures, wastewater treatment accounts for a considerable proportion of total energy use. For instance, Perry *et al*. in 2011 introduced that the electricity input for wastewater treatment was around 0.1-1.0% of total electricity load within the local city and community government in the USA, like that in other developed countries. Moreover, with the global population growth, stricter discharge requirements than before, and aged facilities, the annual electricity input for wastewater treatment was likely to approach a higher level that was approximately 3% in the 21st century (McCarty *et al.*, 2011). Initiative (2012) reported that wastewater treatment operations also depleted natural gas and other fuels to treat wastewater to make the discharge satisfied with the permit discharge standards (Initiative, 2012). The impending energy scarcity and global warming are warranting exploring eco-friendly energy sources to reduce fossil fuel depletion. Wastewater, representing a portion of the broader nexus between energy and water, thus, has been paid noteworthy attention for several decades.

1.1.1 Renewable energy resources from domestic waste and wastewater

In domestic waste and wastewater, renewable energy refers to the chemical, thermal or electrical power originating from organic waste and are naturally replenished on a human timescale. Such intensive energy can be obtained through anaerobic digestion and landfills. Under the anaerobic condition, bacteria decompose organics into intermediates, volatile fatty acids (VFAs), and inorganics (amino, sulfide, and phosphate). The intermediates are either biologically converted to gases and liquid (Oreopoulou & Russ, 2007; Zhang *et al.*, 2014) or electrochemically oxidized as electron donors (Table 2-1) (De Arespacochaga *et al.*, 2015; Li *et al.*, 2014; Metcalf & Eddy, 2014; Züttel *et al.*, 2010). The primary energy resources produced by anaerobic digestion and landfills (Table 1-1) are reviewed as follows.

Table 1-1 Renewable energy and produce processes

Fuels	Enthalpy (kJ $mol^{-1)}$	Processes	Sources	Conversion Process
Biogas (CH_4)	-890	AD	Fats, proteins, and carbohydrates	AD + combustion/CHP/Fuel cells
Landfill gas	-890	AT	Municipal solid wastes	AD + combustion/CHP/Fuel cells
Hydrogen (H_2)	-285	AD + microbial electrolysis cell	Fats, proteins, and carbohydrates	AD + bioelectrochemical systems, fermentation, electrochemical reactions
Ammonia (NH_3)	-320	AT + air stripping/ion exchange	Proteins, NH_4^+-N wastewater	AD + AS/EDI
Nitrous Oxide (N_2O)	-82	Anaerobic treatment	Proteins, NH_4^+-N wastewater	Anammox + CANDO
Direct Electron Transfer	-200~-20	Redox enzymes and proteins capable of electro catalyzing	Organic compounds	Microbial fuel cell, electro-catalysis

1) Biogas

Biogas, composed of 47-65% CH_4, 36-41% CO_2, 1-17% N_2, and less than 1% O_2, is the dominant energy resource from wastewater (Rasi *et al.*, 2007). As a gas product of AT process, biogas is from carbohydrates, proteins, and lipids whose energy potentials are summarized in Table 1-2. How much biogas can be generated by these compounds on earth? Take AD as an example, one kilogram of VFA, carbohydrates, proteins, and lipid can produce 370, 415, 496, and 1014 liters biogas in theory but only 350 liters, 350-395 liters, 250-300 liters, and 610-710 liters in practice, respectively. This difference between the ideal and real energy is probably attributed to the incomplete digestion of organics and microorganism growth (Speece, 2008). Another reason to be reckoned with is energy loss caused by the subsequent processes. Mohammad and Hans (2001) reported that the process of biogas converting electricity lost more than 60% of total energy in the form of heat, and such a large proportion of energy led to the ultimate electricity merely accounting for 30-40 % (Farooque & Maru, 2001). These results indicate great possibilities to enhance the real power generation.

Table 1-2 Energy potential of fats, proteins and carbohydrates, and energy conversion

Organics	Theoretical Gas Yield	Real Gas Yield	Methane Content	Energy Potential	
				Theoretical	Practical
	L CH_4 kg^{-1} VS		(%)	kW·h oDM^{-1}	
VFA	370	350	~50		
Carbohydrates	415	350-395	~50	10.50-10.97	7.50-9.80
Proteins	496	250-300	~60	4.97-5.96	3.31-4.64
Lipid	1,014	610-710	~70	4.58-5.29	3.86-4.41

Sources adapted from Møller *et al*., 2004

2) Landfill gas

With population explosion, volumes of municipal solid wastes enriching in numerous constituents (organics, inorganics, ammonium, and heavy metals) is growing at a rate of 1.7 billion tons per day (Achankeng, 2004; Foo & Hameed, 2009). Such a fast rate brings an intransigent paradox around the world. At present, sanitary landfilling is the most commonly used strategy for municipal solid waste management. It disposes accounting approximately 95% of the total municipal solid waste collected worldwide and produces cubic kilometers of landfill gas and landfill leachate (Baldasano *et al.*, 2003; Kurniawan *et al.*, 2006). Landfill gas, similar with biogas, roughly composes of 45-60% methane and 40-60% carbon dioxide. It has been comprehensively used in many areas such as boiler, dryer, and process heater (Shrestha, 2008), leachate evaporation (Yedla *et al.*, 2001), pipeline-quality gas (Themelis & Ulloa, 2007), and electricity generation (Urban *et al.*, 2009). There is a typical case of landfill gas utilization that The United States Environmental Protection Agency carries out a Landfill Methane Outreach Program (LMOP) that prevents the direct methane emissions from landfill sites and reduces the indirect CO_2 emission by energy generated with landfill gas. Up to date, LMOP has reduced the methane emission from hundreds of U.S. landfills and exempted CO_2 emissions (totaling approximately 38.9 $MMTCO_2e$ in 2015), illustrated that landfill gas could make a great contribution to electricity generation and greenhouse gas reduction.

3) Hydrogen gas

Anthropic activity has resulted in the increases in CO_2 emission, atmospheric methane concentration, and the greenhouse effect. To offset these adverse impacts, the

explorations of carbon-free energy has been thriving. Hydrogen energy, as one type of carbon-free fuels, has been the most efficient carrier of energy. To capture H_2, we have employed a wide variety of approaches (e.g., water splitting by solar, proton exchange fuel cell, and syngas reduction) to dissociate hydrogen from water (Shrestha, 2008; Srinivasan, 2006; Züttel *et al.*, 2010). However, these pricey technologies seem to do not promote the broad applications of H_2 energy. Hence many scholars have altered their attention to wastewater and have sought various bio-hydrogen production (Grigoriev *et al.*, 2006; Kotay & Das, 2008).

Biological hydrogen production including direct bio-photolysis, indirect bio-photolysis photo-fermentation, and dark anaerobic fermentation of wastes are prospective alternative approaches. Nuri *et al*. in 2009 researched the rate of hydrogen yield through the continuous fermentative hydrogen production from cheese wastewater and found it reached 7.9 L H_2 L^{-1} per day (Azbar *et al.*, 2009). Chen *et al*. (2005) and Levin & Love (2004) reviewed biological hydrogen production and summarized the prospects and limitations of the practical application of biohydrogen production and the functional microorganism communities (Chen *et al.*, 2005; Levin *et al.*, 2004). Another pathway to gaining hydrogen energy from wastewater is called bio-electrochemical systems. Liu *et al.* (2005) studied hydrogen production from acetate through electrochemically microbial assistance and found that the potential for hydrogen production reached ca. 8-9 mol H_2 mol^{-1} glucose and the energy cost was equivalent to 1.2 mol H_2 mol^{-1} glucose (Liu *et al.*, 2005). Kadier *et al*. (2016) and Logan *et al*. (2008) found that this system could generate hydrogen using substances in wastewater with a faster rate and higher transfer efficiency than traditional

fermentation by the assistance of external applied voltage (Kadier *et al.*, 2016; Logan *et al.*, 2008). Though biological hydrogen has some unsolved problems, hydrogen fuel will be paid more concerns in future due to the intensification of energy scarcity and further deterioration of our environments (Xiang, 2010).

4) Direct electron transfer

Direct electron transfer refers to that some bacteria release the electrons and form potential difference beyond the cell wall. This pathway provides new opportunities for the sustainable energy from biodegradable compounds, especially for wastewater, because chemotrophic microbes metabolize organics and biodegradable compounds and transport the electrons to an electron transport chain under the diverse conditions (Rabaey & Verstraete, 2005). Electron transfer needs appropriate electron carriers. The cell membrane loads a variety of Cytochromes that have different functions and redox potentials (Mehta *et al.*, 2005). The electrons transfer from a low potential electron donor to an acceptor with more positive redox potential by the redox reactions so that they are taken up by the terminal acceptors such as oxygen, sulfate, or nitrate (Kracke *et al.*, 2015). Thauer *et al*. (1977) discussed energy conservation in chemotrophic anaerobic bacteria and found that when bacteria derived reducing equivalents from glucose in the form of NADH to oxygen, the potential difference was about 1.2 V and the energy was to be gained 200 kJ mol^{-1} (2 electrons per molecule of NADH) (Thauer *et al.*, 1977). Madigan *et al*. (2008) reported that sulfate was the electron acceptor, the potential drop was around 100 mV and energy yield was about 20 kJ mol^{-1} (Madigan *et al.*, 2008). In practice, the observed maximal open circuit potentials are the order of 750–800 mV owing to electron transfer resistance and internal resistance (Rabaey &

Verstraete, 2005). Because of the most prominent bottleneck of the low transfer efficiency, we have not yet widely known direct electron transfer.

5) Ammonia gas

Ammonia is another type of carbon-free fuels except for hydrogen. It has been noted and regarded as an alternative fuel to H_2 since it contains 17.6% hydrogen by molecular weight (Comotti & Frigo, 2015; Van Aken *et al.*, 2014) and can release 320 kJ mol $^{-1}$ energy, approximate 10% more than that of H_2 (Atkins & De Paula, 2013; Green, 1982; Schüth *et al.*, 2012). Moreover, NH_3 has some distinct characteristics (e.g., detectable odor (Reich *et al.*, 2001), lighter density and easy to be transported (John *et al.*, 2007). These characteristics endorse the application availability of NH_3 fuel, and related studies have been reported for some years. Zamfirescu & Dincer (2008) and Züttel (2010) used NH_3 gas to feed proton exchange membrane fuel cells and SOFCs, and managed to gain the direct electricity (Zamfirescu & Dincer, 2008; Züttel *et al.*, 2010). Ni *et al*. (2009) reviewed ammonia-fed solid oxide fuel cells and discussed the technical feasibilities of direct NH_3 fuel based on the results of experimental tests and mathematical modeling (Ni *et al.*, 2009). Many authors reviewed hydrogen generation from the catalytic decomposition of NH_3 through electrochemical oxidation with 2.0-14.8 kg NH_3 kg_{cat}^{-1} h^{-1} productivity (Comotti & Frigo, 2015; Schüth *et al.*, 2012). These surveys demonstrate that NH_3 is believed to has a great potential for renewable energy development.

Nevertheless, NH_4^+-N in wastewater has been paid little attention. This situation is probably attributed to the following issues: (1) Unstable NH_4^+-N concentration in wastewater leads to chemical waste (Pontes & Chernicharo, 2011; Westgate, 2009);

(2) The conversion from NH_4^+ to NH_3 produces an intermediate, $NH_3 \cdot H_2O$, and needs alkaline addition (NaOH) and air stripping, which results in low recovery efficiency but high recovery cost (Guštin & Marinšek-Logar, 2011; Lei *et al.*, 2007). (3) Technically, available engines matching AD for direct NH_3 fuel have not yet been well developed (Gross & Kong, 2013; Liu *et al.*, 2003). Even so, the renewed interests in NH_3 fuel raise new research on reducing greenhouse gas emissions and eutrophication, which is the objective of this project.

6) Nitrous oxide (N_2O)

The nitrification-denitrification process released a well-known intermediate (N_2O) that is a perpetrator of the greenhouse effect. Regarding nitrogen energy, some scholars had taken their insights into N_2O. Scherson *et al*. (2013) developed a process named Coupled Aerobic-anoxic Nitrous Decomposition Operation (CANDO) (Scherson *et al.*, 2013), and found that this process decreased by 20% oxygen requirement and 40% biomass production, respectively. Meanwhile, CANDO increased by 60% energy production. From the reactions of CANDO, shown in Eq. 1-1 and Eq. 1-2, CH_4 combustion produces 890 kJ mol^{-1} thermal energy (Eq. 2-1). Upon N_2O added, 82 kJ mol^{-1} extra energy is released from the decomposition of N_2O to N_2 (Eq. 1-2). Integrating Eq. 1-1 and Eq. 1-2, it can be seen that one mole of CH_4 combusting with 4 moles of N_2O releases approximately 30% more stoichiometric energy than with 2 moles of O_2 (Eq. 1-3) (Scherson *et al.*, 2014).

$$CH_{4(g)} + 2O_{2(g)} \rightarrow CO_{2(g)} + 2H_2O_{(l)} \quad \Delta H_R^0 = -890 \text{ kJ mol}^{-1} \tag{1-1}$$

$$N_2O_{(g)} \rightarrow 0.5O_{2(g)} + N_{2(g)} \quad \Delta H_R^0 = -82 \text{ kJ mol}^{-1} \tag{1-2}$$

$$CH_{4(g)} + 4N_2O_{(g)} \rightarrow CO_{2(g)} + 2H_2O_{(l)} + 4N_{2(g)} \quad \Delta H_R^0 = -1219 \text{ kJ mol}^{-1} \tag{1-3}$$

Above results suggest that the energy potentials in wastewater and landfills that biogas, landfill gas, hydrogen, ammonia, and nitrous oxide can be recovered as renewable energy.

1.1.2 Energy recovery technologies related to anaerobic treatment

1) Anaerobic digestion for biogas production

Suitable technologies are crucial for the conversion from organics to electricity. There exist many technologies that have been settled to convert wastewater to energy. AT process has been proved to be the most favorable process for wastewater-energy conversion in the worldwide, which provided 10-15% total energy (Abbasi *et al.*, 2012; Ducharme, 2010; Eckenfelder *et al.*, 1988; Oreopoulou & Russ, 2007). In AT process, functional bacteria degrade organic wastes (fats, proteins, and carbohydrates) to biogas and digestate through their metabolization (Eckenfelder *et al.*, 1988; Oreopoulou & Russ, 2007). According to the differences in functional microorganism groups, AT process is divided four stages (hydrolysis, acidogenesis, acetogenesis, and methanogenesis) and biogas is produced at the fourth stage (Ariesyady *et al.*, 2007).

Built in the mechanism of anaerobic metabolism, numerous anaerobic processes have been employed to increase energy recovery and cut down energy consumption. Wan *et al*. (2016) reviewed the feasible options for biogas capture towards energy neutralization of domestic wastewater treatment and summarized that the process

combined with AT process and biological nitrogen removal (BNR) captured >73% energy (Wan *et al.*, 2016). Specifically, all organics were unified by chemical oxidation demand (COD). According to the energy footprints, 100% COD was anaerobically digested to 65% COD (biogas), 20% COD (activated sludge), and 15% COD (digestate). After the anaerobic process, the 15% COD (digestate) was continuously converted to 4% COD (sludge), 6% COD (nitrogen), and left 5% COD in the effluent via BNR (partial nitrification and Anammox). This system ultimately transformed 73% COD to biogas and discharged only 21% COD (16% COD in digestate and 5% in the effluent) in total (Figure 1-2). Except for energy generation and sludge reduction, Sullivan *et al*. (2007) also reported that the digestate enriched adequate N, P, S, K, Ca, Mg, and other minerals. They found that these resources had been reused to produce fertilizers (Sullivan, 2007). During AT process, anaerobic bacteria convert the organic wastes to biogas under the anaerobic condition rather than aeration, so that reduces the costs of waste treatment. Also, compared to aerobic digestion, AT process has lots of considerable merits (e.g., less sludge yield, fewer requirements for nutrients and area) (Wang *et al.*, 2010). Typically, aerobic treating 100 kg COD produces 30-60 kg sludge, and requires 100 kWh energy input, whereas anaerobic process treating the same amount of COD produces 40-45 m^3 CH_4 but just only yields 5 kg sludge (Metcalf & Eddy, 2014; Nair *et al.*, 2014). The landfill has a similar microbial metabolism process, which can yield cubic meters of landfill gas. Nevertheless, landfill leachate is difficult to be handled using the conventional bio-technologies because of poor biodegradability (BOD_5/COD < 0.3) and high concentration of inorganics, especially heavy metals (Table 1-3).

Inevitably, AT confronts with some challenges (e.g., long start-up time, a tremendous amount of alkalinity addition, vulnerable to NH_4^+ concentration, etc.) (Eckenfelder *et al.*, 1988). Rosnani *et al*. (2011) investigated the factors affecting the start-up procedures of an innovative anaerobic stage reactor and found that this system required at least 34 days and performed at low loading rate and sufficient HRT (Alkarimiah *et al.*, 2011). Demirel *et al*. (2008) found that the accumulation of protons required about 3000 mg L^{-1} calcium carbonate to neutralize H^+ (Demirel *et al.*, 2008). Park & Kim (2016) studied the effect of ammonia on anaerobic degradation of amino acids and concluded that increasing initial NH_4^+-N concentrations from 0 mg NH_4^+-N L^{-1} to 5,000 mg NH_4^+-N L^{-1} resulted in a decrease in deamination efficiency from 100% to 55% (Park & Kim, 2016). Also, Lewis *et al*. (2000) and Chong *et al*. (2012) and Lewis *et al.* (2000) found that the existence of remaining VFAs, dispersed solids, biological nitrogen, and phosphorus in digestate did not reach the discharge standard and required subsequent treatment (Chong *et al.*, 2012; Lewis *et al.*, 2000). These results indicate that parameter optimizations and toxicity controls are important to improve AD performances. Plus, landfill leachate is rich in organics, inorganics, and heavy metals (Table 1-1). Once these compounds seepage into the waterways, irreversible risks will be brought to the natural environments. To dispose landfill leachate, the conventional treatments (recycling and combined treatment with domestic sewage, aerobic and anaerobic processes, and chemical and physical methods), and new treatments (microfiltration, ultrafiltration, nanofiltration and reverse osmosis) have been implemented (Wiszniowski *et al.*, 2006; Zhang *et al.*, 2013).

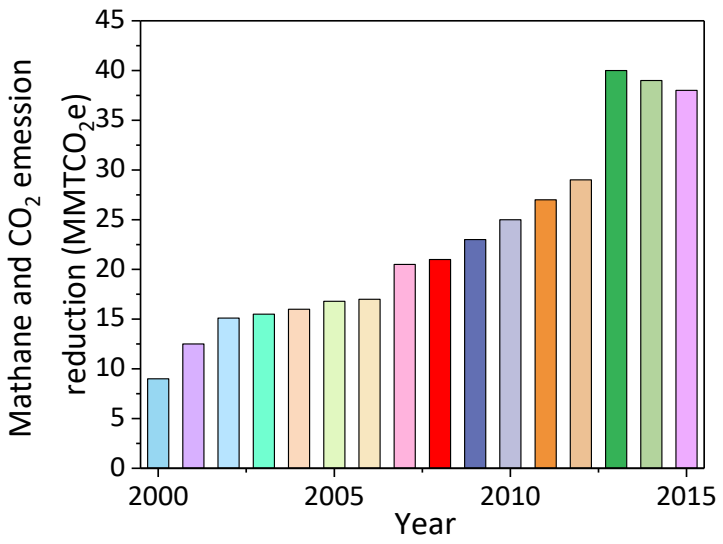

Figure 1-1 LMOP annual emission reductions (2000-2015) (The United States Environmental Protection Agency, 2015).

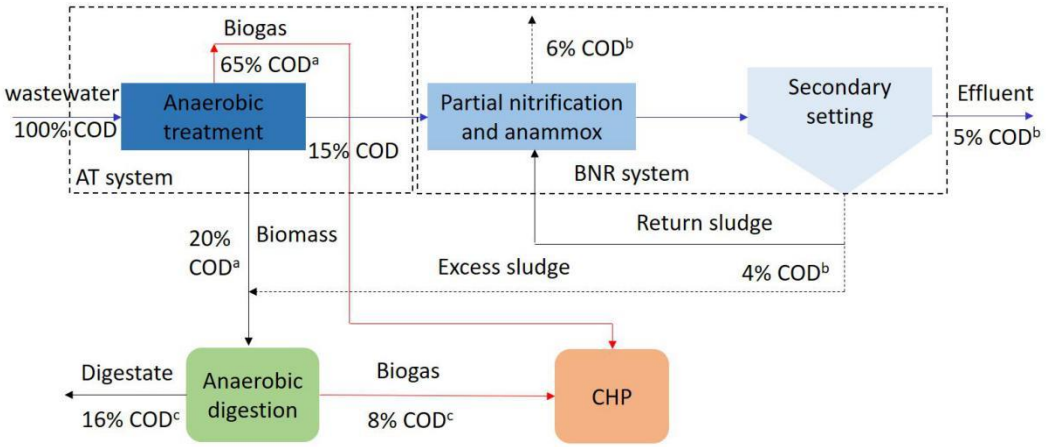

*data adapted from the reference (Krishna *et al.*, 2009); b data adapted from the reference (Metcalf & Eddy, 2014); c data adapted from the reference (Parkin & Owen, 1986).

Figure 1-2 Mass flow in the form of COD in A-B process.

Table 1-3 Leachate composition at dissimilar stages

Parameters	Young	Medium	Old
COD	1,870-50,000	1,184-9,500	100-10,00
BOD	90-25,000	500-1,436	3-800
BOD/COD	0.050-0.670	0.007-0.310	0.01-0.11
pH	5.80-9.10	6.90-9.00	7.00-8.60
SS	950-5,000	480-780	130-1,600
TKN	75-13,000	1,135-1,670	540-1,680
NH_3-N	10-13,000	800-1,330	159-1,590
Al	NA	0.02-0.92	<2.00
Ba	NA	0.006-0.164	0.150
Cu	NA	0.120-0.780	0.005-0.080
Fe	2.70	1.28-3.81	4.10-26.00
Mn	0.04	0.17-16.40	0.13-15.50
Si	NA	3.72-10.48	<5.00

Sources adapted from this reference (Renou *et al.*, 2008); All values except pH and BOD/COD are in mg L^{-1}.

2) Ammonium treatment and heavy metal removal

There are some severe issues existed in AT system as a long-term operation, especially the toxicity of NH_4^+ ion. The released NH_4^+ ion from proteins is accumulated in AD reactor, which inhibits the growth of anaerobic bacteria that are vulnerable to the NH_4^+ ion. As NH_4^+ ion is over accumulated, bacteria stop growing, even being killed, and thus accelerated the decay of the AT performances (Krakat *et al.*, 2017; Rajagopal *et al.*, 2013). To alleviate inhibitions from NH_4^+ ion and improve the yield of biogas, numerous methods including traditional techniques (chemical sedimentation, air stripping, heating, etc.), biological denitrification (nitrification-denitrification, shortcut denitrification and anaerobic ammonia oxidation), and innovational processes (electro-catalytic oxidation, ion exchange, advanced oxidation, etc.) have been used to remove NH_4^+ from digestate and landfill leachate (Dermentzis *et al.*, 2012; Goffin & Calay, 2000; Krakat *et al.*, 2017; Schüth *et al.*, 2012; Vidal-Iglesias *et al.*, 2003), as summarized in Table 1-4.

Biological denitrification is a widely used technology. Scherson *et al*. (2013) and Yang *et al*. (2007) reviewed the nitrification and denitrification process employed for NH_4^+-N wastewater treatment (Scherson *et al.*, 2013; Yang *et al.*, 2007). Nevertheless, these methods had a high cost of energy input due to aeration. Later, some techniques established on the mechanism of shortcut nitrification-denitrification have been implemented. As published by Zhang *et al*. (2007), shortcut nitrification and denitrification from mature municipal landfill leachate removed 70-80% total nitrogen (TN) and saved 40% carbon source (Zhang *et al.*, 2007). Meanwhile, anaerobic ammonium oxidation (Anammox) is present of great interest in recent years. As

reviewed by Zhang *et al*. (2008), Anammox process had been directly scaled up to engineering practice and approached 9.5 kg-N m^{-3} d^{-1} nitrogen removal rate (Zhang *et al.*, 2008). Anammox process is much better than the conventional nitrification-denitrification.

Physical-chemical processes such as ion exchange, absorption, and biosorption have been extensively studied for NH_4^+ removal from wastewater (Gupta *et al.*, 2015). Rahmani and Mahvi (2006) investigated nitrifying bacteria regenerating clinoptilolite zeolite and found that the bio-regeneration efficiency of zeolite reached 87.7-99.8% in the period of 3.5-5.5 hours, cation exchange capacity approached 10.06 (in breakthrough point) and the total capacity of ammonia removal was 18.38 mg NH_4^+ g^{-1} zeolite (Rahmani & Mahvi, 2006). Among these technologies, electrodeionization (EDI) is raising widespread concerns because of its high efficiency of ion separation and concentration (Paidar *et al.*, 2016). Many papers reported that EDI could efficiently separate and concentrate NH_4^+ from different types of NH_4^+-N wastewater. Spiegel *et al*. (1999) used a two-step EDI process and reduced NH_4^+-N concentration from 200 mg L^{-1} to less than 1 mg L^{-1} (Spiegel *et al.*, 1999). Dermentzis *et al.* (2012) and Schiffler (2004) used EDI to extract NH_4^+ for fertilizer production from concentrated NH_4^+-N wastewater and fond that EDI only took 28 minutes at 30 A m^{-2} current density to reduce 1310 mg L^{-1} NH_4^+-N to 50 mg L^{-1} (Dermentzis *et al.*, 2012; Schiffler, 2004). Mondor *et al.* (2008). used EDI to extract NH_4^+ from liquid swine manure for producing nitrogen fertilizer and found that 90% NH_4^+-N was recovered without chemical addition and 1.6 g L^{-1} NH_4^+-N recovery only required 1.0 kWh kg^{-1}-NH_3 energy input (Mondor *et al.*, 2008). Besides, Ali *et al*. (2004), Barak *et al*. (2010)

and Mehanna (2015) reported that H_2 from water splitting was served as an additional fuel of proton exchange membrane fuel cells (Ali *et al.*, 2004; Barak, 2015; Mehanna *et al.*, 2010). These methods save massive doses of chemicals and about ten times energy consumption in comparison to air stripping. Because the produced alkaline condition promotes the transformation of $NH_4^+{}_{(aq)}$ into $NH_{3(g)}$, the settled EDI technique is available for NH_3 removal or recovery.

Regarding the heavy metals in landfill leachate, EDI displays high efficiency as well. Alvarado & Chen (2014) and Yeon *et al*. (2004) reported that EDI was used for heavy metal removal and found that the removal efficiency reached over 85% (Alvarado & Chen, 2014; Yeon *et al.*, 2004). They also found that EDI saved approximate 20% or higher energy than catalytic oxidation and reverse osmosis without phase change and osmotic pressure (Alvarado & Chen, 2014). Huang *et al*. (2007) and Jaroszek & Dydo (2016) applied EDI to treat wastewater streams from pharmaceutical to beverages industries (Huang *et al.*, 2007; Jaroszek & Dydo, 2016).

Table 1-4 Comparison of NH_4^+-N treatment in wastewater among traditional, biological and innovational techniques

Category	Techniques	Transfer	Energy or Resource Utilization	Advantages	Disadvantages
Traditional Techniques	Chemical sedimentation, air stripping, heating, etc.	NH_4^+(aq) to NH_3(g)	Fertilizers	Fast conversion	Doses of chemical input, intensive energy consumption, and secondary pollution
Biological Denitrification	Nitrification-denitrification, shortcut denitrification, anaerobic ammonia oxidation	NH_4^+ to N_2	NA	Low energy input	Slow conversion efficiency, dilute NH_4^+ loading, without Energy or resource utilization
Innovational Processes	Electro-catalytic oxidation, ion exchange, advanced oxidation, etc.	NH_4^+ to N_2 NH_3(g)	Hydrogen and fertilizers	Fast conversion efficiency	Pricy device and intensive electricity input

3) Electricity generating technologies

No matter for biogas, landfill gas, hydrogen, or ammonia, electricity generation is most essential. Combustion engines including internal combustion engine (e.g., reciprocating engine) and external combustion engine (like Stirling engine) are commonly used to convert biogas to electricity following AD and landfills (He *et al.*, 2011). Combined heat and power (CHP) is the most famous because it reuses the residual heat so as to improve the energy efficiency to approximately 80% (Lantz, 2012). Nevertheless, its real electricity conversion efficiency is still no more than 40% (Lefebvre, 1998; Van Dongen *et al.*, 2007). SOFCs, a promising technology for direct electricity generation, has been invented for several decades. This technology cannot only use different kinds of fuels (H_2, biogas, NH_3, syngas, etc.) to directly generate electricity but also has 20-30% higher electricity conversion efficiency than the above-mentioned techniques (Ormerod, 2003; Shiratori *et al.*, 2008; Wojcik *et al.*, 2003; Xu *et al.*, 2017). The comparison of electricity conversion efficiency among petrol internal combustion, diesel internal combustion, coal-fired turbine, gas-fired turbine, and the fuel cell is displayed in Figure 1-3. The electricity conversion efficiency of conventional engines is less than 40-55% on average, whereas that of fuel cell reaches 62%, signifying that fuel cell can achieve 20% more electricity. Hoogers (2002) introduced that electricity generation of SOFCs was completed through electrochemical reactions in a straightforward way, which avoided thermodynamic cycles (Carnot efficiency), thus contribute to higher efficiency than the conventional engines (Hoogers, 2002). Tsukuda *et al*. (2000) reported SOFCs achieved 50-80% electric conversion efficiency using natural gas, syngas, and hydrogen, which was 20%

more than that of CHP (Tsukuda *et al.*, 2000). Tu & Stimming (2004) reviewed the advantages of SOFCs at high operating temperature (> 500 °C) and summarized that SOFCs had fast reaction kinetics of the high- temperature gradients in the region of the fuel inlet (Tu & Stimming, 2004). SOFCs are superior to other engines in materials. Singhal (2007) reviewed the materials of the components of SOFCs (anode, electrolyte, and cathode) and concluded that the materials were cheap and readily available. He also found that many cost-effective materials instead of precious metals could be used, and Ni-YSZ cermet, YSZ, $LaMnO_3$ were the typical materials for the anode, electrolyte, and cathode, respectively, since they have advantages of sufficient ionic conductivity, chemical stability, and mechanical strength high and low maintenance costs (Singhal, 2007).

SOFCs have had a broad spectrum of power generation applications from single to stack scale (Singhal & Egushi, 2011). Ramirez (2002) introduced that portable devices for the distributed generation power plants had been built up. The power outputs depend on the real requirements, e.g., 500 W battery chargers for mobile devices and 100-500 kW for systems (Ramirez, 2002). Minh (2004) reported that the small-scale SOFC systems developed for military, residential, industrial, and transportation applications (Minh, 2004). Williams (2006), Yang *et al*. (2005) reported that the pilot-scale SOFCs had been used in the US, Europe, and Japan (Williams *et al.*, 2006; Yang *et al.*, 2005). Ali *et al*. (2010) reported that SOFCs integrate gas turbines to form large CHP and found that large-scale SOFCs-CHP combined system achieved a 100 kW unit and 46% electrical efficiency (Ali *et al.*, 2010). SOFCs integrating AD to generate

electricity has been investigated in recent years (Bogusch & Grubbs, 2014; De Arespacochaga *et al.*, 2015).

It should be admitted that SOFCs stack is not a perfect technology since it is faced with some challenges as well. For example, the high temperature (> 500 °C) shortens materials lifetime, which is one of the bottlenecks (Laosiripojana *et al.*, 2009; Singhal & Kendall, 2003). Moreover, the corrosion of metal components is another essential issue on the fuel utilization efficiency (Singhal & Kendall, 2003). Besides, sulfur and carbon particles threaten the performances of electrodes, particularly feeding biogas (Kendall & Kendall, 2016). Hence, more efforts should be paid to study SOFCs in future.

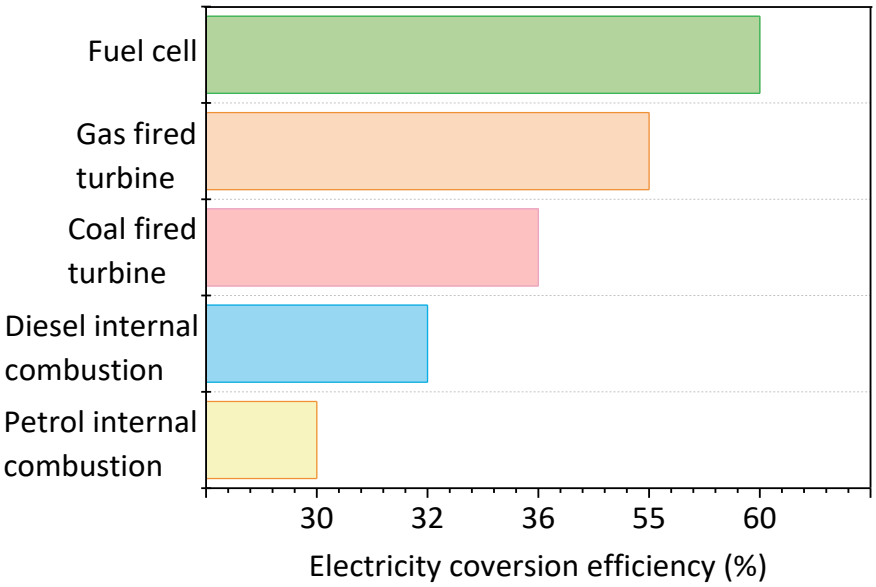

Figure 1-3 Electricity conversion efficiency of presently developed technologies (Lopez & Hestekin, 2015).

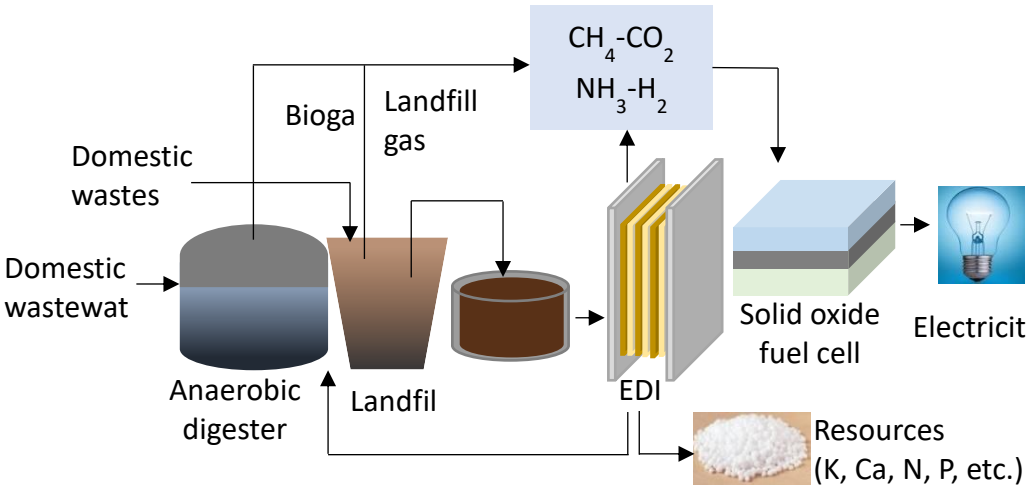

Figure 1-4 AD-EDI-SOFCs hybrid system converting biogas and digestate/leachate to electricity.

1.1.3 Initiated strategy for electricity generation from wastewater

With energy shortage intensifying, interests are altering to develop liquid ammonia as an energy resource because NH_4^+ is only composed of N (82.4%) and H (17.6%) in proportion to molecular weight. Comott and Frigo (2015) and Li *et al*. (2014) reported that NH_4^+-N as an excellent energy carrier was used as hydrogen resource by thermal degradation (Alvarado & Chen, 2014; Comotti & Frigo, 2015). Some scholars detected the maximum energy of ammonia and found that ammonia released 320 kJ mol^{-1} thermodynamic energy, approximately 10% more than 285 kJ mol^{-1} (H_2 enthalpy) as it was thoroughly oxidized (Eq.1-1) (Atkins & De Paula, 2013; Green, 1982; Klerke *et al.*, 2008; Schüth *et al.*, 2012). If we take methane into consideration, one mole CH_4 plus four-mole NH_3 generates 2,125 kJ mol^{-1} thermal energy in theory according to Eq. 1-2. The co-oxidation of NH_3 and CH_4 can release nearly seven times more energy than sole oxidation of NH_3 gas (Eq.1-1) implying that a promising energy potential can be achieved via biogas.

$$NH_{3(g)} + 0.75O_{2(g)} \rightarrow 0.5N_{2(g)} + 1.5H_2O_{(l)} \quad \Delta H_R^0 = -320 \text{ kJ mol}^{-1} \qquad (1\text{-}4)$$

$$CH_{4(g)} + 4NH_{3(g)} + 5O_{2(g)} \rightarrow CO_{2(g)} + 2N_{2(g)} + 8H_2O_{(l)} \quad \Delta H_R^0 = -2{,}125 \text{ kJ mol}^{-1} \qquad (1\text{-}5)$$

Concerning NH_3 as hydrogen fuel, appropriate engines using $NH_{3(g)}$ to generate electricity is a vital problem. It needs to be addressed because $NH_{3(g)}$ is not a flammable fuel. At this aspect, solid oxide fuel cells (SOFCs) is not a better option due to its broad fuel selection from carbonaceous and nitrogenous compounds like H_2, natural gas, biogas, and NH_3 gas or fuel mixture (Goula *et al.*, 2006; Moon *et al.*, 2003). Moreover,

SOFCs have a high efficiency of electricity conversion. Singh *et al*. (2005) and Yi *et al*. (2004) reported that SOFCs had over 50% electricity conversion efficiency and obtained about 20% more energy, compared to the traditional engines (Singh *et al.*, 2005; Yi *et al.*, 2004). SOFCs shows an exceptional resistance capability to carbon toxicity. Bogusch & Grubbs *et al*. (2014) and De Arespacochaga (2015) used syngas mixed with NH_3 feeding SOFCs found that 70% electricity was output and no carbon was deposited in SOFCs because of the reformation of fuel mixture avoiding carbon toxicity for the electrodes (Bogusch & Grubbs, 2014; De Arespacochaga *et al.*, 2015).

The merits of AD/landfill, EDI, and SOFCs enable the technical feasibility of electricity generation from NH_3 and biogas together, whereas studies are still kept vacant at present. Therefore, this thesis configures a topic on sustainable electricity generation from diverse types of NH_4^+-N wastewater/landfills, particularly focusing on concentrated NH_4^+-N wastewater) via the hybrid system (AD-EDI-SOFCs) (Figure 1-4). This system converts the organics to fuel mixture (biogas, NH_3, and H_2,) and converts these compounds to electricity. We hope that this proposed system can make some contributions to upgrading the existing processes of anaerobic treatment and landfill and provide a more sustainable waste(water) management system.

1.2 Objectives

The thesis aims to:

1) Estimate the feasibility of the proposed hybrid system (AD-EDI-SOFCs) for electricity generation from dilute to concentrated NH_4^+-N wastewater.

2) Characterize the mechanism of concentration polarization occurring at the cation exchange membrane and analyze energy consumption around the cation exchange membrane as cathodic supporting electrolyte concentrating.

3) Find out the principle of supporting electrolyte influencing on NH_4^+ transport and reduction at the interface between the cathode and the solution.

1.3 Thesis structure

This thesis has six chapters as follows.

1) Chapter 1 introduces the backgrounds, rationales, objectives, and the structure.

2) Chapter 2 reviews the current statuses concentration polarization occurring at ion exchange membrane and the electric double layer formed at the interface between the electrode and the electrolyte.

3) Chapter 3 presents the optimization of operating parameters (NH_4^+ concentration, applied voltage, and internal electrode distance (IED) and corresponding results on energy upcycle in anaerobic treatment via biogas, NH_3, and H_2 using AD-EDI-SOFC hybrid system.

4) Chapter 4 shows the experimental and theoretical results of Na_2SO_4 supporting electrolyte concentration (0.125 M to 0.75 M) affecting on concentration polarization and resistance distribution in diffusion boundary layer around cation exchange membrane.

5) Chapter 5 discusses effects of Na_2SO_4 supporting electrolyte (0.125-1.5 M) on NH_4^+ transport and reduction in the cathode of electrodeionization through molecular dynamics simulation.

6) Chapter 6 summarizes the main findings, prospects, and future work.

1.4 References

Abbasi, Tauseef, & Abbasi. (2012). Anaerobic digestion for global warming control and energy generation: An overview. *Renewable & Sustainable Energy Reviews, 16*(5), 3228-3242.

Achankeng. (2004). *Sustainability in municipal solid waste management in Bamenda and Yaounde, Cameroon.*

Ali, Mnif, Hamrouni, & Dhahbi. (2010). Electrodialytic desalination of brackish water: effect of process parameters and water characteristics. *Ionics, 16*(7), 621-629.

Ali, Rakib, Laborie, Viers, & Durand. (2004). Coupling of bipolar membrane electrodialysis and ammonia stripping for direct treatment of wastewaters containing ammonium nitrate. *Journal of Membrane Science, 244*(1), 89-96.

Alkarimiah, Mahat, Yuzir, Din, & Chelliapan. (2011). *Operational start-up performance of an innovative anaerobic stage reactor (asr) using synthetic wastewater*. Paper presented at the International Conference on Environment and Industrial Innovation.

Alvarado, & Chen. (2014). Electrodeionization: principles, strategies and applications. *Electrochimica Acta, 132*, 583-597.

Ariesyady, Ito, & Okabe. (2007). Functional bacterial and archaeal community structures of major trophic groups in a full-scale anaerobic sludge digester. *Water Research, 41*(7), 1554-1568.

Atkins, & De Paula. (2013). *Physikalische chemie*: John Wiley & Sons.

Azbar, Dokgöz, Keskin, Korkmaz, & Syed. (2009). Continuous fermentative hydrogen production from cheese whey wastewater under thermophilic anaerobic conditions. *International Journal of Hydrogen Energy, 34*(17), 7441-7447.

Baldasano, Gasso, & Perez. (2003). Environmental performance review and cost analysis of MSW landfilling by baling-wrapping technology versus conventional system. *Waste Management, 23*(9), 795-806.

Barak. (2015). Electrodialysis stacks, systems, and methods for recovering ammonia and monovalent salts from anaerobic digestate In: US Patent 20,150,308,001.

Bogusch, & Grubbs. (2014). Austin Water Utility's Hornsby Bend Biogas-to-Energy CHP Project–Commissioning and startup. *Journal of The Water Pollution Control Federation, 2014*(2), 1-14.

Chen, Tseng, Lee, & Chang. (2005). Fermentative hydrogen production with Clostridium butyricum CGS5 isolated from anaerobic sewage sludge. *International Journal of Hydrogen Energy, 30*(10), 1063-1070.

Chong, Sen, Kayaalp, & Ang. (2012). The performance enhancements of upflow anaerobic sludge blanket (UASB) reactors for domestic sludge treatment–a state-of-the-art review. *Water Research, 46*(11), 3434-3470.

Comotti, & Frigo. (2015). Hydrogen generation system for ammonia–hydrogen fuelled internal combustion engines. *International Journal of Hydrogen Energy*, 40(33), 10673-10686.

De Arespacochaga, Valderrama, Peregrina, Hornero, Bouchy, & Cortina. (2015). On-site cogeneration with sewage biogas via high-temperature fuel cells: Benchmarking against other options based on industrial-scale data. *Fuel Processing Technology, 138*, 654-662.

Demirel, Neumann, & Scherer. (2008). Microbial community dynamics of a continuous mesophilic anaerobic biogas digester fed with sugar beet silage. *Engineering in Life Sciences, 8*(4), 390-398.

Dermentzis, Davidis, Chatzichristou, & Dermentzi. (2012). Ammonia removal from fertilizer plant effluents by a coupled electrostatic shielding based electrodialysis/electrodeionization process. *Global NEST Journal, 14*, 468-476.

Ducharme. (2010). *Technical and economic analysis of Plasma-assisted Waste-to-Energy processes*. Retrieved from

Eckenfelder, Patoczka, & Pulliam. (1988). *Anaerobic versus aerobic treatment in the USA.* Paper presented at the Proceedings of the 5th international symposium on anaerobic digestion.

Farooque, & Maru. (2001). Fuel cells-the clean and efficient power generators. *Proceedings of the IEEE, 89*(12), 1819-1829.

Foo, & Hameed. (2009). An overview of landfill leachate treatment via activated carbon adsorption process. *Journal of Hazardous Materials, 171*(1), 54-60.

Fuerte, Valenzuela, Escudero, & Daza. (2009). Ammonia as efficient fuel for SOFC. *Journal of Power Sources, 192*(1), 170-174.

Goffin, & Calay. (2000). Use of continuous electrodeionization to reduce ammonia concentration in steam generators blow-down of PWR nuclear power plants. *Desalination, 132*(1), 249-253.

Goula, Kiousis, Nalbandian, & Yentekakis. (2006). Catalytic and electrocatalytic behavior of Ni-based cermet anodes under internal dry reforming of CH 4+ CO 2 mixtures in SOFCs. *Solid State Ionics*, 177(119), 2119-2123.

Green. (1982). An ammonia energy vector for the hydrogen economy. *International Journal of Hydrogen Energy, 7*(4), 355-359.

Grigoriev, Porembsky, & Fateev. (2006). Pure hydrogen production by PEM electrolysis for hydrogen energy. *International Journal of Hydrogen Energy, 31*(2), 171-175.

Gross, & Kong. (2013). Performance characteristics of a compression-ignition engine using direct-injection ammonia–DME mixtures. *Fuel, 103*, 1069-1079.

Gupta, Sadegh, Yari, Ghoshekandi, Maazinejad, & Chahardori. (2015). Removal of ammonium ions from wastewater: A short review in development of efficient methods. *Global Journal of Environmental Science and Management, 1*(2), 149-158.

Guštin, & Marinšek-Logar. (2011). Effect of pH, temperature and air flow rate on the continuous ammonia stripping of the anaerobic digestion effluent. *Process Safety and Environmental Protection, 89*(1), 61-66.

He, Zhang, Zeng, & Gao. (2011). A combined thermodynamic cycle used for waste heat recovery of internal combustion engine. *Energy*, 36(12), 6821-6829.

Hoogers. (2002). *Fuel cell technology handbook*: CRC press.

Huang, Xu, Zhang, Xue, & Chen. (2007). Application of electrodialysis to the production of organic acids: state-of-the-art and recent developments. *Journal of Membrane Science*, 288(281), 281-212.

Initiative. (2012). *Water security: the water-food-energy-climate nexus*: Island Press.

Jaroszek, & Dydo. (2016). Ion-exchange membranes in chemical synthesis–a review. *Open Chemistry, 14*(1), 1-19.

John, Olson, Graupner, & Miller. (2007). *Safe, efficient storage of hydrogen in liquid ammonia and ammonia - based solid chemicals*: ChemInform, 38(32).

Kadier, Simayi, Abdeshahian, Azman, Chandrasekhar, & Kalil. (2016). A comprehensive review of microbial electrolysis cells (MEC) reactor designs and configurations for sustainable hydrogen gas production. *Alexandria Engineering Journal, 55*(1), 427-443.

Kendall, & Kendall. (2016). High—temperature solid oxide fuel cells for the 21st century. *Fundamentals, Design and Applications*.

Klerke, Christensen, Nørskov, & Vegge. (2008). Ammonia for hydrogen storage: challenges and opportunities. *Journal of Materials Chemistry*, 18(20), 2304-2310.

Kotay, & Das. (2008). Biohydrogen as a renewable energy resource—prospects and potentials. *International Journal of Hydrogen Energy, 33*(1), 258-263.

Kracke, Vassilev, & Krömer. (2015). Microbial electron transport and energy conservation–the foundation for optimizing bioelectrochemical systems. *Frontiers in Microbiology, 6*.

Krakat, Demirel, Anjum, & Dietz. (2017). Methods of ammonia removal in anaerobic digestion: a review. *Water Science and Technology*, wst2017406.

Krishna, Kumar, & Kumar. (2009). Treatment of low-strength soluble wastewater using an anaerobic baffled reactor (ABR). *Journal of Environmental Management, 90*(1), 166-176.

Kurniawan, Lo, & Chan. (2006). Physico-chemical treatments for removal of recalcitrant contaminants from landfill leachate. *Journal of Hazardous Materials, 129*(1), 80-100.

Lantz. (2012). The economic performance of combined heat and power from biogas produced from manure in Sweden: A comparison of different CHP technologies. *Applied Energy, 98*, 502-511.

Laosiripojana, Wiyaratn, Kiatkittipong, Arpornwichanop, Soottitantawat, & Assabumrungrat. (2009). Reviews on solid oxide fuel cell technology. *Engineering Journal, 13*(1), 65-84.

Lefebvre. (1998). *Gas turbine combustion*: CRC press.

Lei, Sugiura, Feng, & Maekawa. (2007). Pretreatment of anaerobic digestion effluent with ammonia stripping and biogas purification. *Journal of Hazardous Materials, 145*(3), 391-397.

Levin, Pitt, & Love. (2004). Biohydrogen production: prospects and limitations to practical application. *International Journal of Hydrogen Energy, 29*(2), 173-185.

Lewis, Heppell, & Hastings. (2000). *Continuous thermal processing of foods—Pasteurization and UHT Sterilization*. Retrieved from

Li, Huang, Kobayashi, He, & Nagai. (2014). Study on using hydrogen and ammonia as fuels: Combustion characteristics and NOx formation. *International Journal of Energy Research*, 38(39), 1214-1223.

Liu, Grot, & Logan. (2005). Electrochemically assisted microbial production of hydrogen from acetate. *Environmental Science & Technology, 39*(11), 4317-4320.

Liu, Ting, & Checkel. (2003). *Ammonia as a fuel for SI engine* (0148-7191). Retrieved from

Logan, Call, Cheng, Hamelers, Sleutels, Jeremiasse, & Rozendal. (2008). Microbial electrolysis cells for high yield hydrogen gas production from organic matter. *Environmental Science & Technology, 42*(23), 8630-8640.

Lopez, & Hestekin. (2015). Improved organic acid purification through wafer enhanced electrodeionization utilizing ionic liquids. *Journal of Membrane Science, 493*, 200-205.

Madigan, Martinko, Dunlap, & Clark. (2008). Brock biology of microorganisms 12th edn. *International Microbiology, 11*(International Microbiology), 65-73.

McCarty, Bae, & Kim. (2011). Domestic wastewater treatment as a net energy producer–can this be achieved? *Environmental Science & Technology, 45*(17), 7100-7106.

Mehanna, Kiely, Call, & Logan. (2010). Microbial electrodialysis cell for simultaneous water desalination and hydrogen gas production. *Environmental Science & Technology, 44*(24), 9578-9583.

Mehta, Coppi, Childers, & Lovley. (2005). Outer membrane c-type cytochromes required for Fe (III) and Mn (IV) oxide reduction in Geobacter sulfurreducens. *Applied and Environmental Microbiology, 71*(12), 8634-8641.

Metcalf, & Eddy. (2014). Wastewater engineering: treatment and Resource recovery. *McGraw-Hill Education, New York*.

Minh. (2004). Solid oxide fuel cell technology—features and applications. *Solid State Ionics, 174*(1), 271-277.

Mondor, Masse, Ippersiel, Lamarche, & Masse. (2008). Use of electrodialysis and reverse osmosis for the recovery and concentration of ammonia from swine manure. *Bioresource Technology, 99*(15), 7363-7368.

Moon, Ju, & Ryu. (2003). Electrocatalytic reforming of carbon dioxide by methane in SOFC system. *Catalysis today*, 87(81), 255-264.

Nair, George, Malano, Arora, & Nawarathna. (2014). Water–energy–greenhouse gas nexus of urban water systems: Review of concepts, state-of-art and methods. *Resources, Conservation and Recycling, 89*, 1-10.

Ni, Leung, & Leung. (2009). Ammonia - fed solid oxide fuel cells for power generation—A review. *International Journal of Energy Research, 33*(11), 943-959.

Oreopoulou, & Russ. (2007). Anaerobic digestion of organic residues and wastes. *Utilization of by-products and treatment of waste in the food industry*, 53-72.

Ormerod. (2003). Solid oxide fuel cells. *Chemical Society Reviews*, 32(31), 17-28.

Paidar, Fateev, & Bouzek. (2016). Membrane electrolysis—History, current status and perspective. *Electrochimica Acta, 209*, 737-756.

Park, & Kim. (2016). Effect of ammonia on anaerobic degradation of amino acids. *KSCE Journal of Civil Engineering, 20*(1), 129.

Parkin, & Owen. (1986). Fundamentals of anaerobic digestion of wastewater sludges. *Journal of Environmental Engineering, 112*(5), 867-920.

Pontes, & Chernicharo. (2011). Characterization and removal of specific organic constituents in an UASB – trickling - filter system treating domestic wastewater. *Environmental Technology, 32*(3), 281-287.

Rabaey, & Verstraete. (2005). Microbial fuel cells: novel biotechnology for energy generation. *Trends in Biotechnology, 23*(6), 291-298.

Rahmani, & Mahvi. (2006). Use of ion exchange for removal of ammonium: a biological regeneration of zeolite. *Global NEST Journal, 8*(2), 146-150.

Rajagopal, Massé, & Singh. (2013). A critical review on inhibition of anaerobic digestion process by excess ammonia. *Bioresource Technology, 143*, 632-641.

Ramirez. (2002). *The fifth european solid oxide fuel cell forum.* Paper presented at the European Fuel Cell Forum, Lucerne, Switzerland.

Rasi, Veijanen, & Rintala. (2007). Trace compounds of biogas from different biogas production plants. *Energy, 32*(8), 1375-1380.

Reich, Kaiser, & Irvine. (2001). Niobia based rutile materials as SOFC anodes. *Fuel Cells*, 1(3-4), 249-255.

Renou, Givaudan, Poulain, Dirassouyan, & Moulin. (2008). Landfill leachate treatment: review and opportunity. *Journal of Hazardous Materials, 150*(3), 468-493.

Scherson, Wells, Woo, Lee, Park, Cantwell, & Criddle. (2013). Nitrogen removal with energy recovery through N 2 O decomposition. *Energy & Environmental Science, 6*(1), 241-248.

Scherson, Woo, & Criddle. (2014). Production of nitrous oxide from anaerobic digester centrate and its use as a co-oxidant of biogas to enhance energy recovery. *Environmental Science & Technology, 48*(10), 5612-5619.

Schiffler. (2004). Perspectives and challenges for desalination in the 21st century. *Desalination*, 165, 161-169.

Schüth, Palkovits, Schlögl, & Su. (2012). Ammonia as a possible element in an energy infrastructure: catalysts for ammonia decomposition. *Energy & Environmental Science, 5*(4), 6278-6289.

Shiratori, Oshima, & Sasaki. (2008). Feasibility of direct-biogas SOFC. *International Journal of Hydrogen Energy*, 33(21), 6316-6321.

Shrestha. (2008). Landfill gas with hydrogen addition–A fuel for SI engines. *Fuel, 87*(17), 3616-3626.

Singh, Hernández-Pacheco, Hutton, Patel, & Mann. (2005). Carbon deposition in an SOFC fueled by tar-laden biomass gas: a thermodynamic analysis. *Journal of Power Sources, 142*(1), 194-199.

Singhal. (2007). Solid oxide fuel cells. *The Electrochemical Society Interface, 16*(4), 41.

Singhal, & Egushi. (2011). Solid oxide fuel cells 12 (SOFC-XII). *TE Society*.

Singhal, & Kendall. (2003). *High-temperature solid oxide fuel cells: fundamentals, design and applications*: Elsevier.

Speece. (2008). *Anaerobic biotechnology and odor/corrosion control for municipalities and industries*: Archae Press.

Spiegel, Thompson, Helden, Doan, Gaspar, & Zanapalidou. (1999). Investigation of an electrodeionization system for the removal of low concentrations of ammonium ions. *Desalination, 123*(1), 85-92.

Srinivasan. (2006). *Fuel cells: from fundamentals to applications*: Springer Science & Business media.

Sullivan. (2007). *Fertilizing with biosolids*. Retrieved from

Thauer, Jungermann, & Decker. (1977). Energy conservation in chemotrophic anaerobic bacteria. *Bacteriological Reviews, 41*(1), 100.

Themelis, & Ulloa. (2007). Methane generation in landfills. *Renewable Energy, 32*(7), 1243-1257.

Tsukuda, Notomi, & Histatome. (2000). Application of plasma spraying to tubular-type solid oxide fuel cells production. *Journal of Thermal Spray Technology, 9*(3), 364-368.

Tu, & Stimming. (2004). Advances, aging mechanisms and lifetime in solid-oxide fuel cells. *Journal of Power Sources, 127*(1), 284-293.

Urban, Lohmann, & Gómez. (2009). Catalytically upgraded landfill gas as a cost-effective alternative for fuel cells. *Journal of Power Sources, 193*(1), 359-366.

Van Aken, McDonough, Li, Feng, Chathoth, Mamontov, . . . Gogotsi. (2014). Effect of cation on diffusion coefficient of ionic liquids at onion-like carbon electrodes. *Journal of Physics: Condensed Matter, 26*(28), 284104.

Van Dongen, Jetten, & Van Loosdrecht. (2007). *The Combined Sharon/Anammox Process-A Sustainable Method for N-removal from Sludge Water* (Vol. 6).

Vidal-Iglesias, Garcıa-Aráez, Montiel, Feliu, & Aldaz. (2003). Selective electrocatalysis of ammonia oxidation on Pt (100) sites in alkaline medium. *Electrochemistry Communications, 5*(1), 22-26.

Wan, Gu, Zhao, & Liu. (2016). COD capture: a feasible option towards energy self-sufficient domestic wastewater treatment. *Scientific Reports, 6*, 25054.

Wang, Tay, Tay, & Hung. (2010). *Environmental bioengineering* (Vol. 11): Springer Science & Business Media.

Westgate. (2009). *Characterization of Proteins in Effluents from Three Wastewater Treatment Plants that Discharge to the Connecticut River*. Retrieved from

Williams, Strakey, & Sudoval. (2006). US DOE fossil energy fuel cells program. *Journal of Power Sources*, 159(152), 1241-1247.

Wiszniowski, Robert, Surmacz-Gorska, Miksch, & Weber. (2006). Landfill leachate treatment methods: A review. *Environmental Chemistry Letters, 4*(1), 51-61.

Wojcik, Middleton, & Damopoulos. (2003). Ammonia as a fuel in solid oxide fuel cells. *Journal of Power Sources*, 118(111), 342-348.

Xiang. (2010). *Marine Science & Technology in China: A Roadmap to 2050*: Springer Science & Business Media.

Xu, Dong, Zhuang, He, Ni, Feng, & Lee. (2017). Energy upcycle in anaerobic treatment: Ammonium, methane, and carbon dioxide reformation through a hybrid electrodeionization–solid oxide fuel cell system. *Energy Conversion and Management, 140*, 157-166.

Yang, Peng, Liu, Zeng, Mino, & Satoh. (2007). Nitrogen removal via nitrite from municipal wastewater at low temperatures using real-time control to optimize

nitrifying communities. *Environmental Science & Technology, 41*(23), 8159-8164.

Yang, Xia, & Stevenson. (2005). Mn1. 5Co1. 5 O 4 Spinel Protection Layers on Ferritic Stainless Steels for SOFC Interconnect Applications. *Electrochemical and Solid-State Letters*, 8(3), A168-A170.

Yedla, Parikh, & J. (2001). Economic evaluation of a landfill system with gas recovery for municipal solid waste management: a case study. *International Journal of Environment and Pollution, 15*(4), 433-447.

Yeon, Song, & Moon. (2004). A study on stack configuration of continuous electrodeionization for removal of heavy metal ions from the primary coolant of a nuclear power plant. *Water Research, 38*(7), 1911-1921.

Yi, Rao, Brouwer, & Samuelsen. (2004). Analysis and optimization of a solid oxide fuel cell and intercooled gas turbine (SOFC–ICGT) hybrid cycle. *Journal of Power Sources, 132*(1), 77-85.

Zamfirescu, & Dincer. (2008). Using ammonia as a sustainable fuel. *Journal of Power Sources*, 185(181), 459-465.

Zhang, Peng, Wang, Zheng, & Jin. (2007). Organic matter and concentrated nitrogen removal by shortcut nitrification and denitrification from mature municipal landfill leachate. *Journal of Environmental Sciences, 19*(6), 647-651.

Zhang, Su, Baeyens, & Tan. (2014). Reviewing the anaerobic digestion of food waste for biogas production. *Renewable & Sustainable Energy Reviews, 38*, 383-392.

Zhang, Tian, Zhang, Ghulam, Fang, & He. (2013). Investigation on characteristics of leachate and concentrated leachate in three landfill leachate treatment plants. *Waste Management, 33*(11), 2277-2286.

Zhang, Zheng, Tang, & Ren-cun. (2008). Anaerobic ammonium oxidation for treatment of ammonium-rich wastewaters. *Journal of Zhejiang University-Science B, 9*(5), 416-426.

Züttel, Remhof, Borgschulte, & Friedrichs. (2010). Hydrogen: the future energy carrier. *Philosophical Transactions of the Royal Society of London A: Mathematical, Physical and Engineering Sciences*, 368(1923), 3329-3342.

CHAPTER 2 LITERATURE REVIEW

2.1 Introduction

According to the reported literature, energy reuse of NH_4^+-N in wastewater is filled with challenges for some limitations, particularly following AD (Ho, 2008; Reinhard, 2005). Foremost, NH_4^+ has special properties (e.g., unstable concentration, incomplete decomposition, toxicity, and the solubility limit the transform from $NH_4^+{}_{(aq)}$ to $NH_{3(g)}$). These characteristics cause low conversion efficiency of NH_4^+. Second, membrane contaminant is also a server issue because of the complex organic intermediates and bacteria attachment so that pre-treatments (sedimentation and filtration) of digestate is indispensable (Lopez & Hestekin, 2015). Third, EDI is not able to be applied to the separation of weak ions. Smith & Hyde (2000) studied short-bed demineralization altering electrodeionization and found that EDI was hard to remove weakly ionized substances (e.g., silica, carbon dioxide, and VFAs) due to the low current density (Smith & Hyde, 2000). Toward this, strong supporting electrolytes (e. g., NaCl or Na_2SO_4) are needed to enhance the electric current and to improve the deionization efficiency. Fourthly, the deionization efficiency strictly depends on the operation parameters, like voltage loading, surrounding factor. Bouhidel & Lakehal (2006) and Liu *et al*. (2008) investigated the influences of operating factors (e.g., applied voltage,

electrolyte concentration, type, temperature, and flow rate) on EDI performances and found that the deionization efficiency was sensitive to these operating factors (Bouhidel & Lakehal, 2006; Liu *et al.*, 2008).

Besides, concentration polarization of ion exchange membrane is a significant limitation. The phenomenon caused inefficient use of electrical current that reduces the deionization efficiency (Arar *et al.*, 2014; Bouhidel & Lakehal, 2006). Another crucial aspect is the capacitance of the electrode under the different conditions. Berkh *et al*. (2008) studied the relationship between EDI performances and electrodes behaviors, especially the structures and preparties of the electric double layer (EDL) and found that a short-lived intermediate, Rydberg radical NH_4^0, was formed during the potential sweep in the cathodic direction (Berkh *et al.*, 2008). Uncountable scholars have researched ions crossing ion exchange membrane and ion electrochemical reactions in the EDL. They have developed many experimental methods and theories to understand these phenomena. For AD-EDI-SOFCs hybrid system, EDI, as the unique process requiring energy input, is crucial for net energy benefit of the whole AD-EDI-SOFCs system. Therefore, this chapter will review the recently relevant advances in concentration polarization of ion exchange membrane and behaviors of electrodes and summary the main findings.

2.2 Electrodeionization principle

Electrodeionization is a type of ion-exchange technologies that are implemented to desalt and concentrate ions from saline water, amino acid, sugar liquor, organic substances (Tanaka, 2011). EDI reactor has two types: single EDI and continuous EDI

stack. Single EDI cell is only inserted either a cation exchange membrane or an anion exchange membrane while continuous EDI stack is added a group of ion exchange membrane pairs including the cation exchange membrane and the anion exchange membrane (Rizvi, 2010). So, the ion exchange membrane pairs divide the EDI into the dilute chamber and the brine chamber, exhibited in Fig. 2-1. Driven by the electric potential differences, ions cross the cation exchange membrane or anion exchange membrane and reversely transport from one electrolyte to another electrolyte (Parmar & Thakur, 2013; Srivastava & Goyal, 2010). The applied voltage usually leads to unavoidable water dissociation or other redox reactions taking place at the electrodes, as shown in Eq. 2-1 and Eq. 2-2 (Hwang *et al.*, 2003).

At the anode:

$$H_2O_{(l)} \rightarrow 2H^+{}_{(aq)} + 0.5O_{2(g)} + 2e^- \tag{2-1}$$

At the cathode:

$$2H_2O_{(l)} + 2e^- \rightarrow H_{2(g)} + 2OH^-{}_{(aq)} \tag{2-2}$$

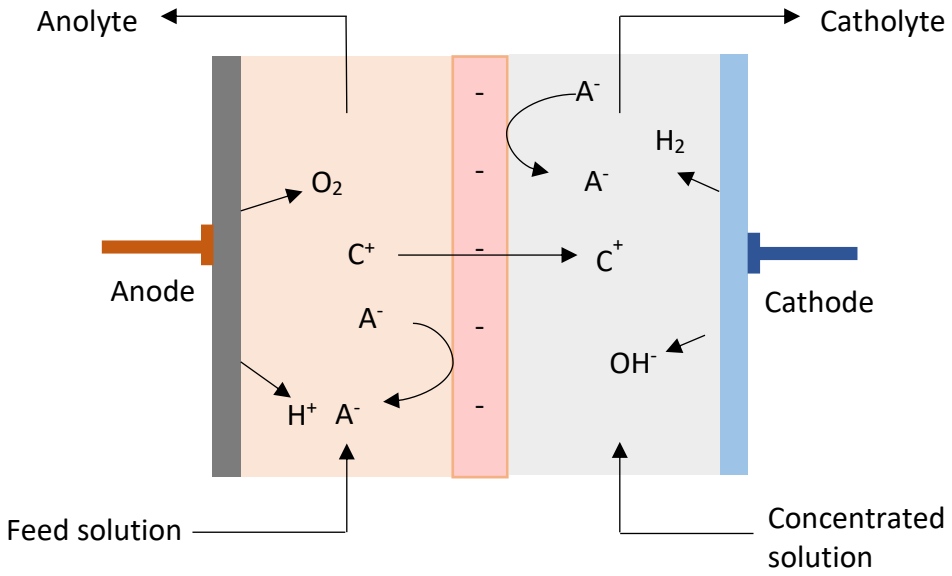

(a)

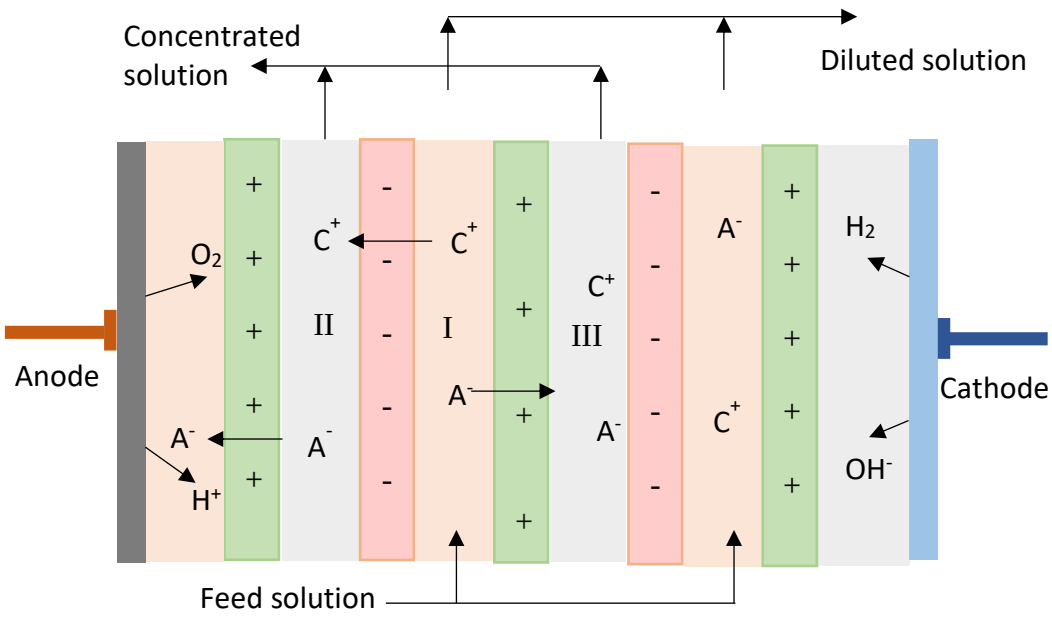

(b)

Figure 2-1 Schematic graphs of a single EDI and continuous EDI stack (Sadrzadeh & Mohammadi, 2008).

Thermodynamics is the fundamental principle that describes the rule of energy changes inevitably generating in the mass transport by leading into the concept of "time" in the system, as described by Eq. 2-3 (Kedem & Katchalsky, 1961).

$$J_i = L_{i1}X_1 + L_{i2}X_2 + ... + L_{in}X_n = \sum_{k=1}^{n} L_{ik}X_k \text{ , (i=1, 2, ···, n)} \qquad (2\text{-}3)$$

where *Xi* and *Ji* are the force and the flux, respectively. L_{ik} is the phenomenological coefficients in which *i* and *k* are components, respectively. In a three-cell EDI system, the cation exchange membrane (K) and the anion exchange membrane (A) are placed between cell II and cell III and cell I and cell II (the unit of EDI stack, Figure 2-1). Based on the irreversible thermodynamics, the electric current (*I*), volume flow (*J*), and mass flux (J_i) are described as the functions of the potential difference (E_c), a pressure difference (E_P), and the chemical potential difference (E_{mi}) as follows (Eq. 2-4 to Eq. 2-6) (Kedem & Katchalsky, 1963).

$$I = L_E \Delta\psi + \Delta L_{EP}\Delta P + \sum_i L_{Ei}\Delta\mu_i \qquad (2\text{-}4)$$

$$J = L_{EP}\Delta\Psi + \Delta L_P \Delta P + \sum_i L_{Pi}\Delta\mu_i \qquad (2\text{-}5)$$

$$J_i = L_{iE}\Delta\Psi + \Delta L_{iP}\Delta P + \sum_i L_{ik}\Delta\mu_i \qquad (2\text{-}6)$$

Salt accumulation $J_{S,K} + J_{S,A}$ and solution accumulation $J_{V,K} + J_{V,A}$ at in the steady state are given by Eq. 2-7 and Eq. 2-10.

$$J_{S,K} + J_{S,A} = (t_k + t_A - 1)\frac{i}{F} - RT\left[(\varpi_K + \varpi_A) - \left\{L_{P,K}\sigma_K(1-\sigma_K) + L_{P,A}\sigma_A(1-\sigma_A)\right\}C_S^*\right]\Delta C$$

(2-7)

$$J_{V,K} + J_{V,A} = (\beta_K + \beta_A)i + RT(\sigma_K L_{P,K} + \sigma_A L_{P,A})\Delta C \qquad (2\text{-}8)$$

$$\Delta C = C^{''} - C^{'} \qquad (2\text{-}9)$$

$$C_S^* = \frac{C^{''} - C^{'}}{\ln(C^{''}/C^{'})} \qquad (2\text{-}10)$$

where t, the transport number; ϖ, the solute permeability; L_P, the hydraulic conductivity; s, the reflection coefficient; b, the electro-osmotic permeability, F, the Faraday constant; R, the gas constant; T, the absolute temperature; and ΔC, the concentration difference, respectively.

The second of great importance is ion transport. The overall mass transport is expressed by Eq. 2-11 and Eq. 2-12.

$$J_s = C^{''}J_V = \lambda i - \mu(C^{''} - C^{'}) = \lambda i - \mu\Delta C \qquad (2\text{-}11)$$

$$J_V = \phi_i + \rho(C^{''} - C^{'}) = \phi_i + \Delta C \qquad (2\text{-}12)$$

Where λ, μ, φ, ρ are the over transport number, the overall solute permeability, the overall electro-osmotic permeability, and the overall hydraulic permeability, respectively.

$$\begin{aligned}&\sigma(L_{PD,K}+L_{P,K})=(L_{P,K}+L_{P,A})\\&=-(L_{PD,K}+L_{PD,A})=-(L_{DP,K}+L_{DP,A}\\&=\frac{\rho}{RT}\end{aligned} \tag{2-13}$$

σ is the membrane pair reflection coefficient; L_{PD} and L_{DP} are the osmotic volume flow coefficient and the ultrafiltration coefficient, respectively. Their relationship is satisfied with the Onsager reciprocal relation, $L_{PD}=L_{DP}$ (Onsager, 1931). The parameters of above equations can be obtained from experimental or partial results. $L_{PD,K}+L_{PD,A}$ and $L_{DP,K}+L_{DP,A}$ are calculated using Eq. 2-13 and plotted against ρ in Figure 2-2. This figure illustrates that the hydraulic conductivity and the exchange conductivity of the membrane pair linearly increase with total hydraulic conductivity (ρ). Also, the hydraulic conductivity and the exchange conductivity show a significant difference with the increase in the total hydraulic conductivity. Hereby, the variation of conductivity indicates that the total hydraulic conductivity makes a greater contribution to the hydraulic conductivity than the exchange conductivity. Above equations about the principle of electrodeionization demonstrate the ion separation are related to many parameters such as the electric current, the reflection coefficient, the hydraulic conductivity, the exchange conductivity, and the solute permeability. In engineering, these parameters lead to the differences in ion transport numbers of between the solution and the membrane and result in the occurrences of concentration polarization.

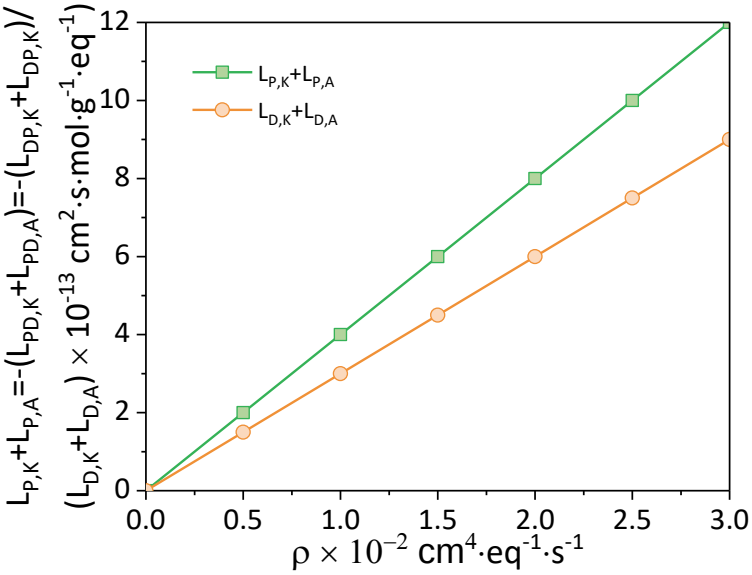

Figure 2-2 Relationship between ρ and L_P, L_{PD}, L_{DP}, and L_D (Tanaka, 2006).

2.3 Concentration polarization in membrane separation processes

2.3.1 Concentration polarization phenomenon

An ion in the solution has a different transport number from that in the membrane. Under the applied electric current, the permeable ion is depleted on the concentrated side but accumulated on another side of the membrane. This difference in ion concentration leads to a potential drop called concentration polarization (Figure 2-3) (Hoek & Tarabara, 2013). Specifically, it refers to a decrease in the concentration of the permeable ion on the feeding side and an increase on the concentrated side of ion exchange membrane under the direct current density. Generally, the formation of concentration polarization experiences four steps: (1) the solute convectively transports towards the membrane by electric forces (Tanaka, 2004); (2) Near the membrane surface, the solute is rejected by the membrane, which leads to the solute accumulating and concentrating at the interface between the membrane surface and the bulk solution (Chamoulaud & Bélanger, 2005; Choi *et al.*, 2001; Tanaka, 2015); (3) Owing to the difference in the concentration, the solute diffuses from the membrane surface towards the feed solution and forms a boundary layer near the surface of the membrane with spatially varying concentration; (4) On the feeding side, the concentration of the permeable ion at the adjacent site to the membrane surface is more dilute than that in the bulk solution (Długołęcki, Ogonowski, *et al.*, 2010). Therefore, the depletion of the solvent means an increase in the fraction of the voltage drop at the interface between the diffusion boundary layer and the ion membrane, which is dissipated in transporting ions across the diffusion boundary layer rather than through the membrane (Rosenberg & Tirrell, 1957).

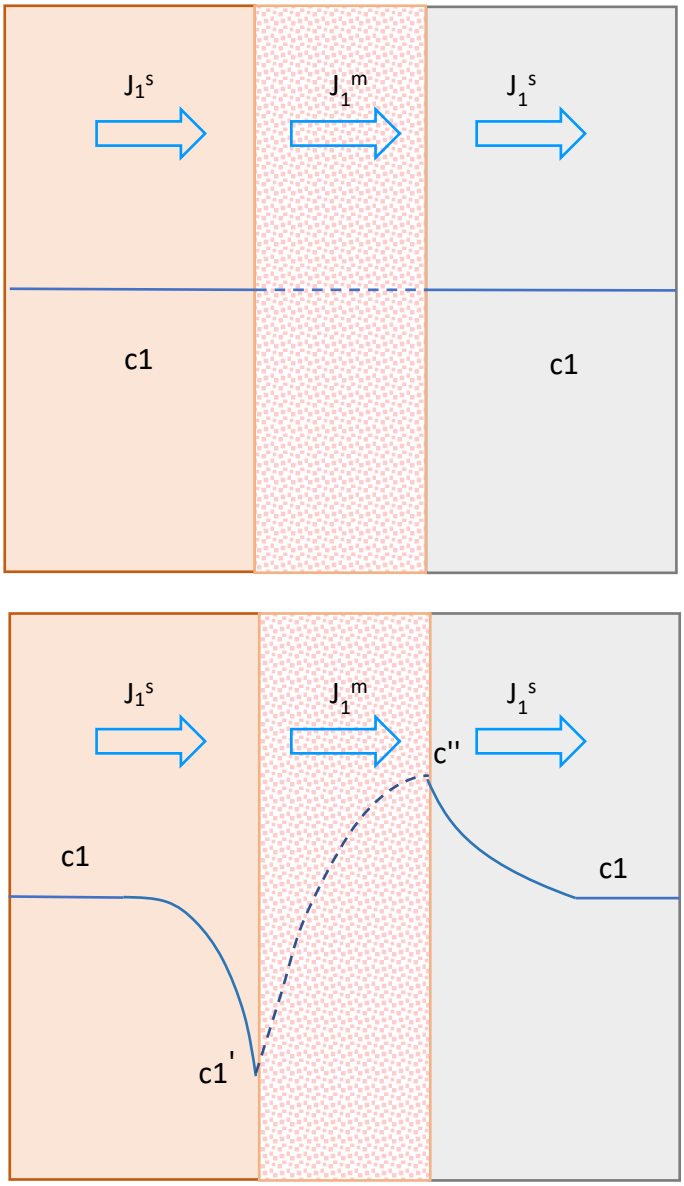

Figure 2-3 Concentration polarization for cationic exchange membrane (Hoek & Tarabara, 2013).

2.3.2 Concentration polarization characterization

The occurrence of concentration polarization is inescapable for any ion-exchange membranes once it works. As usual, it is characterized by the relationship of current density (*I*) and applied voltage (*V*), called *I*-*V* polarization curve (Chamoulaud & Bélanger, 2005). There are three distinct regions on the paradigmatic *I*-*V* curve: the ohmic region (I), the LCD plateau region (II), and the over limiting current region (III) (Choi *et al.*, 2001; Lee *et al.*, 2006; Tanaka, 2011; Tanaka, 2015). Each region provides different information on system resistance, ion transport, and boundary layer thickness (Długołęcki, Anet, *et al.*, 2010; Krol *et al.*, 1999). In details, current density linearly increases with the elevation of the applied voltage, and the reciprocal value of the slope reflects the electrolyte resistance in the zone of the ohmic polarization. Even if the applied voltage continuously elevates, the current density does not increase at all in the region of pseudo-plateau or limiting current density. According to the theory of concentration polarization, the limiting current delivers information about the thickness of the diffusion boundary layer (δ), the diffusion coefficient (D), and the ion transport number (t) (Rubinstein, 1991; Rubinstein & Zaltzman, 2000). In the region of over limiting current density, the high potential drop formed between two sides of ion exchange membrane may result in water dissociation and electroconvection. Water dissociation and electroconvection occurrence distort the diffusion boundary layer, which leads to slow diffusion rates (Rubinstein *et al.*, 1988) (Figure 2-4). Therefore, it is of exceptional importance to profoundly understand the mechanism of concentration polarization.

1) Experimental measurements of current and voltage

Studies on the mechanism of concentration polarization have been carried out for a long time, and the related methods (experimental measurements and theoretical calculations) have been built up. In the earliest stage, Stephen (1973) measured the noise spectrum of solutions containing Na^+ and H^+ ion to study ion transport using commercial cation-exchange membranes (Stern & Green, 1973). Li *et al*. (1983) measured the light scattering spectra from polystyrene latex spheres near a cation exchange membrane and found that fluctuations of electrical noise spectra were induced by turbulent flow on the depleted side of the membrane (Li *et al.*, 1983). Later, Choi *et al*. (2002) directly described the concentration profiles in the boundary layer under and over the limiting currents and found an increase in the concentration of permeable ion at the membrane surface to a sufficient level that produced the over limiting current (Choi *et al.*, 2002). Since the current-voltage method cannot unambiguously estimate the limiting condition in the practical implementations, a new method consisting of measuring current as a function of desalting efficiency and determining the inflection in a q-I curve was set up (Meng *et al.*, 2005). Latest, Fontananova *et al*. (2014) used Pulsed Gradient Spin Echo Nuclear Magnetic Resonance (PGSE-NMR) to measure the variation of water self-diffusion coefficients as a function of the solution concentration and temperature (Fontananova *et al.*, 2014). Though these methods are upgrading, experimental data does not explicitly describe the process of concentration polarization.

2) Model developments

Theoretical simulation of concentration polarization is another imperative approach because it can overcome the difficulties that cannot be precisely described by experiment measurements (Berardi, 2013). As we take NaCl as an example, when the cation exchange membrane is immersed in NaCl solution, the electric current (i) is added. On the diluted side, if the transport number of the Na^+ is 0.4 and that in the cation exchange membrane (t_m) is 0.95, the flux of Na^+ in the solution, the transport numbers of Na^+ in the solution and the membrane, are expressed by Eq. 2-14 and Eq. 2-15, respectively.

$$J_{Na} = t_{Na}(\frac{i}{F}) = 0.4(\frac{i}{F}) \tag{2-14}$$

$$J_{Na} = t_{mNa}(\frac{i}{F}) = 0.95(\frac{i}{F}) \tag{2-15}$$

To keep the mass balance, NaCl concentration should be decreased, and the gradient of the concentration is produced, as expressed by Eq. 2-16.

$$\Delta C = \frac{C - C_0}{\delta} \tag{2-16}$$

The mass balance and the limiting current density in the boundary layer thus are given by Eq. 2-17 and Eq. 2-18.

$$t_{mNa}\frac{i}{F} = D\frac{C - C_0}{\delta} + t_{Na}\frac{i}{F} \tag{2-17}$$

$$i_{\lim} = \frac{FDC}{(t_{mNa} - t_{Na})\delta} \tag{2-18}$$

According to the measured parameters, the *I–V* curve of a cation exchange membrane is shown in Figure 2-5. Within 1.0 V, current density linearly increases as a slop of 100×10^{-6} A, reflecting that the ohmic resistance is 1.0×10^{-4} Ω. In 1.0-2.0 V, the current density is kept at 100×10^{-6} A. If the slop is regarded as zero, the resistance will be infinitely large. Over 2.0 V, the small slop indicated a large increase in resistance. Thus, increasing the slop is an efficient way to reduce the membrane resistance.

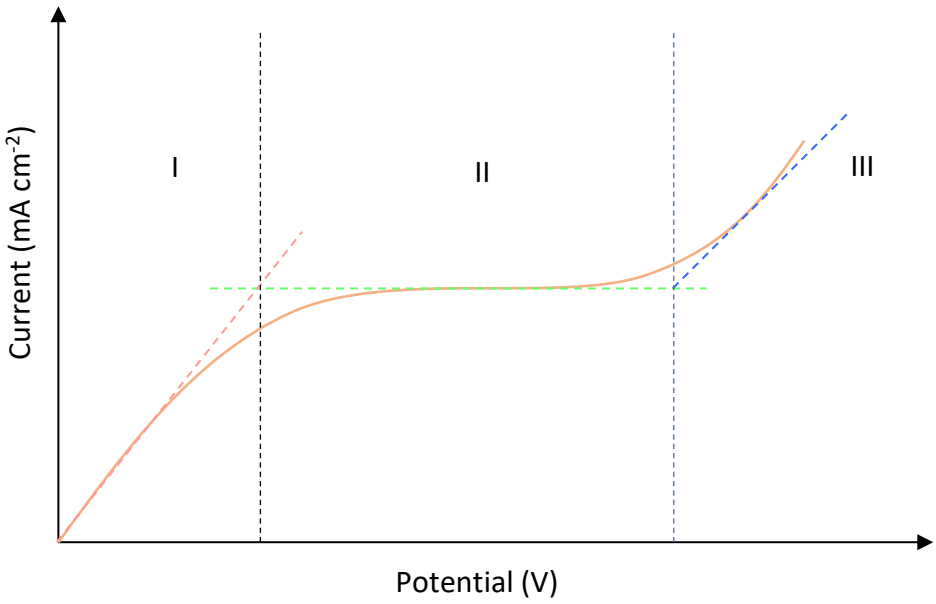

Figure 2-4 Typical current-voltage curve for a cation exchange membrane (Scarazzato *et al.*, 2015).

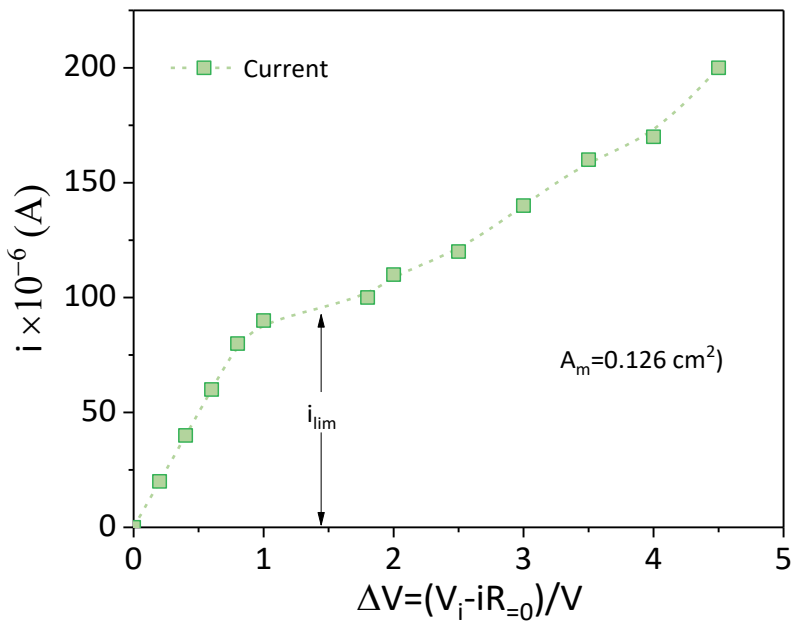

Figure 2-5 Current-voltage curve (Membrane area 0.126 cm^2) (Tanaka *et al.*, 2012).

Looking back at the development of EDI, notable achievements are the mass transport theory (Nernst–Planck equation) developed by Planck in 1890 (Planck, 1890) and Donnan equilibrium theory presented by Donnan in 1924 (Donnan, 1924), which will be described in Chapter 4 in details. Here we only introduced the applications of Nernst–Planck equation. Spiegler (1971) used Nernst–Planck model calculated the current-voltage relationship for the anion exchange membrane that was placed in a 1-1 valent electrolyte solution (Eq. 2-19 to Eq. 2-22) and plotted the potential drop across the membrane as shown in Figure 2-6 (Spiegler, 1971). Upon increasing the voltage, the current reaches a plateau, indicating the limiting current realized and electrolyte concentration drops to zero.

$$\Delta E = 2(R_s + R_m)i + \left[(\frac{\alpha}{\lambda}) + \beta - \gamma \right] \ln \frac{1 + (i/i_{\lim})}{1 - (i/i_{\lim})} \tag{2-19}$$

$$\alpha = -\frac{FD}{t_m - t_+} = \frac{FD}{t_m - t_-} \tag{2-20}$$

$$\beta = \left(\frac{RT}{F} \right) (t_m - t_{m+}) \tag{2-21}$$

$$\gamma = \left(\frac{RT}{F} \right) (t_- - t_+) \tag{2-22}$$

Besides, the method of finite element analysis was used via solving the governing equations (e.g., Nernst−Planck, Navier−Stokes, and Poisson simultaneously) based on hydromechanics and mass transport, and obtained the results of the concentration and potential profiles in macroscope scale (Allen, 2004; Berardi, 2013; Jia & Kim, 2014).

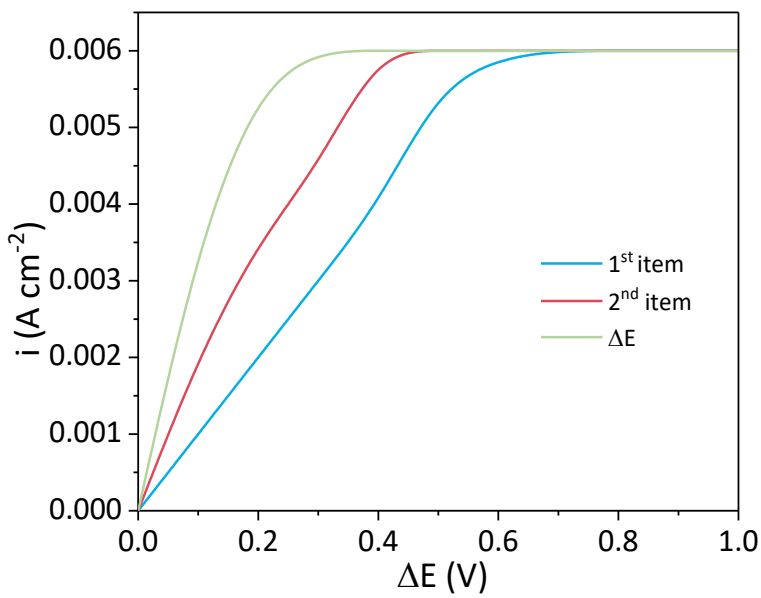

Figure 2-6 Calculated current-voltage curve (Spiegler, 1971) the blue line is the first item, and the red line is the second item in Eq. 2-19.

2.3.3 Concentration polarization consequences and improvements

Concentration polarization phenomenon brings adverse effects on the membrane separation (Nagy & Kulcsár, 2010). Bhattacharjee *et al*. in 1994 reported that concentration polarization caused the loss of driving force and the reduction in permeable flux (Bhattacharjee *et al.*, 1994). Van den Berg & Smolders in 1990 found that the high concentration of the solute near the membrane surface resulted in the formation of a cake or a gel layer and produced an extra resistance (Van den Berg & Smolders, 1990). Chun *et al*. in 2017 also ascertained that the pore blocking and solute adsorption near the membrane surface produced membrane fouling (Chun *et al.*, 2017). Hou *et al*. in 2010 studied the external factor and a robust design for optimizing electrostatic separation for recycling waste printed circuit board and found the relationship between concentration polarization and other phenomena such as salt leakage, intensive energy consumption, and depreciation during ion separations (Hou *et al.*, 2010). They also reported that salt concentration increase resulted in the permeable flux decline, particularly at the concentrated salt solution (> 80 g L^{-1}). Hence, they adjusted the feed concentration within 80 g L^{-1}, which efficiently alleviate concentration polarization.

Up to date, many investigations have been conducted to figure out approaches to relieve concentration polarization (Jang *et al.*, 2015; Liu *et al.*, 2003). Liu *et al*. in 2003 discussed the relationship between the materials of ion exchange membrane and concentration polarization. And they found that the PP membrane displayed better performance than the PVDF and PTFE membranes at high concentration (Liu *et al.*, 2003). Hoek & Tarabara in 2013 investigated the effects of operating parameters on

the magnitude of concentration polarization. They found it depends on the applied potential, concentration difference, flow rate, and pressure (Hoek & Tarabara, 2013). According to above references, almost all studies focused on the feeding side of EDI. Yet, few papers have reported the relationship between the supporting electrolyte and concentration polarization, which is the second research focus of this thesis.

2.4 Electric double layer at metal-solution interface

2.4.1 Electric double layer phenomenon

EDL is a structure on the surface of metals where the excess charge is confined to the near surface region when it is exposed to a fluid (Grahame, 1947). The charged solid surface attracts counterions and repels co-ions from the ionized solute under the fixed current (Figure 2-7). A well-defined capacitor or parallel fluid layers are formed either through crystal lattice defection, molecule dissociation, surface group ionization, or adsorption of external ions in the interfacial region where charge separation occurs (Hunter, 2001; Ney, 2016). EDL lies in the heart of the electrode and is crucial in electrochemistry, corrosion science, and catalysis. Its structures and properties determine the electrochemical reaction kinetics, capacitance, and resistance (Fedorov & Kornyshev, 2014). Gongadze *et al*. in 2009 introduced that the EDL played profound effects on the interface between a charged surface and ionic liquids of physical, chemical, and biological systems (Gongadze *et al.*, 2009). Yu *et al*. in 2004 mentioned that the distribution of small ions in the EDL determined the stability of a charge-stabilized colloidal dispersion and the kinetics of electrochemical reactions (Yu *et al.*, 2004). Lozada-Cassou *et al*. in 1999 reported that the EDL was informative for the

microscopic details of the rational explanation and predicted the electrostatic mobility of charged particles (Lozada-Cassou *et al.*, 1999). For EDI, the studies of EDL are therefore so significant for ion separation processes for environmental protections via developing cost-effective technologies (Alvarado & Chen, 2014; Hou, 2008).

During the past decades, major studied on electrochemical measurements through controlling potential and current were carried out. Bard *et al*. in 1980 implemented cyclic voltammetry (CV) to measure the variation of the electric current with the applied voltage and found the change rate of charge being proportional to sweeping rate using the same constant according to the I-V curve (Bard *et al.*, 1980). Yoon *et al*. in 2000 used chronoamperometry to measure current over time and found that the potentiometer provided electric current for maintaining the surface potential when the charge of EDL accumulated on the electrode surface (Yoon *et al.*, 2000). Ney in 2016 employed the total current response to calculate the net charge of the EDL across the entire electrode as the electrode gradually reached the equilibrium state (Ney, 2016). Unfortunately, experimental tests cannot provide explicit predictions about the variations of the structures and properties of EDL under the complex conditions of the solid-liquid interface.

2.4.2 Classical electrical double layer theory

There are several theories about the EDL of the solid-liquid interface, as summarized in Table 2-1. At the earliest stage, Helmholtz realized that the charged electrodes immersed in electrolytic solutions repelling the co-ions but attracting counterions to their surfaces and developed Helmholtz model to predict the constant differential capacitance that is independent of the charge (Helmholtz, 1853). This earliest model

did not consider diffusion/mixing of ions. Later, both Gouy in 1910 and Chapman in 1913 found that the capacitance of EDL was not a constant and they thus modified Helmholtz model and developed Gouy-Chapman model. This model defines the diffusion layer but overestimates the capacitance of the EDL (Namisnyk & Zhu, 2003). Stern combined the Helmholtz model with the Gouy-Chapman model and named Gouy-Chapman-Stern model (Watts-Tobin & Mott, 1961). This model assumed ions in the diffuse layer interact via Coulombic force. Grahame in 1947 proposed Grahame model based on Gouy-Chapman-Stern model (Grahame, 1947). Bockris in 1963 suggested EDL should include the action of the solvent (Bockris *et al.*, 1963). But this model is not commonly used. Although these models have some merits such as Helmholtz is the simplest model, Gouy-Chapman defines diffusion layer, and Bockris/Devanthan/Müller fixes alignment to the electrode surface, Gouy-Chapman-Stern model is the most commonly applied one to characterized EDL.

Table 2-1 Comparison of EDL theories

Model	Description	Limitation	Reference
Helmholtz	The constant differential capacitance is independent of the charge density; The dielectric constant and the double-layer thickness affect charge distribution.	Earliest and simplest model; Considers diffusion/mixing of ions, adsorption possibility, and the interaction between solvent dipole moments and the electrode.	(Helmholtz, 1853; Namisnyk & Zhu, 2003)
Gouy-Chapman	Modified from Helmholtz model; Ions are mobile in EDL, by concentration gradients and the electric potential gradients; Defines diffusion layer.	Overestimates the capacitance of the EDL; Treats ion as point-charges, resulting in unrealistically large ion concentrations.	(Ehrenstein, 2001; Namisnyk & Zhu, 2003)

Stern	Combines Helmholtz model and Gouy-Chapman model; Distinguishes Stern layer from diffuse layer; Ions in diffuse layer are mobile under the coupled influence of diffusion and electrostatic forces; Describes finite size and find that the ion's closest to the electrode is on the order of ionic radius.	Treats ions as point charges; Assumes ions in the diffuse layer interact via Coulombic force; Assumes the dielectric permittivity and the fluid viscosity to be constant always.	(Stern, 1924; Watts-Tobin & Mott, 1961)
Grahame	Proposes that some ionic or uncharged species can penetrate the Stern layer.	Only considers electrostatic adsorption for Continuum models of EDLCs; Does not prevail electroneutrality within the EDL.	(Grahame, 1947; Nakamura *et al.*, 2011)
Bockris/ Devanthan/	The attached solvent like water has a fixed alignment to the electrode surface;	IHP passes through the first layer center; OHP passes through the second adsorption layer center;	(Bockris *et al.*, 1963; Bockris *et al.*, 1965)

Müller	1st layer displays a strong orientation to the electric field; Defines the zeta potential.	The diffuse layer is the region beyond the OHP.

Gouy-Chapman-Stern model is a product of the continuation and development of Helmholtz model and the Gouy–Chapman Model in series. In this model, the EDL is divided into three parallel charged layers (Figure 2-7). In the first layer, the surface charge (either positive or negative) is adsorbed onto the electrode to form a compact charge layer called the inner Helmholtz plane (IHP) (Hingerl, 2013; Iozzo *et al.*, 2015). With electrically screening, the region in which ions are attracted through Coulombic interaction is the second layer named the outer Helmholtz plane (OHP) (Iozzo *et al.*, 2015; Pilon *et al.*, 2015). With the distance becoming further away from the electrode, free ions moving in the fluid via electric attractions and thermal motion form a thick layer, defined as the diffuse layer (DL) (Cagle *et al.*, 2010; Iozzo *et al.*, 2015). The potential at this location decreases to zero known as the zeta potential (Ibrahim, 2011; Ney, 2016), and the relative distance is the EDL thickness (Han *et al.*, 2013; Namisnyk & Zhu, 2003).

The profiles of potential drop and charge density are two primary items for the EDL. The potential drop, $\Delta\Psi$, starting with an assumption of quasi-equilibrium is thought to consist of the drop across the stern layer and the DL based on the Poisson equation for a one-dimensional system, as described in Eq. 2-23.

$$\frac{d^2\psi}{dx^2} = -\frac{\rho}{\varepsilon} \tag{2-23}$$

where x, ψ, ρ, and ε are the direction perpendicular to the surface, the relative electrical potential in the diffuse layer, the volume charge density in the system, and the dielectric constant of the medium, respectively. From Boltzmann distribution, the number of ions (N_i) per unit volume is presented in Eq. 2-24.

$$N_i = N_{i0} \exp\left(\frac{z_i e\psi}{KT}\right) \tag{2-24}$$

In this equation, N_{i0}, z_i, and e are the bulk concentration of ions, the valence of ion (i), and the electrical charge, respectively. k and T are the Boltzmann constant and the absolute temperature, respectively.

The volume density of charge is expressed by Eq. 2-25

$$\rho = \sum_i N_i z_i e = \sum_i z_i e N_{i0} \exp\left(-\frac{z_i e\psi}{kT}\right) \tag{2-25}$$

By combining equations 2-24 and 2-25, the Poisson-Boltzmann (PB) equation can be obtained:

$$\frac{d^2\psi}{dx^2} = \frac{-1}{\varepsilon} \sum_i z_i e N_{i0} \exp\left(-\frac{z_i e\psi}{kT}\right) \tag{2-26}$$

If the electrolyte is a symmetric z:z electrolyte system, Eq. 2-26 can be simplified to Eq. 2-27.

$$\frac{d^2\psi}{dx^2} = \frac{2zeN_0}{\varepsilon} \sinh\left(-\frac{z_i e\psi}{kT}\right) \tag{2-27}$$

If the thickness of the inner (Stern) layer is small compared to the parallel plane width w, the diffuse layer boundaries are assumed located at $x = +\, w/2$ and $x = -w/2$. Thus, the electrical potential profile (ψ) (Eq. 2- 28 and Eq. 2-29) can be obtained using the PB equation via the following boundary conditions.

$$\frac{d\psi}{dx} = 0 \quad \text{and } \Psi=\Psi_m \quad \text{at} \quad x=0 \tag{2-28}$$

$$\psi = \psi_d \quad \text{at } x=\pm w/2 \tag{2-29}$$

In these equations, some simplifications are processed, such as the two capacitances in series and ignoring the moment from the inner Helmholtz plane, to describe the total capacitance of EDL (Eq. 2-30).

$$\frac{1}{C} = \frac{1}{C_S} + \frac{1}{C_D} \tag{2-30}$$

$$C_S = \frac{\varepsilon_S}{h_S} \tag{2-31}$$

$$C_D = C_D^0 \cosh\left(\frac{ze\psi}{2k_B T}\right) \tag{2-32}$$

where C_S and C_D are derived assuming a Gouy-Chapman diffuse layer. The total capacitance of the system is simplified in terms of the dimensionless parameter δ (Eq. 2-33.

$$C = \frac{C_D}{C_D \Big/ C_S + \operatorname{sech}\left(\frac{ze\psi}{2k_B T}\right)} \tag{2-33}$$

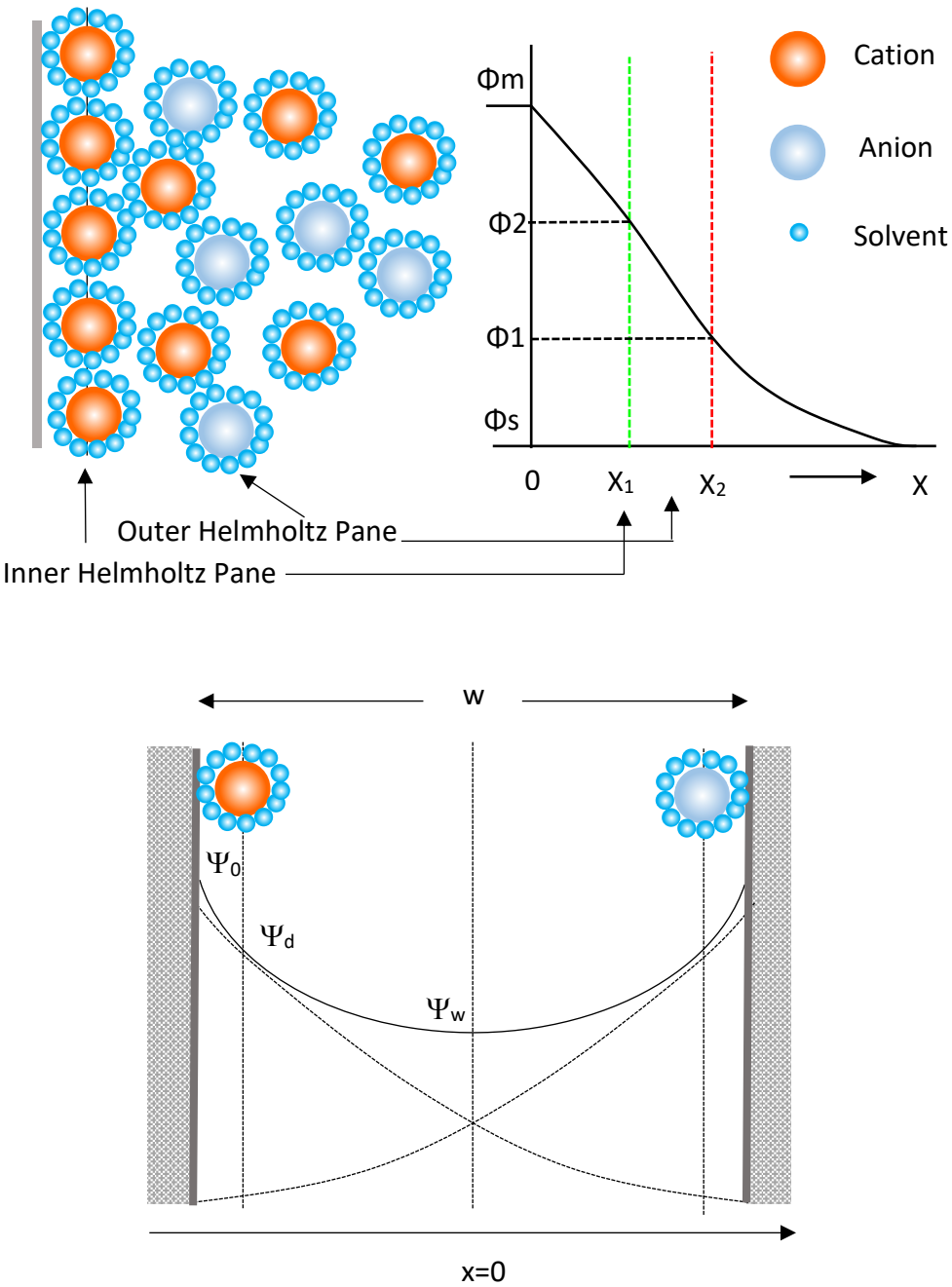

Figure 2-7 Schematic diagram of the EDL model of Gouy–Chapman–Stern and potential distribution of the double layer with constant dielectric constants (Ibrahim, 2011).

2.4.3 Molecular dynamic simulation of electric double layer

Before molecular dynamic simulation appeared on the scene, the property prediction of a molecular substance is only used approximate theories such as the van der Waals equation, the Debye–Hückel theory, and the Boltzmann equation. For liquids, the Debye–Hückel theory was proposed by Debye and Hückel (1923) to explain electrolytes departing from the solid plane. The Debye–Hückel theory is a linearized Poisson–Boltzmann model and gives accurate descriptions of mean activity coefficients (Chang, 2005). Yet, having a quite limited knowledge and insufficient information about the intermolecular interactions, Debye–Hückel theory is not able to provide us with an estimate of the properties of interest.

The thickness of the EDL is about 10-100 Å, and the thickness of IHP is thick (10 Å), which means that the interactions of atoms are exceptionally intimate because the radius of an atom is approximate 10 Å. In other words, the repulsion or absorption plays an indispensable role in the formation of the EDL. To describe the interaction of atoms in the EDL, Monte Carlo simulations (Frenkel & Smit, 2001), density functional theory (DFT) (Patra, 2015), and MD simulation has been used to account for atom behaviors in the EDL such as the effects of finite ion size and the fluid-structure around the EDL (Zarzycki *et al.*, 2010), as summarized in Table 2-2.

Table 2-2 Comparison of EDL simulations

Theory	Advantage	Limitation	Reference
Debye-hückel theory	Describes thermodynamic properties of ionic fluids; Linearization of PB equation.	Dilute electrolytes, on the order of 0.01 M Complete dissociation of electrolytes into ions; Each ion is surrounded by oppositely charged ions, on average.	(Chang, 2005; Xiao & Song, 2011)
Density functional theory	Low computational effort; Possible to simulate many particles; Over a wide range of surface potentials and ionic concentrations.	Has theoretical and numerical difficulties simulating bonded molecules with angle constraints; Mostly pairwise potentials; Do not represent the true interaction of particles.	(Gillespie *et al.*, 2005; Jiang *et al.*, 2011)
Monte Carlo (MC)	Generate an ensemble of representative configurations for a complex macromolecular system; Improve the ability of MD to sample conformations.	Poor conformational sampling; Lacks an objective time definition; Limited to a gas or other low-density systems.	(Frenkel & Smit, 2001)
Molecular Dynamics simulations (MD)	Have a large probability of selecting random moves; Better handle collective motions; Have potentials defining the forces between particles; Define the time evolution of the molecular system;	Simulation timescales remain a challenge; Limited to liquids and crystals; Force fields are inherently approximations Covalent bonds cannot break or form.	(Frenkel & Smit, 2001; Xiang *et al.*,

	Provide the actual trajectory of the system, transport properties such as viscosity coefficients.	2014; Zarzycki *et al.*, 2010)

Among these models, MD simulation provides the most fundamental and flexible platform for analysis of the equilibrium and transport properties of the many-body system. MD has been widely utilized because it unambiguously describes the dynamic properties of the EDL (e.g., viscosity, diffusion, thermal conductivity, and structural relaxation). In addition, MD simulation does not have complicated assumptions for the description of interatomic/intermolecular interaction in a proposed system following the regulations as reported (Allen, 2004).

1) Molecular dynamics simulation principles

To measure an observable quantity in a MD simulation, the observable system as a function of the positions and momenta are expressed by Newton's equations of motion, such as the average kinetic energy per degree of freedom, as shown in Eq. 2-35.

$$\left\langle \frac{1}{2} m v_{\alpha}^{2} \right\rangle = \frac{1}{2} k_B T \tag{2-34}$$

This equation is used as an operational definition of the temperature. In practice, the total kinetic energy of the system is measured and divided by the number of degrees of freedom N_i *(=3N-3)* for a system containing *N* particles with fixed total momentum. Due to the fluctuation of the total kinetic energy, the instantaneous temperature is expressed in Eq. 2-36.

$$T(t) = \sum_{i=1}^{N} \frac{m_i v_i^2(t)}{k_B N_f} \tag{2-35}$$

According to thermal equilibrium, the following relation holds by Eq. 37.

$$\left\langle v_\alpha^2 \right\rangle = \frac{k_B T}{m} \tag{2-36}$$

where v_α^2 is the velocity of a given particle. Using this relation, the instantaneous temperature is redefined by Eq. 2-38.

$$k_B T(t) \equiv \sum_{i=1}^{N} \frac{m v_\alpha^2(t)}{N_f} \tag{2-37}$$

If interactions of molecular particles consist of contributions from such as the ideal gas behavior, the external potential field, excess hard sphere repulsions, Lennard-Jones attractions, Coulombic forces, and short-range electrostatic interactions, the bond stretching interactions are described a harmonic potential; angle bending is represented by a harmonic potential on the angle, and dihedral angles are represented with a cosine series; improper torsions are occasionally enforced with a harmonic term, and non-bonded atoms are described with a 12-6 Lennard-Jones plus Coulombic interaction.

$$U_{lj}(r) = \frac{q_i q_j}{r} + 4\varepsilon_{lj}\left[\left(\frac{\sigma_{ij}}{r}\right)^{12} - \left(\frac{\sigma_{ij}}{r}\right)^{6}\right] \tag{2-38}$$

where U_{ij}, r, q, ε, σ are the non-bonded potential energy, the distance of separation, point charge, the energy parameter, and the distance parameter, respectively.

As two species (i and j) described by different potentials interact, their interaction is estimated by a Lennard-Jones potential with parameters that are determined using the Lorentz-Berthelot mixing rules to combine individual parameters as shown in Eq. 2-40 and Eq. 2-41.

$$\sigma_{ij} = \frac{1}{2}\left(\sigma_i + \sigma_j\right) \tag{2-39}$$

$$\varepsilon_{ij} = \sqrt{\varepsilon_i \varepsilon_j} \tag{2-40}$$

Long-range Coulombic interactions were calculated through a particle-particle particle mesh (PPPM) solver (Hockney & Eastwood, 1988). The results of energy are shown in Figure 2-8 (a). Energy above x-axis means atom repulsion force while below x-axis means atom attraction force. For two atoms, as the distance is infinitely far away from each other, the force is zero, indicating that no interaction takes place between these two atoms. With the distance (r) shortening, atoms display an attractive interaction ($r > r_0$). At $r=r_0$, the absorbing force is maximum. As the distance (r) further shortening ($r < r_0$), the repulsion interaction is enhanced.

2) Setting up molecular dynamics simulations

In molecular dynamics simulations, the time-dependent behavior of the system is obtained by integrating Newton's equations of motion (Eq. 2-35) using one of the numerical integrators and the potential energy function (Eq. 2-39). The results are a time series of conformations, which is called a trajectory followed by each atom corresponding to Newton's laws of motion. The flowchart of MD simulation is shown in Figure 2-8(b), including eight main steps (initial coordinate, structure minimization, solvation, initial velocities, heating dynamics, equilibration dynamics, production dynamics, and analysis of trajectory).

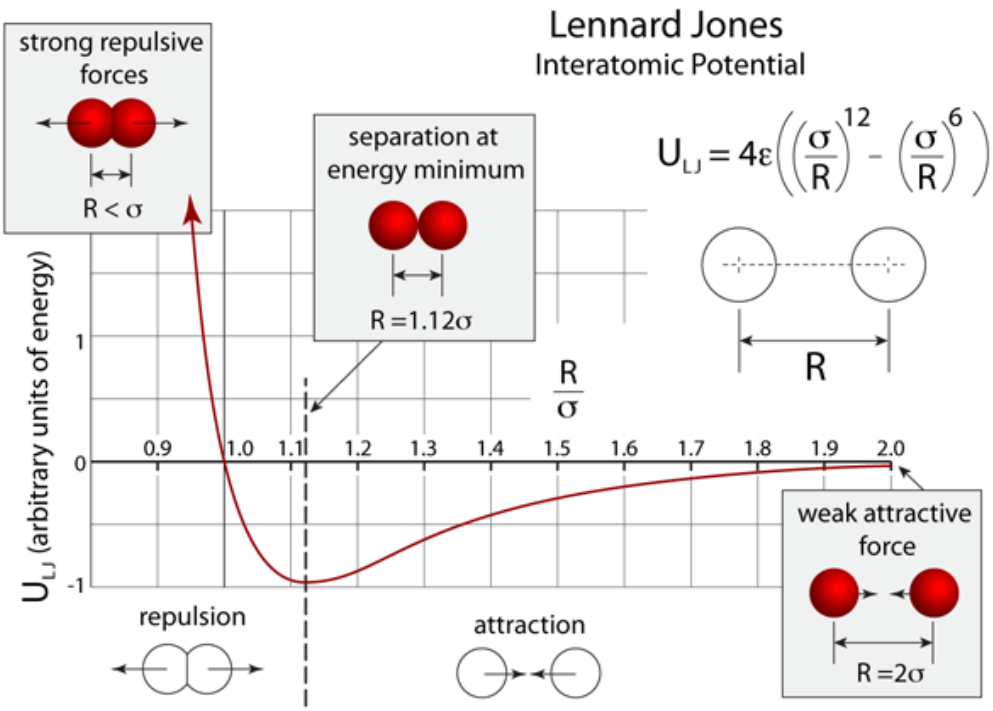

(a)

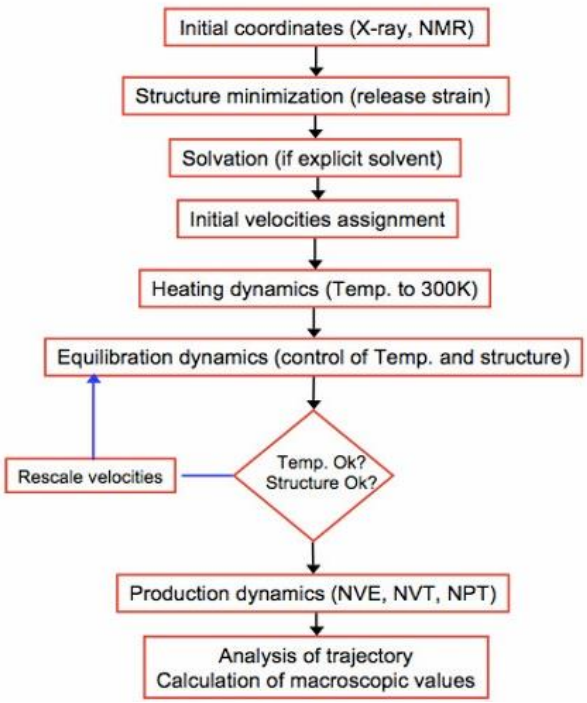

(b)

Figure 2-8 A graph of strength versus distance for the 12-6 Lennard-Jones potential (Hodgman, 1951) (a); Flowchart of molecular dynamics simulations (Yang *et al.*, 2015) (b).

2.4.4 Electric double layer improvement

According to the definition of the capacitance (C) for a given physical resistor, as the capacitance is fixed by its geometric and the dielectric constant expressed by Eq. 2-41 (Terzic *et al.*, 2012), it is hard to increase the capacitance.

$$C = \frac{\varepsilon A}{d} \tag{2-41}$$

where ε, A, and d are the permittivity of dielectric, plate area, the distance between plates, respectively. This equation shows that it is possible to change the capacitance by increasing relative plate area, dielectric constant, and decreasing plate distance. Elzbieta & Francois (2001) and Gabelich *et al*. (2003) demonstrated that the EDL properties were affected by electrode materials and found that the high surface area and high electrical conductivity contributed to excellent performances for energy storage and capacitive desalination (Frackowiak & Beguin, 2001; Gabelich *et al.*, 2003) Largeot *et al*. (2008) and Scholz (2010) studied the relationship of ion size and the effective thickness of EDL. They found that the smaller size of ion radius formed a ticker EDL and a larger capacitance (Largeot *et al.*, 2008; Scholz, 2010). Scholz (2010) also demonstrated the effects of the electrolyte type and the concentration profiles on the structure and property of the EDL in his book (Scholz, 2010). Häfeli *et al*. (2013) systematically introduced the ionic radius affecting the relationship between charge and mobility (Häfeli *et al.*, 2013). Other studies also explicitly indicate that the structure and properties of the EDL are influenced by many factors (solvent properties, electrode surface charge, pore size, ionic size, electrolyte type, voltage, temperature) significantly influences on the formation of EDL. Also, ionic size, electrolyte type,

voltage, temperature affect the capacitance of EDL (Casadellà *et al.*, 2016; Długołęcki, Anet, *et al.*, 2010; Krol *et al.*, 1999). However, the behaviors of NH_4^+ in the EDL have not yet been investigated which is the third research motivation of this thesis.

2.5 Perspectives

The coming years will see the continuous development of EDI towards a mature technology with many applications. EDI for contemporary developments has been extensively investigated in academic and industrial fields (Ran *et al.*, 2017). Still many open questions associated with energy and environment for ion exchange membrane and electrodes are to be addressed in future. Considering the importance of ion exchange membrane, worldwide interests in membrane materials and membrane process is to be increasing. The development of polymer material candidates with high perm selectivity and chemical stability and precise control of micro-morphology is crucial to study mass transport (Nagarale *et al.*, 2006). Although different types and sizes of ion exchange membranes (i.e., heterogeneity, homogeneity, interpenetrating network polymer, radiation grafting of polymers, bipolar membranes) have been developed, suitable preparation methods of ion exchange membranes with high performances is to be further fulfilled (Galama *et al.*, 2016; Yaroslavtsev & Nikonenko, 2009). Whatever are membrane materials or preparation methods, but the core issues focus the in-depth understanding of water dissociation and ions transport mechanism (Berezina *et al.*, 2008; Kononenko, 2014; Zhang *et al.*, 2016). The advanced research areas include limiting current, polarization curve, and diffusion, which is investigated through experimental tests and theoretical simulations (Butylskii *et al.*, 2016; Nebavskaya *et al.*, 2017).

Regarding the electrode, further research will have to identify the excellent materials and the electrochemical process (Porada *et al.*, 2013). Cost considerations that are of the key to make EDI an affordable mass-market technology lead to explore new materials, such as activated carbons (the most appropriate pore size and pore size distribution) as the material choice for the electrodes (Agartan *et al.*, 2017; Zornitta *et al.*, 2017). Other major avenues to improve EDI systems are parameter optimization and advanced electrode design. Take activated carbons as an example, these areas including the class of activated carbons, the parameter optimization, the potential for chemical modifications, and nanoparticles inclusion within the electrode, has only begun to be exploited. Moreover, the next generation of EDI electrode design may employ asymmetry electrodes based on the film thickness, porosity, material chemistry, and/or PZC. Such electrodes may potentially enable the future systems with much more robust and more efficient performances than current systems (Porada *et al.*, 2013). Many challenges remain in the understanding of the electrochemical process of the electrodes. In future, the accurate electrolyte and electrode models that account for polarization effects are critical for simulations. Due to complex electrode geometries, the exclusion of electrode polarization leads to significant artifacts, especially for the study of dynamics of mass transport (Burt *et al.*, 2014).

2.6 Summary

This chapter reviewed the studies of electrodeionization on its principle, concentration polarization of ion exchange membrane, and the behaviors of the EDL. Irreversible thermodynamics is the classical and underlying theory of over mass transport phenomena across the ion exchange membrane. Owing to the difference in ion

transport numbers in between the solution and the membrane, the accumulated permeable ion leads to the occurrence of concentration polarization during ion separation under the applied electric current. The magnitude of concentration polarization generates three distinct regions of the electric current: the ohmic region (I), the LCD plateau region (II), and the over limiting current region (III). Nernst–Planck equation and Donnan equilibrium are two essential theories used to describe the mass transport and the potential profiles of ion species. The effects of supporting electrolyte on concentration polarization have not yet been widely studied. From the published literature, we know that the EDL lies in the heart of the electrode because it is crucial for water dissociation and the redox reactions. Nowadays, EDL's behaviors are studied via classically theoretical calculation, advanced MD simulations, DFT, and even quantum mechanics. For the classical theories, Gouy-Chapman-Stern Model has been mostly used. For MD simulations, Debye–Hückel theory, density functional theory, Monte Carlo simulations, and MD simulations have been utilized more often. For the simulations of the interface of solid-liquid, MD simulations based on Newton's equations of motion is widely implemented since it provides the most fundamental and flexible platform for analysis of the equilibrium and transport properties of a classical many-body system from atomic level. The improvements of the capacitance of the EDL can be realized by increasing the permittivity of dielectric and plate area and reduce the distance between plates. Of cause, the capacitance of the EDL is affected by many parameters, but the co-ion competition in the EDL has not been explicitly described and thus will be replenished in this thesis.

2.7 References

Agartan, Akuzum, Mathis, Ergenekon, Agar, Gogotsi, & Kumbur. (2017). *Capacitive Deionization Performance of Thermally Surface Modified Activated Carbon Cloth Electrodes.* Paper presented at the Meeting Abstracts.

Allen. (2004). Introduction to molecular dynamics simulation. *Computational Soft Matter: From Synthetic Polymers to Proteins, 23*, 1-28.

Alvarado, & Chen. (2014). Electrodeionization: principles, strategies and applications. *Electrochimica Acta, 132*, 583-597.

Arar, Yüksel, Kabay, & Yüksel. (2014). Various applications of electrodeionization (EDI) method for water treatment—A short review. *Desalination, 342*, 16-22.

Bard, Faulkner, Leddy, & Zoski. (1980). *Electrochemical methods: fundamentals and applications* (Vol. 2): wiley New York.

Berardi. (2013). *Simulation of concentration polarization at a microchannel-nanochannel interface*: Rutgers The State University of New Jersey-New Brunswick.

Berezina, Kononenko, Dyomina, & Gnusin. (2008). Characterization of ion-exchange membrane materials: properties vs structure. *Advances in colloid and interface science, 139*(1), 3-28.

Berkh, Shacham-Diamand, & Gileadi. (2008). Reduction of ammonium ion on Pt electrodes. *Journal of The Electrochemical Society, 155*(10), F223-F229.

Bhattacharjee, Sharma, & Bhattacharya. (1994). Surface interactions in osmotic pressure controlled flux decline during ultrafiltration. *Langmuir, 10*(12), 4710-4720.

Bockris, Devanathan, & Müller. (1963). *On the structure of charged interfaces.* Paper presented at the Proceedings of the Royal Society of London A: Mathematical, Physical and Engineering Sciences.

Bockris, Müller, Wroblowa, & Kovac. (1965). Experimental and theoretical examination of methods of obtaining double-layer parameters. *Journal of Electroanalytical Chemistry, 10*(5-6), 416-434.

Bouhidel, & Lakehal. (2006). Influence of voltage and flow rate on electrodeionization (EDI) process efficiency. *Desalination, 193*(1-3), 411-421.

Burt, Birkett, & Zhao. (2014). A review of molecular modelling of electric double layer capacitors. *Physical Chemistry Chemical Physics, 16*, 6519-6538

Butylskii, Mareev, Nikonenko, Pismenskaya, Larchet, Dammak, . . . Apel. (2016). In situ investigation of electrical inhomogeneity of ion exchange membrane surface using scanning electrochemical microscopy. *Petroleum Chemistry, 56*(11), 1006-1013.

Cagle, Feng, Qiao, Huang, Sumpter, & Meunier. (2010). Structure and charging kinetics of electrical double layers at large electrode voltages. *Microfluidics and Nanofluidics, 8*(5), 703-708.

Casadellà, Schaetzle, Nijmeijer, & Loos. (2016). Polymer inclusion membranes (PIM) for the recovery of potassium in the presence of competitive cations. *Polymers, 8*(3), 76.

Chamoulaud, & Bélanger. (2005). Modification of ion-exchange membrane used for separation of protons and metallic cations and characterization of the membrane by current–voltage curves. *Journal of Colloid and Interface Science, 281*(1), 179-187.

Chang. (2005). *Physical chemistry for the biosciences*: University Science Books.

Choi, Lee, & Moon. (2001). Effects of electrolytes on the transport phenomena in a cation-exchange membrane. *Journal of Colloid and Interface Science, 238*(1), 188-195.

Choi, Park, & Moon. (2002). Direct measurement of concentration distribution within the boundary layer of an ion-exchange membrane. *Journal of Colloid and Interface Science, 251*(2), 311-317.

Chun, Mulcahy, Zou, & Kim. (2017). A Short Review of Membrane Fouling in Forward Osmosis Processes. *Membranes, 7*(2), 30.

Długołęcki, Anet, Metz, Nijmeijer, & Wessling. (2010). Transport limitations in ion exchange membranes at low salt concentrations. *Journal of Membrane Science, 346*(1), 163-171.

Długołęcki, Ogonowski, Metz, Saakes, Nijmeijer, & Wessling. (2010). On the resistances of membrane, diffusion boundary layer and double layer in ion exchange membrane transport. *Journal of Membrane Science, 349*(1), 369-379.

Donnan. (1924). The theory of membrane equilibria. *Chemical Reviews, 1*(1), 73-90.

Ehrenstein. (2001). Surface charge. *Biophysics Textbook on-line. Biophysical Society, Bethesda, Maryland*.

Fedorov, & Kornyshev. (2014). Ionic liquids at electrified interfaces. *Chemical Reviews, 114*(5), 2978-3036.

Fontananova, Zhang, Nicotera, Simari, van Baak, Di Profio, . . . Drioli. (2014). Probing membrane and interface properties in concentrated electrolyte solutions. *Journal of Membrane Science, 459*, 177-189.

Frackowiak, & Beguin. (2001). Carbon materials for the electrochemical storage of energy in capacitors. *Carbon, 39*(6), 937-950.

Frenkel, & Smit. (2001). *Understanding molecular simulation: from algorithms to applications* (Vol. 1): Academic press.

Gabelich, Yun, & Coffey. (2003). Pilot-scale testing of reverse osmosis using conventional treatment and microfiltration. *Desalination, 154*(3), 207-223.

Galama, Hoog, & Yntema. (2016). Method for determining ion exchange membrane resistance for electrodialysis systems. *Desalination, 380*, 1-11.

Gillespie, Valiskó, & Boda. (2005). Density functional theory of the electrical double layer: the RFD functional. *Journal of Physics: Condensed Matter, 17*(42), 6609.

Gongadze, Petersen, Beck, & van Rienen. (2009). *Classical Models of the Interface between an Electrode and an Electrolyte.* Paper presented at the COMSOL Conference.

Grahame. (1947). The electrical double layer and the theory of electrocapillarity. *Chemical Reviews, 41*(3), 441-501.

Häfeli, Schütt, Teller, & Zborowski. (2013). *Scientific and clinical applications of magnetic carriers*: Springer Science & Business Media.

Han, Roh, Jo, & Kang. (2013). A novel co-precipitation method for one-pot fabrication of a Co–Ni multiphase composite electrode and its application in high energy-density pseudocapacitors. *Chemical Communications, 49*(63), 7067-7069.

Helmholtz. (1853). Ueber einige Gesetze der Vertheilung elektrischer Ströme in körperlichen Leitern mit Anwendung auf die thierisch - elektrischen Versuche. *Annalen der Physik, 165*(6), 211-233.

Hingerl. (2013). Polarimetric and other optical probes for the solid–liquid interface. In *Ellipsometry at the Nanoscale* (pp. 493-527): Springer.

Ho. (2008). *Ion selective removal using wafer enhanced electrodeionization*: University of Arkansas.

Hockney, & Eastwood. (1988). *Computer simulation using particles*: crc Press.

Hodgman. (1951). *Handbook of chemistry and physics* (Vol. 71): LWW.

Hoek, & Tarabara. (2013). *Encyclopedia of Membrane Science and Technology*: Wiley Online Library.

Hou. (2008). *Electrical double layer formation in nanoporous carbon materials*: Georgia Institute of Technology.

Hou, Wu, Qin, & Xu. (2010). Electrostatic separation for recycling waste printed circuit board: a study on external factor and a robust design for optimization. *Environmental Science & Technology, 44*(13), 5177-5181.

Hunter. (2001). *Foundations of colloid science*: Oxford University Press.

Hwang, Onuki, Nomura, Kasahara, & Kim. (2003). Improvement of the thermochemical water-splitting IS (iodine–sulfur) process by electro-electrodialysis. *Journal of Membrane Science*, 220(221), 129-136.

Ibrahim. (2011). Corrosion Inhibitors in the Oilfield. In: Version.

Iozzo, Tong, Wu, & Furlani. (2015). Numerical analysis of electric double layer capacitors with mesoporous electrodes: effects of electrode and electrolyte properties. *The Journal of Physical Chemistry C, 119*(45), 25235-25242.

Jang, Nam, Hwang, Lee, & Choi. (2015). Effect of operating parameters on temperature and concentration polarization in vacuum membrane distillation process. *Desalination and Water Treatment, 54*(4-5), 871-880.

Jia, & Kim. (2014). Multiphysics simulation of ion concentration polarization induced by nanoporous membranes in dual channel devices. *Analytical Chemistry, 86*(15), 7360-7367.

Jiang, Meng, & Wu. (2011). Density functional theory for differential capacitance of planar electric double layers in ionic liquids. *Chemical Physics Letters, 504*(4), 153-158.

Kedem, & Katchalsky. (1961). A physical interpretation of the phenomenological coefficients of membrane permeability. *The Journal of General Physiology, 45*(1), 143-179.

Kedem, & Katchalsky. (1963). Permeability of composite membranes. Part 1.—Electric current, volume flow and flow of solute through membranes. *Transactions of the Faraday Society, 59*, 1918-1930.

Kononenko. (2014). Characterization of ion-exchange membrane.

Krol, Wessling, & Strathmann. (1999). Concentration polarization with monopolar ion exchange membranes: current–voltage curves and water dissociation. *Journal of Membrane Science, 162*(1), 145-154.

Largeot, Portet, Chmiola, Taberna, Gogotsi, & Simon. (2008). Relation between the ion size and pore size for an electric double-layer capacitor. *Journal of the American Chemical Society, 130*(9), 2730-2731.

Lee, Strathmann, & Moon. (2006). Determination of the limiting current density in electrodialysis desalination as an empirical function of linear velocity. *Desalination, 190*(1-3), 43-50.

Li, Fang, & Green. (1983). Turbulent light scattering fluctuation spectra near a cation electrodialysis membrane. *Journal of Colloid and Interface Science, 91*(2), 412-417.

Liu, Vane, & Peng. (2003). Theoretical analysis of concentration polarization effect on VOC removal by pervaporation. *Journal of Hazardous Substance Research, 4*(5), 5_1.

Liu, Zhang, Zhang, & Mo. (2008). Performance evaluation of electrodeionization process based on ionic equilibrium with plate and frame modules. *Desalination, 221*(1-3), 425-432.

Lopez, & Hestekin. (2015). Improved organic acid purification through wafer enhanced electrodeionization utilizing ionic liquids. *Journal of Membrane Science, 493*, 200-205.

Lozada-Cassou, González-Tovar, & Olivares. (1999). Nonlinear effects in the electrophoresis of a spherical colloidal particle. *Physical Review E, 60*(1), R17.

Meng, Deng, Chen, & Zhang. (2005). A new method to determine the optimal operating current (Ilim') in the electrodialysis process. *Desalination, 181*(1-3), 101-108.

Nagarale, Gohil, & Shahi. (2006). Recent developments on ion-exchange membranes and electro-membrane processes. *Advances in colloid and interface science, 119*(2), 97-130.

Nagy, & Kulcsár. (2010). The effect of the concentration polarization and the membrane layer mass transport on membrane separation. *Desalination and Water Treatment, 14*(1-3), 220-226.

Nakamura, Sato, Hoshi, & Sakata. (2011). Outer Helmholtz Plane of the Electrical Double Layer Formed at the Solid Electrode–Liquid Interface. *ChemPhysChem, 12*(8), 1430-1434.

Namisnyk, & Zhu. (2003). *A survey of electrochemical super-capacitor technology*. Paper presented at the Australian Universities Power Engineering Conference.

Nebavskaya, Sarapulova, Sabbatovskiy, Sobolev, Pismenskaya, Sistat, . . . Nikonenko. (2017). Impact of ion exchange membrane surface charge and hydrophobicity on electroconvection at underlimiting and overlimiting currents. *Journal of Membrane Science, 523*, 36-44.

Ney. (2016). *Electrical double layer potential distribution in nanoporous electrodes from molecular modeling and classical electrodynamics analysis*: Rochester Institute of Technology.

Onsager. (1931). Reciprocal relations in irreversible processes. I. *Physical Review, 37*(4), 405.

Parmar, & Thakur. (2013). Heavy metal Cu, Ni and Zn: Toxicity, health hazards and their removal techniques by low cost adsorbents: A short overview. *International Journal of Plant, Animal and Environmental Sciences*, 3(3), 143-157.

Patra. (2015). Structure of fully asymmetric mixed electrolytes around a charged nanoparticle: a density functional and simulation investigation. *RSC Advances, 5*(32), 25006-25013.

Pilon, Wang, & d'Entremont. (2015). Recent advances in continuum modeling of interfacial and transport phenomena in electric double layer capacitors. *Journal of The Electrochemical Society, 162*(5), A5158-A5178.

Planck. (1890). Ueber die Potentialdifferenz zwischen zwei verdünnten Lösungen binärer Electrolyte. *Annalen der Physik, 276*(8), 561-576.

Porada, Zhao, Van Der Wal, Presser, & Biesheuvel. (2013). Review on the science and technology of water desalination by capacitive deionization. *Progress in Materials Science, 58*(8), 1388-1442.

Ran, Wu, He, Yang, Wang, Jiang, . . . Xu. (2017). Ion exchange membranes: New developments and applications. *Journal of Membrane Science, 522*, 267-291.

Reinhard. (2005). Advanced electrodeionization for fluid recycling. In: Google Patents.

Rizvi. (2010). *Separation, extraction and concentration processes in the food, beverage and nutraceutical industries*: Elsevier.

Rosenberg, & Tirrell. (1957). Limiting currents in membrane cells. *Industrial & Engineering Chemistry, 49*(4), 780-784.

Rubinstein. (1991). Electroconvection at an electrically inhomogeneous permselective interface. *Physics of Fluids A: Fluid Dynamics, 3*(10), 2301-2309.

Rubinstein, Staude, & Kedem. (1988). Role of the membrane surface in concentration polarization at ion-exchange membrane. *Desalination, 69*(2), 101-114.

Rubinstein, & Zaltzman. (2000). Electro-osmotically induced convection at a permselective membrane. *Physical Review E, 62*(2), 2238.

Sadrzadeh, & Mohammadi. (2008). Sea water desalination using electrodialysis. *Desalination, 221*(1-3), 440-447.

Scarazzato, Buzzi, Bernardes, Tenório, & Espinosa. (2015). Current-voltage curves for treating effluent containing HEDP: determination of the limiting current. *Brazilian Journal of Chemical Engineering, 32*(4), 831-836.

Scholz. (2010). *Electroanalytical methods* (Vol. 1): Springer.

Smith, & Hyde. (2000). *Short-bed demineralization: an alternative to electrodeionization.* Paper presented at the Sixth International Conference on Cycle Chemistry in Fossil Plants (EPRI), Columbus, Ohio (June 2000).

Spiegler. (1971). Polarization at ion exchange membrane-solution interfaces. *Desalination, 9*(4), 367-385.

Srivastava, & Goyal. (2010). *Novel biomaterials: decontamination of toxic metals from wastewater*: Springer Science & Business Media.

Stern. (1924). Theory of the electrical double layer.(In German.). *Electrochemistry, 30*, 508-516.

Stern, & Green. (1973). Noise generated during sodium and hydrogen ion transport across a cation exchange membrane. *The Journal of Physical Chemistry, 77*(12), 1567-1572.

Tanaka. (2004). Concentration polarization in ion-exchange membrane electrodialysis: The events arising in an unforced flowing solution in a desalting cell. *Journal of Membrane Science, 244*(1), 1-16.

Tanaka. (2006). Irreversible thermodynamics and overall mass transport in ion-exchange membrane electrodialysis. *Journal of Membrane Science, 281*(1), 517-531.

Tanaka. (2011). Ion-exchange membrane electrodialysis for saline water desalination and its application to seawater concentration. *Industrial & Engineering Chemistry Research, 50*(12), 7494-7503.

Tanaka. (2015). *Ion exchange membranes: fundamentals and applications*: Elsevier.

Tanaka, Moon, Nikonenko, & Xu. (2012). Ion-exchange membranes. *International Journal of Chemical Engineering, 2012*.

Terzic, Terzic, Nagarajah, & Alamgir. (2012). Capacitive sensing technology. In *A Neural Network Approach to Fluid Quantity Measurement in Dynamic Environments* (pp. 11-37): Springer.

Van den Berg, & Smolders. (1990). Flux decline in ultrafiltration processes. *Desalination, 77*, 101-133.

Watts-Tobin, & Mott. (1961). Electrochem. Acta., 4: 79. *Philosophical Magazine, 6*, 133.

Xiang, Liu, Mi, & Leng. (2014). Molecular dynamics simulations of polyamide membrane, calcium alginate gel, and their interactions in aqueous solution. *Langmuir, 30*(30), 9098-9106.

Xiao, & Song. (2011). A molecular Debye-Hückel theory and its applications to electrolyte solutions. *The Journal of Chemical Physics, 135*(10), 104104.

Yang, Yu, Mu, Shi, Wei, Guo, & Qi. (2015). A molecular dynamics study of bond exchange reactions in covalent adaptable networks. *Soft Matter, 11*(31), 6305-6317.

Yaroslavtsev, & Nikonenko. (2009). Ion-exchange membrane materials: properties, modification, and practical application. *Nanotechnologies in Russia, 4*(3-4), 137-159.

Yoon, Lee, Hyeon, & Oh. (2000). Electric double - layer capacitor performance of a new mesoporous carbon. *Journal of The Electrochemical Society, 147*(7), 2507-2512.

Yu, Wu, & Gao. (2004). Density-functional theory of spherical electric double layers and ζ potentials of colloidal particles in restricted-primitive-model electrolyte solutions. *The Journal of Chemical Physics, 120*(15), 7223-7233.

Zarzycki, Kerisit, & Rosso. (2010). Molecular dynamics study of the electrical double layer at silver chloride− electrolyte interfaces. *The Journal of Physical Chemistry C, 114*(19), 8905-8916.

Zhang, Ma, Wang, Wang, Shi, & Liu. (2016). Investigations on the interfacial capacitance and the diffusion boundary layer thickness of ion exchange membrane using electrochemical impedance spectroscopy. *Journal of Membrane Science, 502*, 37-47.

Zornitta, García-Mateos, Lado, Rodríguez-Mirasol, Cordero, Hammer, & Ruotolo. (2017). High-performance activated carbon from polyaniline for capacitive deionization. *Carbon, 123*, 318-333.

CHAPTER 3 ENERGY UPCYCLE IN ANAEROBIC TREATMENT: AMMONIUM, METHANE, AND CARBON DIOXIDE REFORMATION THROUGH A HYBRID ELECTRODEIONIZATION–SOLID OXIDE FUEL CELLS SYSTEM

3.1 Introduction

Energy extraction from wastewater streams as a way to eliminate environmental pollution and offset fossil fuel consumption has gained increasing attention (Abbasi *et al.*, 2012; Hall *et al.*, 2013). In chapter 1, AD and landfill are introduced as most adaptable approach converting wastewater and municipal solid waste into biogas (approximately 60% CH_4 and 40% CO_2) and digestate/leachate (400-13,000 mg L^{-1} NH_4^+-N) (Daelman *et al.*, 2012; Jain *et al.*, 2014; Karthikeyan & Visvanathan, 2013; Raboni *et al.*, 2013). Though conventional engines (CHP and cogeneration with gas engines) are the well-established following processes using biogas to generate electricity (Lantz, 2012; Wongchanapai *et al.*, 2013), the electricity conversion efficiencies are always limited around 30-40% (Bogusch & Grubbs, 2014; De Arespacochaga *et al.*, 2015). Besides, a proportion of energy such as NH_4^+-N stored in

digestate/leachate has paid little attention. Thus, further improvements are needed (McKendry, 2002; Simith *et al.*, 2014; Venkatesh, 2013; Wu & Wang, 2006).

NH_4^+-N used to be either removed in the form of N_2 or recovered as fertilizers by the conventional methods and the new denitrification processes. Whereas NH_4^+-N can be recovered as an alternative energy to hydrogen fuel now (Klerke *et al.*, 2008). Upon NH_3 decomposing to N_2 and H_2, 320 kJ mol^{-1} thermal energy can be harvested as shown in Table 1-1 and Eq. 1-1. However, the most key step is the conversion of $NH_4^+{}_{(aq)}$ to $NH_{3(g)}$ that is filled up challenges due to the special properties of NH_3 (incombustibility, incomplete decomposition, toxicity, and solubility) (Lan *et al.*, 2010; Schartela *et al.*, 2003). Other constraints such as the low conversion efficiency from NH_4^+ to NH_3, high cost, and NO_x emissions reduce the motivation to explore NH_3 energy (Ahn *et al.*, 2010). Fortunately, EDI displays promising potential for $NH_{3(g)}$ recovery from wastewater streams. Srivastava & Goyal (2010) studied the directional movement of NH_4^+ ion. This behavior was driven by electric potential gradients that promoted the accumulation and concentration of NH_4^+. And such that concentrated NH_4^+ was harvested with low energy consumption (Srivastava & Goyal, 2010). Ahn *et al*. (2010) investigated the factors that impact ion migration. They observed that the applied current in EDI created an alkaline condition to increase the transformation of $NH_4^+{}_{(aq)}$ into $NH_{3(g)}$ to reduce the dosage of alkaline application (Ahn *et al.*, 2010). Moreover, Mehanna *et al*. (2010) took insights into the microbial electrodialysis cell for simultaneous water desalination and hydrogen gas production and found that the by-product of the cathode (H_2) at the cathode of the electrodialysis served as an additional fuel (Mehanna *et al.*, 2010).

As reviewed in Chapter 1, SOFCs are not only capable of converting to electricity from complex fuels but also have a high energy conversion efficiency, > 50% (Siavashi *et al.*, 2014; Wang *et al.*, 2013). Moreover, SOFCs generates electrical power through electrochemical reactions and does not go through thermal cycles, so as to be not limited by the Carnot efficiency (Tsukuda *et al.*, 2000). The mechanism of SOFCs generating power is shown in Figure 3-1, and electrochemical reactions are described in Eq. 3-1 to Eq. 3-7. In details, CH_4 reforms with $H_2O_{(g)}$ or CO_2 and produces H_2 or CO. The produced H_2 or CO are oxidized to $H_2O_{(g)}$ and CO_2 by oxygen ions (O^{2-}) and releases electrons (e^-) at the anode. The electrons follow through the external circuit and reach the cathode. As O_2 molecules accept tow electrons, O^{2-} is produced again. Then, O^{2-} goes through a dense electrolyte and comes back to the anode. The shift reactions of CH_4 and H_2O gas take place at the anode as described by Eq. 3-1 to Eq. 3-3.

$$CO_{2(g)} + CH_{4(g)} \rightarrow 2CO_{(g)} + 2H_{2(g)} \tag{3-1}$$

$$CH_{4(g)} + H_2O_{(g)} \rightarrow CO_{(g)} + 3H_{2(g)} \tag{3-2}$$

$$CO_{(g)} + H_2O_{(g)} \rightarrow CO_{2(g)} + H_{2(g)} \tag{3-3}$$

The reformations of mixture gas (CH_4, CO_2, and H_2O) produce H_2 and CO to avoid carbon particle deposition. The electrochemical reactions catalyzed by the activated materials take place at the solid electrodes (Figure 3-1 (a) and Eq. 3-4 to Eq. 3-6).

At the anode

$$H_{2(g)} + O^{2-} \rightarrow H_2O_{(g)} + 2e^- \quad (3\text{-}4)$$

$$CO_{(g)} + O^{2-} \rightarrow CO_{2(g)} + 2e^- \quad (3\text{-}5)$$

At the cathode

$$0.5O_{2(g)} + 2e^- \rightarrow O^{2-} \quad (3\text{-}6)$$

NH_3 as the fuel goes through thermal decomposition into N_2 and H_2. The generated H_2 is oxidized in the standard way (Figure 3-1 (b) and Eq.3-7) (Stambouli & Traversa, 2002).

$$NH_{3(g)} \rightarrow N_{2(g)} + H_{2(g)} \quad (3\text{-}7)$$

Such numerous benefits of energy recovery via the co-oxidation of NH_3 and CH_4 enlightens us to combining AD, EDI, and SOFCs. Therefore, this chapter aims to estimate the feasibility of this hybrid system under the different operating parameters (feeding concentration of NH_4^+-N, the internal distance between the anode and the cathode, and the applied voltage).

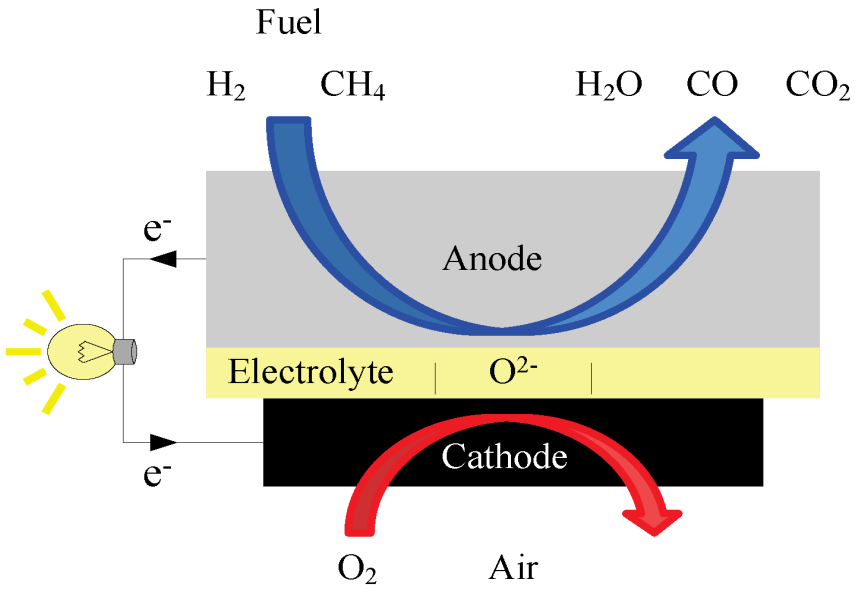

(a)

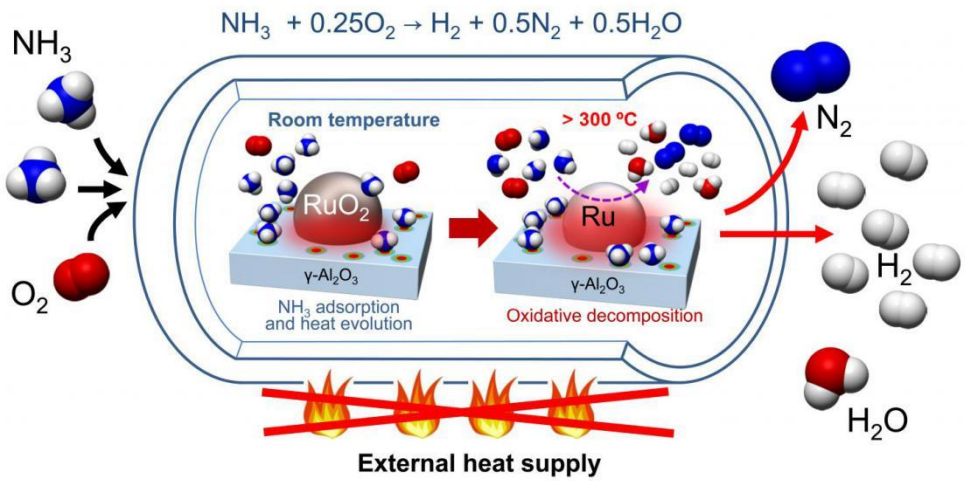

(b)

Figure 3-1 Mechanism of SOFCs using CH_4 and H_2 (Mirzababaei & Chuang, 2014) (a); NH_3 as fuels (Nagaoka *et al.*, 2017) (b).

3.2 Materials and methods

3.2.1 Experiment setups and operations

1) Anaerobic digester

Semi-continuous batch digestion in a digester with 3.0 L working volume was performed. The reactor was equipped with a temperature-controlled water bath (36 to 38 °C) and fed with secondary activated sludge with 3% volatile solid (VS) from a local secondary wastewater treatment plant, Hong Kong. The hydraulic retention time (HRT) was fixed at 15 days, and the biogas yield was 0.32 L g^{-1} VS added.

2) Electrodeionization cell

EDI reactor was composited of two channels (the effective volume of each channel, 20 mL) serving as the function of NH_4^+ deionization (Figure 3-2(a)). EDI cells were made of two square Perspex frames with internal dimensions of 6 cm × 6 cm × 0.5 cm and a 2-cm wall thickness. The anodic electrode was titanium (Ti) coated with platinum (Pt) with dimensions of 4 cm × 4 cm × 1 mm (Shenzhen 3N Industrial Equipment CO., Ltd., China), and the cathode was Ti coated with iridium ruthenium molybdenum (Ir-MMO) with the same dimensions. The corresponding channels were separated by a cation exchange membrane (IONSEP® AM-C, Hangzhou Iontech Environmental Technology CO., Ltd, China). The EDI cells were sealed by two pieces of silicon shim and locked by screws.

Under the applied voltage, the direction movement of NH_4^+ promoted the accumulation and concentration of NH_4^+ ion. The synthetic NH_4^+-N wastewater in the

EDI's anode contained 0.0125 to 0.25 mol L^{-1} ammonia sulfate, $(NH_4)_2SO_4$. The same concentration of sodium sulfate, Na_2SO_4, was the supporting electrolyte in the cathode of EDI. All batch experiments were carried out at room temperature (25 ± 2 °C). Each set of experiments included a series of applied voltages (0.5-8.0 V), and each cycle was 2.0 h. The real-time current and voltage were recorded by a Keithley 2700 (Tektronix, Inc., USA). Under the optimal applied voltage, the IED of the EDI was set at 7.5, 15.0, 30.0, and 80.0 mm per 2.0 h per cycle. The produced NH_3 gas in the cathode channel was absorbed by 1 mol L^{-1} H_2SO_4 solution. Then it was measured through the modified Berthelot method, as shown in Figure 3-2(b).

As applied voltage increase, the electrochemical reactions took place at the surfaces of the electrodes, which was analyzed by the electrochemical working station (CorrWare®, Scribner Associates Inc., USA). CV sweeping was performed with the three-electrode system (anode, cathode and reference electrode), as shown in Figure 3-2(c). In this thesis, all reference electrode was Ag/AgCl reference electrode. To explore the kinetics of the oxidation and reduction, the sweeping rate was settled at 0.1-100 mV s^{-1}.

(a)

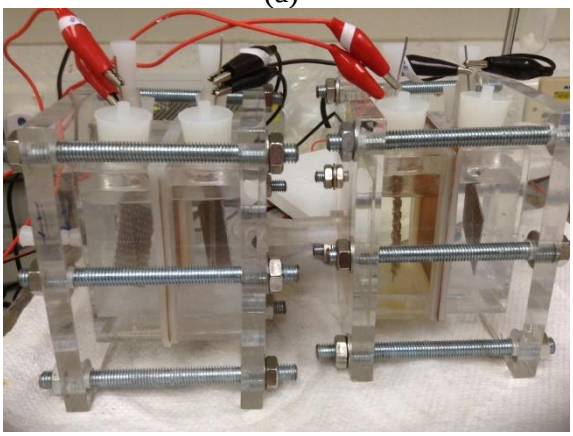

(c)

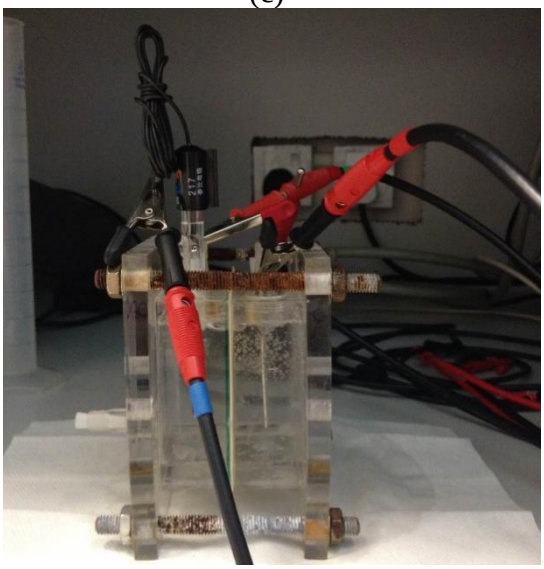

(b)

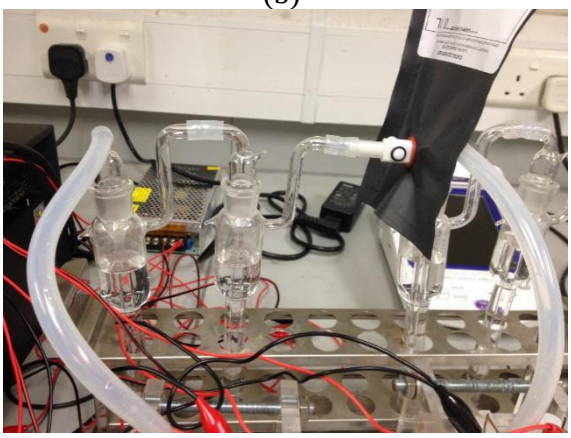

Figure 3-2 Lab-scale electrodeionization: A home-made single EDI reactor (a); a set-up for gas purification and collection (b); Electrochemical reaction detection (c).

3) Landfill Leachate Treatment

This study selected West New Territories (WENT) Landfill in Nim Wan, Tuen Mun, Hong Kong as the case. Characteristics of the Hong Kong West New Territories (WENT) Landfill are summarized in Table 3-1. The schematic graph of WENT Landfill is shown in Figure 3-3(a). It has 110 ha, 61 Mm^3 designed capacity and the real waste intake is about 7,300 tons per day for municipal waste and construction waste. The landfill gas yield is about 7,185 m^3 h^{-1}, containing around 60% CH_4. The generated landfill gas is used to treat ammonia and generate electricity. WENT landfill produces 1,800 m^3 raw landfill leachate per day, in which NH_3-N concentration is 2,900 mg L^{-1}, and total inorganic nitrogen is 7,000 mg L^{-1}. pH is 8.0-9.0.

Landfill leachate used in this study was raw landfill leachate that was directly collected from pipelines. Raw landfill leachate was treated through semi-continuous tests that used a three-channel EDI reactor (anode–sample–cathode), as illustrated in Figure 3-3(a) and 3-3(b). The raw landfill leachate was fed at an influent rate of 2 mL min^{-1}. The anode and the cathode channels were fed with 0.005 mol L^{-1} of H_2SO_4 and Na_2SO_4, respectively. Under the optimal applied voltage and IED, gas evolution led to self-circulation of collection solutions and the generated gases were collected for subsequent analyses.

Table 3-1 Characteristics of the Hong Kong West New Territories (WENT) Landfill*

Parameter	Value	Unit
Waste Intake	7,300	ton d^{-1}
Landfill Gas Yield	7,185	m^3 h^{-1}
CH_4 Percentage	60	%
Raw Landfill Leachate	1,800	m^3 d^{-1}
NH_3-N	2,900	mg L^{-1}
NO_x-N	1.25	mg L^{-1}
Total Inorganic Nitrogen	7,000	mg L^{-1}
Total Nitrogen	7,500	mg L^{-1}
pH	8.00-9.00	-

*Data provided by the West New Territories (WENT) Landfill in Hong Kong

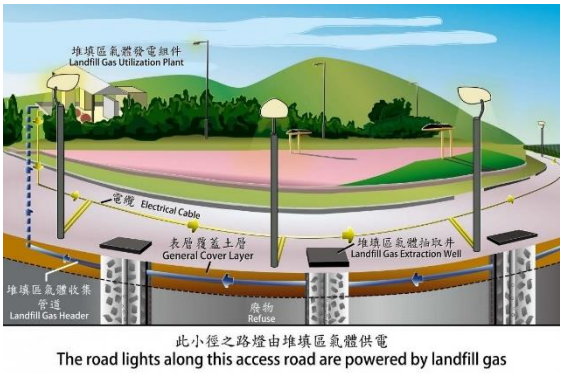

(a)

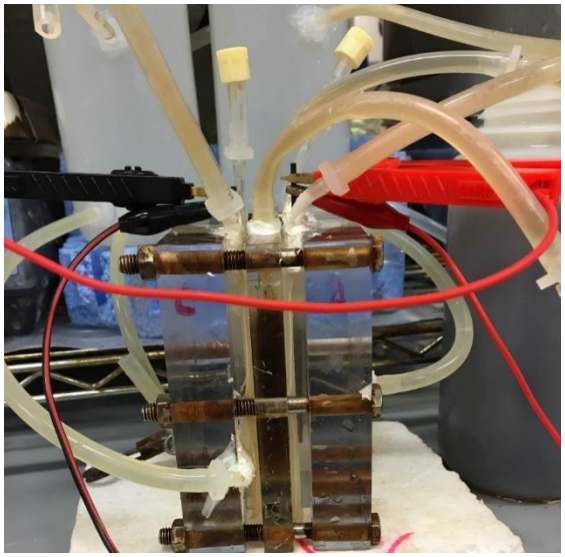

(c)

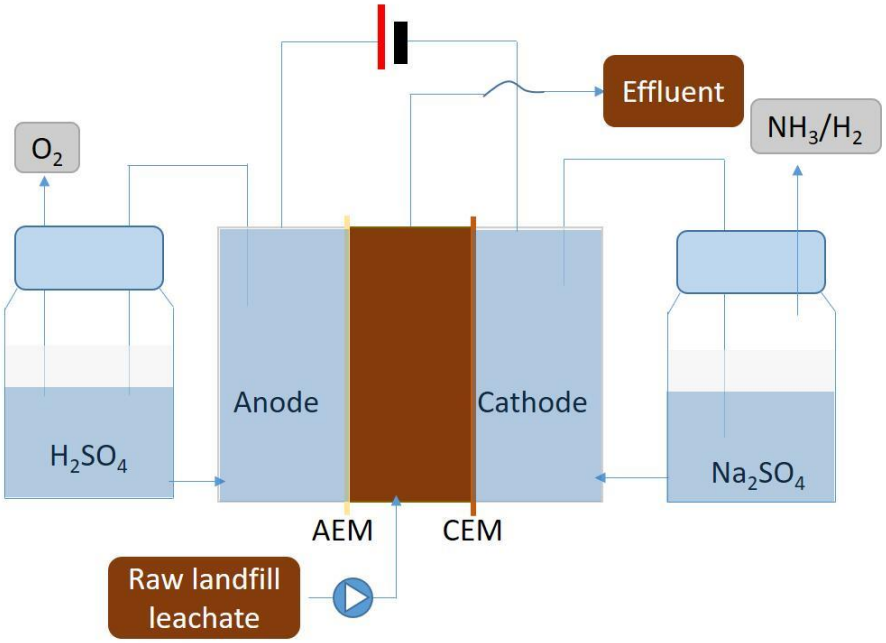

(b)

Figure 3-3 Landfill leachate treatment: Landfill leachate collection from West New Territories (WENT) Landfill in Nim Wan, Tuen Mun, Hong Kong (a); Schematic graph of landfill leachate treatment (b); Home-made set-up for landfill leachate (c).

4) Solid oxide fuel cells preparation

SOFCs were composed of three-layer button reactors in charge of electricity generation reactors, respectively. Single cell with an anode-supported, thin-film dual-layer electrolyte configuration was prepared via a tape casting process, spray deposition and subsequent high-temperature sintering. The composition of SOFCs included anode ($NiO+(ZrO_2)_{0.92}(Y_2O_3)_{0.08}$ (YSZ, NiO:YSZ = 6:4 by weight), electrolyte (YSZ), a cathode ($Sm_{0.2}Ce_{0.8}O_{1.9}$ (SDC) interlayer and a $Ba_{0.5}Sr_{0.5}Co_{0.8}Fe_{0.2}O_{3-\delta}$ (BSCF)). BSCF and SDC powder were synthesized using a combined EDTA-citrate complexing sol-gel process, which was the same with that in our previous paper. NiO and YSZ were commercial products obtained from Chengdu Shudu Nano-Science Co., Ltd., and Tosoh, respectively. SOFCs were operated as follows: first, the double electrolyte layers (YSZ|SDC) were constructed through a wet powder spraying technique. Then, the YSZ suspension was sprayed onto the anode substrate followed by calcination using the spraying gun (HD-130 A) at 1400 °C for 5 h. The procedure was repeated to let the SDC suspension (buffering layer) deposited onto the dense YSZ surface subsequently (Dong *et al.*, 2014). After that, the formed three-layered pellets were then calcined at 1350 °C for 5 h in air. Last, BSCF slurry was sprayed onto the inner surface of the SDC interlayer and fired at 1000 °C for 2 h in air to function as the cathode layer.

After preparations were ready, the polarization curves (I-V) and (P-I) of the coin-shaped fuel cells were tested using a Keithley 2420 source meter built up a four-probe configuration at 550 to 750 °C finally (Su *et al.*, 2012). During the test, synthetic fuel mixtures (H_2, NH_3–H_2, CH_4–CO_2) and a biogas generated from a lab-scale digester

(Biogas with a mixture of 68% CH_4 and 32% CO_2 (v/v) was obtained in our lab from a semi-continuous AD reactor fed with local sewage sludge) were fed into the anode chamber at a flow rate of 100 mL min^{-1} with ambient air in the cathode chamber. The schematic graph and real reactors of AD-EDI and SOFC system are shown in Figure 3-4.

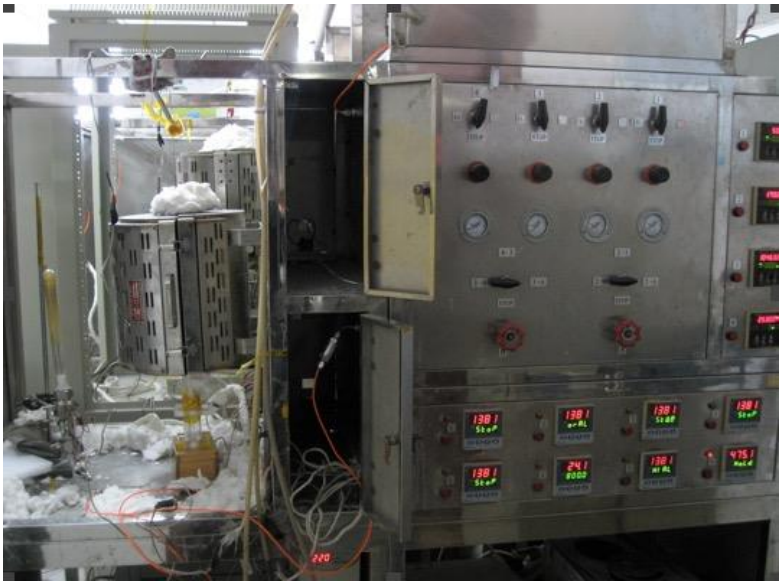

Figure 3-4 Lab-scale SOFCs (graphs provided by Dong's lab).

3.2.2 Chemical analysis

1) Ammonium and ammonia measurement

The modified Berthelot method was employed for the direct determination of ammonia (Cogan, 2015). This method needed two colorimetric reagents called reagent I and reagent II. Reagent I consisted of 0.02 g of sodium nitroprusside and 10 g phenol dissolved in one-liter MiniQ water. Reagent II contained 6.0 g sodium hydroxide and 1.2 mL of 15% sodium hypochlorite in one-liter MiniQ water. Stored solution was prepared by 5.35 g ammonium chloride and 9.61 g buffer solution of citric acid and sodium citrate (pH = 4.0). The standard curve was obtained through five different concentration gradients. In details, the stored solution was firstly diluted and set as 0.05 mmol L^{-1}, 0.1 mmol L^{-1}, 0.25 mmol L^{-1}, 0.5 mmol L^{-1} and 1 mmol L^{-1}. MiniQ water was used as the blank control. Then, 6 colorimetric tubes (25 mL volume) were prepared and injected 100 ul diluted solution, 12.5 mL reagent I, and 12.5 mL reagent II, respectively, for each colorimetric tube. Continuously, these colorimetric tubes were placed in a water-bath container and kept at 37 °C constant temperature. After 20 min later, these tubes were detected using UV spectrophotometer (UV-2100 UV/VIS Spectrophotometer, Qualitest International Inc.) at 620 nm wavelength. Same procedure was conducted 3 times to gain the average values. The standard curve is shown in Figure 3-5.

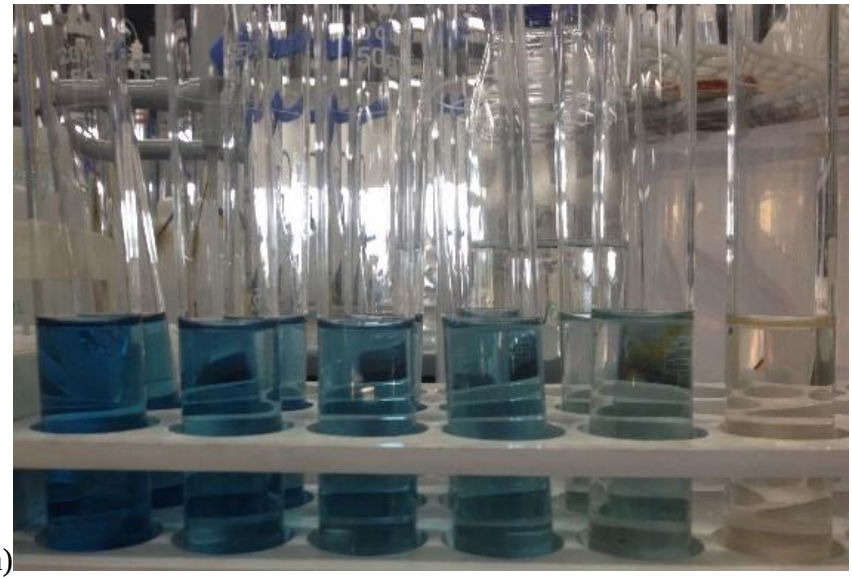

(a)

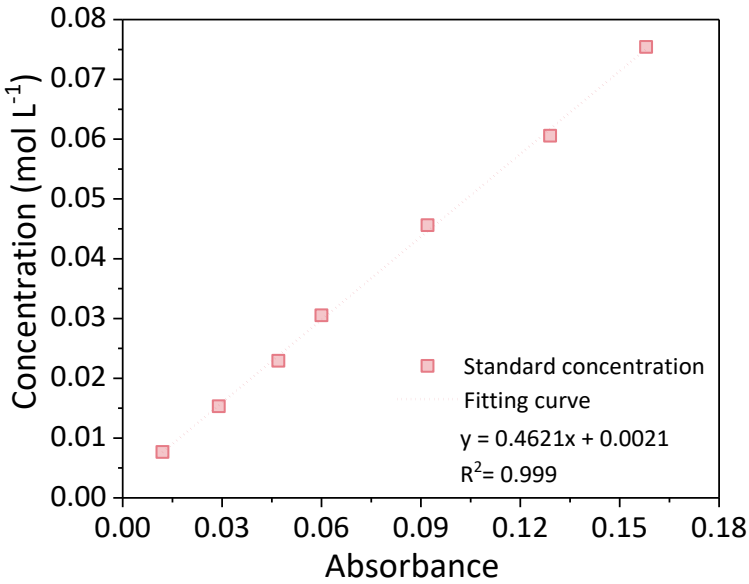

(b)

Figure 3-5 The standard curve of NH_4^+-N determination.

2) Nutrient compound measurements

Nitrite, nitrate, phosphate, and sulfate were measured using standard methods of wastewater treatment. Total nitrogen (TN) was analyzed with 720 °C catalytic thermal decomposition/chemiluminescence methods using TOC-L analyzers (TOC-LCSH/CPH, Shimadzu).

Methane, carbon dioxide, hydrogen, and nitrogen were determined using gas chromatography (Agilent 4890D; J&W Scientific, USA) using an HP-MoleSieve column (30 m × 0.53 mm × 50 m) (Ramió-Pujol *et al.*, 2015); Helium gas as the carrier gas, was injected at a rate of 6 mL min^{-1}. The temperatures of the injection port, separation column, and TCD detector were 200 °C, 35°C, and 200 °C, respectively. The 200 µL samples were injected by micro syringes (Shanghai Anting Scientific., China).

The determination of metal ions was conducted using an Agilent 7500cx ICP-MS (Agilent Technologies, Santa Clara, CA, USA) (Dai *et al.*, 2012).

3.2.3 Calculations

The deionization efficiency (E_p) is expressed as Eq.3-8.

$$E_p = \frac{c_i^0 - c_i^t}{c_i^0} \times 100\% \tag{3-8}$$

where c_i is the concentration of i and the superscripts 0 and t are the time of the beginning and end of the trial, respectively.

Current Efficiencies (E_c) is defined as the efficiency of electric current used to drive ion separation.

$$E_c = F \times (V_0 \times C_0 - V_f \times C_f) / n \times I \times \Delta t \tag{3-9}$$

where F is the Faraday constant; V_0 and V_f are the initial and final volumes of the diluted solution, respectively; c_0 and c_f are the initial and final concentrations of the electrolyte; n is the number of membrane pairs; and I is the current during the time interval Δt (Wisniewska & Winnicki, 1991).

Energy Balance Ratio (EBR) refers to the energy input to output as expressed by Eq. 3.10 to evaluate the efficiency of the EDI–SOFC system.

$$R_{EBR} = \frac{W_{out} \times r}{W_{in}} \tag{3-10}$$

where W_{out} is the thermal energy of CH_4, NH_3, and H_2; r is the electricity conversion efficiency of the SOFC, and W_{in} is the energy consumption.

W_{in} is calculated as follows.

$$W_{in} = Q \times \phi_{ap} \tag{3-11}$$

$$Q = I \times t = \int i \times dt \tag{3-12}$$

$$W_{out} = m_j \times \Delta H \tag{3-13}$$

where ϕ_{ap} is the applied voltage; Q is the electric quantity; m_j is the mass of fuel species, and ΔH is enthalpy.

3.3 Results

3.3.1 Ammonium recovery

Optimizations of applied voltage, IED, and ammonium concentration in the EDI were investigated through adjusting the applied voltage (0.5 to 8.0 V), IED (7.5 to 80 mm), and influent ammonium concentrations (0.025 to 0.5 M) (Figure 3-6). The deionization efficiency of NH_3 linearly increases with an increase in applied voltage and reaches the highest value of 80% at 8.0 V. The corresponding EBR based on the recovery of NH_3 and H_2, are 1.67 at 3.0 V and 0.86 at 8.0 V, respectively, when the IED is 15 mm (Figure 3-6(a)), indicating that 3.0 V is the optimal voltage, which is apparently lower than the voltage of 17.5 V as reported (Ippersiel *et al.*, 2012).

Under this applied voltage (3.0 V), the IED was shortened from 80 mm to 7.5 mm. The deionization efficiency of NH_3 and EBR reciprocally increases from 64.8% and 1.67 to 84.8% and 1.99, respectively, as the IED narrowed from 15 mm to 7.5 mm. However, the deionization efficiency of NH_3 and EBR decreases to 12% and 1.09, as the IED expanding to 60 mm (Figure 3-6(b)). This variation of NH_4^+ deionization efficiency signifies that the IED brings more significant influences than the applied voltage, which can be verified by Stock's model (Chen *et al.*, 2015; Griffiths, 1999). The deionization rate at the optimal conditions of the applied voltage and IED climbs to 80 mM d^{-1} within 0.5 h but drops to 20 mM d^{-1} at 2.0 h, signifying that deionization efficiency does not increase with extended operating time (Figure 3-6(c)). This effect

is likely to be related to Donnan equilibrium when ion migration stops as the concentration gradient narrows (Biesheuvel & Van der Wal, 2010; Biesheuvel *et al.*, 2011).

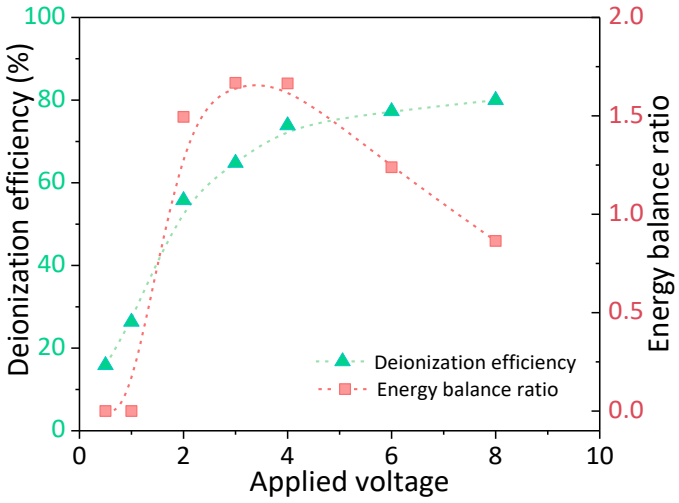
Deionization efficiency (%)
Energy balance ratio
Applied voltage
Deionization efficiency
Energy balance ratio
0
20
40
60
80
100
0.0
0.5
1.0
1.5
2.0
0
2
4
6
8
10

(a)

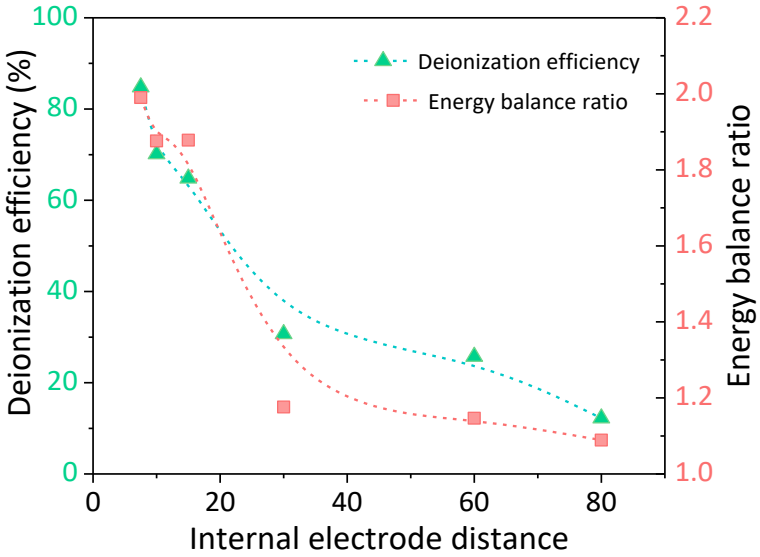
Deionization efficiency (%)
Energy balance ratio
Internal electrode distance
Deionization efficiency
Energy balance ratio
0
20
40
60
80
100
1.0
1.2
1.4
1.6
1.8
2.0
2.2
0
20
40
60
80

(b)

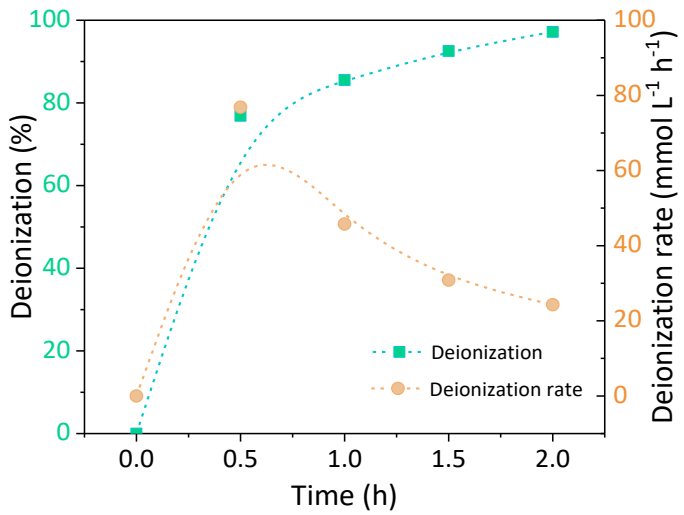

(c)

Figure 3-6 Deionization efficiency of EDI with 0.5-8.0 V applied voltage (a); Deionization efficiency at 7.5-80 mm IED (b); Deionization efficiency and rate as a function of operating time (c).

The deionization efficiency is related to the drift velocity (μ) of ions defined as Eq. 3-14.

$$\mu = \frac{m\sigma\Delta\phi}{\rho efl} \tag{3-14}$$

where μ, the drift velocity of the electrons (m s^{-1}); m, the molecular mass of the solution (kg); $\Delta\phi$, the voltage applied to the conductor (V); ρ, the density (mass per unit volume) of the conductor (kg m^{-3}); e, the elementary charge (C); f, the number of free electrons per ion; l, the length of the conductor (m); σ, the electric conductivity of the medium at the given temperature (S m^{-1}). As other parameters are constants in this test, the drift velocity is only associated with the ratio of $\Delta\phi$ to l, which represents the electric field strength of EDI (Schmidt *et al.*, 2011). Thus, the drift velocity linearly increases as the applied voltage increases, but reciprocally as l extending. Figure 3-7 shows the relationships between applied voltage, IED, and drift velocity. The drift velocity is enhanced by increasing the applied voltage and narrowing the IED.

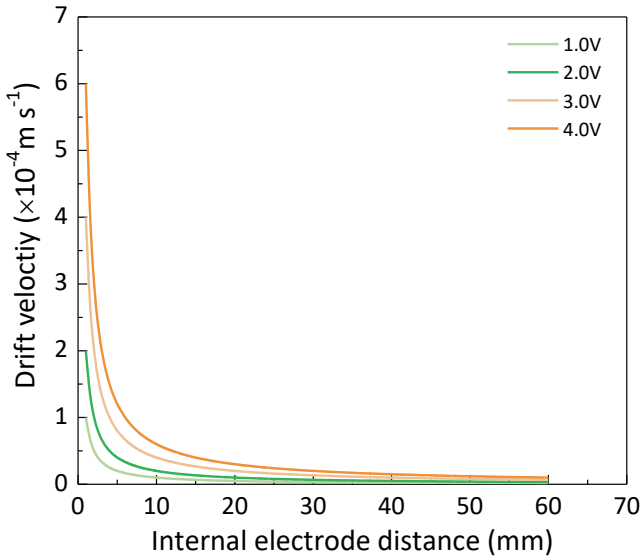

(a)

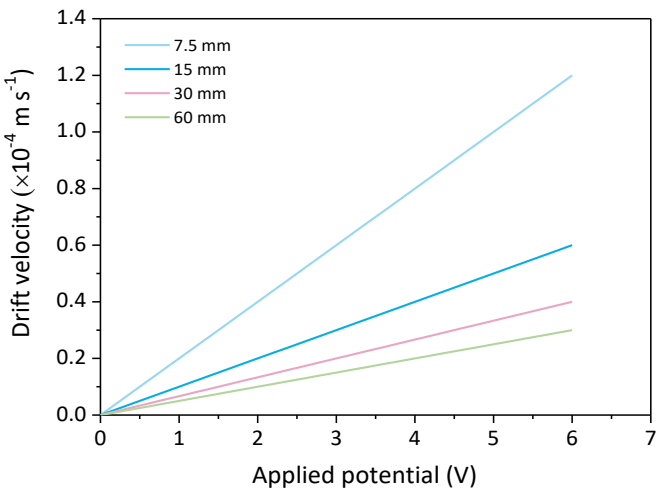

(b)

Figure 3-7 Drift velocity of NH_4^+ varying with the applied voltage (a); Drift velocity of NH_4^+ varying with the IED (b).

As previously mentioned, applied voltage accelerates the drift velocity of ions companied by water splitting to O_2 and H_2. It means that energy input is distributed to the processes of ion migration, water splitting and ohmic loss, which is indexed by current efficiency. The current efficiency was gained via the indirect methods as introduced by Tilak & Chen in 1999 (Tilak & Chen, 1999). The indirect approach to measure the ammonium current efficiency stems from the material balance (i.e., input+generation-loss=output) of the ammonium. if the electricity, Q (in kA), flows into a cell, the theoretical production of ammonium ($m_{theo.}$) in the concentrate channel in 24h is equal to:

$$m_{theo.} = 8,0533 \times Q \tag{3-15}$$

But the actual weight of the ammonium produced is always lower than the theoretical amount because ion migration is together with the water splitting and internal ohmic loss. Hence, the current efficiency (η_{CE}) is expressed by Eq. 3-16.

$$\eta_{CE} = \frac{m_{act.}}{m_{theo.}} \times 100\% \tag{3-16}$$

where $m_{act.}$is the actual amount produced mass.

The current efficiency is summarized in Table 3-2. The current efficiency of ions displays an almost linear drop from 95% at 500 V m^{-1} to 6.0 % at 8,000 V m^{-1}. The current efficiency of ohmic loss increases from 5% at 500 V m^{-1} to 29.09% at 3,000 V m^{-1} and then slightly decreases to 23.02% at 8,000 V m^{-1}. Apparently, the current efficiency of water splitting increases from 0% at 500 V m^{-1} to 70.97% at 8,000 V m^{-1}. The distributions of current efficiency indicate that water splitting and ohmic loss

consumes more energy than ion migration when the electric field strength increases to 3,000 V m^{-1}. These results explain the reason why the deionization rate does not increase when the applied voltage elevates always.

Due to the accumulation of ammonia and water splitting, both ammonia and hydrogen are generated with the increase in the electric field strength of 500 to 8,000 V m^{-1}. As shown in Table 3-2, the ratio of ammonia to hydrogen increases from 0 to 0.33 at 4,000 V m^{-1}, then increases to 0.4 at 8,000 V m^{-1}, suggesting that the ratio of ammonia to hydrogen reaches a stable stage even though the yield of hydrogen has a significant increase. We can conclude that hydrogen promotes the conversion of ammonium to ammonia at the price of intensive energy consumption. Therefore, the EDI stack should be operated at low applied potential and high current density.

Table 3-2 Current efficiencies of ion migration, water splitting, and ohmic loss

Electric Field Strength (V m^{-1})	Current Efficiency (%)			NH_3/H_2
	Ion Migration	Water Splitting	Ohmic Loss	
500	95.00	0.00	5.00	0.00
1,000	90.00	0.00	10.00	0.00
2,000	61.23	13.54	25.23	0.10
3,000	33.35	37.56	29.09	0.30
4,000	10.68	62.39	26.93	0.33
6,000	8.01	67.75	24.237	0.36
8,000	6.00	70.97	23.02	0.40

3.3.2 Ammonium reduction

Of particular interest is that we detected N_2 in the cathode of EDI. We assume whether N_2 formation results from electrochemical reactions as the voltage rises. If our hypothesis is correct, it means that NH_3 recovery will be enhanced at the cathode. To check how N_2 is produced, mass balance and electrochemical oxidation were carried out. Figure 3-8(a) shows the mass balance of nitrogen in the species of NH_4^+, NH_3, nitrite (NO_2^-), nitrate (NO_3^-), and N_2. Three nitrogen compounds (NH_4^+, NH_3, and N_2) are detected, and the other species are all below detection levels of 0.2 N mg L^{-1}. Approximately 60%, 30%, and 10% of nitrogen exist as the sorts of NH_4^+, NH_3, and N_2, respectively. For raw landfill leachate, their respective percentages are 87.5%, 1.7%, and 0.38%, respectively. The conversion ammonium to ammonia in the batch tests with synthetic wastewater is better than that of the semi-continuous tests with the raw landfill leachate. It is attributable to the complicated composition of raw landfill leachate.

To investigate whether the formation of N_2 was related to NH_4^+ reduction, we performed CV sweeping at a scanning rate of 0.5 to 10 mV s^{-1} using Ag/AgCl as the reference electrode within 0 to 1.5 V (Figure 3-8(b)). We do not see any oxidation peaks but see a reduction peak presented at 0.23 V on the CV curve for each scanning cycle, indicating the possible electrochemical dissociation of NH_4^+. Although a few studied on the mechanism of NH_4^+ reduction, Simons *et al*. (1969) proposed that NH_4^+ reduction was a three-step process (Eq.3-15): (1) Under the applied voltage, NH_4^+ accepted an electron and became $[NH_4^0]_{(ads)}$ at the interface between the cathode and the solution; (2) $[NH_4^0]_{(ads)}$ dissociated to $H_{(ads)}$ and $NH_{3(ads)}$; (3) as the accumulation

of $H_{(ads)}$ and $NH_{3(ads)}$, H_2 and NH_3 were produced under the assistance of alkaline solution (Simons *et al.*, 1969).

$$NH_{4\,(aq)}^{+} + e^{-} \rightarrow \left[NH_4^0 \right]_{(ads)} \rightarrow H_{(ads)} + NH_{3(ads)} \rightarrow 0.5H_{2(g)} + NH_{3(g)} \qquad (3\text{-}17)$$

Additionally, NH_3 generation is related to water splitting. The generated OH^- promotes the equilibrium reaction of NH_4^+ to NH_3 progressing (Eq.3-16 and Eq. 3-17). The reduction of NH_4^+ makes favorable contributions to the yields of NH_3 and H_2.

$$H_2O_{(l)} + e^{-} \rightarrow OH^{-}{}_{(aq)} + 0.5H_{2(g)} \qquad (3\text{-}18)$$

$$NH_{4\,(aq)}^{+} + OH^{-}{}_{(aq)} \leftrightarrow NH_3 gH_2O_{(l)} \leftrightarrow NH_{3(g)} + H_2O_{(l)} \qquad (3\text{-}19)$$

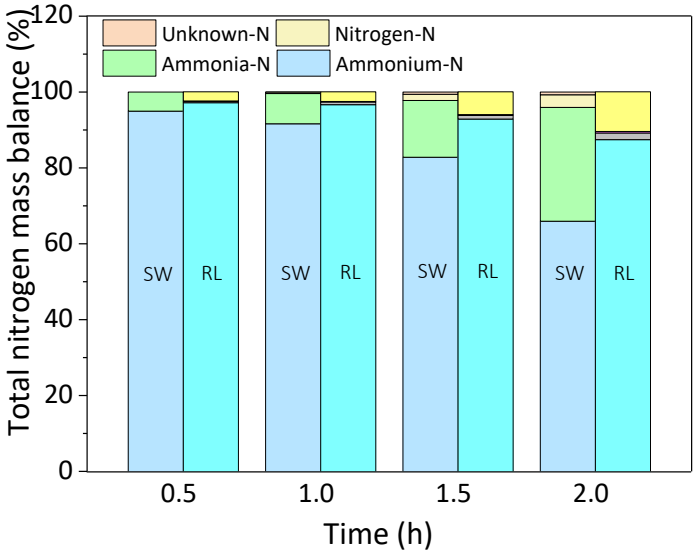

(a)

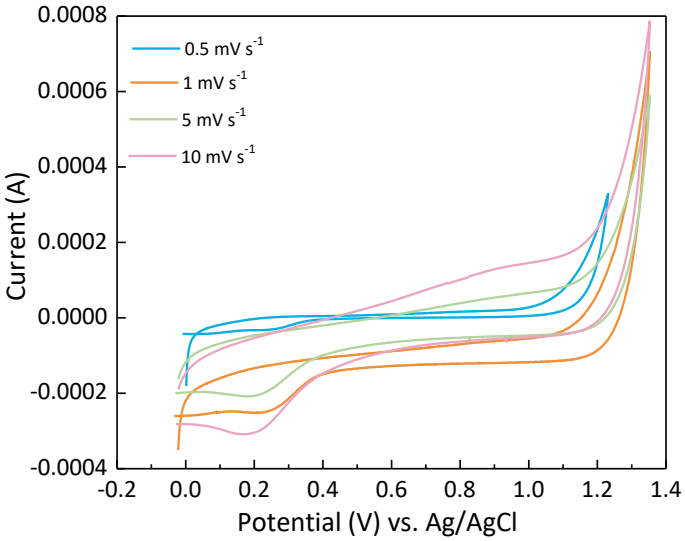

(b)

Figure 3-8 Total nitrogen mass balance in terms of ammonium, ammonia and other nitrogen species of synthetic wastewater (SW) and raw landfill leachate (RL) (a); CV curves of EDI at 0–1.23 V vs. Ag/AgCl under 0.5–10 mV s^{-1} for the anolyte (b).

3.3.3 Solid oxide fuel cell performances

1) Polarization curves of ammonia-hydrogen

To estimate energy output, the performances of SOFCs were tested with pure H_2 at 100.0 mL min^{-1}, operating temperatures at 550 to 750 °C. An open circuit voltage value (OCV) of 1.134 V is obtained at 750 °C, which approaches to the Nernst potential of 1.23 V (Ma *et al.*, 2007) (Figure 3-9(a)). At 750 °C, fed with H_2 from 20% to 60% by volume (v/v) of NH_3 in the NH_3–H_2 fuel stream, SOFCs achieves 1.056-1.085 V OCV, slightly lower than that obtained from pure H_2, which may be caused by lower H_2 partial pressure in NH_3–H_2 fuel stream (Figure 3-9(b)). This trend is consistent with the results of the theoretical simulation (Ma *et al.*, 2007). The peak of the power density declining from 1194 mW cm^{-2} at 20% NH_3 to 1018 mW cm^{-2} at 60% NH_3 might be related to insufficient H_2 supply from NH_3 decomposition. With the increase in NH_3 concentration, the incomplete decomposition of NH_3 occurring results in the hydrogen pressure decreasing (Cheddie, 2012). Because ammonia decomposition is an endothermic process, the concentrated NH_3 absorbs a significant amount of thermal energy and reduces the local temperature. Thereby, the kinetics of ammonia decomposition is slowed with the increase in the percent of ammonia gas (Hajimolana *et al.*, 2011). During the throughout process, fortunately, NO_x was not detected in the off-gas even though O_2 was as the electron acceptor. Our results are expected from the reported findings (Krishnan *et al.*, 2007; Spinner *et al.*, 2012).

Above results can be further explained by the mechanism of NH_3 decomposition at the high temperature (Eq. 3-18 to Eq. 3-20). Fed with NH_3–H_2 fuel stream, NH_3 decomposition includes three steps: 1) ammonia adsorption onto catalyst sites; 2) N-H

bond cleavage; 3) N atoms re-combinative desorption (Boudart & Djéga-Mariadassou, 2014; Dekker & Rietveld, 2006; Fuerte *et al.*, 2009; Kordesch *et al.*, 1999).

$$NH_3 + X* \rightarrow NH_3* + X \tag{3-20}$$

$$NH_3* + X \rightarrow NH_2* + H* + X \tag{3-21}$$

$$2N* \rightarrow N_2 + 2* \tag{3-22}$$

where * is an active site, and *X* is a species adsorbed onto the activated site. Bradford *et al*. (1997) and Vitvitskii *et al*. (1990) found that the released hydrogen inhibited the decomposition reaction with diluted NH_3 (Bradford *et al.*, 1997; Vitvitskii *et al.*, 1990). Chellappa *et al*. (2002) and Evgeny & Alexis (1991) found that hydrogen inhibition was eliminated as ammonia concentration increased and confirmed that the combinative desorption of nitrogen atoms determines the reaction rate with higher NH_3 pressure (Chellappa *et al.*, 2002; Shustorovich & Bell, 1991). Collectively, these results suggest that suitable NH_3 percentage can achieve an ideal process of NH_3 decomposition.

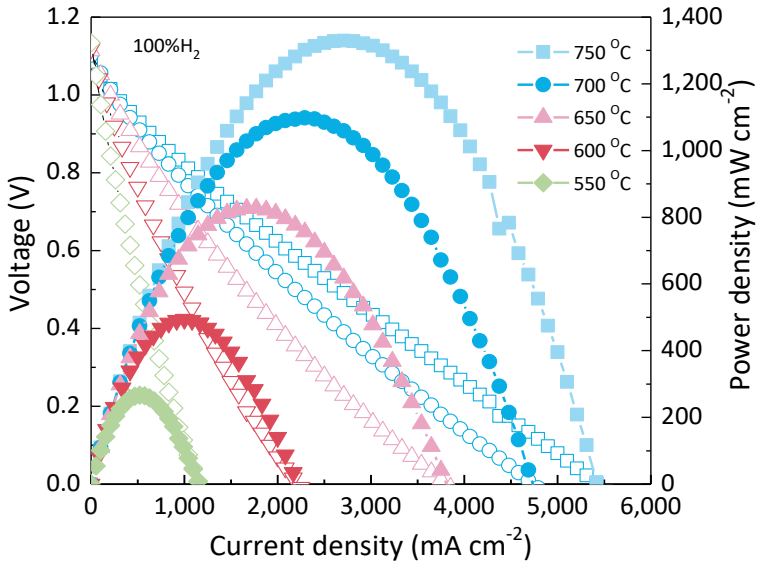

(a)

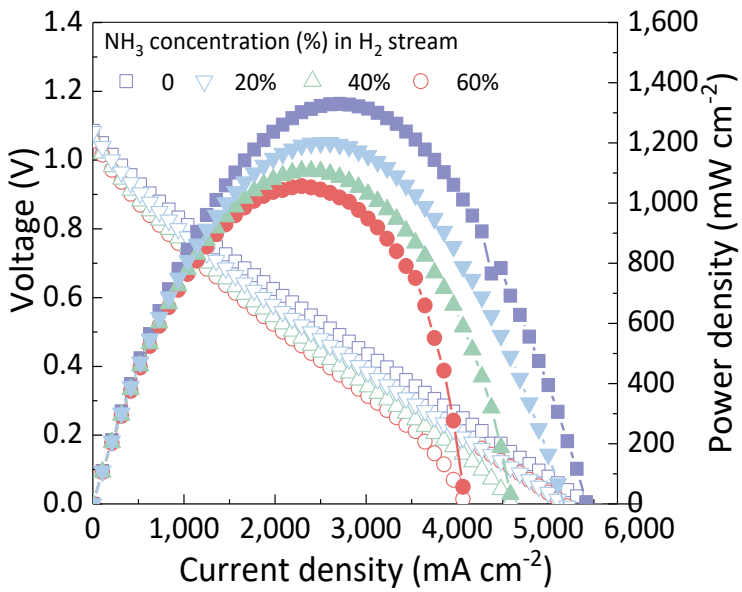

(b)

Figure 3-9 V-I and P-I polarization curves of the SOFCs fed with 100% H_2 at 550-750 °C (a); 0-60% NH_3 in H_2–NH_3 mixture at 750 °C (b).

2) Polarization curves of methane-carbon dioxide and real biogas

With 20%, 40%, 60%, and 80% (v/v) CH_4 in CH_4–CO_2 fuel stream, an increasing trend of OCV value (from 1.0-1.17 V) with an increase in CH_4 percent was obtained (Figure 3-10(a)). Although the slight drop of OCV at 80% CH_4 takes place, 1.0 V to 1.17 V OCV approaches the theoretical value, indicating a dense electrolyte and decent sealing of SOFC during the testing. For the CH_4–CO_2 fuel stream in the stability test, carbon deposition was not apparently observed, which may be related to CH_4 reformation as reported elsewhere (Dincer *et al.*, 2015; Kuhn & Napporn, 2010; Suddhasatwa, 2007).

Many scholars studied the mechanism of methane reformation and found that the process of CH_4 reforming including many possible paths was far more complicated than expected (Bradford & Vannice, 1999; Valdés-Pérez & Zeigarnik, 2000; Wang *et al.*, 1996; Zhang *et al.*, 1996). So, we summary the primary process of CH_4 reforming, which can be approximated with the following simplified steps with sufficient accuracy: 1) CH_4 is dissociated to C* and H_2 (Eq. 3-21); 2) CO_2 dissociation to form CO and O* (Eq. 3-22); 3) carbon oxidation to CO (Eq. 3-23) (Iyer *et al.*, 2003).

$$CH_4 + * \rightarrow C* + 2H_2 \tag{3-23}$$

$$CO_2 + * \rightarrow CO + O* \tag{3-24}$$

$$C* + O* \rightarrow CO \tag{3-25}$$

As biogas (about 70% CH_4) produced from our laboratory-scale AD reactor fed SOFCs, we estimated the energy potential of EDI-SOFCs. About 900 mW cm^{-2} peak power

density is obtained (Figure 3-10(b)), which is close to the results of mixed fuel of 60% CH_4 and 40% CO_2. Based on 50% energy conversion efficiency (Valdés-Pérez & Zeigarnik, 2000; Zhang *et al.*, 1996), our experimental results of NH_3-H_2 and CH_4-CO_2 indicate that EDI-SOFCs is feasible for power generation from biogas and extracted NH_3-N from AD digestate and landfill leachate.

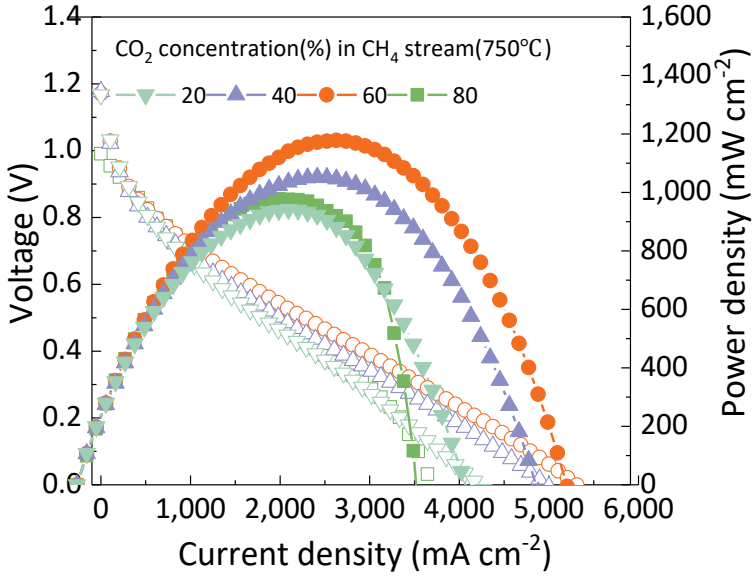

(a)

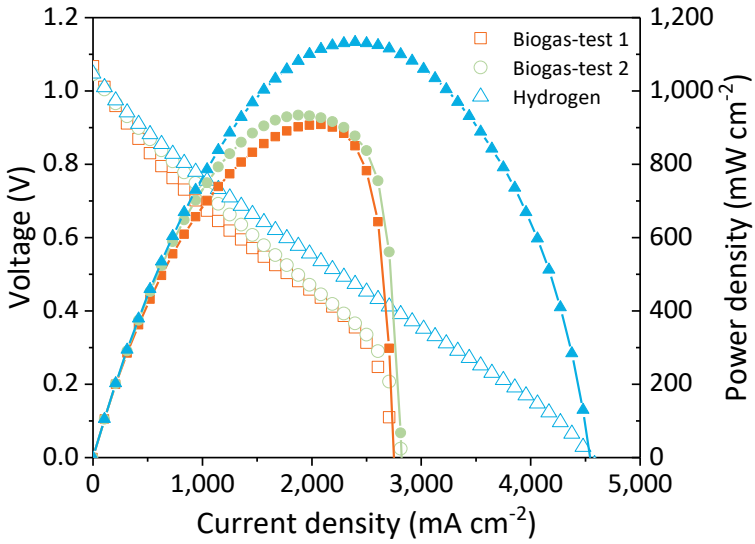

(b)

Figure 3-10 V-I and P-I polarization curves of the SOFC fed with 20–80% CH_4 in CO_2–CH_4 mixture at 750 °C (a); Real biogas with a mixture of 68% CH_4 and 32% CO_2 (v/v) from a lab-scale AD reactor at 750 °C (b).

3.3.4 Energy balance of EDI–SOFCs system

The energy balance of EDI-SOFCs was investigated for various NH_4^+-N concentration (0.025 to 0.5 M) under the optimal conditions. EBR value varies with the increase in NH_4^+-N concentration in synthetic wastewater (Table 3-3). When the influent of NH_4^+-N content is lower than 0.1 M, EBR is below 1.0, indicating a need for external energy input. As NH_4^+-N concentrating from 0.025 M to 0.25 M, EBR value increases from 0.5 to 1.20 but drops to 1.13 as NH_4^+-N reaching 0.50 M. The optimal EBR is 1.20, demonstrating that 20% net energy can be output. The variation of EBR value is related to the current efficiency of NH_4^+ migration. The conductivity and the current increase when NH_4^+-N increases from 0.025 M to 0.1 M. As a result, both energy input and H_2 and NH_3 recovery increased. However, the magnitude of the chemical energy potential of recovered NH_3 and H_2 is not significantly increased even lower than that of energy input. These results suggest that the EDI–SOFCs system is most economically feasible for medium to high NH_4^+-N waste streams. Moreover, the energy potential was estimated using a local raw landfill leachate in Hong Kong to predict the commercial application of this hybrid system. The results show that 98% NH_4^+ is removed via the semi-continues EDI stack and the EBR approaches 1.76 (Table 3-3), signifying that the EDI–SOFCs system offers an economic strategy for sustainable landfill leachate management.

Table 3-3 Energy benefits from different concentrations of ammonium wastewater through the EDI–SOFCs system*

Experiment	NH_4^+-N Concentration	Deionization	Treatment Capacity	Operating Period	Energy Recovery	Energy Input	Net Energy Revenue	Energy Balance Ratio
	M	%	$m^3\ d^{-1}$	hr	kJ $m^{-3}\ d^{-1}$			
Batch	0.025	95	0.00024	2	45,853.1	92,584.2	-46,731.1	0.50
	0.05	92	0.00024	2	70,493.6	93,649.8	-23,156.3	0.75
	0.10	87	0.00024	2	87,117.7	114,604.0	-27,486.3	0.76
	0.25	83	0.00024	2	134,437.9	112,441.9	21,996.0	1.20
	0.50	76	0.00024	2	185,549.8	163,890.2	21,659.6	1.13
Semi-continuous	0.21	98	0.00288	0.16	71,391.2	40,578.7	30,812.5	1.76

* The detailed calculation is available in the supporting information.

Table 3-4 summarizes the potential benefits of the EDI–SOFCs system considering oxygen demand, sludge production, and EBR. Calculations started with 1.0 mol COD. The productions of sludge for Nitrification–Denitrification, Nitrification–Anammox, CANDO, AD-EDI–SOFC are 26.0, 18.3, 15.8 and 13.3 g, respectively. The yields of biogas are 0.85, 1.29, 1.29 and 1.80 mol, respectively, and their responding energy are 753, 1,142, 1,186 and 2,388 J. Compared to conventional nitrification-denitrification (Wett, 2007), nitrification–Anammox (Van Dongen *et al.*, 2007), and CANDO (Sommer *et al.*, 2013), EDI produces less 18.7 to 50% sludge, and depletes less 55.9 to 80.5% energy. This great energy benefit mainly attributes to no demand oxygen and hydrogen and ammonia as two extra energy resources. The final energy costs of ammonia recovery by EDI is 2.32 kWh kg^{-1}-NH_3 that is 5% of 16.9 kWh kg^{-1}-NH_3 by ammonia stripping.

Table 3-4 Comparisons of ammonium removal/recovery processes integrated with anaerobic treatment per removal of 1 mole of NH_4^+ with 3.47 mole of biodegradable COD (a biodegradable COD/N ratio of 7.9), typical of U.S. medium strength wastewater (Henze *et al.*, 2008; Safoniuk, 2004).

Processes	Sludge Yield	Oxygen Requirement	Energy Sources				Energy Potential*	Energy Input**	Energy Balance Ratio	Reference
			CH_4	N_2O	NH_3	H_2				
	g		mol				kJ			
Nitrification–Denitrification	26.00	52	0.85	-	-	-	753	219.2	3.43	(Yang *et al.*, 2007)
Nitrification–Anammox	18.30	42	1.29	-	-	-	1,142	176.9	6.45	(Van Dongen *et al.*, 2007)
CANDO	15.80	42	1.29	0.58	-	-	1,186	176.9	6.70	(Kim *et al.*, 2010)
EDI–SOFCs	13.30	-	1.80	-	0.80	1.86	2,388	113.6	21.02	This study

*Estimated according to ΔH_R^0 of Eq.1 to Eq. 6. **1.17 kWh kg^{-1} O_2 (Fenu *et al.*, 2010), and 2.32 kWh kg^{-1}-NH_3 recovery (this study)

Also, the Hong Kong West New Territories Landfill was studied to evaluate the integration of the EDI–SOFCs system entirely. The energy consumption and recovery are summarized in Table 3-5, and the techno-economic evaluation is depicted in Figure 3-11. The comparison between the AS-CHP system and EDI-SOFCs system integrated with the existing plant indicates that the later generates 0.56×10^5 MWh more energy than the former per year. Moreover, the later consumes 1.06×10^5 MWh less power input. Consequently, the EBR increases from 1.11 (AS-CHP) and 1.75 (EDI-SOFCs). This result reveals that the EDI–SOFCs system can yield about 60% more electricity than the existing system. Most importantly, gas generated by EDI provide 4.21×10^5 MWh energy for the whole system. Besides, there is 4.04×0^5 MWh uncaptured energy per year. Therefore, with the incorporation of EDI-SOFCs system, it is believed that more energy can be harvested from landfills.

Table 3-5 Comparison of net energy balances of the AS–CHP and EDI–SOFCs integrated systems in the Hong Kong West New Territories (WENT) Landfill (10^5 MW·h per year)

	Process	AS–CHP	EDI–SOFCs
Energy Distribution	Heat Recovery	3.29	-
	Electricity Generation	0.17	4.02
	Non-captured Energy	0.39	4.04
Total Energy Potential		3.85	8.06
Effective Energy Captured		3.46	4.02
Energy Input Required		3.29	2.32
Energy Balance Ratio		1.11	1.75

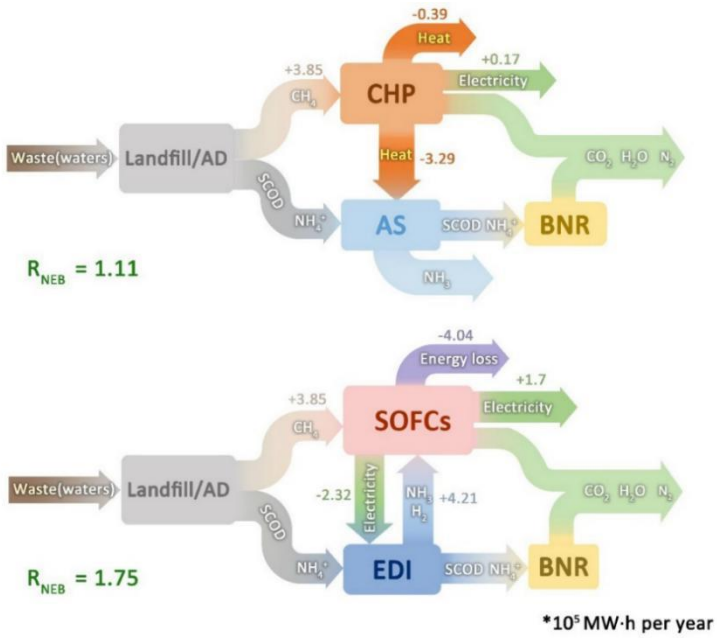

Figure 3-11 Comparisons of mass and energy flow between AS–CHP and EDI–SOFCs.

3.3.5 Inorganic ion removal

Aside from NH_4^+ ion, landfill leachate also contains a significant portion of inorganic ions. Some of them like K^+, Ca^{2+}, Na^+, NO_3^-, and PO_4^{3-} can be reused as fertilizers. Other ions such as Cl^-, Zn^{2+}, Cu^{2+}, Pb^+, Cr^{3+} must be removed before discharging due to the toxicity and adverse effects. The semi-continuous EDI reactor was used to treat the raw landfill leachate, and the results show that the conductivity and salinity of the landfill leachate decrease from 88.2 mS cm^{-1} and 7.85% to 2.26 mS cm^{-1} and 0.1%, respectively. EDI has over 80% removal efficiency of cations and high kinetic deionization in K^+, NO_3^-, and PO_4^{3-} (Table 3-6 and Figure 3-12). Interestingly, most of the detected metal ions have faster mobilities over NH_4^+, which may be related to the natures of an ion. As found by Foo & Hameed (2009) ions have smaller ion radii but larger valences (Foo & Hameed, 2009). As each ion differs in size, valence, diffusion coefficient, and conductivity from other ions, it exhibits different migration kinetics (Salis & Ninham, 2014). In this study, among the predominant species of H^+, K^+, NH_4^+, and Na^+, the order of their mobilities is listed, $H^+ > K^+ > Na^+ > NH_4^+$, as shown in Figure 3-12.

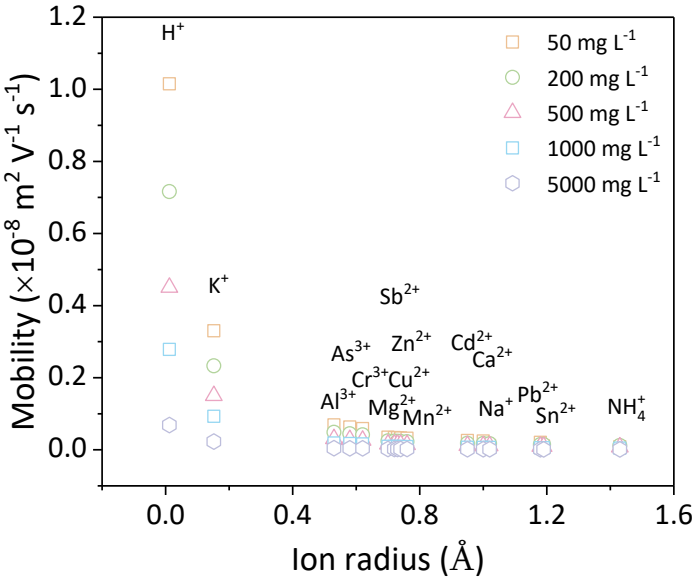

Figure 3-12 Mobility of ions as functions of ion radii and concentration (mg L^{-1}).

Table 3-6 Ions and metals removal/recovery performance from the raw landfill leachate through the semi-continuous EDI reactor

Pollutants	Raw Landfill Leachate	Effluent	Removal Efficiency
	mg L^{-1}		(%)
PO_4^{3-}	414.00	20.60	95.02
NO_2^--N	1.40	0.56	96.14
NO_3^--N	104.00	8.50	83.65
SO_4^{2-}	319.00	112.50	64.73
NH_4^+	2,956.60	61.50	98.97
Ag	0.24	0.02	92.59
Al	1.53	0.69	54.52
As	0.27	0.02	91.81
Ba	0.08	0.01	90.00
Ca	25.34	2.71	89.32
Co	0.10	0.02	84.31
Cr	0.79	0.02	96.97
Cu	0.05	0.00	89.71
Fe	2.13	0.08	96.07
K	884.38	1.87	99.79
Mg	60.11	2.33	96.12
Ni	0.39	0.03	92.83
Pb	0.14	0.02	85.71
Sb	0.04	0.00	94.44
Se	0.04	0.03	20.00
Sr	0.15	0.03	77.63
Zn	1.41	0.04	97.23

3.4 Summary

In this chapter, we introduced a simple and sustainable AD-EDI–SOFCs hybrid system to extract energy from wastewater streams. For batch tests, EDI removes 95% and 76% nitrogen from diluted (0.025 M) concentrated (0.5 M) synthetic NH_4^+ sewage, respectively. EBR reaches 1.13 from 0.50 at the relevant concentrations. During NH_4^+ deionization process, an interesting finding is that NH_4^+ reduction in the cathode facilitates NH_3 and H_2 generation at 0.23 V vs. Ag/AgCl reference electrode. Based on the recovered fuels (NH_3 and H_2), EDI achieves 60% higher in energy output than conventional nitrogen removal processes under the optimal conditions (3.0 V applied voltage and 7.5 mm IED). The performances of SOFCs tested at 750 °C indicate that NH_3, H_2, and biogas from wastewater streams can be used as energy resources. The case study of the landfill site demonstrates that energy benefit is upgraded from 1.11 (existing system) to 1.75 (this study). EDI stack removes 80% of average inorganic ions including heavy metals and nutrient elements from raw landfill leachate. Therefore EDI-SOFCs coupled with the AD is promising for upgrades of anaerobic processes for energy potential extraction from both carbonaceous and nitrogenous pollutants.

3.5 References

Abbasi, Tauseef, & Abbasi. (2012). Anaerobic digestion for global warming control and energy generation: An overview. *Renewable & Sustainable Energy Reviews, 16*(5), 3228-3242.

Ahn, Kim, Park, Rahm, Pagilla, & Chandran. (2010). N2O emissions from activated sludge processes, 2008− 2009: Results of a national monitoring survey in the United States. *Environmental Science & Technology, 44*(12), 4505-4511.

Biesheuvel, & Van der Wal. (2010). Membrane capacitive deionization. *Journal of Membrane Science, 346*(2), 256-262.

Biesheuvel, Zhao, Porada, & Van der Wal. (2011). Theory of membrane capacitive deionization including the effect of the electrode pore space. *Journal of Colloid and Interface Science, 360*(1), 239-248.

Bogusch, & Grubbs. (2014). Austin Water Utility's Hornsby Bend Biogas-to-Energy CHP Project–Commissioning and startup. *Journal of The Water Pollution Control Federation, 2014*(2), 1-14.

Boudart, & Djéga-Mariadassou. (2014). *Kinetics of heterogeneous catalytic reactions*: Princeton University Press.

Bradford, Fanning, & Vannice. (1997). Kinetics of NH 3 decomposition over well dispersed Ru. *Journal of Catalysis, 172*(2), 479-484.

Bradford, & Vannice. (1999). CO2 reforming of CH4. *Catalysis Reviews—Science and Engineering, 41*(1), 1-42.

Cheddie. (2012). Ammonia as a hydrogen source for fuel cells: A review. *System, 250*(10.4), 400.

Chellappa, Fischer, & Thomson. (2002). Ammonia decomposition kinetics over Ni-Pt/Al 2 O 3 for PEM fuel cell applications. *Applied Catalysis A: General, 227*(1), 231-240.

Chen, Tang, Wang, Song, Tang, & Wu. (2015). Field-amplified sample injection in capillary electrophoresis with amperometric detection for the ultratrace analysis of diastereomeric ephedrine alkaloids. *Electrophoresis, 36*(16), 1953-1961.

Cogan. (2015). *The development of low cost autonomous chemical sensors for environmental monitoring.* Dublin City University,

Daelman, van Voorthuizen, van Dongen, Volcke, & van Loosdrecht. (2012). Methane emission during municipal wastewater treatment. *Water Research, 46*(11), 3657-3670.

Dai, Cao, Fang, Liu, Dong, Pan, & Wang. (2012). Schiff base-chitosan grafted multiwalled carbon nanotubes as a novel solid-phase extraction adsorbent for determination of heavy metal by ICP-MS. *Journal of Hazardous Materials, 219*, 103-110.

De Arespacochaga, Valderrama, Peregrina, Hornero, Bouchy, & Cortina. (2015). On-site cogeneration with sewage biogas via high-temperature fuel cells: Benchmarking against other options based on industrial-scale data. *Fuel Processing Technology, 138*, 654-662.

Dekker, & Rietveld. (2006). Highly efficient conversion of ammonia in electricity by solid oxide fuel cells. *Journal of Composites, Technology and Research, 3*(4), 499-502.

Dincer, Colpan, Kizilkan, & Ezan. (2015). *Progress in clean energy*: Springer.

Dong, Chen, Chen, & Shao. (2014). Surprisingly high activity for oxygen reduction reaction of selected oxides lacking long oxygen-ion diffusion paths at intermediate temperatures: A case study of cobalt-free BaFeO3-δ. *ACS Applied Materials & Interfaces, 6*(14), 11180-11189.

Fenu, Roels, Wambecq, De Gussem, Thoeye, De Gueldre, & Van De Steene. (2010). Energy audit of a full scale MBR system. *Desalination, 262*(1), 121-128.

Foo, & Hameed. (2009). An overview of landfill leachate treatment via activated carbon adsorption process. *Journal of Hazardous Materials, 171*(1), 54-60.

Fuerte, Valenzuela, Escudero, & Daza. (2009). Ammonia as efficient fuel for SOFC. *Journal of Power Sources, 192*(1), 170-174.

Griffiths. (1999). *Introduction to electrodynamics* (Vol. 3): Prentice Hall Upper Saddle River, NJ.

Hajimolana, Hussain, & Wan Daud. (2011). Comparativestudy on the performance of a tubular solid oxide fuel cell fuelled by ammonia and hydrogen. *Chemeca 2011: Engineering a Better World: Sydney Hilton Hotel, NSW, Australia, 18-21 September 2011*, 2021.

Hall, Barnard, & Moss. (2013). *Biomass for energy in the developing countries: current role, potential, problems, prospects*: Elsevier.

Henze, van Loosdrecht, Ekama, & Brdjanovic. (2008). *Biological wastewater treatment: Principles, modelling and design*: IWA publishing.

Ippersiel, Mondor, Lamarche, Tremblay, Dubreuil, & Masse. (2012). Nitrogen potential recovery and concentration of ammonia from swine manure using electrodialysis coupled with air stripping. *Journal of Environmental Management, 95*, S165-S169.

Iyer, Norcio, Kugler, & Dadyburjor. (2003). Kinetic modeling for methane reforming with carbon dioxide over a mixed-metal carbide catalyst. *Industrial and Engineering Chemistry Research, 42*(12), 2712-2721.

Jain, Powell, Smith, Townsend, & Tolaymat. (2014). Life-cycle inventory and impact evaluation of mining municipal solid waste landfills. *Environmental Science & Technology, 48*(5), 2920-2927.

Karthikeyan, & Visvanathan. (2013). Bio-energy recovery from high-solid organic substrates by dry anaerobic bio-conversion processes: A review. *Reviews in Environmental Science and Bio/Technology, 12*(3), 257-284.

Kim, Kim, Ye, Lee, Shin, McCarty, & Bae. (2010). Anaerobic fluidized bed membrane bioreactor for wastewater treatment. *Environmental Science & Technology, 45*(2), 576-581.

Klerke, Christensen, Nørskov, & Vegge. (2008). Ammonia for hydrogen storage: challenges and opportunities. *Journal of Materials Chemistry*, 18(20), 2304-2310.

Kordesch, Gsellmann, Cifrain, Voss, Hacker, Aronson, . . . Daniel-Ivad. (1999). Intermittent use of a low-cost alkaline fuel cell-hybrid system for electric vehicles. *Journal of Power Sources, 80*(1), 190-197.

Krishnan, Jayaweera, Bao, Perez, Lau, Hornbostel, . . . Gupta. (2007). *Effect of coal contaminants on solid oxide fuel system performance and service life*. Retrieved from

Kuhn, & Napporn. (2010). Single-chamber solid oxide fuel cell technology—From its origins to today's state of the art. *Energy, 3*(1), 57-134.

Lan, Tao, & Irvine. (2010). A direct urea fuel cell: Power from fertiliser and waste. *Energy & Environmental Science, 3*(4), 438-441.

Lantz. (2012). The economic performance of combined heat and power from biogas produced from manure in Sweden: A comparison of different CHP technologies. *Applied Energy, 98*, 502-511.

Ma, Ma, Zhou, Yan, Gao, & Meng. (2007). A high-performance ammonia-fueled SOFC based on a YSZ thin-film electrolyte. *Journal of Power Sources, 164*(1), 86-89.

McKendry. (2002). Energy production from biomass (Part 2): Conversion technologies. *Bioresource Technology, 83*(1), 47-54.

Mehanna, Kiely, Call, & Logan. (2010). Microbial electrodialysis cell for simultaneous water desalination and hydrogen gas production. *Environmental Science & Technology, 44*(24), 9578-9583.

Mirzababaei, & Chuang. (2014). La0. 6Sr0. 4Co0. 2Fe0. 8O3 Perovskite: A stable anode catalyst for direct methane solid oxide fuel cells. *Catalysts, 4*(2), 146-161.

Nagaoka, Eboshi, Takeishi, Tasaki, Honda, Imamura, & Sato. (2017). Carbon-free H 2 production from ammonia triggered at room temperature with an acidic RuO 2/γ-Al 2 O 3 catalyst. *Science Advances, 3*(4), e1602747.

Raboni, Torretta, Viotti, & Urbini. (2013). Experimental plant for the physical-chemical treatment of groundwater polluted by municipal solid waste (MSW) leachate, with ammonia recovery. *Revista Ambiente & Água, 8*(3), 22-32.

Ramió-Pujol, Ganigué, Bañeras, & Colprim. (2015). Incubation at 25 Celsius prevents acid crash and enhances alcohol production in Clostridium carboxidivorans P7. *Bioresource Technology, 192*, 296-303.

Safoniuk. (2004). Wastewater engineering: Treatment and reuse. *Chemical Engineering Journal, 111*(7), 10-12.

Salis, & Ninham. (2014). Models and mechanisms of Hofmeister effects in electrolyte solutions, and colloid and protein systems revisited. *Chemical Society Reviews, 43*(21), 7358-7377.

Schartela, Brauna, Schwarzb, & Reinemannc. (2003). Fire retardancy of polypropylene/flax blends. *Polymer, 44*(20), 6241-6250.

Schmidt, Bakale, Khrapak, & Yoshino. (2011). *Drift velocity of ions and electrons in non-polar dielectric liquids at high electric field strengths.* Paper presented at the Dielectric Liquids (ICDL), 2011 IEEE International Conference on.

Shustorovich, & Bell. (1991). Synthesis and decomposition of ammonia on transition metal surfaces: bond-order-conservation-Morse-potential analysis. *Surface Science, 259*(3), L791-L796.

Siavashi, Saidi, & Rahimpour. (2014). Purge gas recovery of ammonia synthesis plant by integrated configuration of catalytic hydrogen-permselective membrane reactor and solid oxide fuel cell as a novel technology. *Journal of Power Sources, 267*, 104-116.

Simith, Stadler, Cao, Love, Raskin, & Skerlos. (2014). Navigating wastewater energy recovery strategies: A life cycle comparison of anaerobic membrane bioreactor and conventional treatment systems with anaerobic digestion. *Environmental Science & Technology, 48*(10), 5972-5981.

Simons, Cairns, & Surd. (1969). The performance of direct ammonia fuel cells. *Journal of The Electrochemical Society, 116*(5), 556-561.

Sommer, Christensen, Schmidt, & Jensen. (2013). *Animal manure recycling: treatment and management*: John Wiley & Sons.

Spinner, Vega, & Mustain. (2012). Recent progress in the electrochemical conversion and utilization of CO2. *Catalysis Science & Technology, 2*(1), 19-28. doi:10.1039/c1cy00314c

Srivastava, & Goyal. (2010). *Novel biomaterials: decontamination of toxic metals from wastewater*: Springer Science & Business Media.

Stambouli, & Traversa. (2002). Solid oxide fuel cells (SOFCs): A review of an environmentally clean and efficient source of energy. *Renewable & Sustainable Energy Reviews, 6*(5), 433-455.

Su, Shao, Lin, Wu, & Wang. (2012). Solid oxide fuel cells with both high voltage and power output by utilizing beneficial interfacial reaction. *Physical Chemistry Chemical Physics, 14*(35), 12173-12181.

Suddhasatwa. (2007). *Recent trends in fuel cell science and technology*: New York, USA, Springer press.

Tilak, & Chen. (1999). Calculation of the current efficiency of the electrolytic sodium chlorate cells. *Journal of applied electrochemistry, 29*(10), 1237-1240.

Tsukuda, Notomi, & Histatome. (2000). Application of plasma spraying to tubular-type solid oxide fuel cells production. *Journal of Thermal Spray Technology, 9*(3), 364-368.

Valdés-Pérez, & Zeigarnik. (2000). How hard is mechanism elucidation in catalysis? Combinatorial analysis of C1 chemistry. *Journal of Chemical Information and Computer Sciences, 40*(3), 833-838.

Van Dongen, Jetten, & Van Loosdrecht. (2007). *The Combined Sharon/Anammox Process-A Sustainable Method for N-removal from Sludge Water* (Vol. 6).

Venkatesh. (2013). Economic-environmental analysis of handling biogas from sewage sludge digesters in WWTPs (wastewater treatment plants) for energy recovery: Case study of Bekkelaget WWTP in Oslo (Norway). *Energy, 58*, 220-235. doi:10.1016/j.energy.2013.05.025

Vitvitskii, Gaidei, Toporkova, Kiseleva, & Melikhov. (1990). Kinetics of catalytic decomposition of ammonia. *Journal of Applied Chemistry of the USSR, 63*(9, II), 1883-1886.

Wang, Lu, & Millar. (1996). Carbon dioxide reforming of methane to produce synthesis gas over metal-supported catalysts: state of the art. *Energy & Fuels, 10*(4), 896-904.

Wang, Ran, Su, Guo, Farrusseng, & Shao. (2013). Ammonia-mediated suppression of coke formation in direct-methane solid oxide fuel cells with nickel-based anodes. *Journal of Power Sources, 240*, 232-240.

Wett. (2007). Development and implementation of a robust deammonification process. *Water Science and Technology, 56*(7), 81-88.

Wisniewska, & Winnicki. (1991). Electrodialytic desalination of effluents from zinc-coating processes: Removal of Zn 2+ and CL− ions from model solutions. *Desalination, 84*(1), 163-176.

Wongchanapai, H., Saito, & Yoshida. (2013). Performance evaluation of a direct-biogas solid oxide fuel cell-micro gas turbine (SOFC-MGT) hybrid combined heat and power (CHP) system. *Journal of Power Sources, 223*, 9-17.

Wu, & Wang. (2006). Combined cooling, heating and power: a review. *Progress in Energy and Combustion Science, 32*(5), 459-495.

Yang, Peng, Liu, Zeng, Mino, & Satoh. (2007). Nitrogen removal via nitrite from municipal wastewater at low temperatures using real-time control to optimize nitrifying communities. *Environmental Science & Technology, 41*(23), 8159-8164.

Zhang, Tsipouriari, Efstathiou, & Verykios. (1996). Reforming of methane with carbon dioxide to synthesis gas over supported rhodium catalysts: I. Effects of support and metal crystallite size on reaction activity and deactivation characteristics. *Journal of Catalysis, 158*(1), 51-63.

CHAPTER 4 CONCENTRATION POLARIZATION IN CATION EXCHANGE MEMBRANE ELECTRODEIONIZATION: EFFECT OF CATHODIC SUPPORTING ELECTROLYTE CONCENTRATION

4.1 Introduction

Electrodeionization (EDI), a process with an excellent ion separation capability, has been applied in various areas, including ammonium (NH_4^+) recovery from nitrogen-rich wastewaters(Arar *et al.*, 2014; Greenlee *et al.*, 2009; Strathmann, 2000; Tanaka, 2011; Tanaka, 2015; Xu *et al.*, 2017). The performances of EDI rely on the concentration polarization of ion exchange membrane (Tanaka, 2003, 2004). Concentration polarization, as mentioned in Chapter 2, refers to the difference in the concentration of permeable ion between the diluted and concentrated boundary layers (Aguilella *et al.*, 1991; Długołęcki, Anet, *et al.*, 2010; Spiegler, 1971; Tanaka, 2003). The phenomenon of concentration polarization is produced owing to a larger transport number of permeable ion in the ion exchange membrane than in the bulk solution. As a result, the concentration of permeable ion decreases on the diluted side but increases on the concentrated side (Law *et al.*, 1997; Spiegler, 1971). The variations of

permeable ion concentration usually cause a non-uniform distribution of the electric current around cation exchange membrane or anion exchange membrane (Choi *et al.*, 2002; Güler *et al.*, 2014; Wang *et al.*, 2012). The large potential drop leads to the concentration of permeable ion dropping to zero on the diluted side and climbing to the maximum on the concentrated side. At this moment, the corresponding current approaches LCD and does not change anymore (Krol *et al.*, 1999; Lee *et al.*, 2006). With continuous current input, the potential drop between the diluted and concentrate sides is over 1.23 V and causes water dissociation into OH^- and H^+. The produced OH^- and H^+ cannot immediately replenish the lack of electric current at the membrane interface. Therefore, water dissociation at the membrane significant soars the resistance and the energy consumption of the system.

LCD is studied mostly because it reflects the magnitude of concentration polarization such as the thickness of diffusion boundary layer, the resistance of the membrane, potential drop and so on. LCD is as functions of various parameters (e.g., applied current density, permeable ion concentration, solution flow rate, geometric structure) (Fidaleo & Moresi, 2005; Inenaga & Yoshida, 1980; Spiegler, 1971). Choi *et al*. (2001) found that supporting electrolyte of the dilute channel was one crucial factor (Choi *et al.*, 2001). Ndjomgoue-Yossa *et al*. (2015) reported that increasing ionic strength and conductivity of supporting electrolyte increased LCD (Ndjomgoue-Yossa *et al.*, 2015). Conversely, Anouti *et al*. (2012), Onsager & Kim (1957), Petrowsky & Frech (2008) and Sigvartsen *et al*. (1991). Studied the concentration dependence of ionic transport and aqueous ion liquid solutions affecting ion transport properties and found that the molar conductivity and drift velocity decrease as supporting electrolyte concentrating,

which enhanced the concentration polarization (Anouti *et al.*, 2012; Onsager & Kim, 1957; Petrowsky & Frech, 2008; Sigvartsen *et al.*, 1991). Selman & Newman (1971) investigated the supporting electrolyte concentration affecting on the thickness of the boundary layer in EDI and found that supporting ions usually extended a further distance from the ion exchange membrane and formed an extra diffusion boundary layer (Selman & Newman, 1971). These studies elaborate that in the supporting electrolyte, a greater diffusion coefficient the ion has, a thicker boundary layer is built around ion exchange membrane. Since ammonium salt is a type of weak electrolyte, the Na_2SO_4 electrolyte is used to enhance the solution conductivity as usual. The increased electric current can improve the ammonia recovery. Under the applied voltage, Na^+ and SO_4^{2-} migrate toward the anode and the cathode, respectively, as shown in Figure 4-1 (Taky *et al.*, 1992; Tedesco *et al.*, 2016). Owing to co-ion repulsion from the cation membrane, SO_4^{2-} cannot cross the cation exchange membrane but accumulates on the right-side boundary layer. This behavior leads to the increase in the boundary layer thickness (Długołęcki, Ogonowski, *et al.*, 2010; Taky *et al.*, 1992) and a small flux of permeable ion (Bhattacharya & Hwang, 1997). However, we know little of effects brought by cathodic supporting electrolyte (Na_2SO_4) presently. The objective of this chapter is to investigate the relationship between concentration polarization and the concentration of SO_4^{2-} supporting ion. Therefore, based on the Nernst-plank equation and the Donnan equilibrium, numerical simulations on the concentration distribution, LCD, boundary layer thickness, and resistance against concentration variation of cathodic electrolyte (Na_2SO_4) are carried out and followed by experimental validation.

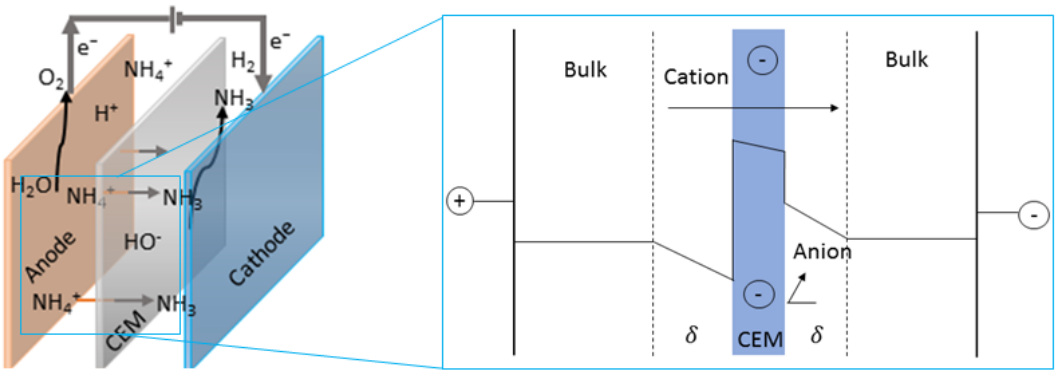

Figure 4-1 Schematic diagram of cation through ion exchange membrane.

4.2 Model development

4.2.1 Modeling mass and current distribution

1) Modeling approach of domain

In COMMSOL, the dilute, membrane and concentrate channel are set as 3 domains, referring to *domain 1*, *domain 2* and *domain 3*, respectively. The fluxes of ion in channels (*domain 1* and *domain 3*) are expressed by the Nernst-Planck equation (Eq. 4-1) (Rohman, 2008; Yang *et al.*, 2016), based on mass balance and the electroneutral condition in a 2-D model using Tertiary Current Distribution, as displayed in Figure 4-2.

$$J_i = -D_i \frac{\partial c_i}{\partial x} - \frac{z_i F}{RT} D_i c_i \frac{\partial \varphi}{\partial x} + c_i v \tag{4-1}$$

where c_i is the ion concentration of species i and J_i is the ion flux. The right side represents the concentration diffusion, electrical migration, and convection, respectively. D_i, and z_i are the ion diffusion coefficient, ion charge, and the flow rate, respectively. F, R, T, and ϕ are the Faraday constant, the universal gas constant, the absolute temperature and the electrical potential, respectively. To simplified the calculations, we do not consider the convection process, Eq. 1 is simplified to Eq. 4-2:

$$J_i = -D_i \frac{\partial c_i}{\partial x} - \frac{z_i F}{RT} D_i c_i \frac{\partial \varphi}{\partial x} \tag{4-2}$$

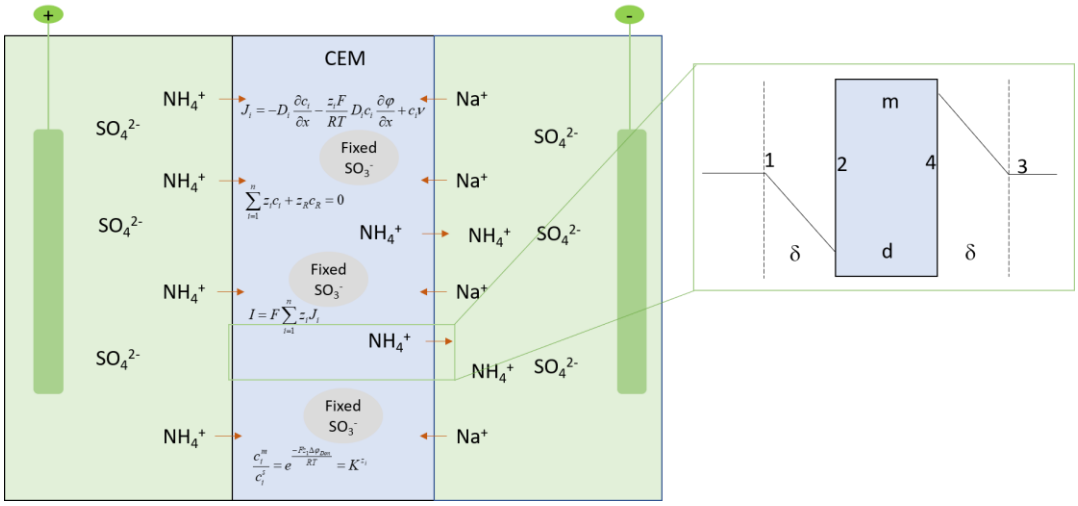

Figure 4-2 Schematic diagram of cation through ion exchange membrane.

For $(NH_4)_2SO_4$ || Na_2SO_4, Na^+, NH_4^+ and SO_{4a}^{2-} and SO_{4c}^{2-} can be marked by type 1, 2, 3 and 4, respectively. So the relationships of concentration for type 1, type2, type 3 and type 4 are expressed by Eq. 4-3 and Eq. 4-4.

$$c_1 = 2c_2 \tag{4-3}$$

$$c_1 = 2c_2 \tag{4-4}$$

The relationship of the dilute and concentrate concentration channels is set as c_2=c_4, so the ion fluxes and current are rewritten to Eq. 4-5 to Eq. 4-7.

$$J_1 = \frac{D_1}{D_1 + 2D_2 + D_3 + 2D_4}\frac{I}{F} - \frac{2D_1(D_2 - D_1 + D_4 - D_3)}{D_1 + 2D_2 + D_3 + 2D_4}\frac{\partial c_2}{\partial x} \tag{4-5}$$

$$I = z_1J_1 + z_2J_2 + z_3J_3 + z_4J_4 = F\left[J_1 + J_3 - 2(J_2 + J_4)\right] \tag{4-6}$$

$$J_1 + J_3 = \frac{IT_c}{F} \tag{4-7}$$

where I and t_c refers to current density and the transport number of cation.

Substituting Eq. 4-5 and Eq. 4-6 into Eq. 4-7 gives the below equation of typ 1 (Eq. 4-8).

$$J_1 = \frac{It_c}{2F} \tag{4-8}$$

Combining Eq. 4-5, Eq. 4-6 and Eq. 4-8 gives Eq. 4-9.

$$\frac{\partial c_2}{\partial x} = \frac{(D_1 + D_3) - T_c(D_1 + 2D_2 + D_3 + 2D_4)}{2(D_1 + D_3)(D_2 - D_1 + D_4 - D_3)} \frac{I}{F} \tag{4-9}$$

Ion transport in the membrane (Position m) is similar with that transport in the channels (Dai *et al.*, 2012). The flux of J_i^m is expressed by Eq. 4-10.

$$J_i^m = -D_i^m \left(\frac{\partial c_i^m}{\partial x} + \frac{z_i c_i^m F}{RT} \frac{\partial \varphi'}{\partial x} \right) \tag{4-10}$$

The total flux of cation in the CEM is expressed by Eq. 4-11 and Eq. 4-12.

$$J_1^m + J_3^m = \frac{I t_{cm}}{F} \tag{4-11}$$

$$J_2^m + J_4^m = \frac{i(1 - t_{cm})}{2F} \tag{4-12}$$

where t_{cm} is the transport number of cation in the CEM.

The concentration relationship of cations and anions is written by Eq. 4-13.

$$c_1^m + c_3^m - 2(c_2^m + c_4^m) - c_R = 0 \tag{4-13}$$

where c_R refers to the concentration of counter ion in the CEM.

2) Modeling approach of boundaries

At the DBL (δ_1), the concentration linearly dependent on the thickness of layers, the concentrations of type 1 and type 2 can be expressed as Eq.4-14 and Eq. 4-15.

$$c_2\big|_{x=\delta_1} = c_0 + \frac{(D_1 + D_3) - T_c(D_1 + 2D_2 + D_3 + 2D_4)}{2(D_1 + D_3)(D_2 - D_1 + D_4 - D_3)} \frac{I\delta_1}{F} \tag{4-14}$$

$$c_1\big|_{x=\delta_1} = 2c_0 + \frac{(D_1+D_3)-T_c(D_1+2D_2+D_3+2D_4)}{(D_1+D_3)(D_2-D_1+D_4-D_3)}\frac{I\delta_1}{F} \tag{4-15}$$

The potential at the bulk-diffusion interface and the potential linearly varies with the thickness of the layer, so that the potential can be written as Eq. 4-16 and Eq. 4-17.

$$\varphi\big|_{x=0} = \frac{d\varphi_0}{d\delta_0} \tag{4-16}$$

$$\varphi\big|_{x=\delta_1} = \varphi\big|_{x=1} + \frac{D_2-D_1+D_4-D_3}{D_1+2D_2+D_3+2D_4}\frac{RT}{F}\cdot\frac{(D_1+D_3)-T_c(D_1+2D_2+D_3+2D_4)}{2(D_1+D_3)(D_2-D_1+D_4-D_3)}\frac{I}{F} - \frac{IRT}{2F^2c_2(D_1+2D_2+D_3+2D_4)} \tag{4-17}$$

Moreover, the membrane potential is written by Eq. 4-18 (Moshtarikhah *et al.*, 2017).

$$\varphi_m = \varphi_{sol} + \varphi_{Don} = \varphi_{sol} + \frac{RT}{z_{i+}F}\ln\frac{c_{i+,m}}{c_{i+,dil}} \tag{4-18}$$

where $c_{i+,m}$ and $c_{i+,dil}$ are the concentration of cation species *i* in the membrane and the solution, respectively.

In the ion exchange membrane (*domain 2*), all the counter ions are fixed in a matrix. Namely, the concentration of permeable ion does not change. The current density can be expressed through electrolyte conductivity by Eq. 4-19 (Zourmand *et al.*, 2015).

$$I = -\sigma_m \Delta\varphi_m \tag{4-19}$$

where σ_m is the conductivity of the CEM.

At steady state, the mass transport is expressed by Eq. 4-20 to Eq. 4-23 through Donnan equilibrium (Moshtarikhah *et al.*, 2017).

$$\frac{c_i^m}{c_i^s} = e^{\frac{-Fz_1\Delta\varphi_{Don}}{RT}} = K^{z_i} \tag{4-20}$$

where K is the constant of Donnan equilibrium.

The concentrations of type 1 and type 2 at position 1 and position 2 are written by Eq. 4-21 to Eq. 4-23, respectively.

$$\frac{c_1^1\big|_{x=\delta_1}}{c_1^1\big|_{x=\delta_1}} = \left(\frac{c_2^1\big|_{x=\delta_1}}{c_2^1\big|_{x=\delta_1}}\right)^{\frac{1}{2}} \tag{4-21}$$

$$\frac{c_1^2\big|_{x=\delta_1+d}}{c_1^1\big|_{x=\delta_1+d}} = \left(\frac{c_2^2\big|_{x=\delta_1+d}}{c_2^1\big|_{x=\delta_1+d}}\right)^{\frac{1}{2}} \tag{4-22}$$

$$c_1^1 = 2c_2^1 \tag{4-23}$$

The ions (type 3 and type 4) in the concentrated interface have the same behavior with type 1 and type 2. Their concentrations in the CEM can be calculated by Eq. 4-24 to Eq. 4-31, respectively.

$$\sum z_i c_i + \varepsilon c_R = 0 \tag{4-24}$$

$$-\frac{1}{2}c_R + c_1^2 - c_2^2 = 0 \tag{4-25}$$

$$-\frac{1}{2}c_R + c_3^4 - c_4^4 = 0 \tag{4-26}$$

$$\frac{c_1^2 = \left(c_1^1\right)^2 - 4c \pm \sqrt{\left(2cc_R - c_1^1\right)^2 - 16\left(c_2^1 * \frac{1}{2}c_R\right)^2}}{4c_2^1 + \frac{1}{2}c_R} \tag{4-27}$$

$$\frac{c_2^2 = \left(c_1^1\right)^2 - 4c \pm \sqrt{\left(2cc_R - c_1^1\right)^2 - 16\left(c_2^1 * \frac{1}{2}c_R\right)^2}}{8c_2^1} \tag{4-28}$$

$$\frac{c_3^4 = \left(c_3^3\right)^2 - 4c \pm \sqrt{\left(2cc_R - c_3^3\right)^2 - 16\left(c_4^3 \frac{1}{2}c_R\right)^2}}{4c_4^3 + \frac{1}{2}c_R} \tag{4-29}$$

$$\frac{c_4^4 = \left(c_3^3\right)^2 - 4c \pm \sqrt{\left(2cc_R - c_3^3\right)^2 - 16\left(c_4^3 * \frac{1}{2}c_R\right)^2}}{8c_4^3} \tag{4-30}$$

$$\begin{aligned} c_1^2 &= c_0 + \frac{1}{2}c_R - 1 + \frac{i\delta_1}{F}\frac{D_1 + D_3 - T_c(D_1 + D_3 + 2(D_4 + D_4)}{2(D_1 + D_3)(D_2 - D_1 + D_4 - D_3)} \\ &\pm \sqrt{\left[c_0 + \frac{i\delta_1}{F}\frac{D_1 + D_3 - T_c(D_1 + D_3 + 2(D_4 + D_4)}{2(D_1 + D_3)(D_2 - D_1 + D_4 - D_3)}\right] \cdot \left[c_0 - 4c_R + \frac{i\delta_1}{F}\frac{D_1 + D_3 - T_c(D_1 + D_3 + 2(D_4 + D_4)}{2(D_1 + D_3)(D_2 - D_1 + D_4 - D_3)}\right]} \end{aligned} \tag{4-31}$$

Under these conditions, the fluxes of type 1 and type 2 in the right-side boundary are equal that in the left-side boundary. So, the concentrations of type 1 at position 2 and position 4, as written in Eq. 4-32.

$$c_1^4 = c_1^3 + \frac{(D_1 + D_3) - T_c(D_1 + 2D_2 + D_3 + 2D_4)}{2(D_1 + D_3)(D_2 - D_1 + D_4 - D_3)} \frac{i\delta_1}{F} \tag{4-32}$$

3) Solver

The simulations of mass and potential distribution were completed through COMSOL Multiphysics 5.2a. When solving for the electrolyte potential, *domain 1* and *domain 3* use Tertiary Current Distribution, and *domain 2* uses Second Current Distribution. These two parts are combined using a linear extrusion operator. A two-dimensional EDI divided into two channels (the dilute channel and the concentrate channel) by a cation exchange membrane (CEM) was configured, as depicted in Figure 4-3. The visible operation window is shown in Figure 4-4. The dilute channel was inflowed $(NH_4)_2SO_4$ with 0.25 M fixed concentration and the concentrate channel was inflowed Na_2SO_4 with 0.125-0.75 M varied concentration. In these equations, electrochemical reaction and water transport through the membranes were neglected for the sake of model simplification. The parameters used to calculate the distribution of NH_4^+ concentration in the boundary layer are available in these references (Dai *et al.*, 2012; Długołęcki *et al.*, 2008; Li & Gregory, 1974). The dependent parameters can be obtained from Appendix I. The diffusion coefficient of each ion was not changed at various positions. The simulations of mass transport in CEM were simulated through MATLAB R2016b that uses one-dimensional space to obtain the solution at the steady state.

4.2.2 Electric resistance analysis

For EDI, the total resistance $\Re_{tot}$ equals the sum of the resistance of the solution ($\Re_{sol}$), the resistance of the membrane ($\Re_{mem}$), the resistance of the diffusion layer ($\Re_{DBL}$), the resistance of the Donnan interfacial layer ($\Re_{don}$), and the resistance of the electrode ($\Re_{el}$) (Dai *et al.*, 2012) (Eq. 4-33).

$$\Re_{tot} = \Re_{sol} + \Re_{diff} + \Re_{don} + \Re_{el} \tag{4-33}$$

The perturbation frequency ranges are usually divided into three regions (high, medium-, and low-frequency ranges). Each region reflects its corresponding resistance. In high-frequency ranges, the total impedance of the membrane system is expressed as Eq. 4-34 (Bason *et al.*, 2007; Freger & Bason, 2007).

$$Z_{tot}(\omega) = \Re_{mem} + \Re_{sol} \tag{4-34}$$

In low-frequency ranges, the total resistance is expressed as Eq. 4-35.

$$\begin{aligned} Z_{tot}(\varpi) = (\Re_{mem} + \Re_{sol} + \frac{\Re_{don}}{1+\varpi^2 c_{don}^2 \Re_{don}^2} + \frac{\Re_{dif}}{1+\varpi^2 c_{dif}^2 \Re_{dif}^2}) \\ -(\frac{c_{don}\Re_{don}^2}{1+\varpi^2 c_{don}^2 \Re_{don}^2} + \frac{c_{dif}\Re_{dif}^2}{1+\varpi^2 c_{dif}^2 \Re_{dif}^2})\varpi j \end{aligned} \tag{4-35}$$

$\Re_{el}$ and $\Re_{don}$, are negligible so that Eq. 4-35 is simplified to Eq. 4-36.

$$Z_{tot}(\varpi) = (\Re_{mem} + \Re_{sol} + \frac{\Re_{dif}}{1+\varpi^2 c_{dif}^2 \Re_{dif}^2}) - (\frac{c_{dif}\Re_{dif}^2}{1+\varpi^2 c_{dif}^2 \Re_{dif}^2})\varpi j \tag{4-36}$$

where j = √-1,

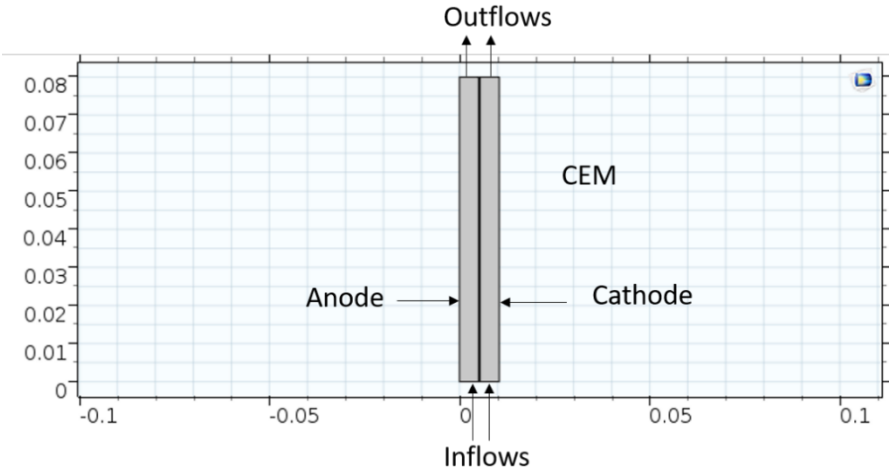

Figure 4-3 Geometric graph of 2D EDI model.

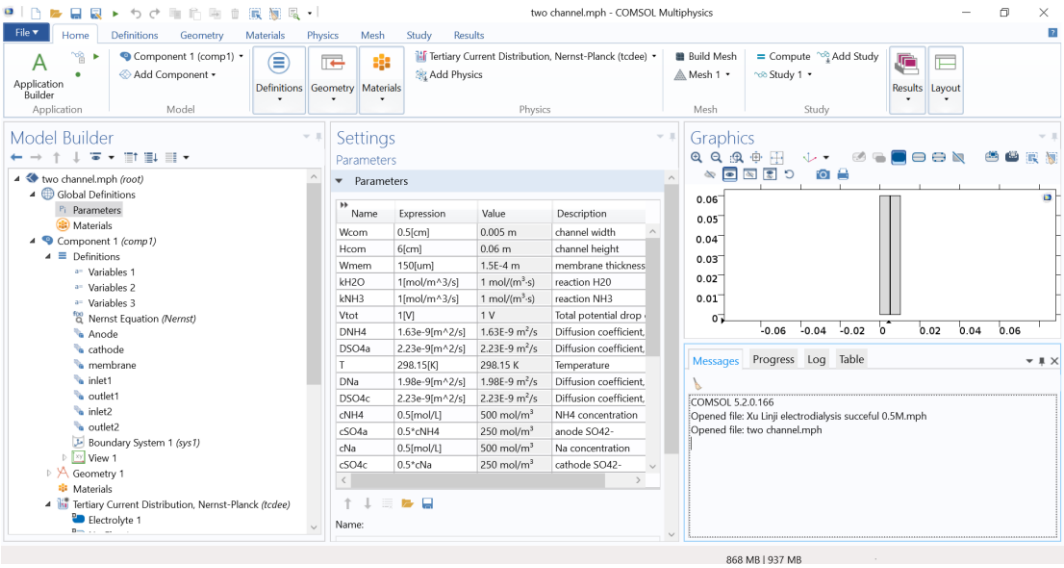

Figure 4-4 COMSOL 5.2 operation window.

4.3 Experimental measurements

4.4.1 Electrodeionization setup

The EDI cell structure and the electrode material were the same as that mentioned in Chapter 3. The anodic channel was fixed at 0.25 M $(NH_4)_2SO_4$, and the cathodic channel was fed with Na_2SO_4 (0.125 M to 0.75 M). DC power source (3.0 V DC; PS-305DM, Hong Kong Longwei instrumentation Co., Ltd.) was applied to the EDI cell. All tests were conducted at around 25.2 °C and 1 atm.

4.4.1 Current-voltage measurement

The current-voltage curve was measured based on the method devised by (Choi *et al.*, 2002). The EDI was divided into two compartments (20 cm^3) by a cation exchange membrane. The anolyte, $(NH_4)_2SO_4$, was fixed at 0.25 M, and the concentration of the catholyte, Na_2SO_4, was increased from 0.125 M to 1.5 M. Both were fed into the respective channels at a flow rate of 1.0 mL min^{-1}. The DC power source was applied between the two Ag/AgCl electrodes. Stepwise current supply was added to the EDI at a scanning rate of 30 mA min^{-1} through the electrochemical working station (CorrWare®, Scribner Associates Inc., USA). The electrodes were connected to a Keithley 2700 multimeter (Tektronix, Inc., USA). The potential drops of the two sides of the membrane were recorded and stored every 30 s.

4.4.1 Electrochemical impedance spectroscopy measurements

EIS was measured according to the method developed in Fu's report (Fu *et al.*, 2004). The membrane was equilibrated for 24 h with the solution before each set of

measurements, based on the method used in this reference (Wang *et al.*, 2012). The impedances were recorded with frequencies ranging from 50 to 15,000 kHz. Each experimental point was taken as the average of three acquired points to minimize noise effects. The parameters that were used to calculate the distribution of NH_4^+ concentration in the boundary layer were available in these references (Długołęcki *et al.*, 2008; Li & Gregory, 1974; Wang *et al.*, 2012).

4.4 Results and discussion

4.4.1 Model validation

At the steady state, the transported NH_4^+ through the CEM was calculated by Eq. 4-20. The experiment trials were carried out to verify the simulated results. Figure 4-5 shows the theoretical and experimental results of EDI under the conditions of 0.25 M $(NH_4)_2SO_4$, 0.125-1.5 M of Na_2SO_4 supporting electrolyte, and 3.0 V applied voltage. Below 0.75 M, theoretical and experimental results of the removal efficiency match well. However, with the concentration of Na_2SO_4 escalating, the difference in removal efficiency between theoretical and experimental results become significant, which is thought to be impacted by many factors, such as the characteristics of supporting electrolyte (the hydraulic viscosity, solubility, and conductivity), concentration polarization and co-ion repulse. Therefore, the concentration range of 0.125-0.75 M Na_2SO_4 electrolyte was used for simulations of mass transport and potential distribution.

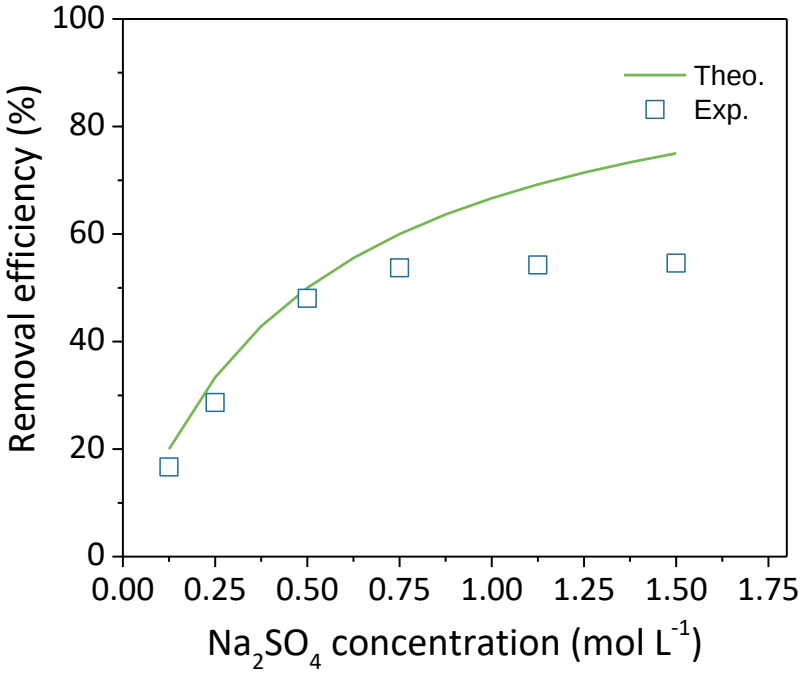

Figure 4-5 The removal efficiency of NH_4^+ for theoretical and experimental for 0.125-1.5 mol L^{-1} Na_2SO_4 electrolyte.

4.4.2 Mass transport

Concentration diffusion and electrical migration are two principle forces that generate the concentration difference, as described by the Nernst-plank equation and the Einstein equation (Sistat & Pourcelly, 1997). Fig. 4-6(a) shows the concentration profiles of NH_4^+ and Na^+ (cut line 2D) at the position with point 1 (x=0, y=0) and point 2 (x=0, y=H/2). The dilute-side of Fig. 4-6(b) displays the variation of NH_4^+ ion concentration at the stationary stage. Under the conditions of 0.125 M to 0.75 M Na_2SO_4 electrolyte, NH_4^+ ion concentration decreases from 500 mol m^{-3} in the channel to around 320 mol m^{-3} at the interface of the DBL and the CEM. The zoom-up window illustrates indifference lines of NH_4^+ ion concentration, which are 331.01 mol m^{-3}, 328.33 mol m^{-3}, 326.64 mol m^{-3}, and 325.41 mol m^{-3}, respectively. The right side shows the changes of Na^+ ion profile along with x-axis under the same concentrations. On the contrary, the concentration of Na^+ at the concentrated side of the CEM and the DBL is significantly changed by the increased concentration of supporting electrolyte, which are 236.49 mol m^{-3}, 398.42 mol m^{-3}, 722.31 mol m^{-3}, 971.78 mol m^{-3}, respectively. Fig. 3(b) illustrates the concentrations of NH_4^+ and Na^+ in the CEM under the concentrations of 0.125-0.75 M Na_2SO_4 based on Donnan equilibrium. Specifically, the concentration of NH_4^+ ion decreases from 787.03 mol m^{-3} at 0.125 M Na_2SO_4 electrolyte to 317.16 mol m^{-3} at 0.75 M Na_2SO_4 electrolyte. However, the concentration of Na^+ experiences an apparent increase from 212.97 mol m^{-3} to 682.84 mol m^{-3} under the same concentration of supporting electrolyte. The comparison of concentration profiles in the DBL and the CEM between NH_4^+ and Na^+ reveals that the concentration of supporting electrolyte dominantly influences on NH_4^+ transport in

the CEM instead of the DBL. These results account for the unremarkable improvement of ion removal through the concentration of supporting electrolyte increases.

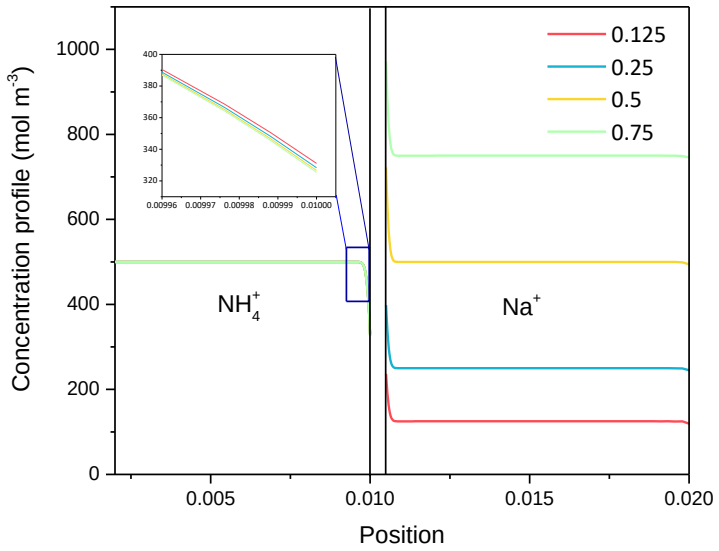

(a)

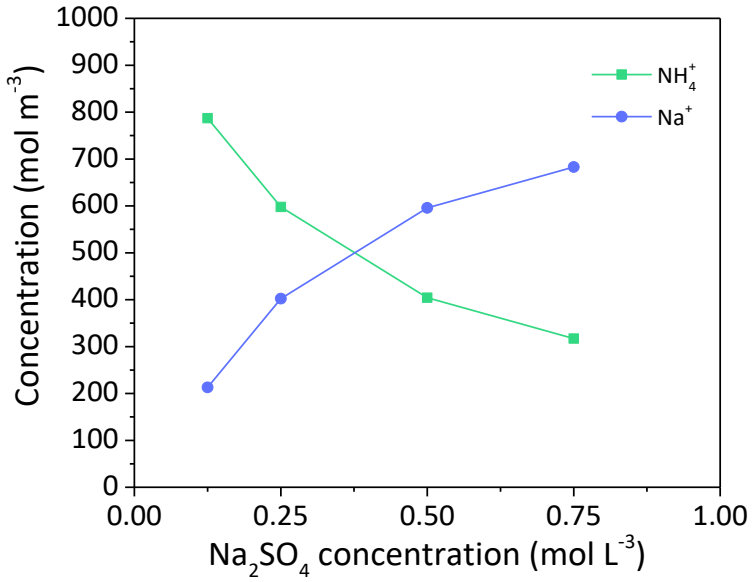

(b)

Figure 4-6 NH_4^+ and Na^+ concentration profile in the boundary layer (a) and in CEM (b) at 0.125-0.75 M Na_2SO_4.

4.4.3 Potential distribution

The cell potential drop of EDI is displayed in Figure 4-7. The electrolyte potential linearly decreases to around 0.5 V at the interface and continuously declines to 0.08V in CEM, which demonstrates that the CEM leads to a great part of potential losses. However, the potential returns 0.5 V at 0.75 M and 1.5 V at 0.125 M at the interface of the Na^+ DBL and the CME, which is because of the increase in Na^+ concentration in the CEM. Interestingly, the potential experiences a reverse variation with the concentration of Na_2SO_4 electrolyte increasing, resulting from the decline in the concentration ratio of the cations in the CEM and the DBL. As a result, the cell potential drops through the CEM at 0.125-0.75 M are -1.006 V, -0.503 V, -0.252 V, and -0.101 V respectively. φ_{don}, the different between φ_m and φ_{sol}, are -0.68 V, -0.178 V, 0.0724 V, 0.223 V, respectively. From these results, the ratios of cations in the CEM ($c_{i,m}$) and in the DBL ($c_{i,dil}$) is less than one when the concentration of Na_2SO_4 electrolyte is below than 0.25 M. This is due to the scarcity of cation in the CEM, leading to concentration polarization. In words, cation should be supplied through other paths such as water dissociation and concentration diffusion. When the concentration of Na_2SO_4 electrolyte is over 0.25 M, the Donnan potential becomes positive, which means $c_{i,m}$ is larger than $c_{i,dil}$. As aforementioned, the increase in cation mainly refers to Na^+. Namely, Na^+ transporting into the CEM can provide sufficient cation to resisting the occurrence of concentration polarization. Herein, the variations of Donnan potential disclose that increasing the concentration of supporting electrolyte can relieve concentration polarization. As we take increasing NH_4^+ transport and

alleviating concentration polarization into consideration, the concentration of Na_2SO_4 electrolyte should be control within 0.5 M.

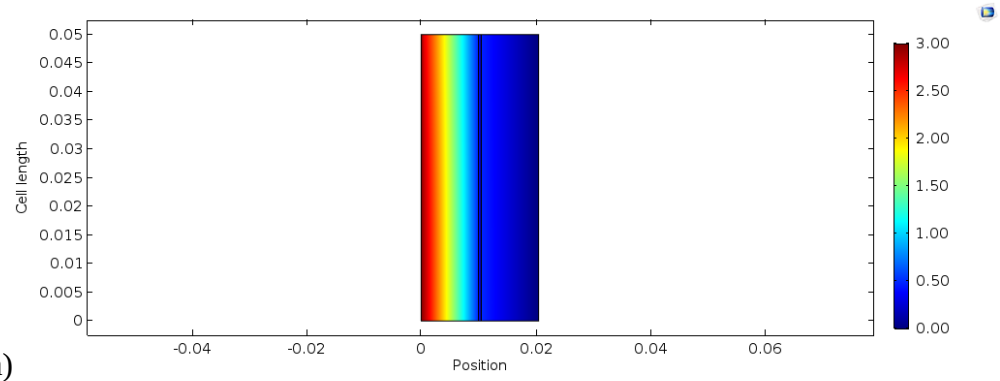

(a)

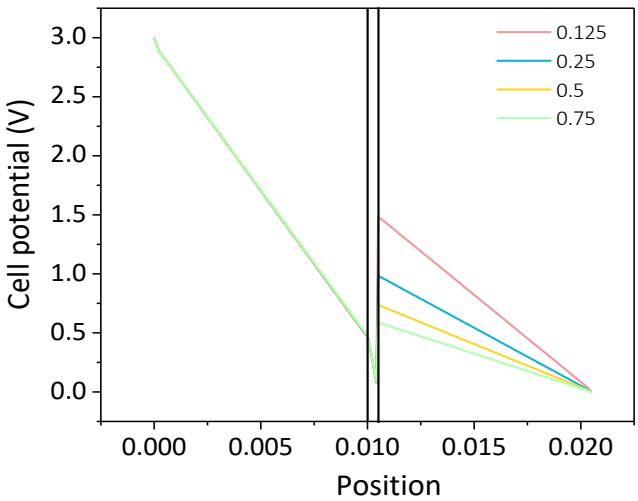

(b)

Figure 4-7 Potential profile of EDI at 0.125 M to 0.75 M Na_2SO_4: (a) snapshot image of the electrolyte potential drop (0.5 M); (b) 1D cut-off surface of potential profile across the membrane.

4.4.4 Electric resistance analysis

Boundary layer formation results in the variation of electric resistance. The resistance distribution across the individual section was analyzed by EIS at 0.125-0.75 M Na_2SO_4 electrolyte. Each spectroscopic image has three different regions located in the respectively high-, middle-, and low-frequency ranges and each region reflects the corresponding resistance of the solution, the membrane, the boundary layer, and even water dissociation, as illustrated in Figure 4-8 (a). The division of Figure 4-8 (a) shows the different part of the resistance. The total resistance decreases from 50 Ω to the minimum value of 34 Ω when the Na_2SO_4 concentration increases from 0.125 M to 0.75 M. In the high-frequency range, the ohmic resistance of electrolyte decreases from 22 Ω at 0.125 M to 10 Ω at 0.75 M, as shown in Figure 4-8(b). This trend signifies that the increasing ionic strength reduces the ohmic resistance. In the low-frequency range, a notable fluctuation is observed, which may be related to water dissociation and ion scarcity. Particularly, a distinct increase in the resistance with concentrated Na_2SO_4 (> 0.5 M) is observed. The phenomenon is caused by the scarcity of ion in DBL, signifying that concentration polarization much easier occurs in the concentrated solution than the dilute solution. This finding is critical to the large-scale application of EDI for the concentrated channel will result in serious concentration polarization. Once this happens, the operation of EDI will lead to great energy consumption and poor capability of desalination. Therefore, the concentration of the supporting electrolyte must be regularly alternated depending on the concentration gradient of the electrolyte. The proportion of the resistances between the boundary layers and the bulk solution is only around 0.4 with the Na_2SO_4 concentration in the range of 0.125 to 0.5

M, indicating that the solution conductivity of the dilute supporting electrolyte determines the resistance of the EDI stack. However, the proportion is beyond 0.5 for high concentration 0.75 M, implying that the total resistance is not determined by the dilute bulk solution but by DBL.

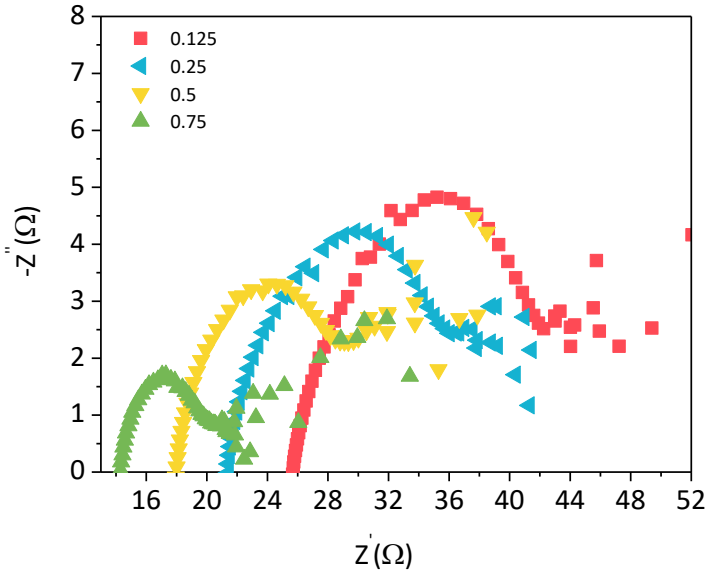
0.125
0.25
0.5
0.75
-Z''(Ω)
Z'(Ω)
0
1
2
3
4
5
6
7
8
16
20
24
28
32
36
40
44
48
52

(a)

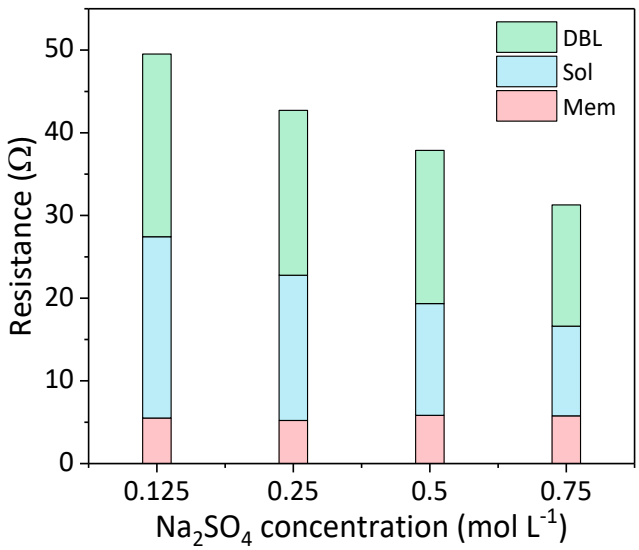
DBL
Sol
Mem
Resistance (Ω)
0
10
20
30
40
50
0.125
0.25
0.5
0.75
Na2SO4 concentration (mol L-1)

(b)

Figure 4-8 Electrical resistance distribution at 0.125 M to 0.75 M Na_2SO_4 supporting electrolyte: (a) electrochemical impedance spectroscopies; (b) electrical resistance composition.

4.4.5 Diffusion boundary layer thickness

In EDI, the regions around the cation exchange membrane are defined as the dilute and concentration diffusion boundary layers, in which the thickness of the Donnan layer is usually neglected (Dai *et al.*, 2012). The concentrate DBL is assumed consisting of Na^+ diffusion layer and SO_4^{2-} migration layer. Due to overlapping, SO_4^{2-} migration layer is thought to be the same Na^+ diffusion layer. The boundary layer thickness is calculated through LCD. Figure 4-9 illustrates that the LCD increases from 14 to 20 mA cm^{-2} in the range of 0.125 to 0.75 M Na_2SO_4, indicating the boundary layer has a different thickness. With the voltage continuously elevating, the current density rises to a high value of 45 mA cm^{-2} in the third area, defined as the over limiting current density (Rubinstein & Shtilman, 1979). Under the over LCD, water dissociation occurs, which has adverse effects on the performance of the membrane, such as high resistance and poor permeability (Tanaka, 2002). In theory, the limiting current density (I_{lim}) is evaluated by Eq. 16.

$$I_{\lim} = \frac{cDzF}{\delta(t_m - t_s)} \qquad (4\text{-}37)$$

where t_m and t_s are the transport numbers in the membrane and the solution, respectively.

Based on the measured LCD, the thickness of the boundary layer is calculated and summarized in Table 1. The experimental thickness formed by NH_4^+ ion drops from 320 μm at 0.125 M Na_2SO_4 to 285 μm at 0.75 M Na_2SO_4. The theoretical thickness of the DBL is predicted by the concentration distribution. It decreases from 295 μm at 0.125 M to 224 μm at 0.75 M, as listed in Table 1. However, the concentrate Na^+ DBL increases from 54.34 μm to 181.44 μm with Na_2SO_4 electrolyte concentrating. The trend of the DBL thickness is consistent with the changes of electric resistant and the magnitude of concentration polarization for the dilute range, demonstrating that the thickness of the dilute DBL can be reduced through increasing the concentration of supporting electrolyte. It is noteworthy that the experimental thickness is therefore obviously greater than the simulated thickness. This difference between the experimental thickness and simulated thickness is because the experimental current includes all processes caused by bubble formation, such as ion migration, water dissociation, and ionic convection, whereas the theoretical simulation only focuses ion migration and diffusion.

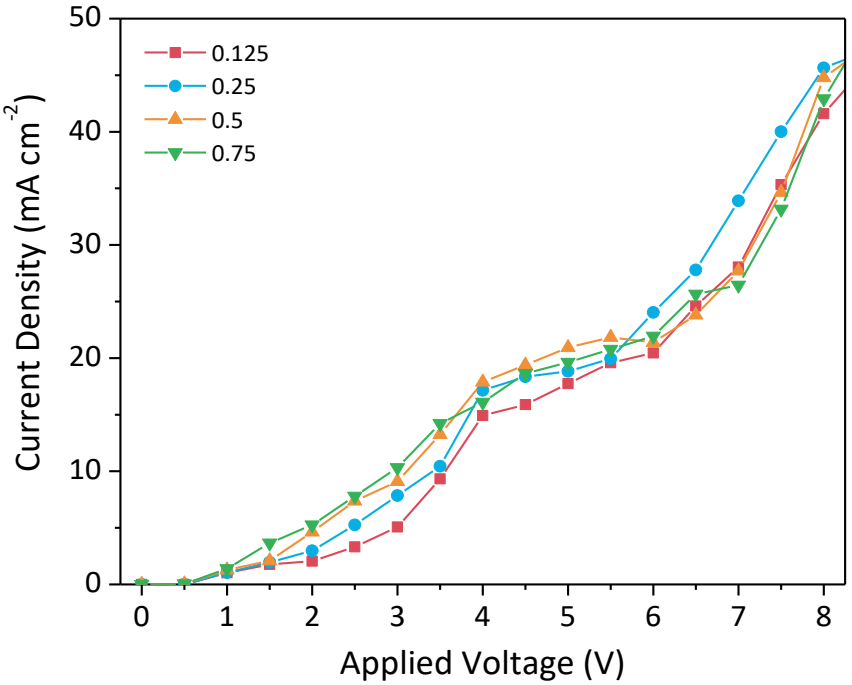

Figure 4-9 Current-potential curves at 0.125 M to 0.75 M Na_2SO_4.

Table 4-1 The experimental and theoretical thicknesses of the boundary layer.

Na_2SO_4 Concentration	Real-time Current Density	Limiting Current Density	Exper.	Thero.	*error	Exp.	The.	*error	Exp.	The.
			BL Thickness (NH_4^+)			BL Thickness (cathodic Na^+)			BL Thickness (total)	
mol L^{-1}	mA cm^{-2}		μm			μm			μm	
0.125	15.69	17.89	320.33	294.94	0.08	54.34	69.65	-0.28	374.67	364.59
0.25	18.44	18.83	304.34	258.06	0.15	81.13	82.90	-0.02	385.47	340.96
0.50	22.13	21.94	271.20	230.84	0.15	92.84	122.28	-0.32	364.04	353.12
0.75	21.69	20.10	285.14	224.29	0.21	152.03	181.44	-0.19	437.17	405.73

Average	0.20	0.09
Std. Dev.	0.11	0.39

Note: $* \, error = \frac{Exper. - Theor.}{Exper.}$

4.4.6 Electricdeionzation performances

1) Current and conductivity

Because of different concentrations of Na_2SO_4, the real current density crossing the complete system waves at the range of 2.0 mA cm^{-2} to 7.0 mA cm^{-2} (Figure 4-10). In details, the average current density increases from 3.0 mA cm^{-2} at 0.125 M to 6.0 mA cm^{-2} at 0.5 M. Nevertheless, the average current density of the system does not increase anymore although Na_2SO_4 solution concentrating, indicating that increasing the concentration of the supporting electrolyte does make positive effects at the concentrated solution (Figure 4-10(a)). This is because the ion conductivity of supporting electrolyte is quite limited. Additionally, as shown in Figure 4-10(b), the ion conductivity of Na_2SO_4 solution linearly climbs from 0 ms cm^{-1} at MiniQ water to 150 ms cm^{-1} at 0.5 M. But it gradually goes up 200 ms cm^{-1} and reaches the podium at 1.5 M. The notable fluctuations are caused by water dissociation and bubbles.

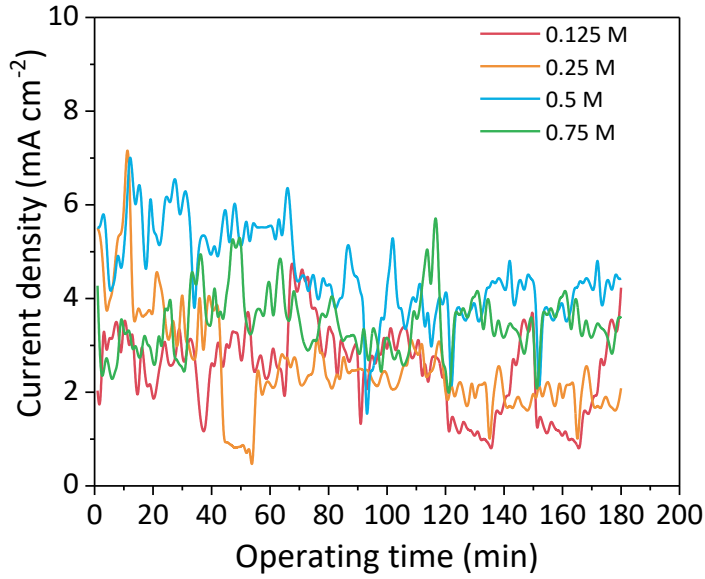

(a)

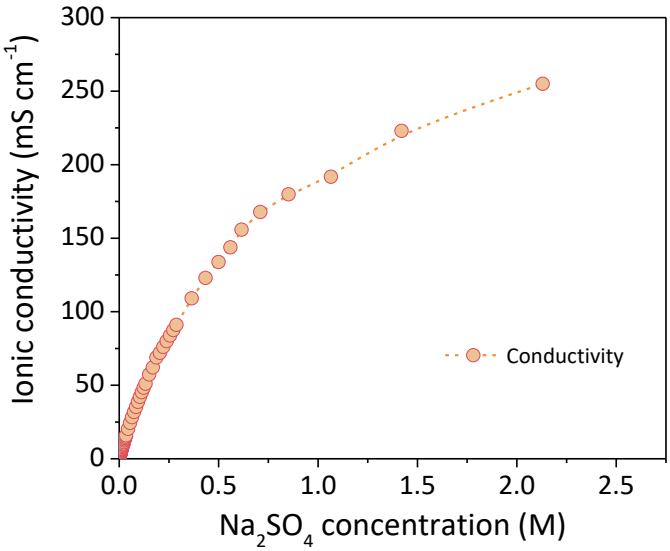

(b)

Figure 4-10 The real current density of the complete system at 0.125-0.75 M (a); Ion conductivity of the Na_2SO_4 solution (b).

2) Deionization efficiency

Due to the differences in current density, EDI displays unequal deionization efficiencies. Figure 4-10 shows the variations of deionization efficiencies as Na_2SO_4 solution is in the range of 0.125-0.75 M. Specifically, deionization efficiency soars from 50% at 0.125 M to 90% at 0.75 M. Notably, the deionization efficiency for concentrated Na_2SO_4 solution becomes indistinct even though the concentration of Na_2SO_4 solution increases (Figure 4-11(a)). Concerning the ration of deionization, it can be seen from Figure 4-11(b) that the maximum rate occurs at 40 min to 60 min. After 60 min, the ration of NH_4^+ deionization drops to 0 or 4 mol L^{-1} h^{-1} due to the deionization neutralization or donna equilibrium. Additionally, it is found that the lower concentration of supporting electrolyte reaches the peak of deionization rate earlier, such that the deionization rate for 0.125 M reaches 5.0 mol L^{-1} h^{-1} at 40 min while it from 0.75 M reaches 9.0 mol L^{-1} h^{-1} at 60 min. This phenomenon may be related to ion compensation at concentration situation.

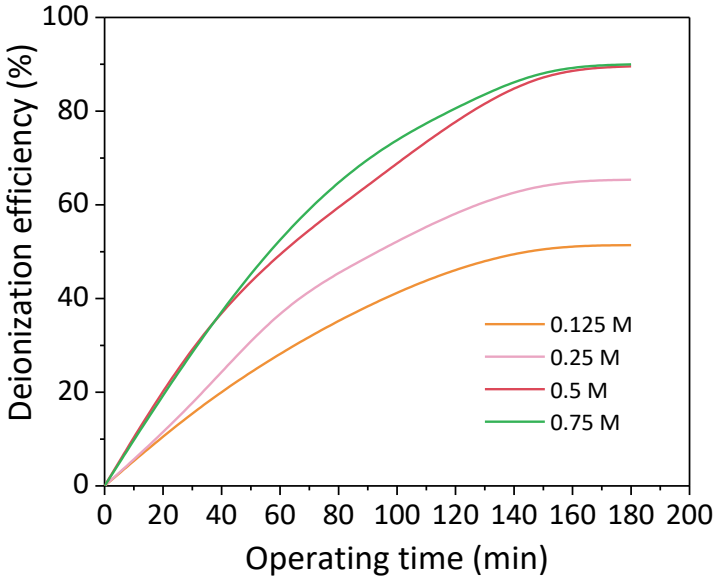

(a)

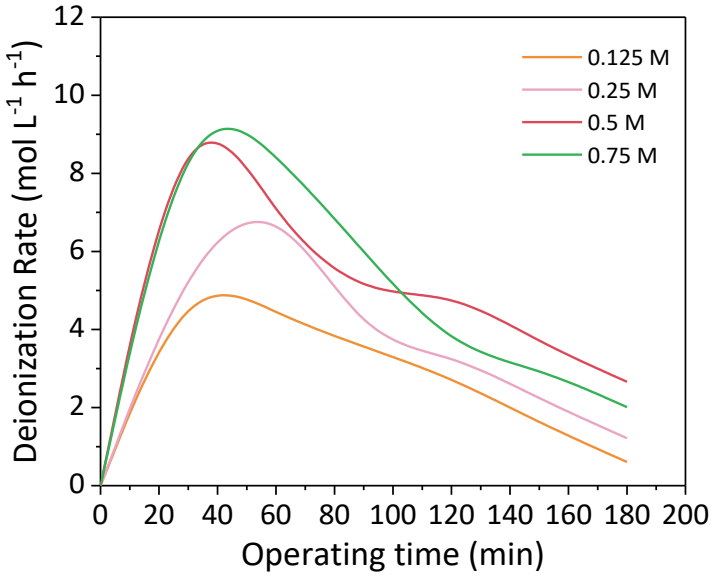

(b)

Figure 4-11 The deionization efficiency (a); Deionization efficiency rate within 180 min for 0.125-0.75 M Na_2SO_4 solution (b).

3) Gas yield

As found in Chapter 3, the reduction of NH_4^+ in the cathode of EDI is a crucial reaction to generate N_2. Thus, the mass balance in the form of total nitrogen was conducted. Figure 4-12(a) illustrates the mass balance of nitrogen for the anode, the cathode, ammonia, nitrogen, and statistic error of nitrogen. In details, the nitrogen of the anode falls from 9 mmol at 0.125 M to 2 mmol at 0.75 M. However, the nitrogen of the cathode increases from 7 mmol to 10 mmol at relative concentration. Apparently, the nitrogen of ammonia is accumulated from 2 mmol at 0.125 M to 6 mmol, which is promoted by the increase in the current density. As for the undetected nitrogen, it is so little that it can be ignored.

The gas produced by EDI system was collected. Figure 4-12(b) (blue scatter) shows that the total gas production increases from 120 mL h^{-1} at 0.125 M to 200 mL h^{-1} at 0.75 M. The analysis of gas composition indicates that the percentage of H_2 increases, which is caused by water splitting. In other words, water dissociation is enhanced with Na_2SO4 solution concentrating. It is known the generation of bubbles around the surface of the electrode leads to the decrease in the effective area. Figure 4-12(b) (red scatter-line) displays the relationship between gas yield and effective area. The increase in Na_2SO_4 solution contributes to a little bit of expanding of effective area from 10.5 cm^2 at 0.125 M to 11.25 cm^2 at 0.5 M, which it shrinks to 11.0 cm^{-2} at 0.75 M.

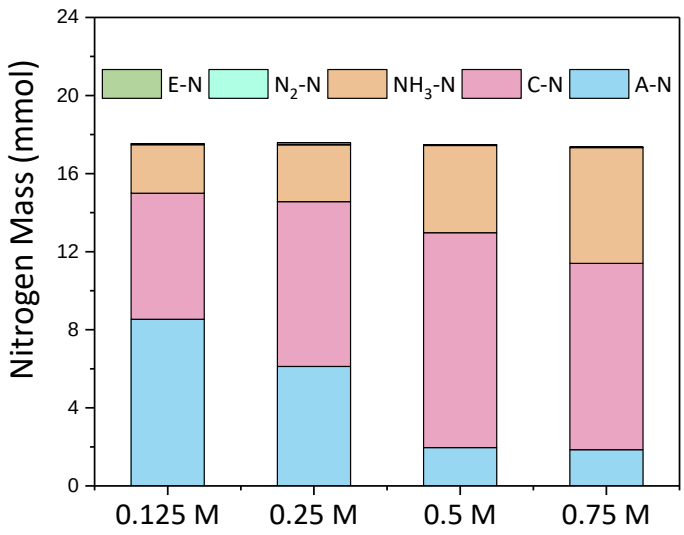

(a)

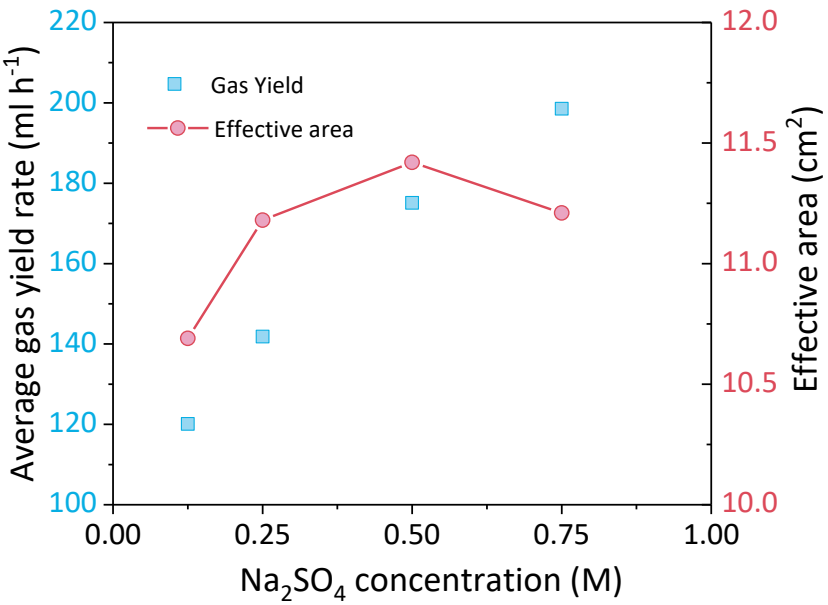

(b)

Figure 4-12 The constitution of gas generated by EDI system at 125-0.75 M Na_2SO_4 solution (a); The average rate of gas production and effective area at 125-0.75 M Na_2SO_4 solution (b).

4) Energy benefits

Owing to the effects of concentration polarization and water dissociation, EDI has different performances for energy recovery and energy consumption. Table 4-2 summarizes NH_4^+ removal efficiency, energy consumption, energy conversion from generated hydrogen and ammonia, and energy balance ratio as Na_2SO_4 concentration increases from 0.125-0.75 M. The highest removal efficiency is 80.81%, obtained at 0.75 M, but the highest energy balance ratio is 2.11, achieved at 0.5 M. This inconsistent result is because of the differences in energy consumption and energy recovery. Specifically, energy consumption increases from 969.23 J at 0.125 M to 1,439.49 J at 0.75 M while energy recovery from H_2 and NH_3 increases from 1478.8 J at 0.125 M to 2886.92 J at 0.5 M, but declines to 863.15 J at 0.75 M. Thus, the energy balance ratio is the highest at 0.5 M. These results demonstrate that the concentration of supporting electrolyte noticeably effects on the overall performances. The concentration of supporting electrolyte should equal to the concentration of the anolyte.

Table 4-2 Comparison of energy balance at 0.125-1.5 M Na_2SO4 supporting electrolyte

Na_2SO_4 Concentration	Removal Efficiency	Energy Consumption	Hydrogen	Ammonia	Energy Balance
mol L^{-1}	%	J			
0.125	46.64	969.23	680.60	798.2	1.53
0.250	58.69	988.03	693.81	935.58	1.65
0.500	78.34	1,369.73	961.84	1,925.08	2.11
0.750	80.81	1,229.19	863.15	1,439.49	1.87

4.5 Summary

This chapter introduced the investigation on the effects of cathodic electrolyte concentration on concentration polarization, boundary thickness, and electric resistance through theoretical simulations followed by experimental validation. The magnitude of the concentration polarization is enhanced by the increase in the concentration of the cathodic electrolyte. The left-side boundary layer is formed by the NH_4^+ ion. Concentration diffusion makes much more notable contributions to the reduction in the concentration of NH_4^+ than electric migration in the boundary layer. The concentration of NH_4^+ decreases from 0.25 M at 0.5 M Na_2SO_4 to 0.01 M at 0.125 M Na_2SO_4 on the left-side boundary layer while the increases in NH_4^+ and SO_4^{2-} concentration build up a thick boundary layer on the right-side. The distributions of NH_4^+ and SO_4^{2-} concentration increase the limiting the current density from 14 mA cm^{-2} to 20 mA cm^{-2}. The boundary layer thickness of NH_4^+decreases from 320 μm to 285 μm. As the Na_2SO_4 concentration continuously increasing, SO_4^2 forms a boundary layer of 70 μm at 0.125 M to 181 μm at 0.75 M. The potential difference reaches 2.0 V and results in water dissociation. The resistance of the bulk solution decreases with the concentrating Na_2SO_4 solution. The resistance is determined by the solution resistance under the dilute or middle concentration (0.125-0.5 M). However, it is decided by the boundary layer resistance under the concentrated solution (> 0.75 M). The differences in current density contributed the different deionization efficiencies at 0.125-0.75 M. The maximum of energy balance ratio is 2.11 at 0.5 M.

4.6 References

Aguilella, Mafe, Manzanares, & Pellicer. (1991). Current-voltage curves for ion-exchange membranes. Contributions to the total potential drop. *Journal of Membrane Science, 61*, 177-190.

Anouti, Jacquemin, & Porion. (2012). Transport properties investigation of aqueous protic ionic liquid solutions through conductivity, viscosity, and NMR self-diffusion measurements. *The Journal of Physical Chemistry B, 116*(14), 4228-4238.

Arar, Yüksel, Kabay, & Yüksel. (2014). Various applications of electrodeionization (EDI) method for water treatment—A short review. *Desalination, 342*, 16-22.

Bason, Oren, & Freger. (2007). Characterization of ion transport in thin films using electrochemical impedance spectroscopy: II: Examination of the polyamide layer of RO membranes. *Journal of Membrane Science, 302*(1-2), 10-19.

Bhattacharya, & Hwang. (1997). Concentration polarization, separation factor, and Peclet number in membrane processes. *Journal of Membrane Science, 132*(1), 73-90.

Choi, Lee, & Moon. (2001). Effects of electrolytes on the transport phenomena in a cation-exchange membrane. *Journal of Colloid and Interface Science, 238*(1), 188-195.

Choi, Park, & Moon. (2002). Direct measurement of concentration distribution within the boundary layer of an ion-exchange membrane. *Journal of Colloid and Interface Science, 251*(2), 311-317.

Dai, Cao, Fang, Liu, Dong, Pan, & Wang. (2012). Schiff base-chitosan grafted multiwalled carbon nanotubes as a novel solid-phase extraction adsorbent for determination of heavy metal by ICP-MS. *Journal of Hazardous Materials, 219*, 103-110.

Długołęcki, Anet, Metz, Nijmeijer, & Wessling. (2010). Transport limitations in ion exchange membranes at low salt concentrations. *Journal of Membrane Science, 346*(1), 163-171.

Długołęcki, Nymeijer, Metz, & Wessling. (2008). Current status of ion exchange membranes for power generation from salinity gradients. *Journal of Membrane Science, 319*(1), 214-222.

Długołęcki, Ogonowski, Metz, Saakes, Nijmeijer, & Wessling. (2010). On the resistances of membrane, diffusion boundary layer and double layer in ion exchange membrane transport. *Journal of Membrane Science, 349*(1), 369-379.

Fidaleo, & Moresi. (2005). Optimal strategy to model the electrodialytic recovery of a strong electrolyte. *Journal of Membrane Science, 260*(1), 90-111.

Freger, & Bason. (2007). Characterization of ion transport in thin films using electrochemical impedance spectroscopy: I. Principles and theory. *Journal of Membrane Science, 302*(1-2), 1-9.

Fu, Xu, Cheng, Yang, & Pan. (2004). Fundamental studies on the intermediate layer of a bipolar membrane: Part III. Effect of starburst dendrimer PAMAM on water dissociation at the interface of a bipolar membrane. *Journal of Membrane Science, 240*(1), 141-147.

Greenlee, Lawler, Freeman, Marrot, & Moulin. (2009). Reverse osmosis desalination: water sources, technology, and today's challenges. *Water Research, 43*(9), 2317-2348.

Güler, van Baak, Saakes, & Nijmeijer. (2014). Monovalent-ion-selective membranes for reverse electrodialysis. *Journal of Membrane Science, 455*, 254-270.

Inenaga, & Yoshida. (1980). Effect of an unstirred layer on ion transport through a membrane. *Journal of Membrane Science, 6*, 271-282.

Krol, Wessling, & Strathmann. (1999). Concentration polarization with monopolar ion exchange membranes: current–voltage curves and water dissociation. *Journal of Membrane Science, 162*(1), 145-154.

Law, Wen, & Solt. (1997). Thickness and concentration profile of the boundary layer in electrodialysis. *Desalination, 109*(1), 95-103.

Lee, Strathmann, & Moon. (2006). Determination of the limiting current density in electrodialysis desalination as an empirical function of linear velocity. *Desalination, 190*(1-3), 43-50.

Li, & Gregory. (1974). Diffusion of ions in sea water and in deep-sea sediments. *Geochimica et cosmochimica acta, 38*(5), 703-714.

Moshtarikhah, Oppers, de Groot, Keurentjes, Schouten, & van der Schaaf. (2017). Nernst–Planck modeling of multicomponent ion transport in a Nafion membrane at high current density. *Journal of applied electrochemistry, 47*(1), 51-62.

Ndjomgoue-Yossa, Nanseu-Njiki, Kengne, & Ngameni. (2015). Effect of electrode material and supporting electrolyte on the treatment of water containing Escherichia coli by electrocoagulation. *International Journal of Environmental Science and Technology, 12*(6), 2103-2110.

Onsager, & Kim. (1957). The relaxation effects in mixed strong electrolytes. *The Journal of Physical Chemistry, 61*(2), 215-229.

Petrowsky, & Frech. (2008). Concentration dependence of ionic transport in dilute organic electrolyte solutions. *The Journal of Physical Chemistry B, 112*(28), 8285-8290.

Rohman. (2008). Mathematical model of ion transport in electrodialysis process. *Bulletin of Chemical Reaction Engineering & Catalysis, 3*(1-3), 3-8.

Rubinstein, & Shtilman. (1979). Voltage against current curves of cation exchange membranes. *Journal of the Chemical Society, Faraday Transactions 2: Molecular and Chemical Physics, 75*, 231-246.

Selman, & Newman. (1971). Free - convection mass transfer with a supporting electrolyte. *Journal of The Electrochemical Society, 118*(7), 1070-1078.

Sigvartsen, Songstad, Gestblom, & Noreland. (1991). Dielectric properties of solutions of tetra-iso-pentylammonium nitrate in dioxane-water mixtures. *Journal of Solution Chemistry, 20*(6), 565-582.

Sistat, & Pourcelly. (1997). Chronopotentiometric response of an ion-exchange membrane in the underlimiting current-range. Transport phenomena within the diffusion layers. *Journal of Membrane Science, 123*(1), 121-131.

Spiegler. (1971). Polarization at ion exchange membrane-solution interfaces. *Desalination, 9*(4), 367-385.

Strathmann. (2000). Membrane Separation Processes, 4. Concentration Polarization and Membrane Fouling. In *Ullmann's Encyclopedia of Industrial Chemistry*: Wiley-VCH Verlag GmbH & Co. KGaA.

Taky, Pourcelly, Lebon, & Gavach. (1992). Polarization phenomena at the interfaces between an electrolyte solution and an ion exchange membrane: Part I. Ion transfer with a cation exchange membrane. *Journal of Electroanalytical Chemistry, 336*(1-2), 171-194.

Tanaka. (2002). Water dissociation in ion-exchange membrane electrodialysis. *Journal of Membrane Science, 203*(1), 227-244.

Tanaka. (2003). Concentration polarization in ion-exchange membrane electrodialysis—the events arising in a flowing solution in a desalting cell. *Journal of Membrane Science, 216*(1), 149-164.

Tanaka. (2004). Concentration polarization in ion-exchange membrane electrodialysis: The events arising in an unforced flowing solution in a desalting cell. *Journal of Membrane Science, 244*(1), 1-16.

Tanaka. (2011). Ion-exchange membrane electrodialysis for saline water desalination and its application to seawater concentration. *Industrial & Engineering Chemistry Research, 50*(12), 7494-7503.

Tanaka. (2015). *Ion exchange membranes: fundamentals and applications*: Elsevier.

Tedesco, Hamelers, & Biesheuvel. (2016). Nernst-Planck transport theory for (reverse) electrodialysis: I. Effect of co-ion transport through the membranes. *Journal of Membrane Science, 510,* 370-381.

Wang, Wang, Zhang, & Xu. (2012). The concentration, resistance, and potential distribution across a cation exchange membrane in 1: 2 (Na 2 SO 4) type aqueous solution. *Desalination, 284,* 106-115.

Xu, Dong, Zhuang, He, Ni, Feng, & Lee. (2017). Energy upcycle in anaerobic treatment: Ammonium, methane, and carbon dioxide reformation through a hybrid electrodeionization–solid oxide fuel cell system. *Energy Conversion and Management, 140,* 157-166.

Yang, Cao, & Yang. (2016). Mathematical modeling of a three-compartment electro-reactor process with ion-exchange membranes for recycling and resource recovery of desulfurization residuals. *Journal of Electroanalytical Chemistry, 762,* 7-19.

Zourmand, Faridirad, Kasiri, & Mohammadi. (2015). Mass transfer modeling of desalination through an electrodialysis cell. *Desalination, 359,* 41-51.

CHAPTER 5 EFFECTS OF SODIUM SULFATE ON AMMONIUM TRANSPORT AND REDUCTION IN THE CATHODE OF ELECTRODEIONZIATION

5.1 Introduction

As investigated in Chapter 3 and Chapter 4, the concentrated NH_4^+ contained in digestate and landfill leachate can be recovered as an alternative hydrogen fuel by EDI process. As found in Chapter 3, NH_3 production is through NH_4^+ reduction at the cathode via a one-electron transfer (Eq. 3-15) and OH^- neutralization via water dissociation (Eq.3-16 and Eq.3-17) (Little *et al.*, 2015; Simons *et al.*, 1969). At a lower applied voltage (<1.23 V) to avoid water dissociation, the former is likely to occur over the latter. Na_2SO_4 solution is usually used as the supporting electrolyte to enhance the electrolyte conductivity of weak electrolytes such as ammonium solution, as Na^+ has large ionic conductivity, mobility, and electrochemical stability (Alvarado & Chen, 2014; Moon & Yun, 2014; Mousavi *et al.*, 2007; Mousavi *et al.*, 2016; Olson & Bühlmann, 2013; Wenten *et al.*, 2016). The existence of Na^+ whereas often rises an intense competition with NH_4^+. Casadellà *et al*. (2016) studied the cation completion among K^+, Na^+ and NH_4^+ in urine through polymer inclusion membranes and observed a selective recovery order ($K^+ > Na^+ > NH_4^+$) and two-fold flux in Na^+ (4.5×10^{-3} mmol

cm^{-2} h^{-1}) over NH_4^+ (1.5×10^{-3} mmol cm^{-2} h^{-1}) (Casadellà *et al.*, 2016). Liu *et al*. (2016) studied the competitive transports of Na^+ and NH_4^+ in bioelectrochemical systems and concluded that Na^+ in the anolyte facilitated the transport of NH_4^+ due to the Donnan equilibrium at cation exchange membrane-anolyte/catholyte interfaces (Liu *et al.*, 2016). Rosasco *et al*. (1985) investigated cation competition in the electrical double-layer at a well-defined Pt (111) electrode surface and found the strength order of cation retention (Na^+ > NH_4^+) (Rosasco *et al.*, 1985). The hydrated radius also can be influential for the electrochemical activities, e.g., charge density, dielectric constant, and the rate capability (Cagle *et al.*, 2010; Jiang *et al.*, 2016; Yoon *et al.*, 2005; Yoshida & Imoto, 1992). Besides, accumulated Na^+ attracts water molecules and forms a compacted sodium-water protecting layer, which deters the electrochemical reaction kinetics (Ma *et al.*, 2014; Vossen & Forstmann, 1995). Also, the studies on the competition between Na^+ and NH_4^+ demonstrated that Na^+ competitively reduced the effective current efficiency of NH_4^+ and produced an overpotential of the electrode at fixed electric current (Casadellà *et al.*, 2016; Little *et al.*, 2015; Savelyev & MacKerell Jr, 2015). Therefore, these results signifying that the adverse influences of Na^+ cannot be ignored.

Due to the limitations of the experimental techniques for the understanding insights at atom scale level, theoretical simulations (classic simulations and molecular dynamics (MD) simulations) built on EDL theories are capable of delivering insightful information about the interactions between Na^+ and NH_4^+. Pieter *et al*. (2015) used Langmuir model to study NH_4^+ removal from water using sodium hydroxide modified zeolite mordenite and found that Na^+ competition decreased the removal efficiency of

NH_4^+ through different reaction mechanisms (Soetardji *et al.*, 2015). Soroosh & Hai (2014) employed molecular dynamics simulations (flexible-boundary QM/MM) to reveal ion solvation and found that NH_4^+ had a larger discrepancy (the extent of charge transfer by about 0.3 e) and wider distribution than Na^+ (0.1 e) (Pezeshki & Lin, 2014). However, the influences of Na^+ concentration on NH_4^+ transport and reduction in the electric field keeps vacant to date. This can be completed using Atomic/Molecular Massively Parallel Simulator package (LAMMPS) (Joly *et al.*, 2004). The objective of this chapter is to study the mechanism of supporting electrolyte concentration affecting on NH_4^+ behaviors under the fixed applied voltage. With this, we employ LAMMPS combined by electrochemical tests to take insights to the effects of the Na_2SO_4 (0 M to 1.5 M) on NH_4^+ migration, reduction, and electric properties in the cathodic EDL (Figure 5-1).

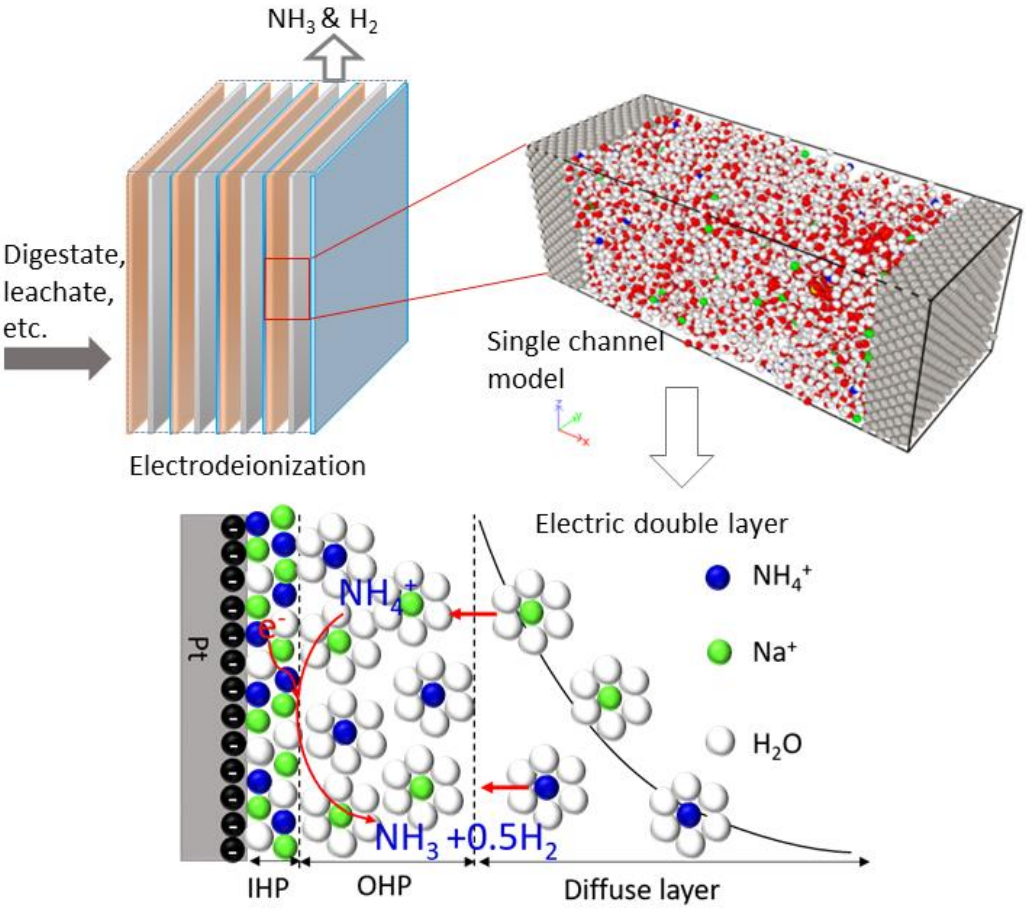

Figure 5-1 The schematic graph of ammonium reduction in the cathodic electric double layer.

5.2 Experiments

5.2.1 Equipment setup

A sandwich type of EDI stack was configured (Figure 5-2(a)). The working volume was 40 cm^3, 60 mm × 60 mm × 11 mm, in which 11 mm includes 10 mm distance between the anode and the cathode and 1 mm thickness of silicone gaskets. The electrodes are plates made of Ti coated 0.02 mm thickness of Pt layer with 16 cm^2 effective area. The original electrolyte was 0.25 M ammonium sulfate, then mixed with 0-1.5 M Na_2SO_4 supporting electrolyte under 25 °C operating temperature. The ionic conductivity was measured by the conductivity meter (Shanghai Leici -chuangyi Instrument And Meter Co., Ltd.). The methods of the chemical determinations can be found in Chapter 3.

5.2.2 Cyclic voltammetry sweeping

The tests of current density versus applied voltage were carried out using above described EDI stack. The scanning electrolyte was the mixture of $(NH_4)_2SO_4$ and Na_2SO_4 under different concentrations in a three-electrode step with Ag/AgCl as the reference electrode. The current was recorded and analyzed by the electrochemical working station (CorrWare®, Scribner Associates Inc., USA) (Figure 5-2(b) and 5-2(c).

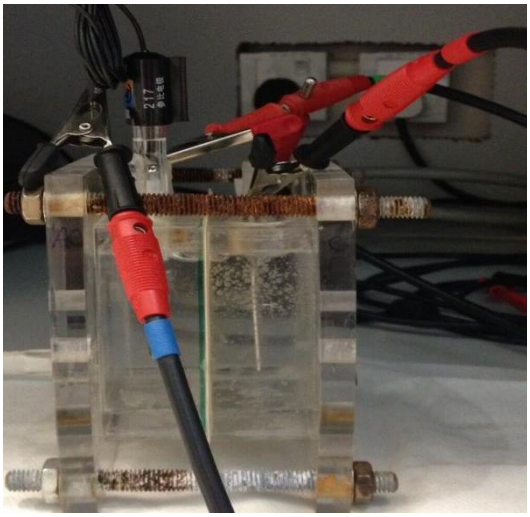

(a)

(b)

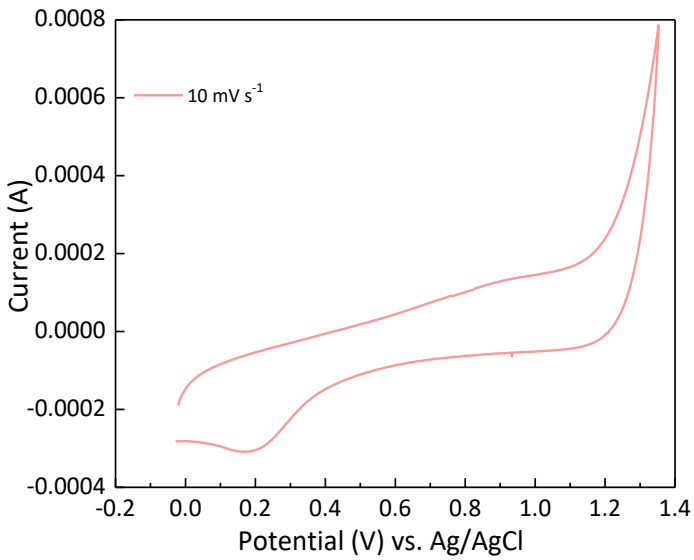

(c)

Figure 5-2 Experiment setup without ion exchange membrane (a); The electrochemical working station for CV sweeping (b); Reference CV curve using 0.25 M ammonium sulfate (c).

5.3 Computational methods

5.3.1 Electrode/electrolyte interface set-up.

The simulation system is a three-dimensions supercell with periodic boundary conditions. The initial model of Pt-solution was constructed by Material Studio 8.0. It was composed of the Pt sheet (50 Å × 50 Å), and the solution aligned in parallel with an interlayer distance of 140 Å. To simulate Pt electrode/electrolyte solution interface, water molecules, and NH_4^+ along with different concentrations of Na^+ and SO_4^{2-} ions are added on the Pt (100) cluster surface (338 atoms), 7 layers for each pole. The difference in Na_2SO_4 was realized via importing different ion number, as shown in Table 5-1. The ion number was increased in the module of the amorphous cell. The raw structure was optimized through energy Forcite with fine quality. Forcefield was cvff. The optimized results are shown in Figure 5-3. Then the structure was exported to .cat file that was the format used to transfer to LAMMPS data file. The atom coordinates can be obtained in appendix II.

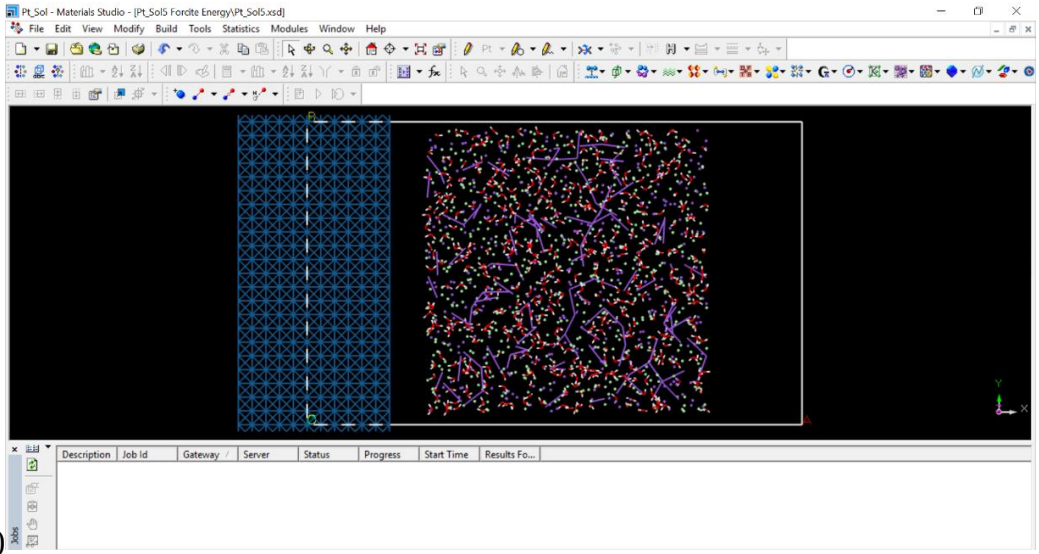

(a)

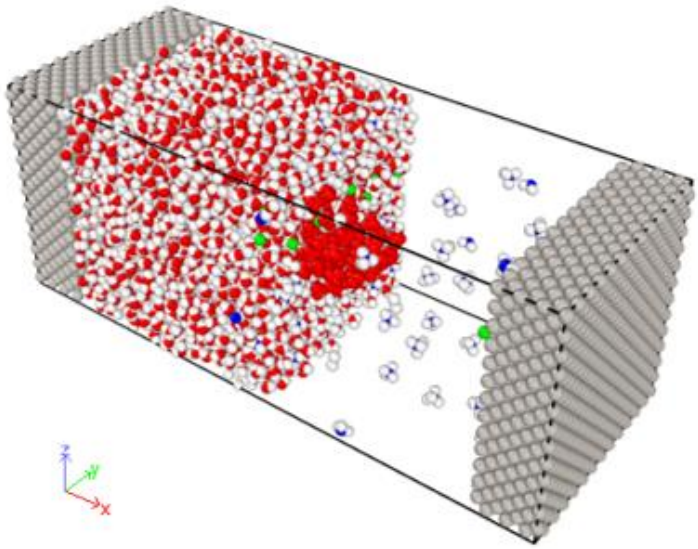

(b)

Figure 5-3 Initial geometry in Material Studio (a); Trajectory of Pt-solution system (b).

Table 5-1 Atom composition of EDI system from 0-1.5 M Na_2SO_4

Na_2SO_4 Concentration M	NH_4^+	Na^+	SO_4^{2-}	H_2O
0.000	72	0	36	4,000
0.125	72	18	45	4,000
0.250	72	36	54	4,000
0.500	72	72	72	4,000
0.750	72	108	90	4,000
1.500	72	216	144	4,000

Table 5-2 Pair potential and cutoff distance between atoms

Atom	ε (eV)	σ (Å)	M (g mol^{-1})	Valence (e)
Ow	0.274	3.608	15.999	-0.798
Hw	0.013	1.098	1.008	0.399
N	0.065	3.262	14.007	-0.120
Hn	0.013	1.098	1.008	0.280
Na	0.738	3.962	22.990	1.000
O	0.240	3.535	15.999	-0.114
S	0.071	4.027	32.064	0.457
Pt (Morse)	1.583	3.024	195.090	0.000

5.3.2 Equilibrium relaxation and data collection

The principle of MD simulations was intruded in Chapter 2. Here the electrically charged simulation system was performed using the LAMMPS package at a nominal temperature of 300 K (Lee *et al.*, 2013). The respective parameters of the energy and length, as summarized in Table 5-2. The atom-atom interactions are simulated using Lennard-Jones (LJ) potential and Coulomb's law, as described by Eq. 2-35 to Eq. 2-41. Bonds and angles among atoms were held by the SHAKE algorithm (Ryckaert *et al.*, 1977). The solvent (water) is typically depicted by the rigid SPC/E water model, and Columbic interactions were computed using the particle-particle particle-mesh (PPPM) algorithm (Jiang *et al.*, 2016). The movement of Pt atoms was ignored, and their positions were frozen. The NVT ensemble simulations at 300 K were carried out with the Nosé-Hoover thermostat and barostat for 1.0 ns. Time integration was performed with 0.5 fs time step using the velocity-Verlet algorithm. Then NPT ensemble simulations at 1.0 atm were carried out under the same conditions as NVT. The average values of pressure and temperature were used to adjudge the status of system relaxation.

After ensuring that the systems indeed reached the thermal equilibrium state, we collected corresponding data of mass density, number density, mean square displacement (MSD), and radial distribution function (RDF) via NVE ensemble for 0.5 ns, as displayed in Figure 5-4. A 3.0 V constant voltage was assigned to the system and its equal force $F = qE$ to each charged atom in the group. To simplify post-process of generated results, the channel is split into a set of bins (1.0 Å in width) along the

direction (x) perpendicular to the surface. The mass density ρ(x) is used to describe the EDL structures. Other data can be utilized to the thermal dynamics of all species.

5.3.3 Post process of data

1) Charge density

Charge density is one of the important properties to describe EDL. According to the axial number density of atoms, the total charge density profile, $\sigma_{q(x)}$, is contributed by ion and water expressed as Eq.5-1.

$$\sigma_{q(x)} = \sum_{i \ni surf} \sigma_i(x) q_i + \sigma_O(x) q_O + \sigma_H(x) q_H \tag{5-1}$$

where σ_i, σ_O, and σ_H are the number densities of ions, water-oxygen, and water-hydrogen, respectively. q_i, q_O, and q_H are the charge carried by ions, water-oxygen, and water-hydrogen, respectively.

2) Electric field and potential profiles

Electric field strength and potential oscillate along with the variation of charge density. Especially, the wall-normal electric field ($E_{q(x)}$) component is calculated by integrating the net charge density as described by Eq. 5-2.

$$E_{q(x)} = -\left(1/\in_0\right) \int_{-\infty}^{x} \sigma_q(x')(x - x')dx' \tag{5-2}$$

Potential is computed by integrating the Poisson equation in one-dimensional as described in Eq. 5-3.

$$\frac{\partial^2 V(x)}{\partial x^2} = -\frac{\sigma(x)}{A_{Pt}\varepsilon_0} \tag{5-3}$$

where $\sigma(x)$, A_{Pt}, and ε_0 are the net charge density, the size of Pt sheet and the vacuum dielectric constant, respectively. Eq. 5-3 was numerically integrated to obtain the potential drop, $V(x)$, as shown in Eq. 5-4 using $x=L/2$ (the middle of the channel) as a reference that was regarded as zero charge density.

$$V(x) = \int\int_{L/2}^{x} \frac{\sigma(x)}{A_G \varepsilon_0} dx^2 \tag{5-4}$$

3) Mean square displacement

Mean Square Displacement (MSD, M^2) is a measure of the deviation time between the position particle and some reference positions (Frenkel & Smit, 2001). Since MSD contains information on the diffusion, it is used to examine the transportation and mixing phenomena (Krishnamurthy *et al.*, 2006). For Brownian motion, the characteristic displacement of a particle is governed by MSD equation, Eq. 5-5.

$$M^2 \equiv \left\langle \left(x - x_0\right)^2 \right\rangle = \frac{1}{N}\sum_{n=1}^{N}\left(x_n\left(t\right) - x_n\left(0\right)\right)^2 \tag{5-5}$$

where N, the number of particles to be averaged; $x_n(0)=x_0$, the reference position of each particle; $x_n(t)$, the position of each particle in determined time t. Following particle tracking, the MSD of the particles was calculated to quantify cation and water transports in EDL.

4) Diffusion coefficient

The diffusion coefficient is the rate of mass transport, as described by the approximate slope of the M^2 versus t curves from Einstein's equation (Eq. 5-6).

$$D = \lim_{t \to \infty} \frac{1}{6t} \left\langle \left[r(t) - r(0) \right]^2 \right\rangle \qquad (5\text{-}6)$$

where r and t are aromatic compound position and time, respectively.

5) Radial distribution function

RDF provides information about the density of atoms at a given radius (r), and it is defined as Eq. 5-7.

$$g(r) = \rho(r) / \rho \qquad (5\text{-}7)$$

where $\rho(r)$ is the local density of atoms and ρ is the overall density of atoms (volume).

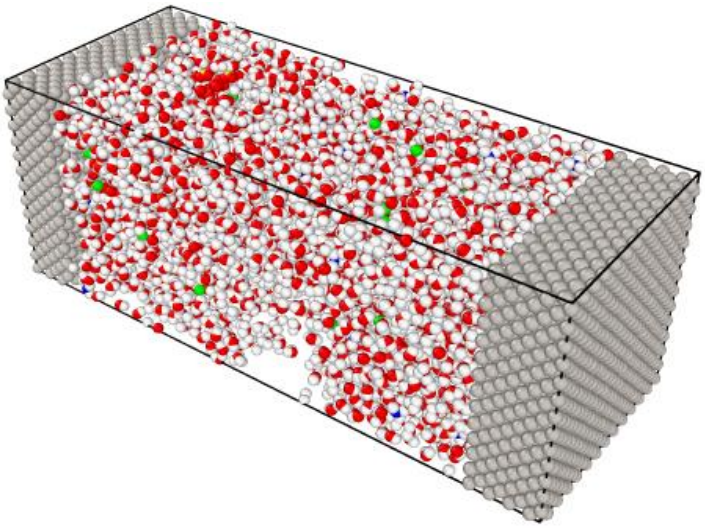

(a)

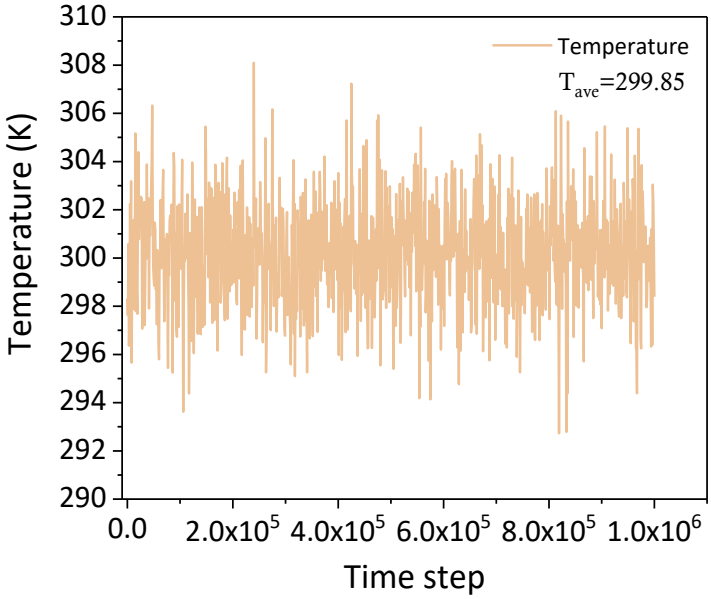
Temperature
T_{ave}=299.85
Temperature (K)
310
308
306
304
302
300
298
296
294
292
290
0.0
2.0x10^5
4.0x10^5
6.0x10^5
8.0x10^5
1.0x10^6
Time step

(b)

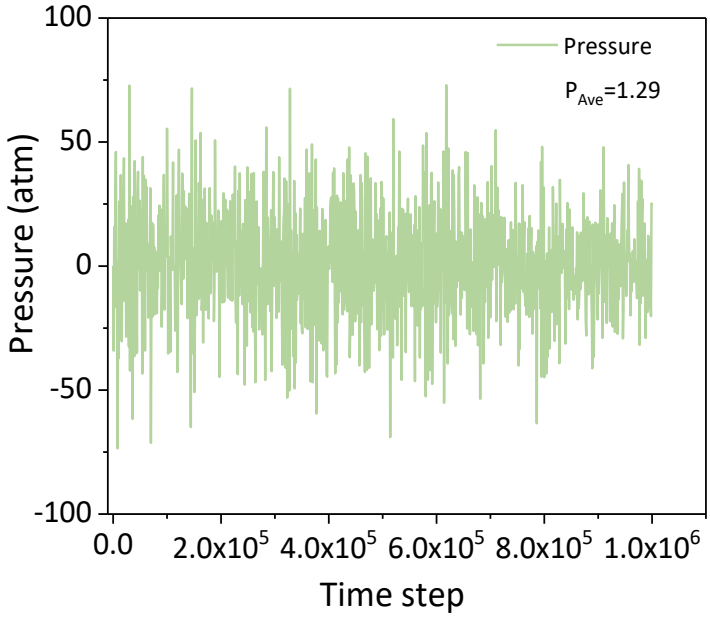

(c)

Figure 5-4 System relaxation and equilibrium: Relaxed structure (a); Average temperature (299.85 K) for NVT (b); Average pressure (1.29 atm) for NPT (c).

5.4 Results

5.4.1 Current density of ammonium reduction

Figure 5-5 shows the variation in the current density of NH_4^+ reduction in the range of 0-1.5 M Na_2SO_4 electrolyte via current-concentration and current-voltage curves. The current density almost linearly climbs from 0 mA cm^{-2} at 0 M to 8.0 mA cm^{-2} at 0.25 M, and slowly increases to 12.2 mA cm^{-2} at 1.5 M. Correspondingly, the slope of 32 at 0.25 M is ten times the slope of 3.3 at 1.5 M, indicating that increasing Na_2SO_4 concentration conditionally prompts a current increase (Figure 5-5(a)). Under 0-1.5 M Na_2SO_4 electrolyte, CV curves were obtained at 10.0 mV s^{-1} sweeping rate, as shown in Figure 5-5(b). A single peak for NH_4^+ reduction appears on each curve in the range of 0–8 V of applied voltage.

In greater details, the current density increases for forwarding sweeping, but declines for backward sweeping. The NH_4^+ reduction peak at 0.23 V decreases from -0.023 mA cm^{-2} to -0.005 mA cm^{-2}, shifting toward the positive y-axis with the bulk Na_2SO_4 electrolyte, suggesting that the concentrated Na_2SO_4 (> 0.25 M) electrolyte brings an adverse effect on NH_4^+ reduction. The current of NH_4^+ reduction has an opposite trend with a system current, suggesting restrained NH_4^+ reduction rather than concentrated Na_2SO_4. In other words, the current used for NH_4^+ reduction decreases due to the existence of Na^+ in the cathode.

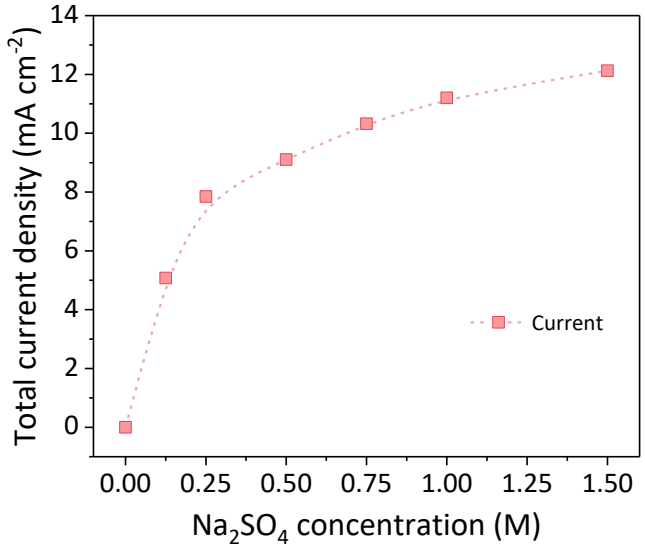

(a)

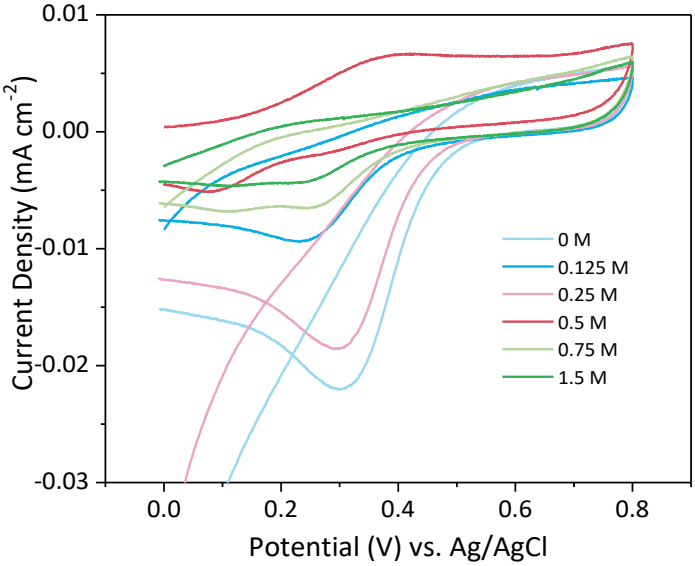

(b)

Figure 5-5 Total current density as a function of Na_2SO_4 concentration (0-1.5 M) (a); Current-voltage curves at 0-0.8 V under 0-1.5 M Na_2SO_4 (b).

5.4.2 Ion transport in the solution

The decrease in the NH_4^+ reduction peak may be caused by the variation in NH_4^+ transport in the solution, which is related to molar conductivity and dynamic viscosity. As displayed in Figure 5-6, the conductivity of Na_2SO_4 experiences a linear drop as a function of the square root of Na_2SO_4 concentration within 0.75 M and a smooth decline at 1.5 M, indicating a limitation in the supporting electrolyte's conductivity capability. The solution viscosity experiences a slow growth from 80 mPas to 95 mPas within 0.25 M, and a sharp climb to 330 mPas at 1.5 M. The visible increase in dynamic viscosity produces a greatly hindered force for ion migration. The trends of molar conductivity and dynamic viscosity demonstrate that both Na^+ and NH_4^+ migrations are slowed in the solution. Table 5-3 summarizes the dynamic of NH_4^+ transport by mobility and transport number. NH_4^+ has increased mobility from 1.01 m^2 V^{-1} s^{-1} to 1.49 m^2 V^{-1} s^{-1} at 0.125 M, but drops to 1.27 m^2 V^{-1} s^{-1} at 1.5 M. The Na^+ and SO_4^{2-} mobilities drop to 1.63 m^2 V^{-1} s^{-1} and 0.81 m^2 V^{-1} s^{-1}, respectively. In terms of transport number, both NH_4^+ and SO_4^{2-} experience falls from 0.17 and 0.5 at 0.125 M to 0.08 and 0.28 at 1.5, respectively, while Na^+ has an increase to 0.64 at 1.5 M. The results of ion transport reveal that the immense hindrance causes the lack of NH_4^+ as an electron carrier, so the local concentration of NH_4^+ is extremely dilute, as this reported reference (Pal *et al.*, 2009). Therefore, increasing Na_2SO_4 concentration up to 0.5 M (> 0.5 M) is not suitable for the over-concentrated conditions.

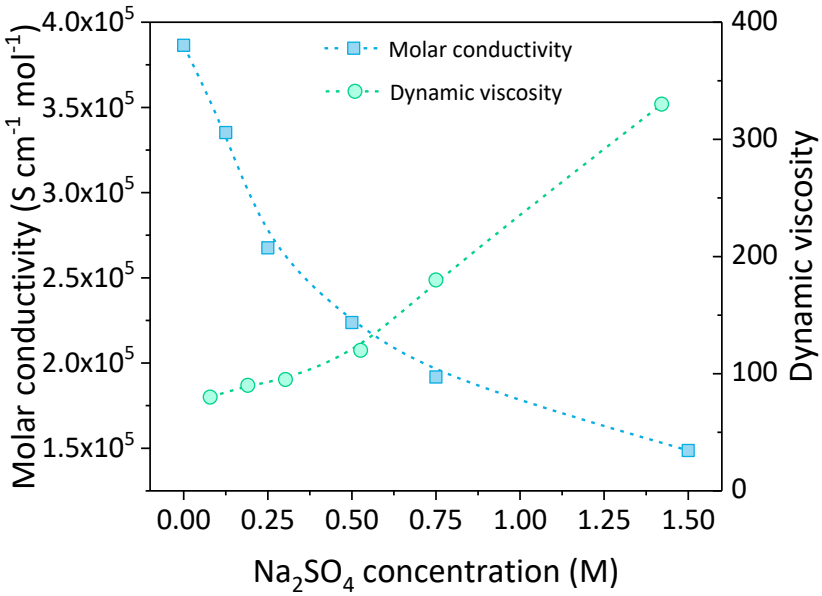

Figure 5-6 Molar conductivity and dynamic viscosity as a function of the Na_2SO_4 concentration (0.125 -1.5 M).

Table 5-3 Mobility and transport numbers of NH_4^+, Na^+, and SO_4^{2-} at 0–1.5 M Na_2SO_4

Na_2SO_4 Concentration (mol/L)	Mobility ($m^2 V^{-1} s^{-1}$) 10^{-8}			Transport Number		
	NH_4^+	Na^+	SO_4^{2-}	NH_4^+	Na^+	SO_4^{2-}
0.000	1.01	-	3.29	0.67	-	0.33
0.125	1.49	4.06	2.03	0.17	0.33	0.50
0.250	1.33	3.40	1.70	0.17	0.42	0.41
0.500	1.29	2.78	1.39	0.11	0.63	0.26
0.750	1.34	2.45	1.22	0.11	0.63	0.26
1.500	1.37	1.87	0.93	0.08	0.65	0.27
0.000	1.27	1.63	0.81	0.08	0.64	0.28

5.4.3 Ion transport in the electric double layer

1) Migration rate in electric double layer

NH_4^+ absorption in the cathode forms an NH_4^+ EDL, and its properties may be influenced by competition from its co-ions (Na^+ and H^+). As swept the CV curve at 0-0.8 V applied voltage, we excluded the competition from H^+. Hence, Na^+ was the dominant ion sharing the total current density with NH_4^+ in the cathode. The migration rates of NH_4^+ and Na^+ in the EDL were quantified using the MSD values of N and Na atoms in 0–1.5 M Na_2SO_4 solution as a function of time (0.5 ns). The average MSD slope of an N atom grows from 2.1874×10^3 at 0 M to 3.1687×10^3 at 0.25 M, but drops to 1.457×10^3 at 1.5 M (Table 5-4). The corresponding diffusion coefficient of NH_4^+ accelerates from 2.1874×10^{-9} m^2 s^{-1} at 0 M to 5.2812×10^{-9} m^2 s^{-1} at 0.25 M, but falls to 2.4319×10^{-9} m^2 s^{-1} at 1.5 M (Figure 5-7(a) and Figure 5-7(b)). The largest diffusion coefficient is obtained at 0.25 M. Na atoms have a similar trend to N atoms, and the maximum diffusion coefficient of Na^+ is 5.6987×10^{-9} m^2 s^{-1} at 0.25 M. In the over-concentrated Na_2SO_4 electrolyte (> 0.5 M), the migration coefficient of Na^+ (3.425×10^{-9} m^2 s^{-1}) is lower than that of NH_4^+ (3.456×10^{-9} m^2 s^{-1}), demonstrating that the concentrated Na^+ not only impedes NH_4^+ migration but also influences itself transport.

The comparison of diffusion coefficients between NH_4^+ and Na^+ demonstrates that adding Na^+ promotes NH_4^+ migration through increasing the conductivity at a diluted concentration ($c_{NH4+} > c_{Na+}$). This result can be explained by the Nernst-Einstein

equation that establishes the relationship between the molar limiting conductivity ($\Lambda_{m,i}^{0}$) and the diffusion coefficient D_i (Belonenko *et al.*, 2012).

$$D_i = \frac{RT}{z_i^2 F^2} \Lambda_{m,i}^{0} \tag{5-8}$$

where z_i , T, F, and R are charge number of ion i, absolute temperature, Faraday's constant, and the ideal gas constant, respectively. For the infinite dilution (non-interacting ions), conductivity relies linearly on diffusion coefficients. However, for the concentrated solution, this formula becomes somewhat more complicated. The diffusion coefficients of both Na^+ and NH_4^+ decrease as Na^+ increases ($C_{NH4+} < C_{Na+}$), which may be related to the charge neutralization of the EDL. Also, water is a contributor to the difference in the diffusion rate. Calculated from the average MSD slope of water molecules using Einstein's equation, the diffusion coefficient is 7.5×10^{-9} m^2 s^{-1}, indicating that water molecules have the fastest migration rate (Figure SI-4). As a result, the order of diffusion constants of NH_4^+, Na^+ and water is $D_{water} > D_{Na+} > D_{NH4+}$ in the diluted concentration, and $D_{water} > D_{NH4+} > D_{Na+}$ in the concentrated Na_2SO_4 solution.

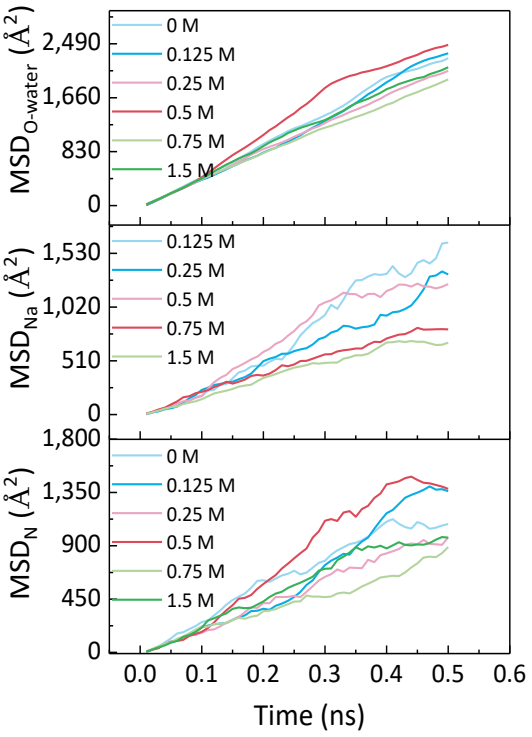

(a)

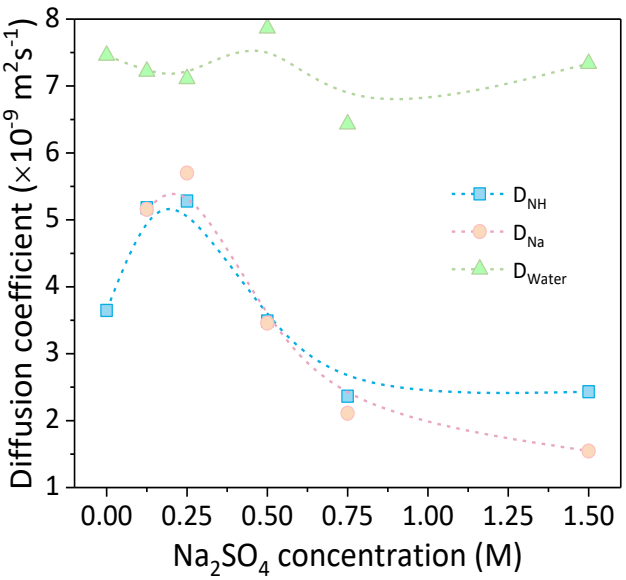

(b)

Figure 5-7 MSD values of N, Na and O-water in 0.5 ns (a); Diffusion rates of NH_4^+, Na^+, and H_2O molecules as a function of Na_2SO_4 concentration (b).

Table 5-4 The average slopes of NH_4^+, Na^+, and H_2O molecules at 0-1.5 M.

Na_2SO_4 Concentration	Ave. $Slope_{NH}$	Ave. $Slope_{Na}$	Ave. $Slope_{water}$
M		$\times 10^3$	
0.000	2.1874	--	4.4741
0.125	3.1079	3.0942	4.3306
0.250	3.1687	3.4192	4.2650
0.500	2.0929	2.0739	4.7187
0.750	1.4182	1.2659	3.8583
1.500	1.4591	0.9272	4.4006

2) Concentration distribution in electric double layer

Since $D_{NH4+} < D_{Na+}$, the concentration distributions of NH_4^+ and Na^+ may be quite different. Figure 5-8 shows the distributions of NH_4^+ and Na^+ mass density along the x-axis at the cathodic surface. Specifically, in the region nearest to the Pt surface, NH_4^+ density increases and presents the largest peak (0.016 g cm^{-3}), which is a compacted charge layer called the inner Helmholtz plane (IHP) (Lim *et al.*, 2013; Morita *et al.*, 2006). As the distance enlarges toward the bulk solution, NH_4^+ density decreases and displays the second peak (0.007 g cm^{-3}), considered the outer Helmholtz plane (OHP). When the distance becomes further from the Pt surface, NH_4^+ density continuously declines and ultimately stabilizes at 0.0045 g cm^{-3}, which is the diffusion layer (DL) (Cagle *et al.*, 2010) (Figure 5-8(a) and 5-8(b)). The distribution profile of Na^+ has similar peaks to that of NH_4^+ on the x-axis, whereas the peak of Na^+ increases from 0 g cm^{-3} at 0 M to 0.018 g cm^{-3} at 1.5 M with the bulk Na_2SO_4 electrolyte concentrate (Figure 5-8(c) and 5-8(d)). The concentration distribution comparison of NH_4^+ and Na^+ shows that the NH_4^+ density reduces from 0.016 g cm^{-3} to 0.003 g cm^{-3}, which is significantly lower than that of Na^+ at the relative concentration. The concentration profiles of NH_4^+ and Na^+ indicate that the shrunken peak of NH_4^+ reduction is caused by the competitive increase in Na^+ concentration, especially in the over-concentrated Na_2SO_4 electrolyte (>0.5 M).

To estimate the activated concentrations of NH_4^+ reduction in the EDL, the ion number densities (NH_4^+ and Na^+) were calculated based on their concentration profiles in the region of the Helmholtz plane (13.5 Å to 10.5 Å). The number density of NH_4^+ gradually drops from 0.00068 # $Å^{-3}$ to 0.0005 # $Å^{-3}$, which is much larger than that of

Na^+ (rising from 0 # $Å^{-3}$) as the bulk Na_2SO_4 electrolyte below 0.75 M. However, the number density of NH_4^+ dramatically declines to 0.00012 # $Å^{-3}$, fifteen folds lower than that of Na^+ (0.00188 # $Å^{-3}$) as the bulk Na_2SO_4 electrolyte increases to 1.5 M. The fall in the NH_4^+ number density signifies that the available NH_4^+ participating in reduction is reduced by Na^+ accumulation.

The phenomena above may be explained by $[NH_4^0]_{ads}$ repulsion. In Eq. 3-15, NH_4^+ reduction experiences the absorption of intermediates, $[NH_4^0]_{ads}$ and H_{ads}. $[NH_4^0]_{ads}$ adsorbed Rydberg radicals, and repulsed NH_4^+ solvent molecules approaching for additional binding. The accumulation of $[NH_4^0]_{ads}$ in the EDL leads to the NH_4^+ concentration reducing (Evleth & Kassab, 1988). Else, Na^+ (+1) absorbs O-water (-0.7982 in SPC/E) and forms an Na-H_2O hydration "atmosphere", which occupies the limited area of the EDL and results in the shrinkage of an available effective area for $[NH_4^0]_{ads}$ absorption (Laidler *et al.*).

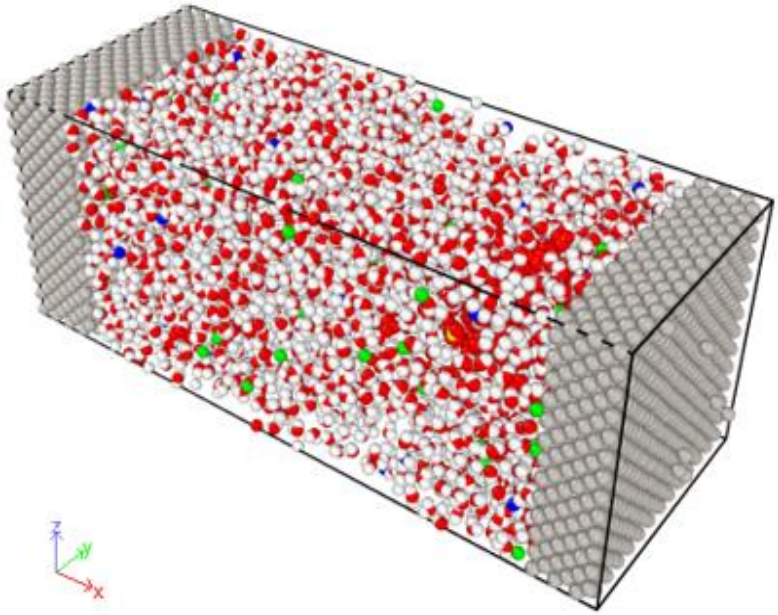

(a)

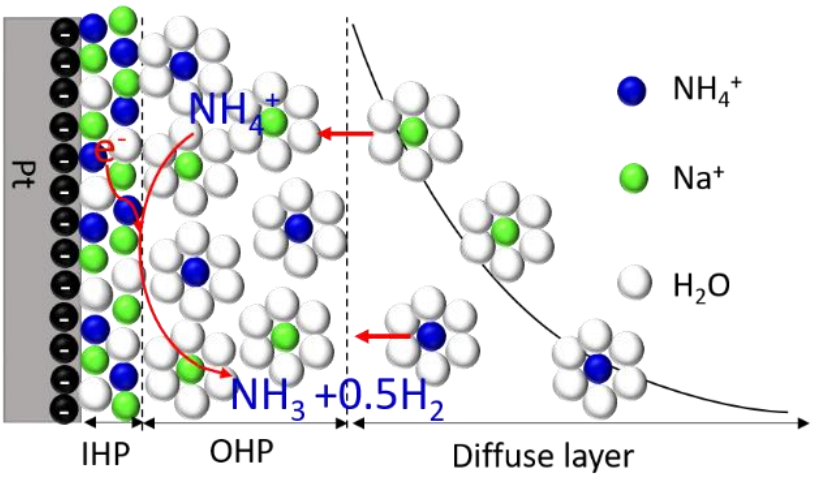

(b)

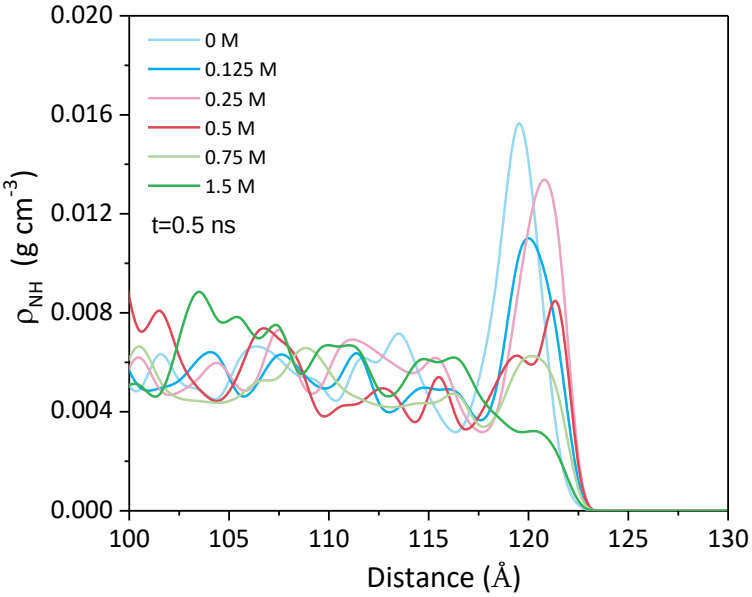

(c)

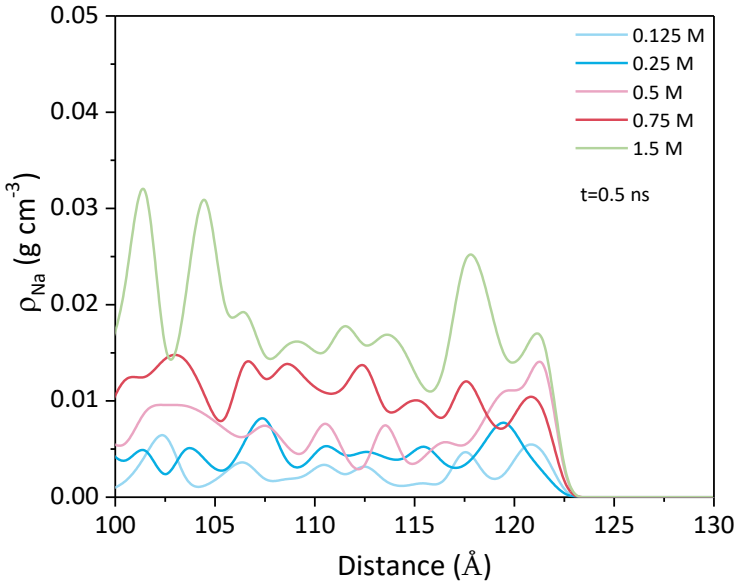

(d)

Figure 5-8 Single channel model of electrodeionization(a); NH_4^+ EDL film (b); concentration profiles of NH_4^+ and Na^+ as a function of Na_2SO_4 concentration (0 to 1.5 M) (c) and (d).

3) Properties of electric double layer

NH_4^+ accumulation forms an NH_4^+ EDL of which the electric properties (e.g., charge density, potential drop, capacitance, and thickness) of which can reflect the kinetics of NH_4^+ reduction. Figure 5-9(a) and 5-9(b) illustrates the charge density profiles and the potential drop of NH_4^+ and Na^+ in the range of 0–1.5 M. There are two pronounced peaks (0.0009 e $Å^{-3}$ and 0.0004 e $Å^{-3}$) referring to the IHP and OHP of the NH_4^+ charge density curve, in which the value of NH_4^+ potential changes from -0.0225 V to 0 V (Figure 5-9(c) and 5-9(d)). Integrating NH_4^+ charge in the x-axis, the charge density and potential drop of NH_4^+ film decline from 0.0041 e $Å^{-3}$ and -0.0226 V at 0 M to 0.0006 e $Å^{-3}$ and -0.0151 V at 1.5 M, respectively. Na^+ charge density and potential increase, but the Na^+ film peaks disappear as Na_2SO_4 becomes over-concentrated. The total charge density and potential drop shift from 0.0011 e $Å^{-3}$ and 0.0095 V to -0.0228 e $Å^{-3}$ and -0.0449 V, respectively, due to the negative charge carried by O in the H_2O molecule (Table 5-5). The decrease in charge density and potential drop of NH_4^+ slow the NH_4^+ reaction.

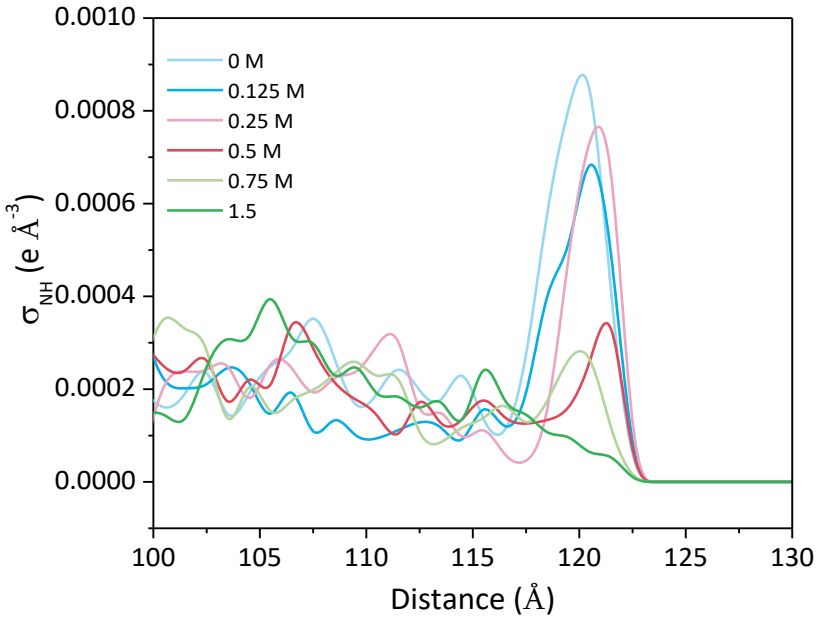
0.0010
0.0008
0.0006
0.0004
0.0002
0.0000
σNH (e Å-3)
0 M
0.125 M
0.25 M
0.5 M
0.75 M
1.5
100
105
110
115
120
125
130
Distance (Å)

(a)

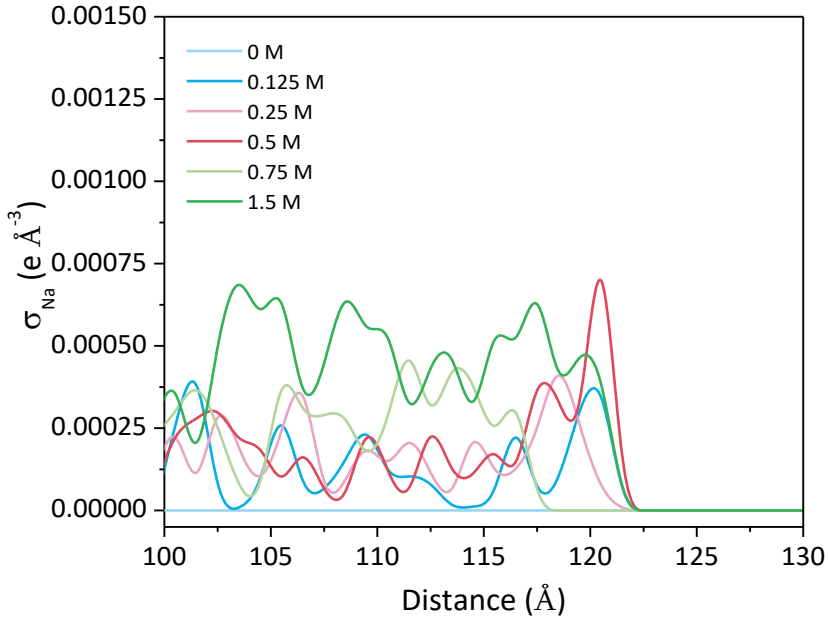
0.00150
0.00125
0.00100
0.00075
0.00050
0.00025
0.00000
σNa (e Å-3)
0 M
0.125 M
0.25 M
0.5 M
0.75 M
1.5 M
100
105
110
115
120
125
130
Distance (Å)

(b)

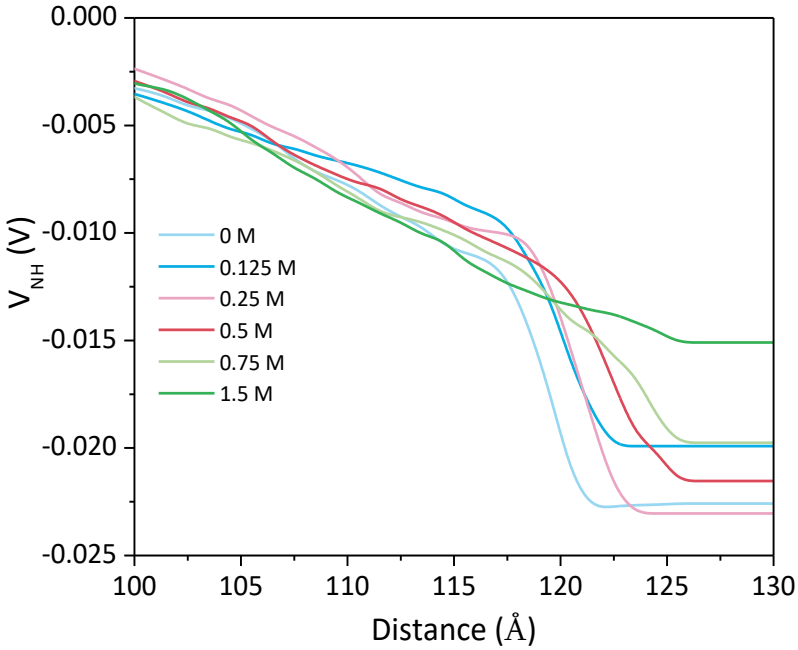

(c)

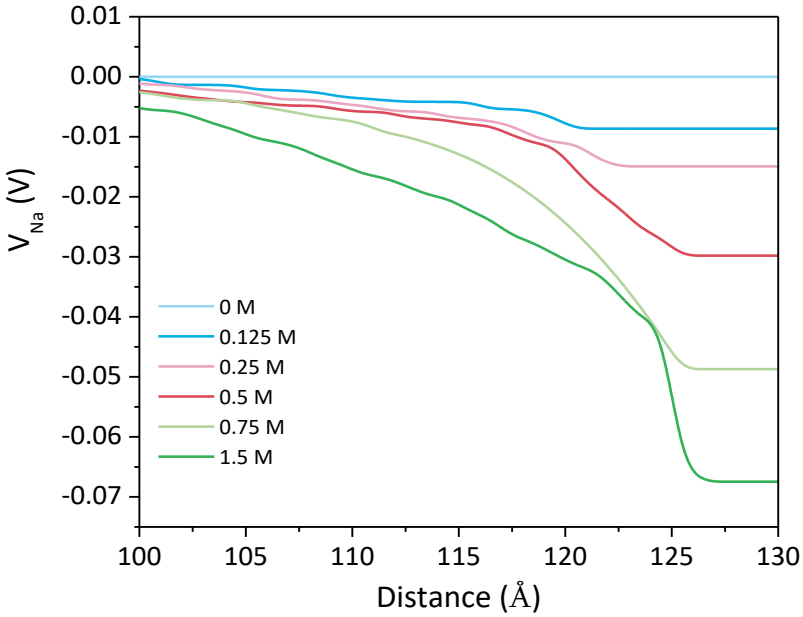

(d)

Figure 5-9 Charge density distributions (a) and (b); Potential NH_4^+ and Na^+ drops along the x-axis under 0 to 1.5 M Na_2SO_4 (c) and (d).

Table 5-5 Electric properties of NH_4^+ film and EDL capacitance

Na_2SO_4 Concentration	Charge Density (e Å^{-3})				Potential Drop (V)				EDL Capacitance
M	NH_4^+	Na^+	H_2O	Total	NH_4^+	Na^+	H_2O	Total	($\times 10^{-19}$ F Å^{-3})
0.000	0.0041	0.0000	-0.0030	0.0011	-0.0226	0.0	0.0321	0.0095	0.1795
0.125	0.0030	0.0013	-0.0083	-0.0040	-0.0220	-0.0086	0.0252	-0.0054	1.1920
0.250	0.0026	0.0015	-0.0125	-0.0083	-0.0230	-0.0149	0.0231	-0.0149	0.8939
0.500	0.0016	0.0024	-0.0235	-0.0194	-0.0215	-0.0298	0.0262	-0.0251	1.2363
0.750	0.0013	0.0010	-0.0312	-0.0290	-0.0198	-0.0487	0.0276	-0.0409	1.1321
1.500	0.0006	0.0031	-0.0265	-0.0228	-0.0151	-0.0645	0.0347	-0.0449	0.8117

Based on the total charge density and potential drop, the relative thicknesses of NH_4^+ and Na^+ EDL as the function of Na_2SO_4 concentration are summarized in Table 5-6. The total thickness of NH_4^+ experiences a slight rise from 19.0 Å at 0 M to 21.0 Å at 0.25 M and an apparent decrease to 16.0 Å at 1.5 M. In the Na_2SO_4 concentrate, the IHP declines to 4.0 Å from 6.0 Å; the OHP increases to 8.5 Å at 0.25 M but decreases to 6.5 Å; and DL varies from 5.5 to 7.0 Å. The comparison of IHP, OHP, and DL reveals that Na_2SO_4 concentration has a greater influence on the Helmholtz layer (IHP and OHP) than the diffusion layer. The total Na^+ thickness increases from 0 Å at 0 M to 23.5 Å at 1.5 M. Similarly, the Helmholtz layer is thicker than the DL. These variations are majorly attributed to the excess accumulation of ions from the diffusion layer and the insufficient supply of ions from the bulk solution (Brown *et al.*, 2016; Kallay *et al.*, 2010; Mahanta & Mishra, 2012). Taking the thickness overlap of NH_4^+ and Na^+ into consideration, the total EDL thickness increases from 19.5 Å at 0 M to 23.5 Å at 1.5 M. According to the Debye–Hückel equation, the charge density of Na^+ absorption causes an increase in the Na^+ EDL (Scholz, 2010). The thick Na^+ layer should have blocked the rate of electron transfer of NH_4^+ reduction in experiments. And the lack of an electron acceptor thus may result in the current density peak of NH_4^+ reduction decreasing. As integrating the experimental and theoretical results of this paper, we find that the increase in the concentration of Na_2SO_4 electrolyte changes the current density of ammonium reduction (from -0.023 mA cm^{-2} to -0.005 mA cm^{-2} at 0.23 V), the diffusion coefficients of water, NH_4^+, and Na^+ ($D_{water} > D_{NH4+} > D_{Na+}$), and the thickness of EDL (from 19.0 Å at 0 M to 23.5 Å at 1.5 M).

Table 5-6 EDL structures and thicknesses (NH_4^+ and Na^+)

Na_2SO_4 Concentration	NH_4^+ Layer (Å)			Na Layer (Å)			Total Thickness
(M)	IHP	OHP	DL	IHP	OHP	DL	(Å)
0.000	6.0	7.5	5.5	--	--	--	19.0
0.125	5.5	8.0	6.0	4.5	4.0	7.5	19.5
0.250	5.5	8.5	7.0	6.0	6.0	6.5	21.0
0.500	5.0	7.0	5.0	8.5	8.5	7.0	24.0
0.750	5.0	6.5	6.0	8.0	7.0	6.0	21.0
1.500	4.0	6.5	5.5	7.5	8.5	7.5	23.5

5.4.4 Hydrogen bond formation in over-concentrated electrolyte

Due to the concentration gradient decrease in NH_4^+, NH_4^+ ion is expected to have a slower migration rate than Na^+ ion. However, a reversible result of NH_4^+ moving faster than Na^+ at >0.5 M Na_2SO_4 after 0.2 ns is an unreported finding. Possible reasons for this are: (1) the smaller size of NH_4^+ (3.31 Å < 3.58 Å) contributes to a larger diffusion coefficient (2.43×10^{-9} m^2 s^{-1} > 1.54×10^{-9} m^2 s^{-1}) (Bohinc *et al.*, 2001); (2) an ionic atmosphere Na-H_2O layer formed via the interaction of Na^+ and H_2O blocks Na^+ transport; and (3) hydrogen bonds are pervasive, which affects water self-diffusion to restrain Na-H_2O diffusion. To reveal this unexpected observation, the RDF of g_{OwHw} (r) was performed (Figure 5-10). The largest peak centers at 4.10 Å and a small peak related to hydrogen bonds appears at 2.14 Å, whereas the g_{NHw}(r) peak centers at 3.83 Å and an insignificant peak appears at the same position, illustrating that the hydrogen bond interaction in NH_4^+ appears much weaker than in water (Ricci *et al.*, 1995). This finding supports the third possible reason. Nelson *et al*. (1987) supported this one, as they found the radius of O-H… :O (2.05 Å) and the energy of O-H… :O (21 kJ mol^{-1}) between H_2O molecules (Nelson *et al.*, 1987). Regarding the second possible reason, due to the ionic Na-H_2O atmosphere built up via the interaction of Na^+ and H_2O, the force of the hydrogen bond network impedes Na-H_2O migration (Hongsirikarn, 2010; Nelson *et al.*, 1987; Van Aken *et al.*, 2014). As shown in Table 5-5, water's charge density increases with Na^+ concentration, which can lead to more hydrogen bonds. These complex interactions demonstrate that the over-concentrated Na_2SO_4 electrolyte generates adverse effects on both NH_4^+ and Na^+ migration.

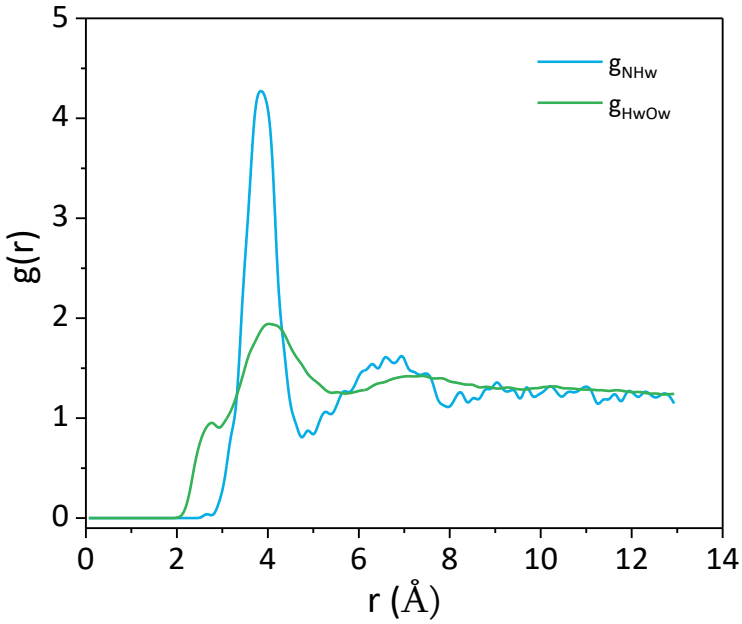

Figure 5-10 Partial NHw and OwHw radial distribution functions obtained at 0.5 M Na_2SO_4.

5.5 Summary

This chapter discussed the effects of Na_2SO_4 supporting electrolytes from 0 M to1.5 M on NH_4^+ reduction in the cathode of EDI using electrochemical analysis MD simulations. The results indicate that although Na_2SO_4 enhances the conductivity and total current, it undermines the NH_4^+ reduction ($NH_{4\,(aq)}^{+} + e^{-} \rightarrow 0.5H_{2(g)} + NH_{3(g)}$). The deteriorated NH_4^+ reduction is caused by the large viscous resistance and the fierce competition from co-ion (Na^+). In concentrated Na_2SO_4 (>0.5 M), the competitive absorption of Na^+ forms a thick layer that blocks NH_4^+ migration and electron transportation in the EDL. The co-ion concentration of the supporting electrolyte (Na_2SO_4) should be less than 0.25 M for NH_4^+ recovery optimization. The migration rate of NH_4^+ (2.43×10^{-9} m^2 s^{-1} at 0.25 M) is faster than that of Na^+ (1.54×10^{-9} m^2 s^{-1} at 0.5 M) probably due to hydrogen bonds. Interestingly, water molecules play a critical role in determining the net charge density and potential drop. The mechanisms present here to disclose the co-ion competition and allow the manipulation of EDI capacity optimization.

5.6 References

Alvarado, & Chen. (2014). Electrodeionization: principles, strategies and applications. *Electrochimica Acta, 132*, 583-597.

Belonenko, Lebedev, & Sudorgin. (2012). Electrical conductivity and diffusion coefficient of electrons in a graphene bilayer. *Technical Physics, 57*(7), 1025-1029.

Bohinc, Kralj-Iglič, & Iglič. (2001). Thickness of electrical double layer. Effect of ion size. *Electrochimica Acta, 46*(19), 3033-3040.

Brown, Goel, & Abbas. (2016). Effect of electrolyte concentration on the stern layer thickness at a charged interface. *Angewandte Chemie International Edition, 55*(11), 3790-3794.

Cagle, Feng, Qiao, Huang, Sumpter, & Meunier. (2010). Structure and charging kinetics of electrical double layers at large electrode voltages. *Microfluidics and Nanofluidics, 8*(5), 703-708.

Casadellà, Schaetzle, Nijmeijer, & Loos. (2016). Polymer inclusion membranes (PIM) for the recovery of potassium in the presence of competitive cations. *Polymers, 8*(3), 76.

Evleth, & Kassab. (1988). Role of Rydberg radicals in electrochemistry. *Pure and Applied Chemistry, 60*(2), 209-214.

Frenkel, & Smit. (2001). *Understanding molecular simulation: from algorithms to applications* (Vol. 1): Academic press.

Hongsirikarn. (2010). *Effect of impurities on performance of proton exchange membrane fuel cell components.* Clemson University,

Jiang, Cheng, Li, & Liu. (2016). Molecular dynamics simulations of the electric double layer capacitance of graphene electrodes in mono-valent aqueous electrolytes. *Nano Research, 9*(1), 174-186.

Joly, Ybert, Trizac, & Bocquet. (2004). Hydrodynamics within the electric double layer on slipping surfaces. *Physical Review Letters, 93*(25), 257805.

Kallay, Preočanin, Kovačević, Lützenkirchen, & Chibowski. (2010). Electrostatic potentials at solid/liquid interfaces. *Croatica Chemica Acta, 83*(3), 357-370.

Krishnamurthy, Bhattacharya, Phelan, & Prasher. (2006). Enhanced mass transport in nanofluids. *Nano Letters, 6*(3), 419-423.

Laidler, Meiser, & Bryan. (2003). *Physical Chemistry* Houghton Mifflin: Boston, MA.

Lee, Templeton, Mandadapu, & Zimmerman. (2013). Comparison of molecular and primitive solvent models for electrical double layers in nanochannels. *Journal of Chemical Theory and Computation, 9*(7), 3051-3061.

Lim, Lu, Chen, & Qiao. (2013). Effects of ion concentration on thermally-chargeable double-layer supercapacitors. *Nanotechnology, 24*(46), 465401.

Little, Smith III, & Hamann. (2015). Electrolysis of liquid ammonia for hydrogen generation. *Energy & Environmental Science, 8*(9), 2775-2781.

Liu, Qin, Luo, He, & Qiao. (2016). Understanding ammonium transport in bioelectrochemical systems towards its recovery. *Scientific Reports, 6.*

Ma, Wang, Gao, & Gao. (2014). Charge and separation characteristics of nanofiltration membrane embracing dissociated functional groups. *Frontiers of Environmental Science & Engineering, 8*(5), 650-658.

Mahanta, & Mishra. (2012). Estimation of electric double layer thickness from linearized and nonlinear solutions of Poisson–Boltzman equation for single type of ions. *Applied Clay Science, 59*, 1-7.

Moon, & Yun. (2014). Process integration of electrodialysis for a cleaner environment. *Current Opinion in Chemical Engineering, 4*, 25-31.

Morita, Kaigaishi, Yoshimoto, Egashira, & Aida. (2006). Effects of the electrolyte composition on the electric double-layer capacitance at carbon electrodes. *Electrochemical and Solid-State Letters, 9*(8), A386-A389.

Mousavi, Wilson, Kashefolgheta, Anderson, He, Bühlmann, & Stein. (2007). *Mousavi, M. P., Wilson, B. E., Kashefolgheta, S., Anderson, E. L., He, S., Bühlmann, P., & Stein, A.* . Retrieved from

Mousavi, Wilson, Kashefolgheta, Anderson, He, Bühlmann, & Stein. (2016). Ionic liquids as electrolytes for electrochemical double-layer capacitors: Structures that optimize specific energy. *ACS Applied Materials & Interfaces, 8*(5), 3396-3406.

Nelson, Fraser, & Klemperer. (1987). Does ammonia hydrogen bond. *Science, 238*(4834), 1670-1674.

Olson, & Bühlmann. (2013). Unbiased Assessment of Electrochemical Windows: Minimizing Mass Transfer Effects on the Evaluation of Anodic and Cathodic Limits. *Journal of The Electrochemical Society, 160*(2), A320-A323.

Pal, Dhar, See, & Katz. (2009). Solution-deposited sodium beta-alumina gate dielectrics for low-voltage and transparent field-effect transistors. *Nature Materials, 8*(11), 898.

Pezeshki, & Lin. (2014). Molecular dynamics simulations of ion solvation by flexible ‐ boundary QM/MM: On ‐ the ‐ fly partial charge transfer between QM and MM subsystems. *Journal of Computational Chemistry, 35*(24), 1778-1788.

Ricci, Nardone, Ricci, Andreani, & Soper. (1995). Microscopic structure of low temperature liquid ammonia: A neutron diffraction experiment. *The Journal of Chemical Physics, 102*(19), 7650-7655.

Rosasco, Stickney, Salaita, Frank, Katekaru, Schardt, . . . Hubbard. (1985). Cation competition in the electrical double-layer at a well-defined electrode surface Li+, Na+, K+, Cs+, H+, Mg2+, Ca2+, Ba2+, La3+, tetramethylammonium, choline and acetylcholine cations at Pt (111) surfaces containing an ordered

layer of cyanide. *Journal of Electroanalytical Chemistry and Interfacial Electrochemistry, 188*(1-2), 95-104.

Ryckaert, Ciccotti, & Berendsen. (1977). Numerical integration of the cartesian equations of motion of a system with constraints: molecular dynamics of n-alkanes. *Journal of Computational Physics, 23*(3), 327-341.

Savelyev, & MacKerell Jr. (2015). Competition among Li+, Na+, K+, and Rb+ monovalent ions for DNA in molecular dynamics simulations using the additive CHARMM36 and Drude polarizable force fields. *The Journal of Physical Chemistry B, 119*(12), 4428-4440.

Scholz. (2010). *Electroanalytical methods* (Vol. 1): Springer.

Simons, Cairns, & Surd. (1969). The performance of direct ammonia fuel cells. *Journal of The Electrochemical Society, 116*(5), 556-561.

Soetardji, Claudia, Ju, Hriljac, Chen, Soetaredjo, . . . Ismadji. (2015). Ammonia removal from water using sodium hydroxide modified zeolite mordenite. *RSC Advances, 5*(102), 83689-83699.

Van Aken, McDonough, Li, Feng, Chathoth, Mamontov, . . . Gogotsi. (2014). Effect of cation on diffusion coefficient of ionic liquids at onion-like carbon electrodes. *Journal of Physics: Condensed Matter, 26*(28), 284104.

Vossen, & Forstmann. (1995). Integral equation theory for the electrode-electrolyte interface with the central force water model. Results for an aqueous solution of sodium chloride. *Molecular Physics, 86*(6), 1493-1516.

Wenten, Khoiruddin, Aryanti, & Hakim. (2016). Scale-up Strategies for Membrane-Based Desalination Processes: A Review. *Journal of Membrane Science and Research, 2*(2), 42-58.

Yoon, Jang, Bok, & Oh. (2005). Complex capacitance analysis on rate capability of electric-double layer capacitor (EDLC) electrodes of different thickness. *Electrochimica Acta, 50*(11), 2255-2262.

Yoshida, & Imoto. (1992). Electric double layer capacitor and method for producing the same. In: Google Patents.

CHAPTER 6 CONCLUSIONS

6.1 Key findings and conclusions

Under the context of eliminating environmental pollution and offsetting fossil fuel consumption in the word, this study initiated a hybrid system, AD-EDI-SOFCs. It was used to directly generate electricity from carbonaceous and nitrogenous pollutants in wastewater and landfills. These pollutants were transforms into biogas, hydrogen, and ammonia via AD or EDI. The produced fuels were used as the fuels of SOFCs through direct reduction or gas reformation. To improve EDI performances, parameter optimizations including the applied voltage, the internal electrode distance, and the NH_4^+-N concentration were carried out through lab-scale experiments. The optimized results and energy benefits were presented in Chapter 3.

1) For batch tests, EDI removes 76-95% nitrogen from 0.025-0.5 M NH_4^+-N synthetic sewage. The optimal conditions of EDI are 3.0 V applied voltage and 7.5 mm IED and 0.25 M NH_4^+-wastewater, which contributes to > 70% NH_4^+ recovery. EBR reaches 1.13 from 0.50 at the relevant concentrations.

2) During NH_4^+ deionization process, an interesting finding is that NH_4^+ reduction in the cathode facilitates NH_3 and H_2 generation at 0.23 V vs. Ag/AgCl

reference electrode. NH_4^+ reduction occurs at room temperature and its products content H_2, which increases H_2 generation.

3) For landfill leachate treatment, EDI-SOFC enhances EBR from 1.11 to 1.75 using the mixture fuels of NH_3, H_2 and landfill gas. EDI removes 80% inorganic ions (heavy metals and nutrient elements) from raw landfill leachate. These results suggest that EDI-SOFCs hybrid anaerobic treatment is a promising process for energy extraction from both carbonaceous and nitrogenous pollutants.

According to the assessment of AD-EDI-SOFCs energy consumption, EDI depleted more than 56% of total energy to extracted and converted NH_4^+ to NH_3. Such a high percentage of energy consumption was thought to be related to the weak conductivity of the NH_4^+ ion and the concentration polarization of ion exchange membrane under at different concentrations of the supporting electrolyte (0.125-0.75 M Na_2SO_4). The related theoretical calculation and experimental tests and corresponding findings were shown in Chapter 4.

1) Under 0.125-0.75 M Na_2SO_4 supporting electrolyte, the EDI has the different current density at the range of 2.0 mA cm^{-2} to 7.0 mA cm^{-2}.

2) An increase in the Na_2SO_4 concentration results in a decrease in the NH_4^+ concentration in the left-side boundary layer and increases in the NH_4^+ and SO_4^{2-} concentration in the right-side boundary layer. The simulated results indicate that the effect of dilute supporting electrolyte on the concentration polarization is less than that of concentrated supporting electrolyte.

3) The experimental results elaborate that the distributions of these two ions contribute to increases in LCD from 14 mA cm^{-2} to 20 mA cm^{-2}, in total boundary layer thickness from 370 μm to 430 μm, and in potential drop from 0.2 V to 2.0 V, but a decrease in total resistance from 50 Ω to 34 Ω under 0.125-0.75 M Na_2SO_4 electrolyte.

4) For dilute Na_2SO_4 (< 0.5 M), the resistance of the bulk solution is dominant. For concentrated Na_2SO_4 (> 0.75 M), the resistance of the bulk solution does not increase with Na_2SO_4 concentration increase so that the resistance of the boundary layer is dominant. Water dissociation much easier occurs under the concentrated Na_2SO_4 electrolyte than the diluted Na_2SO_4 electrolyte.

Also, NH_4^+ reduction in the cathode was found as well, and its reduction peak decayed with the increase in the Na_2SO_4 concentration. To profoundly understand this mechanism, the behaviors of the NH_4^+ ion and the competition from co-ion (Na^+) were described through MD simulations at the different concentrations of the supporting electrolyte (0-1.5 M Na_2SO_4). The related study and its results were demonstrated in Chapter 5.

1) Adding Na_2SO_4 enhances the conductivity and electric current of the system but simultaneously slows NH_4^+ transport in the bulk solution and the EDL.

2) The intense competition from co-ion (Na^+) reduces mass density, charge density and potential drop of NH_4^+ in the EDL. The excess accumulated Na^+ ion forms a thick layer that impedes electron transfer between NH_4^+ and the Pt electrode.

3) Water molecules surrounding the cation ions plays a critical role in determining the net charge density and potential drop. Hydrogen bond formation leads to the migration rate of NH_4^+ (2.43×10^{-9} m^2 s^{-1} at 0.25 M) faster than that of Na^+ (1.54×10^{-9} m^2 s^{-1} at 0.5 M) probably due to hydrogen bonds.

4) The co-ion concentration of supporting electrolyte should be lower than the concentration of reactant if it participates in electrochemical reactions at the electrode. On the contrary, it should be large as much as possible if ions need to be protected from oxidation or reduction at the electrodes.

6.2 Future work

Although this thesis summarized important research and key findings of this project on energy generation from carbonaceous and nitrogenous pollutants via AD-EDI-SOFCs system, some new phenomena discovered during experiments and simulation have not yet been given 100% rational and fundamental explains due to time limitation and other reasons. To obtain a full potential picture of AD-EDI-SOFCs in energy reutilization from NH_4^+-N wastewater/landfill leachate, future research areas are suggested as follows:

1) Operating parameters are exactly crucial for the deionization efficiency. So, research can be carried out on temperature, flow rate, type of ion exchange membrane, electrode materials, etc. These factors affecting the performances of EDI need to be optimized.

2) The exchange rate of NH_4^+ with its counter ion in the cation exchange membrane plays significant roles in the efficiency of NH_4^+ recovery. The

dynamics of NH_4^+ selectively crossing cation exchange membrane can be studied using MD simulations.

3) Because concentration polarization creates large potential drop, water dissociation takes place, even forms a lot of bubbles at the ion exchange membrane. What consequences will be brought by water dissociation still keeps blank. Hence, this area and the approaches to alleviate water dissociation should be the research focuses.

4) NH_4^+ reduction in the cathode is regarded as a three-step process. However, the variation of Gibbs free energy and the transition state of intermediates have not yet been confirmed. So, I suggest that DFT combined MD simulation can be used to study NH_4^+ reduction at the cathode.

APPENDIX I

Operation Parameters in Comsol 5.2

Wcom	0.5[cm]	Channel width
Hcom	6[cm]	Channel height
Wmem	150[um]	Membrane thickness
kH2O	1[mol/m^3/s]	Reaction rate H2O
kNH3	1[mol/m^3/s]	Reaction rate NH3
Vtot	1[V]	Total potential drop over unit cell
DNH4+	1.63e-9[m^2/s]	Diffusion coefficient, NH4+
DSO42-	2.23e-9[m^2/s]	Diffusion coefficient, SO42
T	298.15[K]	Temperature
DNa+	1.98e-9[m^2/s]	Diffusion coefficient, Na+
DSO42-	2.23e-9[m^2/s]	Diffusion coefficient, SO42-a
cNH4+	0.5[mol/L]	NH4+ concentration
cSO42-a	0.5*cNH4	Anode SO42-
cNa	0.5[mol/L]	Na+ concentration
cSO42-	0.5*cNa	Cathode SO42-
cNa_m	1[mol/dm^3]	Membrane charge concentration, Na+
cSO4_m	0.5*cNam	Membrane charge concentration, SO42-
sigma_el	1[S/m]	Electrolyte conductivity

sigma_m	1[S/m]	Membrane conductivity
ep_mem	1	Membrane porosity
DH_mem	1[m^2/s]	Diffusion coefficient in membrane, H+
DNH4_mem	1[m^2/s]	Diffusion coefficient in membrane, NH4+
DNa_m	1.2[m^2/s]	Diffusion coefficient in membrane, Na+
DSO42-_m	2.25[m^2/s]	Diffusion coefficient in membrane, SO42-
v_avg	0.005[m/s]	Channel average flow velocity
F	96485.33289[C/mol]	Faraday constant
R	8.3144598[J/(K*mol)]	Gas constant

APPENDIX II

1. Simulation package set-up

LAMMPS is an acronym for Large-scale Atomic/Molecular Massively Parallel Simulator. It distributed as an open source code under the terms of the GPL running on single processors or in parallel using message-passing techniques and a spatial-decomposition of the simulation domain. The code contains the necessary commands and mathematical formulas to precede molecular interactions. It also is designed to be easy to modify or extend with new functionality. The current version can be downloaded here (http://lammps.sandia.gov/download.html). Select the code the users want, click the "Download Now" button, and the user browser should download a gzipped tar file. Unpack it with the following commands and look for a README to get started.

```
tar -xzvf file.tar.gz
```

“Commands” section is the most important to successfully process LAMMPS simulations, which gives descriptions how a LAMMPS input script is formatted and the input script commands used to define a LAMMPS simulation. This section includes LAMMPS input script, parsing rules, input script structure, commands listed by

category, individual commands, fix styles, compute styles, potentials of pair, bond, angle, dihedral, and improper, kspace solvers, etc.

2. Computer code explanations and modification

Model construction

EDI non-membrane system was build up in Material Studio package. Similarly, Material Studio package can run on single processors or in parallel. The lasts version (Materials Studio 8.0) can be downloaded from this website (http://accelrys.com/resource-center/downloads/updates/materials-studio). Unpack the WinRar file to find following files and double click on the setup file to begin installation. Following the Material Studio User Installation Guide, click Next until Final. Go to Start Menu >>All Programs >>Accelrys and Launch Materials Studio 8.0 (Visualizer) and check for different Modules in modules tab.

```
Forcite
-------
Task             : Energy
Version          : 8.0
Build date       : Dec  5 2014
Host             : LAPTOP-STE37EQ7
Threads          : Scalar
Operating system : Windows
Task started     : Thu Jan 19 01:37:23 2017

---- Energy parameters ----
```

```
Forcefield                      : cvff (Version 2.4)

Charges                         : Forcefield assigned

Electrostatic terms:

  Summation method              : Ewald

  Accuracy                      : 0.0001 kcal/mol

  Buffer width                  : 0.5 A


van der Waals terms:

  Summation method              : Atom based

  Truncation method             : Cubic spline

  Cutoff distance               : 15.5 A

  Spline width                  : 1 A

  Long range correction         : YES

  Buffer width                  : 0.5 A



---- Current structure ----


Total energy                    :     -366837.879463 kcal/mol


Contributions to total energy (kcal/mol):

  Valence energy (diag. terms)  :         344.358

    Bond                        :         215.070

    Angle                       :         129.288

    Torsion                     :           0.000
```

```
    Inversion                    :           0.000
  Valence energy (cross terms)   :         -46.669
    Stretch-Stretch              :          -2.699
    Stretch-Bend-Stretch         :         -43.970
    Bend-Bend                    :           0.000
    Torsion-Bend-Bend            :           0.000
  Non-bond energy                :     -367135.569
    van der Waals                :     -362649.308
    Long range correction        :        -786.222
    Electrostatic                :       -3700.039



Task terminated                : Thu Jan 19 01:37:27 2017
Total CPU time used by Forcite: 4 seconds (3.53s)


Termination status : Normal
```

LAMMPS data File

0.25 M $(NH_4)_2SO_4$ and 0.25 Na_2SO_4

```
LAMMPS data file. msi2lmp v3.9.8 / 06 Oct 2016 / CGCMM for
/afs/crc.nd.edu/user/x/xlinji/lammps-17Nov16/tools/msi2lmp/Pt_Sol/Ptsalt_0.25


  17398 atoms

   8504 bonds

   4756 angles

      0 dihedrals

      0 impropers


   8 atom types

   3 bond types

   3 angle types

   2 improper types


     1.638830000   137.855000000 xlo xhi

    -1.075635747    50.461090150 ylo yhi

    -1.230750256    50.443012424 zlo zhi


Masses


   1  15.999400 # o*

   2   1.007970 # hw

   3  14.006700 # n+

   4   1.007970 # h+
```

```
   5  22.990000 # Na
   6  15.999400 # o
   7  32.064000 # s
   8 195.090000 # Pt

Pair Coeffs # lj/class2/coul/long

   1   0.2740000000   3.6080000000 # o*
   2   0.0130000000   1.0980000000 # hw
   3   0.0650000000   3.2620000000 # n+
   4   0.0130000000   1.0980000000 # h+
   5   0.7380000000   3.9624000000 # Na
   6   0.2400000000   3.5350000000 # o
   7   0.0710000000   4.0270000000 # s
   8   9.1447000000   2.9034000000 # Pt

Bond Coeffs # class2

   1      0.9700   563.2800 -1428.2200  1902.1200 # o*-hw
   2      1.0119   448.6300  -963.1917  1248.4000 # n+-h+
   3      0.0000     0.0000     0.0000     0.0000 # o-s

Angle Coeffs # class2

   1   103.7000    49.8400   -11.6000    -8.0000 # hw-o*-hw
   2   106.1100    45.3280   -14.0474     1.9350 # h+-n+-h+
```

```
  3      0.0000      0.0000      0.0000      0.0000 # o-s-o

Improper Coeffs # class2

  1      0.0000      0.0000
  2      0.0000      0.0000

Bond Bond Coeffs

  1     -9.5000      0.9700      0.9700
  2      2.8266      1.0119      1.0119
  3      0.0000      0.0000      0.0000

Bond Angle Coeffs

  1     22.3500     22.3500      0.9700      0.9700
  2     10.1080     10.1080      1.0119      1.0119
  3      0.0000      0.0000      0.0000      0.0000

Angle Angle Coeffs

  1     -1.9852     -1.9852     -1.9852    106.1100    106.1100    106.1100
  2      0.0000      0.0000      0.0000      0.0000      0.0000      0.0000
```

*The coordinates of all atoms are ignored because of space limitation.

LAMMPS input file

```
units              real

dimension          3

boundary           p   p   p

atom_style         full

pair_style         hybrid lj/cut/coul/long 13.0 morse 10.0

pair_modify        tail no mix arithmetic

kspace_style       pppm 1.0e-5

bond_style         harmonic

angle_style        harmonic


read_restart       restart4.nvt


pair_coeff   1   1     lj/cut/coul/long       0.2740000000        3.6080000000
#o*      o*

pair_coeff   2   2     lj/cut/coul/long       0.0130000000        1.0980000000
#hw      hw

pair_coeff   3   3     lj/cut/coul/long       0.0650000000        3.2620000000
#n+      n+

pair_coeff   4   4     lj/cut/coul/long       0.0130000000        1.0980000000
#h+      h+

pair_coeff   5   5     lj/cut/coul/long       0.7380000000        3.9624000000
#Na      Na

pair_coeff   6   6     lj/cut/coul/long       0.2400000000        3.5350000000
#o       o

pair_coeff   7   7     lj/cut/coul/long       0.0710000000        4.0270000000
#s       s

pair_coeff   8   8     morse                  13.00000000          1.583000000
3.02420000                                #Pt      Pt
```

```
pair_coeff   1   8      lj/cut/coul/long          0.1481             3.1810
# Pt   o*

pair_coeff   2   8      lj/cut/coul/long          0.0322             1.9260
# Pt   hw

pair_coeff   3   8      lj/cut/coul/long          0.0721             3.0080
# Pt   n+

pair_coeff   4   8      lj/cut/coul/long          0.0322      1.9260          #
Pt   h+

pair_coeff   5   8      lj/cut/coul/long          0.2430      3.3582          #
Pt   Na

pair_coeff   6   8      lj/cut/coul/long          0.1386      3.1445          #
Pt   o

pair_coeff   7   8      lj/cut/coul/long          0.0754      3.3905          #
Pt   s



group sol type 1 2 3 4 5 6 7

group Pt type 8

group Ow type 1

group Hw type 2

group N type 3

group Hn type 4

group Na type 5

group Os type 6

group S type 7


#---------------neighborlist-----------------------------------

#minimize 0.0 1.0e-8 100000 10000000
```

```
neighbor        4.0 bin

neigh_modify delay 0 every 20 check yes

#write_data MinPtsalt_0.25M.data

#---------------trajectory output--------------------------------

restart 2000 res1.1 res1.2

dump 1 all xyz 2000 Ptsalt_0.25Mnve.xyz

dump_modify 1 element o h n h Na o s Pt



#--------------variable definition and initilization------------

variable vtimpstep equal 0.5

timestep $[vtimpstep]

variable Pdamp  equal  $[vtimpstep]*100

variable Tdamp  equal  $[vtimpstep]*100


#----------------log output and NVT equilibrium----------------

thermo 20000

thermo_style custom step temp epair emol etotal pe press ke lx ly lz

thermo_modify flush yes



fix 1 sol shake 1.0e-5 100 0 b 1 a 1


#fix NPT3 all npt temp 200 200 $[Tdamp]  x 1 1 $[Pdamp] y 1 1 $[Pdamp] z 1 1
$[Pdamp]

#run     1000000

#unfix NPT3
```

```
fix NVE all nve

fix fE sol efield 0.01714286 0.0 0.0          #0.01714286V/A in x direction


compute cOw Ow chunk/atom bin/1d x lower 1.0      # 1 A per bin

fix cOw Ow ave/chunk 20000 1 20000 cOw density/mass density/number ave running file densOw.txt

compute cHw Hw chunk/atom bin/1d x lower 1.0      # 1 A per bin

fix cHw Hw ave/chunk 20000 1 20000 cHw density/mass density/number ave running file densHw.txt

compute cN N chunk/atom bin/1d x lower 1.0        # 1 A per bin

fix cN N ave/chunk 20000 1 20000  cN density/mass density/number ave running file densN.txt

compute cHn Hn chunk/atom bin/1d x lower 1.0      # 1 A per bin

fix cHn Hn ave/chunk 20000 1 20000 cHn density/mass density/number ave running file densHn.txt

compute cNa Na chunk/atom bin/1d x lower 1.0      # 1 A per bin

fix cNa Na ave/chunk 20000 1 20000 cNa density/mass density/number ave running file densNa.txt

compute cOs Os chunk/atom bin/1d x lower 1.0      # 1 A per bin

fix cOs Os ave/chunk 20000 1 20000 cOs density/mass density/number ave running file densOs.txt

compute cS S chunk/atom bin/1d x lower 1.0        # 1 A per bin

fix cS S ave/chunk 20000 1 20000  cS density/mass density/number ave running file densS.txt


compute rdfOwOw all rdf 100 1 1

fix rdfOwOw all ave/time 20000 1 20000  c_rdfOwOw[*] file rdfOwOw.txt mode vector

compute rdfOwHw all rdf 100 1 2
```

```
fix rdfOwHw all ave/time 20000 1 20000  c_rdfOwHw[*] file rdfOwHw.txt mode
vector

compute rdfOwN all rdf 100 1 3

fix rdfOwN all ave/time 20000 1 20000  c_rdfOwN[*] file rdfOwN.txt mode vector

compute rdfOwHn all rdf 100 1 4

fix rdfOwHn all ave/time 20000 1 20000  c_rdfOwHn[*] file rdfOwHn.txt mode
vector

compute rdfOwNa all rdf 100 1 5

fix rdfOwNa all ave/time 20000 1 20000  c_rdfOwNa[*] file rdfOwNa.txt mode
vector

compute rdfOwOs all rdf 100 1 6

fix rdfOwOs all ave/time 20000 1 20000  c_rdfOwOs[*] file rdfOwOs.txt mode
vector

compute rdfOwS all rdf 100 1 7

fix rdfOwS all ave/time 20000 1 20000  c_rdfOwS[*] file rdfOwS.txt mode vector

compute rdfOwPt all rdf 100 1 8

fix rdfOwPt all ave/time 20000 1 20000  c_rdfOwPt[*] file rdfOwPt.txt mode
vector


compute rdfHwHw all rdf 100 2 2

fix rdfHwHw all ave/time 20000 1 20000  c_rdfHwHw[*] file rdfHwHw.txt mode
vector

compute rdfHwN all rdf 100 2 3

fix rdfHwN all ave/time 20000 1 20000  c_rdfHwN[*] file rdfHwN.txt mode vector

compute rdfHwHn all rdf 100 2 4

fix rdfHwHn all ave/time 20000 1 20000  c_rdfHwHn[*] file rdfHwHn.txt mode
vector

compute rdfHwNa all rdf 100 2 5

fix rdfHwNa all ave/time 20000 1 20000  c_rdfHwNa[*] file rdfHwNa.txt mode
vector
```

```
compute rdfHwOs all rdf 100 2 6

fix rdfHwOs all ave/time 20000 1 20000  c_rdfHwOs[*] file rdfHwOs.txt mode
vector

compute rdfHwS all rdf 100 2 7

fix rdfHwS all ave/time 20000 1 20000  c_rdfHwS[*] file rdfHwS.txt mode vector

compute rdfHwPt all rdf 100 2 8

fix rdfHwPt all ave/time 20000 1 20000  c_rdfHwPt[*] file rdfHwHw.txt mode
vector


compute rdfNN all rdf 100 3 3

fix rdfNN all ave/time 20000 1 20000 c_rdfNN[*] file rdfNN.txt mode vector

compute rdfNHn all rdf 100 3 4

fix rdfNHn all ave/time 20000 1 20000 c_rdfNHn[*] file rdfNHn.txt mode vector

compute rdfNNa all rdf 100 3 5

fix rdfNNa all ave/time 20000 1 20000 c_rdfNNa[*] file rdfNNa.txt mode vector

compute rdfNOs all rdf 100 3 6

fix rdfNOs all ave/time 20000 1 20000 c_rdfNOs[*] file rdfNOs.txt mode vector

compute rdfNS all rdf 100 3 7

fix rdfNS all ave/time 20000 1 20000 c_rdfNS[*] file rdfNS.txt mode vector

compute rdfNPt all rdf 100 3 8

fix rdfNPt all ave/time 20000 1 20000 c_rdfNPt[*] file rdfNPt.txt mode vector


compute rdfHnHn all rdf 100 4 4

fix rdfHnHn all ave/time 20000 1 20000 c_rdfHnHn[*] file rdfHnHn.txt mode vector

compute rdfHnNa all rdf 100 4 5

fix rdfHnNa all ave/time 20000 1 20000 c_rdfHnNa[*] file rdfHnNa.txt mode vector

compute rdfHnOs all rdf 100 4 6
```

```
fix rdfHnOs all ave/time 20000 1 20000 c_rdfHnOs[*] file rdfHnOs.txt mode vector

compute rdfHnS all rdf 100 4 7

fix rdfHnS all ave/time 20000 1 20000 c_rdfHnS[*] file rdfHnS.txt mode vector

compute rdfHnPt all rdf 100 4 8

fix rdfHnPt all ave/time 20000 1 20000 c_rdfHnPt[*] file rdfHnPt.txt mode vector


compute rdfNaNa all rdf 100 5 5

fix rdfNaNa all ave/time 20000 1 20000  c_rdfNaNa[*] file rdfNaNa.txt mode
vector

compute rdfNaOs all rdf 100 5 6

fix rdfNaOs all ave/time 20000 1 20000  c_rdfNaOs[*] file rdfNaOs.txt mode
vector

compute rdfNaS all rdf 100 5 7

fix rdfNaS all ave/time 20000 1 20000  c_rdfNaS[*] file rdfNaS.txt mode vector

compute rdfNaPt all rdf 100 5 8

fix rdfNaPt all ave/time 20000 1 20000  c_rdfNaPt[*] file rdfNaPt.txt mode
vector


compute rdfOsOs all rdf 100 6 6

fix rdfOsOs all ave/time 20000 1 20000  c_rdfOsOs[*] file rdfOsOs.txt mode
vector

compute rdfOsS all rdf 100 6 7

fix rdfOsS all ave/time 200000 1 200000  c_rdfOsS[*] file rdfOsS.txt mode vector

compute rdfOsPt all rdf 100 6 8

fix rdfOsPt all ave/time 200000 1 200000  c_rdfOsPt[*] file rdfOsPt.txt mode
vector


compute rdfSS all rdf 100 7 7

fix rdfSS all ave/time 200000 1 200000  c_rdfSS[*] file rdfSS.txt mode vector
```

```
compute rdfSPt all rdf 100 7 8
fix rdfSPt all ave/time 200000 1 200000  c_rdfSPt[*] file rdfSPt.txt mode vector

compute msdOw Ow msd
fix msdOw all ave/time 20000 1 20000 c_msdOw[*] file msdOw.txt mode vector
compute vacfOw Ow vacf
fix vacfOw all ave/time 20000 1 20000 c_vacfOw[*] file vacfOw.txt mode vector

compute msdHw Hw msd
fix msdHw all ave/time 20000 1 20000 c_msdHw[*] file msdHw.txt mode vector
compute vacfHw Hw vacf
fix vacfHw all ave/time 20000 1 20000 c_vacfHw[*] file vacfHw.txt mode vector

compute msdN N msd
fix msdN all ave/time 20000 1 20000 c_msdN[*] file msdN.txt mode vector
compute vacfN N vacf
fix vacfN all ave/time 20000 1 20000 c_vacfN[*] file vacfN.txt mode vector

compute msdHn Hn msd
fix msdHn all ave/time 20000 1 20000 c_msdHn[*] file msdHn.txt mode vector
compute vacfHn Hn vacf
fix vacfHn all ave/time 20000 1 20000 c_vacfHn[*] file vacfHn.txt mode vector

compute msdNa Na msd
fix msdNa all ave/time 20000 1 20000 c_msdNa[*] file msdNa.txt mode vector
compute vacfNa Na vacf
```

```
fix vacfNa all ave/time 20000 1 20000 c_vacfNa[*] file vacfNa.txt mode vector

compute msdOs Os msd
fix msdOs all ave/time 20000 1 20000 c_msdOs[*] file msdOs.txt mode vector
compute vacfOs Os vacf
fix vacfOs all ave/time 20000 1 20000 c_vacfOs[*] file vacfOs.txt mode vector

compute msdS S msd
fix msdS all ave/time 20000 1 20000 c_msdS[*] file msdS.txt mode vector
compute vacfS S vacf
fix vacfS all ave/time 20000 1 20000 c_vacfS[*] file vacfS.txt mode vector

run 1000000

write_restart Ptsalt_0.25_7.efield1
write_data Ptsalt_0.25_7.efield1
```